Title
Hybrid Simulation of the Seismic Response of Squat Reinforced Concrete Shear Walls

Permalink
https://escholarship.org/uc/item/2xw5h8xc

Author
Whyte, Catherine Alexandra

Publication Date
2012

Peer reviewed|Thesis/dissertation

Hybrid Simulation of the Seismic Response of Squat Reinforced Concrete Shear Walls

By

Catherine Alexandra Whyte

A dissertation submitted in partial satisfaction of the

requirements for the degree of

Doctor of Philosophy

in

Engineering – Civil and Environmental Engineering

in the

Graduate Division

of the

University of California, Berkeley

Committee in charge:

Professor Bozidar Stojadinovic, Chair
Professor Stephen Mahin
Professor John Strain

Fall 2012

Hybrid Simulation of the Seismic Response of Squat Reinforced Concrete Shear Walls

Abstract

Hybrid Simulation of the Seismic Response of Squat Reinforced Concrete Shear Walls

by

Catherine Alexandra Whyte

Doctor of Philosophy in Engineering – Civil and Environmental Engineering

University of California, Berkeley

Professor Bozidar Stojadinovic, Chair

Most industrial and nuclear facilities rely on reinforced concrete structural walls as their primary seismic lateral-force-resisting components. These walls commonly have an aspect ratio smaller than 0.5 and have a very high stiffness and strength. There is a significant uncertainty regarding the behavior of these walls under earthquake loading, their failure modes, and their expected strengths and deformation capacities. Hybrid simulation is an effective experimental method to examine these issues: it enables simulation of the seismic response of squat and thick shear walls without the need to recreate the, often very large, mass associated with the rest of the prototype structure. A new method for hybrid simulation of the earthquake response of stiff specimens using a high-precision displacement encoder was developed and verified in this study. This method was implemented for hybrid simulation of seismic response of two large-scale squat reinforced concrete shear walls.

In order to examine the response of squat reinforced concrete walls to earthquake ground motion and to investigate the effect of ground motion sequence, two nominally identically 8 in thick models of a prototype 36 in thick structural wall, typically found in nuclear facility structures, were tested. Each wall experienced a different ground motion level loading sequence. After an initial combined shear and flexural response, a sliding shear failure occurred at the base of the walls. This response was quasi-brittle: the walls rapidly lost strength with small increments of post-peak strength deformation. A nominally identical specimen was tested at the State University of New York at Buffalo. Though the quasi-static cyclic test method has been

1

shown to accurately predict the seismic failure modes of ductile, often flexure-dominated, specimens, there is considerable uncertainty associated with the predictive ability of the quasi-static cyclic test method when the tested specimens have brittle or quasi-brittle failure modes. In these cases, the effect of load magnitude history is so significant that it alters the deformation demand and the sequence of seismic failure modes. The quasi-static cyclic test at Buffalo was compared to the hybrid seismic response simulation experiments at Berkeley to evaluate its effectiveness with capturing the wall response to ground motion sequences.

The findings from the hybrid simulation tests were that displacement control hybrid simulation using a high-precision encoder for displacement feedback is an effective way to perform large-scale hybrid tests of stiff specimens. This new method is useful to address the shortcomings with understanding the dynamic behavior of these types of specimens. The results of the two wall hybrid simulation tests indicate that different earthquake magnitude sequences do not have a significant effect on the force-deformation response and the failure mode sequence of squat walls. After comparing the hybrid simulation test results to the quasi-static cyclic test at Buffalo, the quasi-static cyclic test was determined to be adequate for testing the quasi-brittle wall specimens. It effectively captured the global response of the squat shear walls in earthquake ground motion sequences.

Comparison of wall response to code based predictive equations showed that the code equations overpredict the peak shear strength of these squat rectangular walls by factors as large as 2. Modifications to code recommendations for the initial stiffness and peak shear strength of these walls are offered, and a definition for the "essentially elastic" region, used in nuclear facility design, is also suggested.

To my Grandparents

TABLE OF CONTENTS

LIST OF FIGURES

LIST OF TABLES

ACKNOWLEDGMENTS

Dr. Susan Garfin, Mrs. Kathy Wong, Mr. Kendall Young, and Mr. Kai Stoeckenius, knew how to put a smile on my face early in the morning and encouraged me to finish writing this thesis.

I am thankful to Mr. Michael Mills for his enduring love, support, and encouragement. He stood by my side through everything, and he is a very special person in my heart.

I am grateful to my Mom and Dad, who have been unwavering in their love and their enthusiasm for my pursuits. They have been continuously supportive of me through every step of my education. I am extremely fortunate, and my love goes to my wonderful family.

1 Introduction

1.1 MOTIVATION

Low-aspect-ratio reinforced concrete walls are commonly used as the lateral-force-resisting system in nuclear and industrial structures. Knowledge about strength and deformation capacities of these walls comes from laboratory tests, but there is substantial scatter in this data. The source of this scatter is the complex interaction of flexure, shear, and sliding shear failure modes that these walls experience. Size effects associated with small scale models and the predetermined cycles of a quasi-static loading sequence commonly employed for testing both contribute to uncertainties about squat wall behavior in ground motion excitations. Additionally, nuclear facility structures are very stiff and have a short natural vibration period, putting them in the acceleration sensitive range of a typical earthquake response spectrum. Though nuclear facility structures are designed to remain "essentially elastic" in a design basis earthquake (DBE), any small yielding of a structure in the acceleration sensitive region causes a large increase in displacement ductility demand. With the quasi-brittle nature of these walls, such that they initially behave in a ductile flexural mode and transition to a brittle shear mode, the displacement ductility capacities are very limited, and the walls can abruptly lose strength. Thus, it is critical to understand the strength and deformation capacities of these walls such that this "essentially elastic" state can be defined appropriately. Furthermore, a sequence of earthquakes, a main shock followed by an aftershock of different intensities, may have a further adverse effect on the post-yield response of squat walls. This issue has not been investigated before. Finally, as a result of the scatter in test data, analysis models have also been shown to poorly predict the behavior of squat shear walls and must be improved with new experimental findings.

1.2 BACKGROUND

Most industrial and nuclear facilities are low-rise reinforced concrete buildings with a large footprint. Generally, their structural walls are used as the primary seismic lateral-force-resisting components. In nuclear facility structures, the walls are designed to have as few openings as possible to prevent radiation leaks. This design is also typical in industrial structures to simplify construction; few access points and windows are required. Thus, the resulting structural systems are comprised of long walls with a relatively short height. Nuclear facility walls are designed to be thick for radiation shielding as well as blast and fire protection. Similar thick walls are also found in industrial structures. The combination of a squat and thick wall geometry results in a

high initial wall stiffness. The structure which contains many of these walls then becomes very stiff also, i.e. has a very short fundamental mode vibration period. Consequently, the seismic shear demands on such structures can be very large. Most design codes define squat walls to have an aspect ratio ≤ 2.0. In nuclear facility structures, this aspect ratio is commonly ≤ 0.5. Figure 1.1 below shows an example of a squat wall during construction for a nuclear reactor in Finland.

Figure 1.1 Shear Wall in Finland's Nuclear Reactor in Olkiluoto <http://www.enviro-space.com>

The "essentially elastic" design goal for shear walls in nuclear facility structures in a DBE means the walls experience only a slight amount of yielding in such an event. However, this approach is potentially problematic for a very stiff structural element. The displacement ductility demand for a very stiff structure (with a short natural vibration period) may be very large even if the structure yields only slightly (Chopra, 2007). Therefore, it is important to investigate behavior of stiff shear walls in case the structure experiences an earthquake ground motion that introduces much larger seismic shear demands than those considered in design. To further complicate matters, current building code equations have been shown to generally overpredict the peak shear strength capacity of squat reinforced concrete shear walls, and do so excessively in some cases. From test data compiled by Gulec (2005), the design equations were shown to overpredict peak shear strength by a factor larger than 3.

Design codes promote energy dissipation through the ductile mechanism of flexural yielding rather than shear. Flexural behavior is considered safer because the structural element can be designed to safely undergo significant deformation before failure. This design is very effective for tall slender walls, which bend easily: the flexural behavior of these structural walls is well-characterized (Paulay et al. 1982). However, squat walls tend to fail in shear and/or in sliding shear because their geometry restricts them from bending easily. Both shear failure modes are undesirable because they constitute a quasi-brittle response, such that the structural element loses strength and stiffness rapidly with small increments of inelastic deformation.

Due to the quasi-brittle behavior and complexity of interacting failure modes in squat shear walls, there is significant uncertainty with identifying a backbone curve to describe the wall behavior. Additionally, there is a lack of adequate testing. The majority of squat shear wall tests have been performed on a shaking table or quasi-statically. Shaking table tests are advantageous because they use the actual ground motion input. However, in most cases, the walls are built at a very small scale to accommodate shaking table dimensions. Reducing the scale of a reinforced concrete model involves appropriately scaling both the aggregate and rebar sizes. Thus, it is very difficult to match the behavior of the scaled specimen to the prototype, so it is imperative that tests be performed at the largest possible scale. Many previous squat walls tests were performed with a quasi-static loading sequence. The standard quasi-static reinforced concrete testing protocol from ITG 1.1 (ACI ITG/T1.1-01 2001) requires a series of predetermined cycles with increasing amplitude, which represent the increasing drifts the structure is expected to experience in the ground motion considered. It is unclear, however, if this protocol adequately represents the actual seismic demands on a squat wall in a typical nuclear or industrial structure. Additionally, most quasi-static tests of squat walls have not had the thickness characteristic of nuclear or industrial type walls. Therefore, hybrid simulation is a good choice for testing squat walls because it combines a dynamic response simulation with a large scale physical test. A large scale test reduces any size effects. The use of a ground motion input avoids the uncertainty whether the quasi-static test is representative of ground motion behavior. Additionally, hybrid simulation incorporates a numerical model, so one component can be tested in large scale and other aspects of the structure can be modeled numerically.

1.3   RESEARCH OBJECTIVES AND SCOPE

The research described in this dissertation contributes to the NEES-R Project: Performance-Based Design of Squat Concrete Walls of Conventional and Composite Construction. This is a collaboration between researchers at The State University of New York at Buffalo, University of California, Berkeley, and University of Washington. The State University of New York at Buffalo and University of California, Berkeley teams are focused on experimental testing, aiming to improve understanding of the capacities of squat shear walls and to provide test data for calibrating numerical models. The University of Washington team is focused on numerical modeling to better quantify squat wall demands.

Since the data obtained by Gulec (2005) came from many experimental sources with a variety of testing parameters, the University at Buffalo team investigated the behavior of squat walls with varying aspect ratios and reinforcement ratios using standard quasi-static loading and a consistent test setup for all cases. The University of California, Berkeley team conducted hybrid simulations of earthquake response on two squat walls, which are the focus of this dissertation, to investigate the effect of ground motion load sequence, compare to the quasi-static test results, and validate the finite element models. No vertical load was applied to the wall specimens.

Hybrid simulation of the earthquake response of squat shear walls is challenging due to the high stiffness of the walls. Conventional displacement-controlled hybrid simulation cannot achieve small enough displacement increments to ensure a smooth force response for a stiff specimen. Force control methods and a high-precision displacement controlled method were

considered, and the latter was selected for testing. The hybrid simulation tests were used to investigate the effect of loading sequence on squat walls.

The following summarizes the project objectives for the Berkeley tests:

- Establish a hybrid testing method that accommodates a stiff specimen.
- Perform two hybrid simulations of the earthquake response of two nominally identical squat shear walls, investigating the effect of different ground motion loading sequences.
- Validate the use of quasi-static testing for stiff squat shear walls through comparison to hybrid simulation seismic response data.
- Contribute to improvements of code-based predictions of squat wall peak shear strength and initial stiffness.
- Provide data to improve and validate finite element models of squat shear walls.
- Contribute data to improve and validate design models for strength and deformation capacity of squat walls.

1.4   ORGANIZATION OF DISSERTATION

The steps performed at University of California, Berkeley to achieve the objectives outlined above will be presented as follows: Chapter 2 will provide a literature review, including squat wall failure modes, previous experimental programs, and current design codes. Chapter 3 will present an introduction to hybrid simulation and existing displacement and force control methods. The selected high-precision displacement control method using an encoder will be described. Chapter 4 will address the necessary modifications to the *nees@Berkeley* hybrid simulation laboratory for encoder control and describe validation tests performed for using this new method. Chapter 5 will introduce the experimental program for the two hybrid simulation tests of seismic response of squat shear walls. Chapter 6 will present the results for each of the squat shear walls and compare their behaviors. Chapter 7 will compare the hybrid simulation results to the cyclic quasi-static test performed at the University at Buffalo using a nominally identical squat shear wall. Chapter 8 will compare the hybrid simulation tests results to the results from an OpenSees model using the Flexure-Shear Interaction Displacement-Based Beam-Column Element, developed by Massone et al. (2006). Chapter 9 will summarize and draw conclusions from the squat shear wall tests and recommend future studies.

2 Squat Wall Behavior

2.1 INTRODUCTION

This research is motivated by four principal concerns: 1) The interaction between flexure, shear, and sliding shear failure modes in squat reinforced concrete walls must be better characterized. 2) Design code equations do not predict the peak shear strength of squat walls with sufficient certainty, even in cases of monotonic loading. 3) Load history affects wall behavior, but difficulties persist to test such stiff wall specimens with ground motion excitations at large scale. Monotonic and also quasi-static cyclic tests have been performed on squat walls, but very few tests have examined ground motion excitations, except on a shaking table in very small scale. 4) Nuclear facility structures are designed to remain "essentially elastic" in a DBE earthquake, meaning they will only experience a small amount of yielding. However, stiff structures develop large deformation ductility demands if they are not strong enough to remain elastic. Thus, the available deformation ductility capacity of squat walls is important to quantify in order to determine the appropriate force demand to use for design.

2.2 SHEAR FAILURE MODES

Design codes intend walls to dissipate energy in a ductile fashion in flexure (bending) and suppress any shear failure. This design goal is achieved in tall walls, but squat walls, with aspect ratios ≤ 2.0, tend to fail in a mixed flexure-shear mode or in pure shear. As the aspect ratio of the wall decreases, the wall is much more likely to fail in pure shear. Reference to a "shear failure" means one (or more) of the three shear failure modes described here. Two of these modes are pure shear modes and one is a sliding shear mode. All modes occur in the plane of the wall (no out-of-plane behavior). The failures are brittle in nature, meaning they occur suddenly, and are not preceded by significant yielding, either in flexure or in tension induced by shear. After Gulec (2005) compiled existing data from tests of squat shear walls beginning in the late 1940s, he reported that the three major failure modes of squat walls are diagonal tension, diagonal compression, and sliding shear.

5

2.2.1 Diagonal Tension Failure

A diagonal tension failure is common in squat walls with light horizontal reinforcement. The horizontal reinforcement, which had been resisting the principal tensile stresses, yields and widely spaced diagonal cracks form. The horizontal reinforcement yields further as the cracks widen. Walls with a rigid beam above them tend to form a corner to corner crack. Otherwise, the walls tend to form a diagonal crack at 45 degrees. This failure mode can be prevented by providing sufficient horizontal reinforcement. An example of diagonal tension failure is shown in Figure 2.1.

Figure 2.1 Diagonal Tension Failure (Gulec 2009, from Hildago 2001)

2.2.2 Diagonal Compression Failure

Adding horizontal reinforcement to prevent a diagonal tension failure can lead to a diagonal compression failure mode instead. In this case, as the specimen experiences cyclic loading, diagonal cracks form in both directions. These are repeatedly opened and closed, which weakens the concrete struts. Ultimately, the concrete struts are crushed near the base of the wall. This type of failure mode occurs for walls with a very high shear stress. It is typically found for walls with flanges or barbells or walls with a high axial load. The shear walls in nuclear facility structures investigated in this dissertation are unlikely to form this failure mode, considering they are rectangular walls and carry a small axial load relative to their axial load capacity. An example of a diagonal compression failure is shown in Figure 2.2.
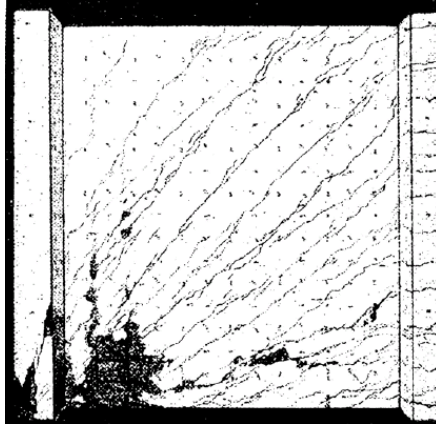
Figure 2.2 Diagonal Compression Failure (Gulec 2009, from Maier and Thurlimann 1985)

2.2.3   Sliding Shear Failure

This failure mode often occurs in walls with sufficient reinforcement to prevent a diagonal tension failure and with low axial loads, so a diagonal compression failure is unlikely. The initial shear transfer mechanism prior to damage is aggregate interlock in the compression zone (Synge 1980). As the wall is cycled, the vertical reinforcement in the tension zone at the base of one end of the wall yields in flexure and elongates. This causes cracking at the interface between the wall and the foundation. Upon load reversal, the elongated vertical bars do not allow the cracks to close. On the other side of the wall, the vertical reinforcement, now in the tension zone, similarly yields and elongates. Upon load reversal, the elongated vertical bars on that side of the wall also do not allow the cracks to close. Now, at the ends of the walls, there is insufficient contact between the wall and the foundation in the compression zone to transfer shear. The wall must slip until enough contact forms between the wall and foundation aggregate to transfer the force. As the wall is cycled, further yielding occurs in the vertical reinforcement, and rough pieces of concrete continue to break, smoothing the surface between the wall and the foundation. The wall must slip even further for aggregate interlock to occur. As aggregate interlock becomes less effective, dowel action of the vertical reinforcing bars becomes the predominant force transfer mechanism (Synge 1980). Each time the wall is cycled, it must slip at least as much as it did in the previous cycle before the concrete bears on the vertical reinforcement to transfer the force again. In the case of thick squat walls, as are prevalent in nuclear facility structures, there may be a substantial portion of the section between the two reinforcement curtains that is essentially unreinforced. The vertical reinforcement may be less effective in holding the cracks closed. Furthermore, the space between the vertical reinforcing bars across the width of the wall may render the dowel action less effective as the sliding shear mechanism develops. A picture of a squat wall sliding shear failure tested by Synge (1980) is shown in Figure 2.3. This wall had an aspect ratio of 0.5 and the following dimensions: 118 in (3000 mm) x 59 in (1500 mm) x 3.9 in (100 mm). These dimensions are very similar to the walls tested in my dissertation, except Synge's walls had approximately half of the thickness and only one curtain of reinforcement instead of two.
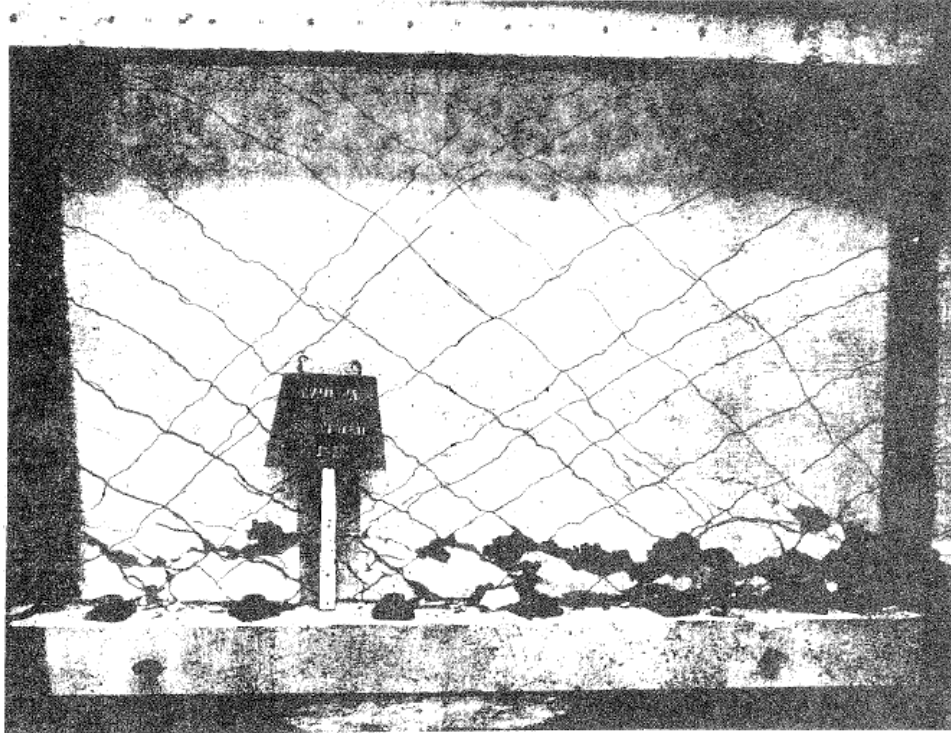
Figure 2.3 Sliding Shear Failure (Synge 1980)

2.3   PREVIOUS SQUAT WALL TESTS

There have been many squat shear wall tests since the late 1940s, but most tests have been performed on small-scale walls that do not have enough thickness to represent a nuclear or industrial structure. When the thickness of a specimen is increased, the force capacity increases very quickly. Most laboratories do not have the equipment that can apply large enough forces to test large-scale specimens with adequate thicknesses. Additionally, most prior squat wall tests were performed quasi-statically.   Since the shear failure modes of concern here are brittle, involving aggregate interlock and friction, they are highly dependent on both the specimen size and the number of cycles that the specimen experiences. Brittle failure involves a variety of fracture phenomena in reinforced concrete, all of which suffer from size effect.

The size effect is explained as follows. For an equivalent nominal stress applied to a larger and smaller specimen, a unit extension of a crack in the larger specimen will release more strain energy because the fracture zone is physically larger. However, this fracture energy (energy dissipated per area of the fracture surface), which is required for a unit extension of a crack, is a property of the material, so it is approximately constant for any specimen size. In order to maintain similarity, the larger specimen must achieve a lesser nominal strength. Thus, the size effect causes the larger specimen to appear weaker, and tests of squat walls in small scale may overestimate the strength of the walls.

Due to the size effect described above, it is important to test walls at the largest scale possible. Additionally, due to the brittle nature of the failure modes of interest, a small scale specimen may not adequately reflect the shear failure mode behaviors of the full-scale specimen. It is unclear whether the standard quasi-static test procedure from ITG 1.1 (ACI ITG/T1.1-01 2001)

8

adequately captures the dynamic response of squat shear walls. This procedure involves predetermining groups of repeated cycles with increasing amplitude that represent drifts the structure is expected to experience in a given ground motion. Though some previous squat shear wall tests were performed dynamically on a shaking table, the small size of the specimens used still introduced size effect problems.

The following provides a brief summary of some of the tests that were included in Gulec's (2005) database of squat wall tests. The general focus of most of these tests was the ultimate in-plane shear strength of walls. The Department of the Army Corps of Engineers funded the first monotonic tests of squat shear walls at MIT and Stanford University in 1949 (Galletly 1952, Benjamin and Williams 1954). Then the Department of the Army funded further tests at MIT (Antebi et al. 1960). The first cyclic tests of squat walls occurred in the 1970s, most famously tests by Barda et al. (1976). Synge (1980), under the supervision of Paulay and Priestley at the University of Canterbury, tested four squat walls with aspect ratios less than 0.5. Two of the walls were rectangular and two had flanges. One wall in each group had conventional orthogonal reinforcement, and the other had diagonal reinforcement. He observed sliding shear failure in the walls. The diagonal reinforcement reduced the base slip and improved the hysteretic behavior. The flanges caused base slip to begin at smaller displacements.

The first earthquake-simulator and nuclear-specific shear wall tests began in 1980 when the Nuclear Regulatory Commission's Office of Nuclear Regulatory Research funded experiments at Los Alamos National Lab (The Seismic Category I Structures Program). Results showed that the elastic stiffnesses measured experimentally were much lower than the theoretical strength-of-materials values. A Technical Review Group (TRG) investigated this discrepancy by testing 15 TRG walls. They determined that the low experimental elastic stiffness results from the Seismic Category I Structures Program were due to experimental errors and possible damage to the specimens during transportation. The results from the TRG structures were more reliable, and the experimentally measured stiffnesses were comparable to the strength-of-materials calculated values (Farrar and Baker 1993).

Wood (1990) reviewed tests of 143 squat shear walls, compiling data from Japanese investigators (Aoyagi, Hirosawa, Kabeyasawa, Kokusho, Ryo, Sugano, Tanabe, Tsuboi, and Yoshizaki) and Stanford University tests (1952-1956). She proposed an equation for a lower-bound estimate of nominal shear strength in squat walls.

Sozen and Moehle (1993) reviewed force-displacement response data from Maier and Thurlimann (1985), Rothe (1992), and Inada (1986). They investigated differences between initial elastic stiffnesses of walls using strength-of-materials calculations and experimentally measured initial elastic stiffnesses. From 41 data sets, they found that measured initial stiffnesses were generally less than the stiffness calculated using the strength-of-materials approach. The mean value of the ratio of measured to calculated stiffness was about 0.7, but there was a wide scatter.

In 2006, a full scale shake table test of a six-story reinforced concrete building with squat shear walls (aspect ratio = 0.5) in each story was performed at E-Defense in Japan. However, this was not a nuclear test, so the wall thicknesses were less than those in a nuclear facility structure. First, there was significant flexural response with uplift of the boundary elements, causing a soft first story. Then diagonal cracking began, and the ultimate failure was sliding-shear along the entire length of the wall connected to the foundation. The behavior of the structure was not predictable with our current understanding of squat shear walls. The experimental results are summarized in Kim (2007).

The SAFE-Structures Armees Faiblement Elancees test program included pseudo-dynamic tests of 13 reinforced concrete squat walls with flanges at ELSA Laboratory in Ispra, Italy (Naze and Sidaner 2001). They investigate dynamic behavior of squat walls, some with Carbon Fiber Reinforced Polymer in horizontal and vertical bands on the exterior of the wall face. The acceleration record used was not specified.

2.4 CURRENT CODES PERTAINING TO SQUAT WALL BEHAVIOR

2.4.1 Structural Design Codes

Sections 11.6, 11.9, and 21.9 of ACI 318-08, *Building Code Requirements for Structural Concrete and Commentary*, give equations for peak shear strength of squat walls. These equations are intended for computing the peak strength of walls in buildings, not nuclear facility structures. Section 11.6 gives equations for shear friction, which relates to sliding shear strength. Section 11.9 gives design provisions for non-seismic lateral loads applied to structural walls, and Section 21.9 gives provisions for seismic lateral loads.

ASCE 43-05 (ASCE 2005), *Seismic Design Criteria for Structures, Systems, and Components in Nuclear Facilities*, provides seismic design criteria for nuclear facility structures. These criteria are more rigorous than building codes, so nuclear facilities to have a lower probability of structural damage in an earthquake than conventional structures. Each component in the nuclear facility structure is assigned a Seismic Design Basis (SDB), which is a combination of a Seismic Design Category (SDC) and a Limit State (LS). The Seismic Design Category determines the design basis earthquake (DBE). The SDC ranges from 1 to 5, where SDC-1 refers to a relatively low-risk structure and SDC-5 refers to a structure containing radioactive material. The LS determines the acceptance criteria. The LSs range from LS-A, meaning collapse prevention, to LS-D, meaning essentially elastic behavior with only slight yielding. Shear walls providing the lateral-force-resisting system in a structure containing radioactive material are designed with SDC-5 and LS-D. Using this designation, the target performance goal is a mean annual probability of 1×10^{-5} that the LS will not be exceeded. Shear controlled walls are defined as having an aspect ratio less than 2.

ASCE/SEI 7-10 (ASCE 2010), *Minimum Design Loads for Buildings and Other Structures*, governs design of industrial facilities. This code does not distinguish between tall and short walls, which behave very differently. Tall walls generally exhibit much greater ductility due to their ability to bend in flexure.

2.4.2 Structural Evaluation Codes

In the mid-1990s, the Federal Emergency Management Agency (FEMA) funded the ATC-33 Project to develop first-generation performance-based earthquake engineering guidelines for structural assessment and rehabilitation of existing buildings. This performance-based approach ensures that force and deformation capacities exceed demands for selected performance and hazard levels. Performance levels include Fully Functional, Immediate Occupancy, Life Safety,

and Collapse Prevention. The earthquake levels for which these performance levels should be achieved are 100-year return period (DBE, 10% in 50-year probability of exceedance) and 2500-year return period (Maximum Considered Earthquake, 2% in 50-year probability of exceedance). This document was published as American Society of Civil Engineers (ASCE) 41-06 (2007), *Seismic Rehabilitation of Existing Buildings* and ASCE 41-06 Supplement No. 1 (2007). Then it was revised further as the *Update to ASCE/SEI 41 Concrete Provisions* (Elwood et al. 2009). These are the current guidelines for existing non-nuclear facility structures. Here, squat walls are considered to have an aspect ratio less than 1.5 and to be controlled by shear. Since squat walls normally have limited ability to deform past the elastic range, they are typically considered to be displacement-controlled components with low ductility capacities or force-controlled components. The former designation is allowable for squat shear walls with axial load $\leq$ $0.15A_gf'_c$ (which is the case for walls in my study), and the latter designation for squat shear walls with higher axial loads.

American Concrete Institute (ACI) 349 (2006), *Code Requirements for Nuclear Safety Related Concrete Structures*, is the current guideline for evaluating existing nuclear facility structures. The code assumes that the shear walls attain their intended "essentially elastic" limit state in a DBE. This code adopts ACI 318-08, Sections 11.9 and 21.9 to predict shear strength of walls in nuclear facility structures.

2.4.3   Shear Wall Backbone Curve

The *Update to ASCE/SEI 41 Concrete Provisions* (Elwood et al. 2009) performance-based earthquake engineering guidelines includes backbone curves for creating nonlinear models. It adopts Wallace's (2007) modification to the backbone curve for the behavior of reinforced concrete walls governed by shear in order to include the cracking point F (shear strength ratio at cracking, V_{cr}/V_n), as shown in Figure 2.4. This curve shows the normalized shear capacity of the wall vs. the drift (wall top displacement/wall height). The strengths at points B and C are both taken to be the nominal shear strength ratio (V_n/V_n), which is calculated using Chapter 21.9 of ACI 318-08. The yield drift ratio is shown as g, the drift ratio corresponding to the start of shear strength degradation is shown as d, and the maximum drift ratio is shown as e. The strength ratio for yielding is shown as f, and the strength ratio for residual strength is shown as c. Drift ratios are g=0.4%, d=1.0%, and e=2.0%. Strength ratios are c=0.2 and f=0.6.
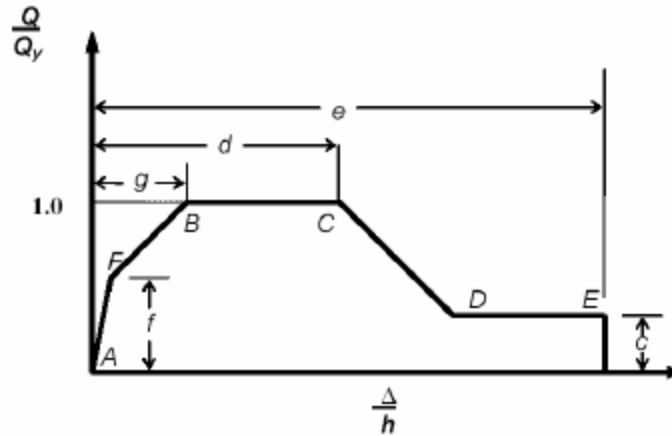
Figure 2.4 Load Displacement Relationship for RC Squat Shear Walls (Wallace 2006)

The shear strength at cracking, V_{cr}, and the drift angle at cracking, γ_{cr}, are calculated using the following equations.

$$V_{cr} = 0.5 V_n \tag{2.1}$$

$$\gamma_{cr} = \frac{V_{cr}}{0.4EA}$$

where A (in2) is the wall gross area (wall length x web thickness), Vn (lb) is the nominal shear strength, and E (psi) is the modulus of elasticity of the concrete. The wall ductility capacity prior to rapidly losing strength is the ratio of the drift at point C divided by the yield drift at point B. This value is 2.5. The wall will only deform 2.5 times its yield displacement before losing capacity. Tall walls generally fail in flexure and are able to maintain their capacity to much larger displacement ductilities.

The following discussion will evaluate the current code understanding of wall behavior by looking at various points on this force-deformation response envelop. The discussion will be organized in terms of Figure 2.4. Estimates of uncracked and cracked stiffnesses will be addressed in Section 2.5. Equations that describe predicted peak shear strengths will be given in Section 2.6. The predicted deformation capacities and post-peak behaviors will be addressed in Sections 2.7 and 2.8, respectively.

2.5   UNCRACKED AND CRACKED STIFFNESSES

The recommended values for uncracked and cracked stiffnesses, given in ASCE 43-05, the Update to ASCE 41, and recommended by Wallace (2006), are summarized in Table 2.1. The modulus of rigidity is G=0.4E.

12

Table 2.1: Recommended Stiffnesses

	Flexural Rigidity	Shear Rigidity
ASCE 43-05: Uncracked Walls	EI	GA
ASCE 43-05: Cracked Walls	0.5EI	0.5GA
Update to ASCE 41: Uncracked Walls	0.8EI	GA
Update to ASCE 41: Cracked Walls	0.5EI	GA
Wallace (2006)	-	0.5GA

For squat reinforced concrete walls, Wallace (2006) shows the proposed backbone curve together with data from a test by Hidalgo et al. (2002), replicated in Figure 2.5. The shear strength at cracking is taken as 0.5 times the peak shear strength. Then the initial uncracked stiffness is taken as the shear stiffness to this cracking point. The shear rigidity is effectively 0.5GA.
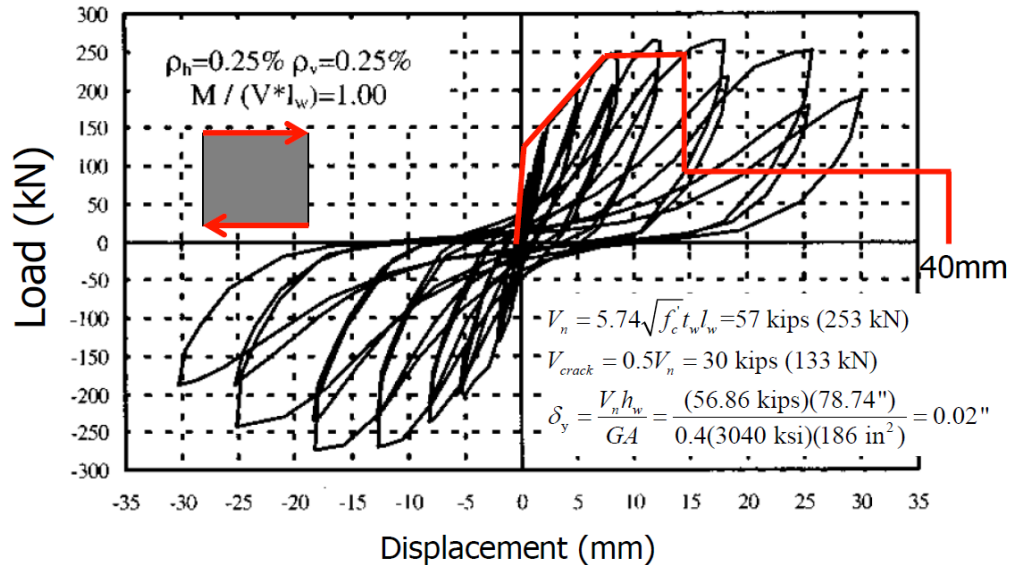
Figure 2.5: Wallace (2006) Backbone Curve with Hidalgo et al. (2002) Test Data

2.6 PREDICTED PEAK SHEAR STRENGTHS

The equations for peak shear strength considered are those recommended by Barda et al. (1976), Wood (1990), Gulec (2009), ACI 318-08 11.6, ACI 318-08 11.9, ACI 318-08 21.9, and ASCE 43-05. These are described in the following sub-sections.

2.6.1 Barda et al. Equation

Barda et al. (1976) presented the following equation for nominal shear strength of shear walls. This equation was derived based on results from experimental tests of 8 squat walls with heavily reinforced flanges.

13

$$V_n = \left(8\sqrt{f'_c} - 2.5\sqrt{f'_c} \frac{h_w}{l_w} + \frac{N_u}{4l_w t_w} + \rho_v f_{yv} \right) dt_w \qquad (2.2)$$

where f'_c (psi) is the concrete compressive strength, h_w is the height of the wall, l_w is the length of the wall, N_u (lb) is the factored axial force (negative in tension), t_w is the thickness of the wall, ρ_v is the vertical web reinforcement ratio, f_{yv} is the yield stress of vertical web reinforcement, and d is the distance from the extreme compression fiber to the area centroid of tension reinforcement. Barda et al. (1976) found that the actual strength of squat shear wall test specimens was significantly higher than that predicted by ACI. Their equation does not consider horizontal reinforcement.

2.6.2   Wood Equation

Wood (1990) compiled peak shear strengths from 143 squat wall tests, including rectangular walls and walls with boundary elements. She offered the following equation to predict nominal shear strength of squat walls,

$$6\sqrt{f'_c} A_w \leq V_n = \frac{A_v f_y}{4} \leq 10\sqrt{f'_c} A_w \qquad (2.3)$$

where f'_c (psi) is the concrete compressive strength, A_w is the gross area of the web of the wall (wall length x web thickness), A_v is the area of the total vertical reinforcement crossing the shear plane, and f_y is the reinforcement yield stress.

2.6.3   Gulec Equation

Gulec (2009) proposed the following equation for peak shear strength of shear-critical rectangular walls with an aspect ratio ≤ 1.0.

$$V_n = \frac{1.5\sqrt{f'_c} A_w + 0.25 F_{vw} + 0.2 F_{vbe} + 0.4P}{\sqrt{\frac{h_w}{l_w}}} \qquad (2.4)$$

where f'_c (psi) is the concrete compressive strength, A_w is the gross area of the web of the wall (wall length x web thickness), F_{vw} is the force attributed to vertical web reinforcement (product of vertical web reinforcement area and reinforcement yield stress), F_{vbe} is the force attributed to boundary element reinforcement, P is the axial force, h_w is the height of the wall, and l_w is the length of the wall.

2.6.4 ACI 318-08 Section 11.6 Equations

The design equations in ACI 318-08 apply to both tall and squat walls. Section 11.6 gives design provisions to prevent a shear transfer failure across a shear plane. For squat walls, this type of failure would occur as a sliding shear failure along the base of the wall. Section 11.6 assumes a crack forms along the shear plane considered, and reinforcement is provided across the crack to resist motion along the crack. The friction between crack faces and the dowel action of the reinforcement crossing the crack resist the applied shear. The nominal shear strength based on the shear-friction model is

$$V_n = A_v f_y \mu \tag{2.5}$$

where the coefficient of friction μ is 1.4λ for concrete placed monolithically, 1.0λ for concrete placed against hardened concrete with the surface intentionally roughened, or 0.6λ for concrete placed against hardened concrete not intentionally roughened. $\lambda = 1.0$ for normal weight concrete and 0.75 for lightweight concrete. V_n should not exceed the smaller of $0.2f'_c A_c$ and $800A_c$. For the purpose of design of shear-friction reinforcement, f_y should not exceed 60 ksi. The shear-friction model assumes that all the shear resistance comes from friction between the crack faces, which oversimplifies the actual behavior, so the coefficient of friction is artificially increased to provide nominal shear strengths that agree with test results. For the concrete placed against hardened concrete not intentionally roughened, most of the resistance is due to dowel action, so an appropriate coefficient of friction is used. The code notes that the shear-friction model conservative estimates the nominal shear strength. It allows use of the following modified shear-friction equation which considers the contribution of dowel action if $\rho f_y > 200$ psi.

$$V_n = 0.8 A_v f_y + A_c K_1 \tag{2.6}$$

where A_v is the area of the total reinforcement crossing the shear plane, f_y is the reinforcement yield stress, and A_c is the area of concrete section resisting shear transfer. $K_1 = 400$ psi, for normal weight concrete, or 200 psi, for lightweight concrete. The first term of the equation represents the contribution of shear-friction with 0.8 as the coefficient of friction, and the second term represents the resistance due to protrusions on the crack surface and dowel action. For the modified shear-friction equation to be valid, $A_v f_y / A_c$ should not be less than 200 psi.

2.6.5 ACI 318-08 Section 11.9 Equations

Section 11.9 gives design provisions for non-seismic lateral loads applied to structural walls. This section intends to prevent a diagonal tension failure and provides a maximum shear strength to prevent a diagonal compression failure. This section is intended mostly for low-rise walls since taller walls are generally controlled by flexure. The nominal shear strength is

$$V_n = V_c + V_s \leq 10 \sqrt{f'_c} \, d t_w \tag{2.7}$$

where V_c is the nominal shear strength of the concrete, V_s is the nominal shear strength of the reinforcement, f'_c (psi) is the concrete compressive strength, d is the distance from the extreme compression fiber to the centroid of tension reinforcement and can be taken as $0.8l_w$, where l_w is the length of the wall, and t_w is the wall thickness. V_c (lb) is the smaller of

$$V_c = 3.3\lambda\sqrt{f'_c}\,dt_w + \frac{N_u d}{4l_w}$$

(2.8)

$$V_c = \left[0.6\lambda\sqrt{f'_c} + \frac{l_w\left(1.25\lambda\sqrt{f'_c} + \frac{0.2N_u}{l_w t_w}\right)}{\dfrac{M_u}{V_u} - \dfrac{l_w}{2}} \right] dt_w$$

(2.9)

where N_u (lb) is the factored axial force (negative in tension), M_u (lb-in) is the factored moment, and V_u (lb) is the factored shear force. The second equation does not apply if the denominator is negative. These equations for the contribution of concrete strength are used to compute the inclined cracking strength of the concrete. The first equation is based on the occurrence of a principal tensile stress of approximately $4\lambda\sqrt{f'_c}$ at the centroid of the shear wall cross section. The second equation is based on the occurrence of a flexural tensile stress of approximately $6\lambda\sqrt{f'_c}$ at a section $l_w/2$ above the section considered. For walls in this study, the first equation controls. V_s is given by

$$V_s = \frac{A_v f_y d}{s}$$

(2.10)

where A_v (in^2) is the area of horizontal reinforcement within distance s, and s (in) is the spacing of horizontal reinforcement. The minimum horizontal reinforcement is $\rho_{h\,min}$=0.25% where the maximum spacing is not less than the smallest of $l_w/5$, 3h, and 18 in. The minimum vertical shear reinforcement ratio $\rho_{v\,min}$ is the larger of 0.25% and

$$\rho_v = 0.0025 + 0.5\left(2.5 - \frac{h_w}{l_w}\right)(\rho_h - 0.0025)$$

(2.11)

where ρ_h is the horizontal shear reinforcement ratio. The maximum spacing of vertical reinforcement is not less than the smallest of $l_w/3$, 3h, and 18 in. The code notes that test data shows that vertical shear reinforcement is more effective for low-rise walls, so the required vertical reinforcement is larger for low-rise walls.

16

2.6.6 ACI 318-08 Section 21.9 Equation

Section 21.9 gives design provisions for seismic design of structural walls. Like Section 11.9, it assumes a diagonal tension failure and provides a maximum shear strength to prevent a diagonal compression failure. The nominal shear strength is

$$V_n = \left(\alpha_c \lambda \sqrt{f'_c} + \rho_h f_{yh} \right) A_w \leq 10 \sqrt{f'_c} A_w \tag{2.12}$$

where α_c is the aspect ratio coefficient equal to 3.0 for $h_w/l_w \leq 1.5$, 2.0 for $h_w/l_w \geq 2.0$, and varies linearly between 3.0 and 2.0 for aspect ratios between 1.5 and 2.0, $\lambda = 1.0$ for normal weight concrete and 0.75 for lightweight concrete, f'_c (psi) is the concrete compressive strength, ρ_h is the horizontal reinforcement ratio, f_{yh} is the horizontal reinforcement yield stress, and A_w is the gross area of the web of the wall (wall length x web thickness). Section 21.9 requires vertical and horizontal web reinforcement to be uniformly distributed across the shear plane to limit inclined crack width. The minimum horizontal and vertical web reinforcement ratio is 0.25%. If the aspect ratio of the wall is ≤2.0, the vertical web reinforcement ratio ρ_v must be greater than or equal to the horizontal reinforcement ratio ρ_h. Maximum reinforcement spacing is 18 in each way. Two curtains of reinforcement are required if V_u exceeds $2 A_w \lambda \sqrt{f'_c}$. The web reinforcement must be in at least two curtains and the maximum spacing is 18 in.

For all sections of ACI 318-08, the nominal shear strengths have been stated. The design shear strength is

$$V_u \leq \phi V_n \tag{2.13}$$

where φ=0.75 for shear.

2.6.7 ASCE 43-05 Equation

ASCE 43-05 uses ACI 349, *Code Requirements for Nuclear Safety-Related Concrete Structures*, for all structural elements except squat shear walls (defined as having an aspect ratio ≤ 2.0). Instead, the following equation, proposed by Barda et al. (1976), is given below for nominal squat shear wall strength. This is similar to the equation found in Chapter 11 of ASCE 349-06 (ASCE 2006).

$$V_n = \left(8.3 \sqrt{f'_c} - 3.4 \sqrt{f'_c} \left(\frac{h_w}{l_w} - 0.5 \right) + \frac{N_u}{4 l_w t_w} + \rho_{se} f_y \right) d t_w \leq 20 \sqrt{f'_c} d t_w \tag{2.14}$$

$$\rho_{se} = A \rho_v + B \rho_h$$

where f'_c (psi) is the concrete compressive strength, h_w is the height of the wall, l_w is the length of the wall, N_u (lb) is the factored axial force (negative in tension), t_w is the thickness of the wall, ρ_{se} is the reinforcement ratio using ρ_h (horizontal) and ρ_v (vertical) reinforcement ratios, f_y is the

yield stress of the reinforcement, and d is the distance from the extreme compression fiber to the area centroid of tension reinforcement. The constants A and B are given in Table 2.2.

Table 2.2: Constants A and B

Aspect Ratio	A	B
$h_w/l_w \leq 0.5$	1	0
$0.5 \leq h_w/l_w \leq 0.5$	$- h_w/l_w + 1.5$	$h_w/l_w - 0.5$
$h_w/l_w \geq 0.5$	0	1

The design shear strength is

$$V_u \leq \phi V_n \tag{2.15}$$

where φ=0.8 for shear.

2.6.8   Uncertainty in Code-Predicted Shear Strengths

Gulec (2005) created a database from the results of tests from 352 squat shear walls (aspect ratio ≤ 2.0). For the 150 rectangular walls in his database, Gulec et al. (2009) presented a box-whisker plot, shown in Figure 2.6, that displayed the ratio of predicted strength to measured strength for 5 design equations. The equations reviewed were from ACI 318-08 Section 21.9 (shown as ACI 21.7 in the plot, from the section name used in the previous edition of the code), ACI 318-08 Section 11.9, Barda et al. (1976), ASCE/SEI 43-05, and Wood (1990). In the worst cases, the design code equations overpredict the peak shear strength of squat walls by a factor >3.
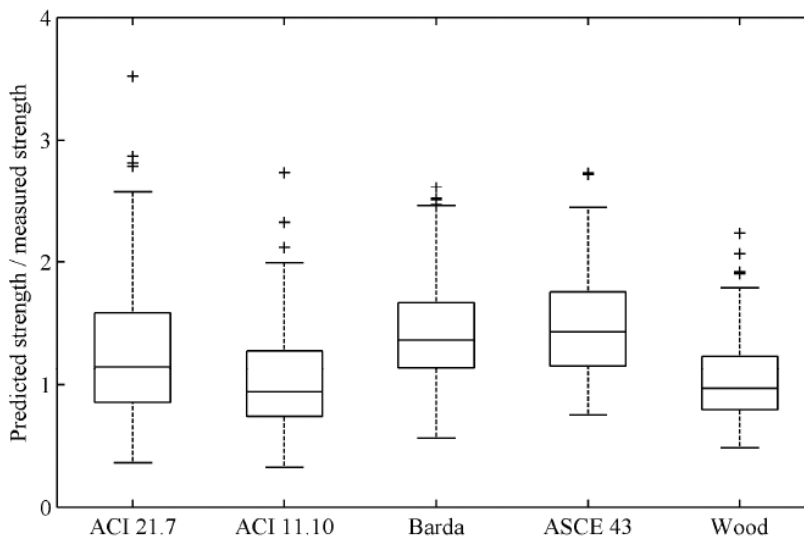
Figure 2.6 Ratio of Predicted to Measured Squat Wall Strength (Gulec 2009)

18

Gulec et al. (2009) concluded that ACI 11.10 was the more accurate of the two ACI sections predicting shear strength. ACI 21.9 overpredicts the shear strength of 67% of the walls. ACI 11.10 overpredicts the shear strength of 49% of the walls. The Barda et al. equation overpredicts the shear strength of 85% of the walls. The ASCE 43-05 equations overpredict the shear strength of 87% of the walls. Hence, Wood's predictive equation is most reliable. It overpredicts the shear strength of only 46% of the walls.

Gulec, Whittaker, and Stojadinovic (2008) reported on the scatter in the ratio of shear strength predicted by code equations to the maximum measured shear strength in a physical test for the rectangular walls in Gulec's database. They reviewed ACI 318-05 Chapter 21, ACI 318-05 Chapter 11, Barda et al. (1977), ASCE/SEI 43-05, and Wood (1990), and concluded that Wood's equation gave the best prediction for peak shear strength. They observed that Chapter 11 of ACI generally gave the lowest estimates of peak shear strength. They found that Barda et al. and ASCE 43-05 significantly overestimated peak shear strength, and they recommended against using these equations for walls with rectangular cross sections.

2.7 DEFORMATION CAPACITY

In ASCE 43-05, an inelastic energy absorption factor, F_μ, is provided for shear controlled walls. This factor ranges from 2 for LS-A to 1 for LS-D. It is similar to the force reduction factor, m, provided in ASCE 41 for non-nuclear facility shear walls. When a force reduction factor is >1, in either of the standards, it ensures that the structure will yield but still retain sufficient strength to prevent deformation past its intended limit state. The factor will not allow the structure to deform past peak strength into the negative stiffness region of the pushover curve. The problem with this approach is that it is difficult to gauge the yield and ultimate strength of squat walls with respect to the seismic demand, so even a small force reduction factor such as 2 could potentially allow the structure to deform too much for the intended limit state.

The limit states in ASCE 41 are classified in a similar way to ASCE 43-05: Immediate Occupancy (IO, similar to LS-C), Life Safety (LS, similar to LS-B), and Collapse Prevention (CP, similar to LS-A). The inelastic energy absorption factors and force reduction factors are summarized in Table 2.3. Additionally, both standards give acceptable drift limits, which are also summarized in Table 2.3.

Table 2.3: ASCE 43 and ASCE 41 Factors and Acceptable Drift Limits

	ASCE 43 F_μ Factor	ASCE 41 m Factor	ASCE 43 Acceptable Drift (%)	ASCE 41 Acceptable Drift (%)
LS-A / CP	2	3	0.75	1
LS-B / LS	1.75	2.5	0.6	0.75
LS-C / IO	1.5	2	0.4	0.4
LS-D	1		0.4	

The squat walls of interest in my study are classified as LS-D, so their Fmu factor=1. ASCE 43-05 Section 8.2.2.2 addresses the issue of the Fmu factor for brittle materials. Here, the Fmu value should be taken as 1. This implies ductility=1 and no post-yield behavior. Figure 2.7 shows these acceptable drift limits superimposed on the Wallace (2006) backbone curve.
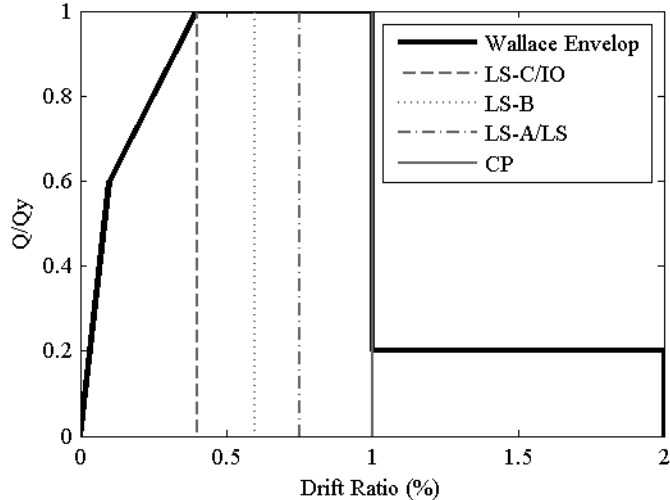
Figure 2.7: Acceptable Drift Limits

Similar to the inelastic energy absorption factor or the force reduction factor mentioned above, ASCE 7-10 gives design coefficients for special reinforced concrete shear walls as Response Modification Coefficient, R=5, Overstrength Factor, Ω_0=2.5, and Deflection Amplification Factor, C_d=5. The R factor is also known as the strength reduction factor (elastic strength demand/inelastic yield strength demand). The importance factor, I, varies for different types of occupancies. It can adjust the R value to limit damage based on the desired seismic performance. Ductility is μ=R/(Ω_0*I). For an Importance Factor=1, the Ductility is 5/(2.5*1)=2. With the uncertainty in the yield and ultimate strength of squat walls, even a ductility of 2 may be too large. In ASCE 7-10, special reinforced concrete walls are defined as those walls complying with ACI 318-08 seismic design requirements in addition to requirements for ordinary reinforced concrete structural walls. There is no distinction in ASCE 7-10 between tall walls and squat walls. The only mention of height is a height limit of 160 ft for walls in Seismic Design Categories D, E, and F. This is a problem because tall walls have a greater ductility than squat walls.

The ASCE 7-10 ductility of 2 is too large for these types of squat shear walls. Even a ductility of 1 could be problematic if the yield point is difficult to define, as is the case with stiff squat walls. Since shear walls in nuclear facility structures are designed to attain an "essentially elastic" limit state in a DBE event, these walls are designed such that they may experience a slight amount of yielding. Since a very stiff structure falls into the acceleration-preserved range of an earthquake response spectrum, the displacement ductility demand may be very large even for a very small amount of yielding (Chopra 2007). Figure 2.8, excerpted from Chopra (2007), shows a plot of ductility demand vs. period for strength reduction factors ranging from 1 to 8. This figure was drawn for the response of an elastoplastic system to the El Centro, CA ground motion, using 5% damping. The nuclear facility structures of interest in this study have a period of approximately 0.14 s. This corresponds to the red line shown in the figure, which falls in the acceleration sensitive region. The strength reduction factor, R_y, is the peak strength divided by the yield strength. The ductility demand, μ, is the peak displacement demand divided by the yield displacement. At yield, both Ry and μ are equal to 1, but for a peak force that is twice the yield force (Ry=2), the displacement demand increases to 3.5 times the yield displacement (μ=3.5).

20
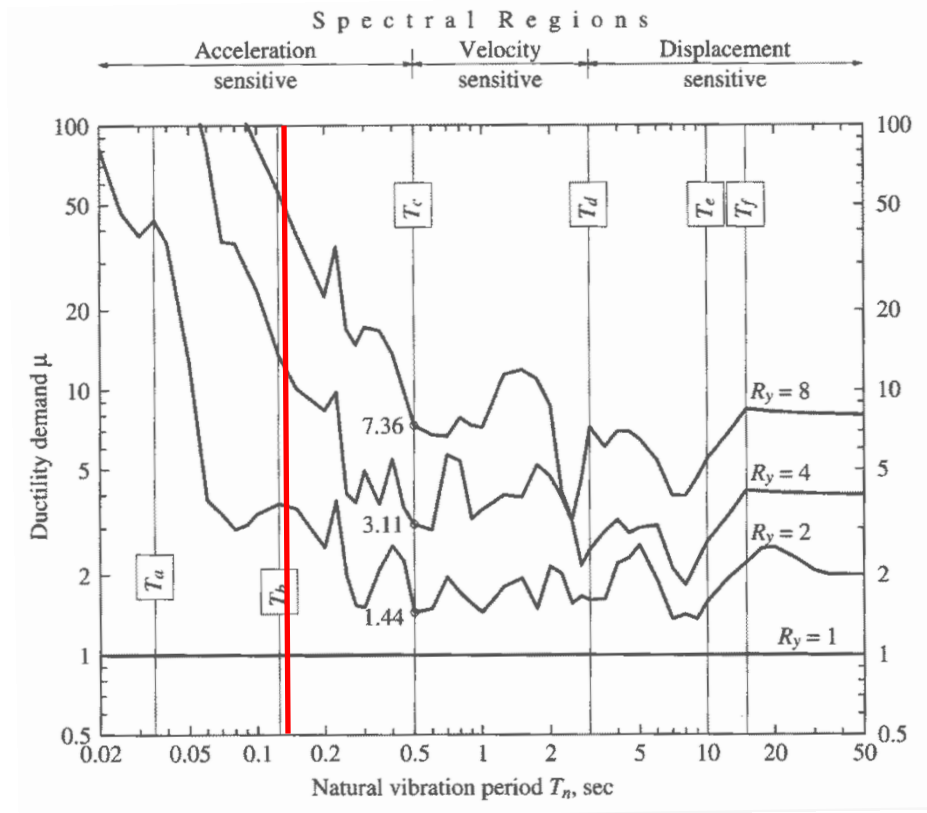
Figure 2.8: Ductility Demand for Varying Strength Reduction Factors (Chopra 2007)

Because the design code equations have been shown to overpredict the peak shear strength capacity of squat reinforced concrete walls, in many cases the walls do not have intended strength capacity. Though "essentially elastic" behavior is intended, these walls are likely to yield sooner than intended in design. Then the walls will have a high displacement ductility demand. It is important to investigate the post-peak behavior of stiff shear walls in case they experience an earthquake ground motion that introduces large seismic shear demands.

2.8   POST-PEAK BEHAVIOR

Paulay et al. (1982) demonstrated the importance of considering the entire shear strength response history. Figure 2.9, excerpted from this paper, shows the rapid degradation of strength post-peak and large displacement when sliding shear occurs.
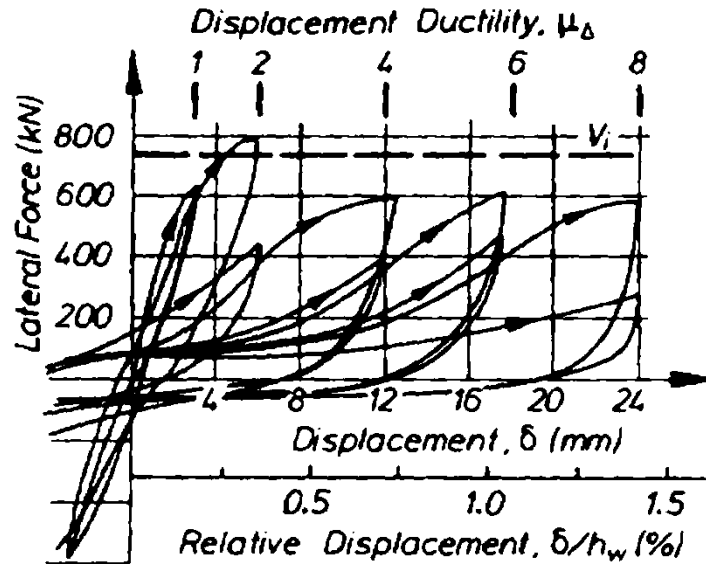
Figure 2.9 Rapid Strength Degradation with Cycling (Paulay et al. 1982)

Gulec, Whittaker, and Stojadinovic (2008) considered shear strengths for the first three load cycles and plotted the rapid drop in strength for three different aspect ratio walls. They plotted the ratio of the second cycle to the first (V_{ult2}/V_{ult}) and the third cycle to the first (V_{ult3}/V_{ult}), as shown in Figure 2.10.
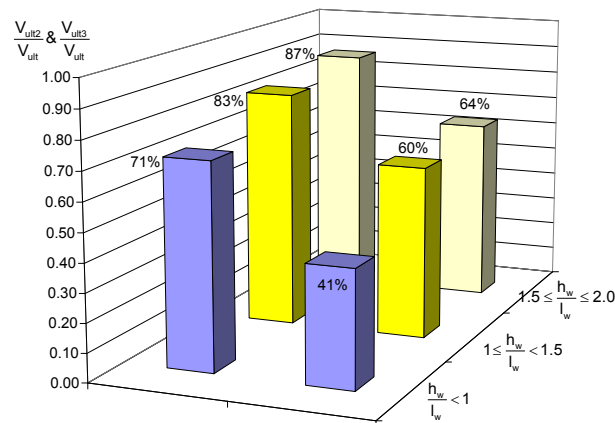
Figure 2.10 Shear Strength Loss with Load Cycling (Gulec et al. 2008)

This decrease in strength in each successive cycle became more apparent as the wall aspect ratio decreased from 2.0 to 1.5 to 1.0.

2.9   SUMMARY

Figure 2.11 superimposes a sketch of the large dispersions associated with strength and displacement capacity onto the Wallace (2006) backbone curve. Quantifying these uncertainties is difficult, but Figure 2.12, excerpted from Gulec (2009), where he expanded his database to 434 squat walls, shows the peak shear strength normalized by wall area and $\sqrt{f'_c}$ vs. the moment-to-shear-ratio. This provides a sense of the dispersion in strengths. Because of the mix of interacting failure modes, there is no attempt at this time to quantify uncertainties associated with displacement capacity.
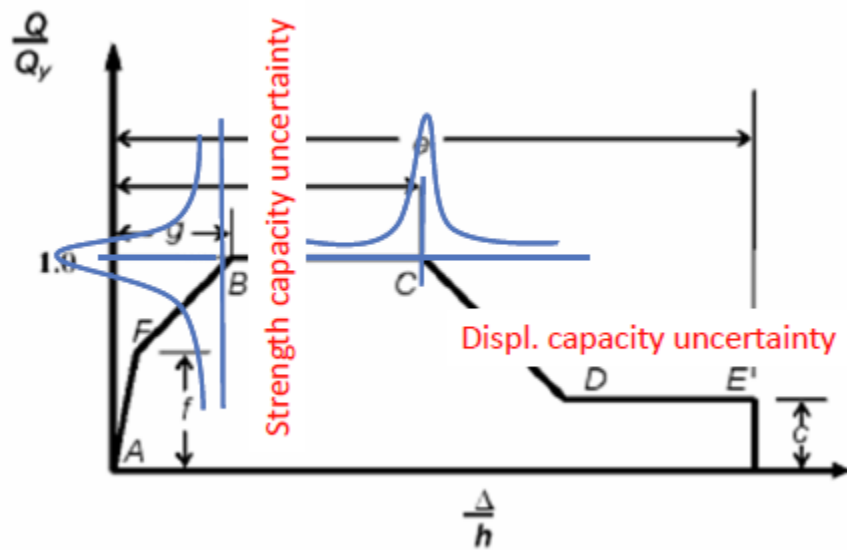
Figure 2.11: Uncertainties in Characterizing Squat Wall Behavior Superimposed on Wallace (2006) Backbone Curve
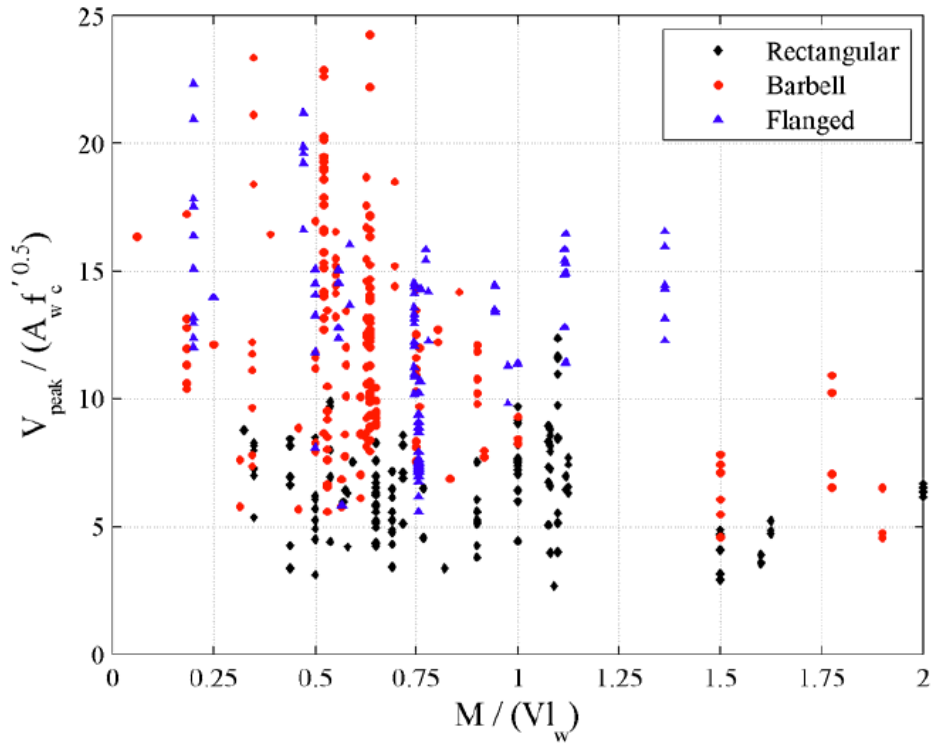
Figure 2.12 Peak Shear Stress vs. Shear Span Ratio (Gulec 2009)

To investigate how these failure modes interact, studies were conducted at The State University of New York at Buffalo and University of California, Berkeley. To minimize any size effect, large scale tests were performed. The tests at Buffalo investigated the effect of aspect ratio and reinforcement ratios using quasi-static testing. Two wall tests, which are the subject of discussion in my dissertation, were performed in hybrid simulation at Berkeley. At Berkeley, the effect of ground motion loading sequence and the adequacy of quasi-static testing for a brittle specimen were investigated. The University of Washington ultimately will use the data to calibrate a numerical model for squat walls.

3 Hybrid Simulation

3.1 INTRODUCTION

Hybrid simulation offers key advantages over conventional testing methods including quasi-static and shake table testing. Quasi-static testing employs actuators to apply pre-defined load or displacement histories to a specimen, designed to represent the expected loading experienced by the prototype during an earthquake. Large or even full scale specimens can be used to overcome the effects of scale and size, but the pre-determined test histories often fall short in reproducing multi-directional action expected in the prototype. In addition, the traditionally slow quasi-static tests do not reflect the dynamic response of the prototype. Although shake table testing applies a ground motion input to a structure and better captures the dynamic properties of the specimen, the size and weight capacity of all but the biggest shaking tables usually restrict the size and scale of the models. This leads to cumbersome similitude compensations such as added mass to compensate for the reduced volume of the specimen, and is likely to introduce errors when replicating construction details in small scale. Hybrid simulation capitalizes on the benefits of the two previous testing techniques by combining a physical quasi-static test with a computer model to simulate dynamic loading.

Since the goal of my research is to apply a ground motion to excite a squat shear wall as if it were in a nuclear facility structure, hybrid simulation is particularly well-suited for this task. The hybrid model represents the nuclear facility structure numerically while testing the squat shear wall physically. Instead of using a predetermined loading pattern, hybrid simulation allows a ground motion input to the model. Finally, in each test, a squat shear wall can be built to large scale since it is the only physical component of the test (instead of creating a physical model that represents the whole system).

3.2 HYBRID SIMULATION BACKGROUND

The pseudodynamic testing method was first investigated in the early 1970s. The first publication implementing online computer-controlled testing was by Takanashi et al. (1975). Some early tests took place at the University of Tokyo and the Building Research Institute (BRI) in Japan, including full scale pseudo-dynamic tests in early 1980s. At the same time, pseudodynamic testing was being investigated at the University of California, Berkeley and at the University of Michigan, Ann Arbor. Shing and Mahin (1983, 1984) and Mahin and Williams (1981) examined experimental error propagation and numerical integration methods.

25

Dermitzakis and Mahin (1985) introduced the concept of substructuring, where a hybrid simulation is composed of any combination of multiple numerical and physical components. Thewalt and Mahin (1987, 1995) improved one-dimensional testing to include six components of excitation. They also proposed a fully implicit numerical integration method that does not require the tangent stiffness or iteration. Instead, they used an analogue electronic device to feedback instantaneous structural restoring forces. They also proposed a method for real-time testing using force control. Nakashima (1990) proposed the Operator-Splitting Method (OSM), where the numerical portion of the hybrid simulation was solved implicitly and the physical portion was solved explicitly. This method eliminated iterations on the physical specimen. Instead, the tangent stiffness of the physical specimen was approximated by the initial stiffness. For softening behavior, this method was unconditionally stable. Then, Shing et al. (1991) developed an implicit integration scheme similar to Thewalt and Mahin (1987). The method of Shing et al. used numerical iteration based on the initial stiffness of the physical structure, but also implemented a displacement reduction factor to avoid displacement overshoot and attempt to load the physical specimen uniformly.

3.3   DISPLACEMENT CONTROL

A hybrid model consists of a physical portion and a numerical portion. The structural components whose behavior is well-understood are typically modeled numerically, and the components that are not well-understood or expect significant nonlinear behavior are modeled physically. A displacement control strategy is most commonly implemented, as summarized in Figure 3.1.
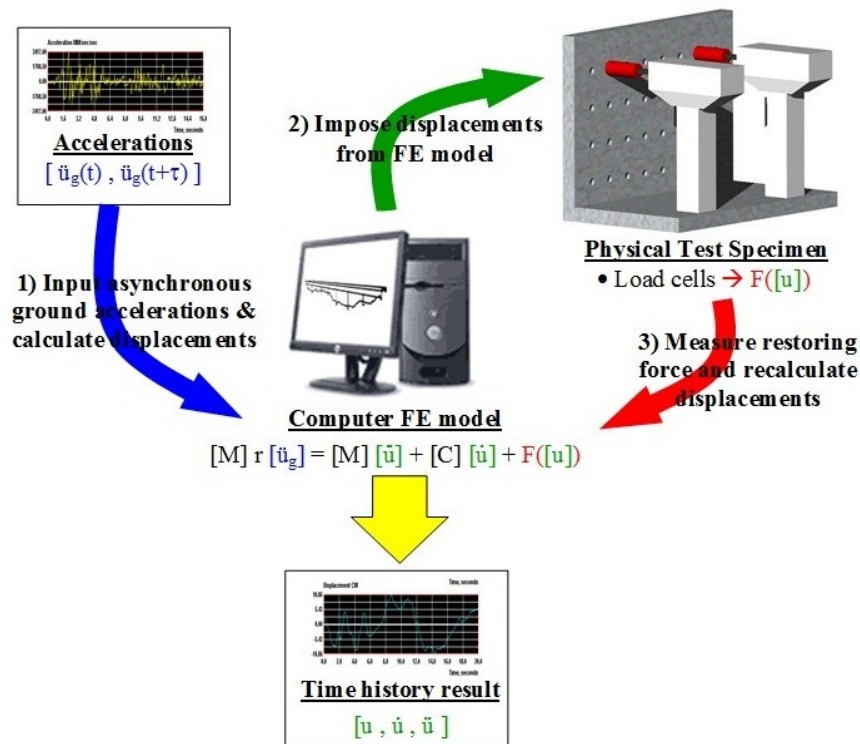
Figure 3.1 Hybrid Simulation in Displacement Control

26

The equation of motion for the hybrid model is discretized in time and given as Equation 3.1.

$$M\ddot{u}_{i+1} + C\dot{u}_{i+1} + R(u_{i+1}) = -MB\ddot{u}_{g,\,i+1} \tag{6.1}$$

M is the mass hybrid model matrix, C is the viscous damping hybrid model matrix, and R is the nodal restoring forces vector, assembled from the restoring forces from the physical and the computer portions of the hybrid model. u is a vector of displacements at each degree of freedom (dof), $\dot{u}$ is a vector of the velocities at each dof, and $\ddot{u}$ is a vector of the accelerations at each dof. Matrix B is the ground acceleration transformation matrix, and $\ddot{u}_g$ is the vector of recorded ground accelerations.

The earthquake acceleration record is provided to the computer finite element model at discrete time steps. At each step, the acceleration is entered into the equation of motion, which represents the structural behavior. A numerical integration technique is employed to solve the equation of motion for a target displacement that the physical test specimen must move to. The actuator applies this target displacement to the specimen and the load cell records the restoring force. This restoring force is entered into the governing equation of motion for the structure, and then the equation is re-solved at the next time step. This process repeats throughout the duration of the ground motion as the response of the structure is recorded.

The high stiffness of squat shear walls poses a challenge to this conventional hybrid simulation displacement control approach. For a stiff specimen, a small increment in displacement corresponds to a large increment in force. Large-scale models of squat walls are stiff and strong: testing to failure often requires forces in excess of 500 kips (2,224 kN), which in turn requires use of one very large actuator or a system of two or more conventional 220 kips (979 kN) actuators. Additionally, to move the specimen smoothly from step to step, large force increments must be avoided. A large force increment could cause the specimen to suddenly change its failure mode or fail completely. This could produce misleading results since the change in specimen behavior would be a result of a poorly-controlled simulation instead of a realistic behavior. Another possible problem with a stiff specimen is that small displacement errors will lead to significant force errors in the simulation, and possibly to instability of the simulation setup. If the specimen is extremely stiff, the required displacement increment to achieve a reasonable-size force increment may become so small that it approaches the tolerance that the laboratory system can control.

The software used for the squat shear wall hybrid simulations included finite element software, Open System for Earthquake Engineering Simulation (OpenSees, 2012), and hybrid simulation framework, Open-source Framework for Experimental Setup and Control (OpenFresco, 2012), both developed at Berkeley. OpenFresco is a flexible framework, suitable for incorporating various finite element software and laboratory hardware (Schellenberg and Mahin 2006). It is advantageous because it supports both displacement and force control methods. Both approaches were considered for the tests, and ultimately a high-precision displacement control method was developed and implemented.

3.4   FORCE CONTROL

Force control is well-suited for testing stiff physical specimens, such as the shear walls which are the subject of this research. In order to move a stiff specimen smoothly without large changes in force, the displacement increments must be sufficiently small. For a very stiff specimen, the required displacement increments may be so small that they approach the actuator tolerance. With force control, the specimen can be moved using reasonably sized force increments.

In one approach to force control, the equations of motion are solved for forces, instead of displacements, at the next time step, t_{i+1}. The forces applied to the physical specimen pass through OpenFresco to the actuator. The first challenge is transforming forces from the finite element model in global degrees of freedom (dofs) to the local actuator dofs. In displacement control, this procedure is easily accomplished by enforcing kinematic compatibility at the nodes. In force control, force equilibrium must be maintained at the nodes. This requirement does not provide a unique transformation in a nonlinear problem. An appropriate force control method must satisfy kinematic compatibility and at least approximately satisfy force equilibrium. The second challenge is that most laboratory control systems operate in displacement control. By regulating the amount of oil flow to the hydraulic actuator, the servovalve controls the velocity of the actuator. Hydraulic actuators generally have very stiff oil columns which can be unstable in force control. The stiff oil column is very sensitive to noise which may come from friction, stick-slip, and breakaway forces on seals (Kim 2009). A stiff specimen needs extra compliance in order to be controlled by a hydraulic actuator in force control. If the specimen softens during the test, this may cause instability in the solution algorithm.

Assuming the force control method is able to transform the dofs and apply forces to the physical specimen, linear variable differential transformers (LVDT) then measure displacements, which are fed back through OpenFresco to the finite element software. Then, the process repeats in the next step for the duration of the ground motion. Kim (2009) researched a number of force control methods and implemented both a Displacement-Based Approach to Acquire Target Forces and a Force-Based Method (Yang, Schellenberg, and Kim) in OpenFresco. These are summarized next.

3.4.1   Force Control Algorithms Proposed by Kim

The finite element software operates in the global coordinate system, and the control system in the laboratory operates in the actuator coordinate system. Since it is difficult to transform target forces from the global system to the actuator system, Kim (2009) first investigated a Displacement-Based Approach to Acquire Target Forces. This approach is summarized in Figure 3.2.
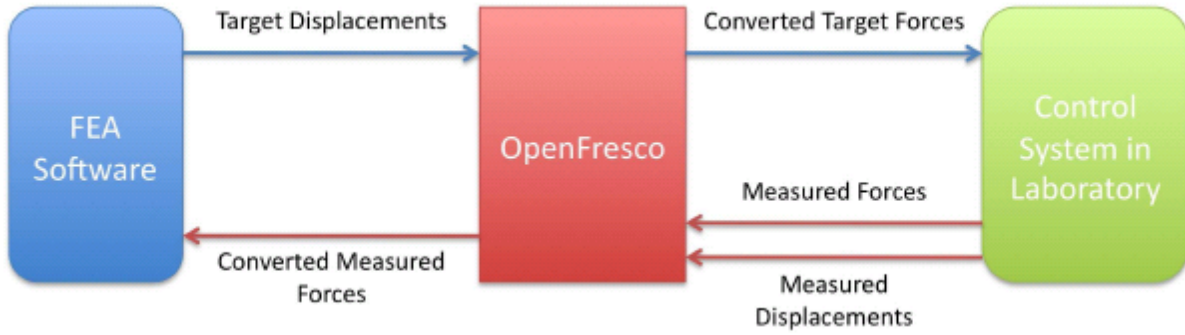
Figure 3.2 Force Control in OpenFresco, Kim (2009)

In the finite element software, the global target displacements, u, are determined and sent to OpenFresco. There, the displacements are converted from global to actuator coordinate system displacements, x. Then, the target displacements are converted to target forces, f, in the actuator coordinate system.   This can be accomplished with a number of methods; Kim (2009) implemented methods that update the tangent stiffness matrix as well as tangent-free methods (BFGS, Broyden, and Krylov Subspace methods) in OpenFresco. The tangent stiffness matrix in the actuator coordinate system, K_t^{act}, is the Jacobian of the resisting forces. The target forces, f, are determined by the following equation.

$$f = K_t^{act}x \tag{6.2}$$

Then, the target forces are sent to the control system and applied to the specimen. After the specimen has moved, the displacements and forces are measured and sent to OpenFresco. The measured displacements are converted to global forces, R, and are returned to the finite element software.

Kim has also implemented the Forced-Based Method in OpenFresco, where forces are directly solved in the finite element model. The difficulty with this approach is software other than OpenSees must be used. This method uses the Modified Dynamic Equilibrium Equation, as shown below.

$$\begin{bmatrix} \mathbf{M} \\ \mathbf{0} \end{bmatrix}\ddot{\mathbf{U}} + \begin{bmatrix} \mathbf{C} \\ \mathbf{0} \end{bmatrix}\dot{\mathbf{U}} + \begin{bmatrix} \mathbf{B}_f\mathbf{Q} \\ \mathbf{B}_x^T(f(\mathbf{Q})+\mathbf{V}_0) \end{bmatrix} = \begin{bmatrix} \mathbf{P}_f - \mathbf{P}_{fw} \\ \mathbf{0} \end{bmatrix} \tag{6.3}$$

B_f is the equilibrium matrix, Q is the element resisting force vector, P_f are the applied nodal loads, P_{fw} are the applied element loads, and B_x is the redundant force influence matrix. The system of equations is solved for element forces, Q, which are sent to OpenFresco. There, they are transformed from the global to the actuator coordinate system, and then are sent to the control system and on to the physical specimen. After moving the physical specimen, the measured displacements are converted from actuator to global coordinates in OpenFresco. Subsequently, they are sent to the finite element model and entered back into the Modified Dynamic Equilibrium Equation as f(Q).

3.4.2 Elkhoraibi and Mosalam Switch Control

Elkhoraibi and Mosalam (2007) implemented switch control hybrid simulation on RC frames, either with or without unreinforced masonry infill walls, and on wood shear walls. Switching between displacement and force control depended on the secant stiffness, K, and the restoring force, R. Two threshold values were implemented to create a buffer zone. This prevented numerous switches between displacement and force control. The lower end of the buffer zone was stiffness, K_d, and the upper end was stiffness, K_f. K_{avg} was the average secant stiffness over 100 values, calculated to prevent noise in the system from displaying unusually large or small stiffnesses. Similarly, R_d, R_f, and R_{avg} existed for the restoring forces. Switching occurred when both the stiffness and restoring force exceed the buffer zone limits in the same direction.

Though the actuator's Proportional, Integral, Derivative (PID) control parameters can be tuned for displacement control without requiring a specimen, a specimen is necessary for tuning in force control to give force feedback. The force control tuning is also stiffness dependent, which was a problem identified by the researchers. Figure 3.3 shows the behavior of their Specimen B, which consisted of two wood shear walls, representing the first story of a two-story wood house with a garage opening in the first story. Displacement control was used for most of the test except for the circled stiff unloading regions.
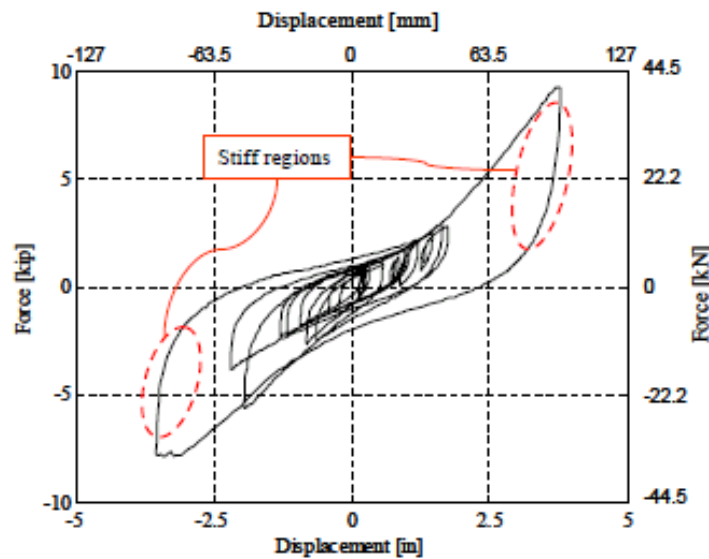
Figure 3.3 Force Deformation Response for Specimen B (Elkhoraibi and Mosalam, 2007)

The lowest stiffnesses exhibited were <3 kips/in and the highest stiffnesses were >30 kips/in. Two shear walls were built, similar to their test specimen B, just for the purpose of tuning for force control. They chose to tune the actuator in force control for the higher range of stiffnesses, around 40 kips/in. The drawback was if displacement control switches to force control at a lower stiffness, the actuator is not tuned for that lower stiffness value. They used this same actuator tuning for their Test Structure A, which was a one-story reinforced concrete frame with an unreinforced masonry infill wall. They did not have extra specimens to replicate the stiffness of Structure A for tuning. This resulted in a suboptimal loading history caused by the improperly

tuned actuator applying an inaccurate force command. There was lag of the actuator in force control due to the difference between applied and measured forces. This caused smaller displacement feedback increments and resulted in compounded errors over multiple steps. These results demonstrate the importance of having a good estimate of the specimen stiffness before the test. Also, using force control for a specimen with changing stiffnesses may not produce smooth results, because the actuator can only be tuned for one stiffness value.

3.5   FORCE VS. DISPLACEMENT CONTROL FOR SQUAT WALL TESTS

Both of Kim's methods were considered for the squat shear wall tests. Table 3.1 summarizes the advantages and disadvantages of each method.

Table 3.1: Consideration of Kim's Force Control Methods

	Displacement-Based	Force-Based
Advantage	Fits existing framework in the laboratory using OpenSees.	Avoids acquiring the tangent stiffness matrix.
Disadvantage	Needs tangent stiffness matrix to convert displacements to forces in the actuator coordinate system.	OpenSees cannot be used because the finite element software must solve for forces.

The outcomes of Elkhoraibi and Mosalam's tests were considered when determining whether force control would be appropriate for the squat shear wall tests. There were considerable drawbacks. An estimate of specimen stiffness was necessary for PID tuning in force control. However, a major problem with the squat shear wall specimens was difficulty approximating stiffness prior to testing. Furthermore, the controller could only be tuned for one stiffness value. Accordingly, Elkhoraibi and Mosalam tuned their controller for the higher range of stiffnesses. The squat shear walls were expected to degrade rapidly and lose a considerable amount of their stiffness. This would lead to poor control after the walls began to lose strength.

Displacement control, as traditionally implemented, would not be sufficient for testing stiff squat shear walls. In order to avoid large force increments for a stiff specimen, very small displacement increments must be commanded. The *nees@berkeley* Equipment Site acquired a digital displacement encoder with a step resolution of 10 microns (0.0004 in). The encoder was used to feedback displacements in the PID loop. It was successfully integrated within the actuator control loop to feedback sufficiently small displacement increments to create smooth loading of the squat shear wall specimen. The next chapter describes the implementation of the encoder in detail.

4   Encoder Control for Stiff Specimens

4.1   INTRODUCTION

Testing a stiff specimen requires small displacement increments in order to produce a smooth force response. Traditional displacement control strategies are inadequate for testing a stiff specimen because the displacement increments cannot be made sufficiently small to avoid jumps in force. Typically, a LVDT is used for displacement feedback, but this instrument lacks the precision to control displacements below 0.001 in (25 microns). In order to test the stiff squat shear walls in my study, a Heidenhain LS 623 1140 mm high precision displacement encoder was implemented for displacement feedback within the PID loop. The encoder step resolution was 0.0004 in (10 microns).

Initially, the encoder was tested and validated against a LVDT by monitoring actuator displacements directly. The actuator was disconnected from the strong wall and placed on the laboratory floor. The LVDT was used to control the actuator displacements; then the encoder was used to control the actuator. After the encoder was confirmed to work well, it was further tested by controlling displacements for a specimen from a previous test with the same experimental setup. This specimen was a two-story steel braced frame, tested by Lai (2012), using the same actuator.

First, the hybrid simulation setup at the *nees@Berkeley* equipment site will be described. Then, modifications to allow use of the encoder will be detailed. The encoder validation tests will be described.

4.2   HYBRID SIMULATION AT THE *NEES@BERKELEY* EQUIPMENT SITE

OpenFresco is used for hybrid simulations at the *nees@Berkeley* laboratory. It is based on a client-server architecture, where the client is the finite element model of the structure and the server is the control system in the laboratory driving the physical specimen. In a local hybrid simulation, the client and server are located in the same laboratory and OpenFresco processes reside on the client side to facilitate the communication between the client and server. In a distributed hybrid simulation, the client is located at one laboratory and the server at another, with OpenFresco processes at both locations. Typical OpenFresco architectures for local and distributed simulations are shown in Figure 4.1.
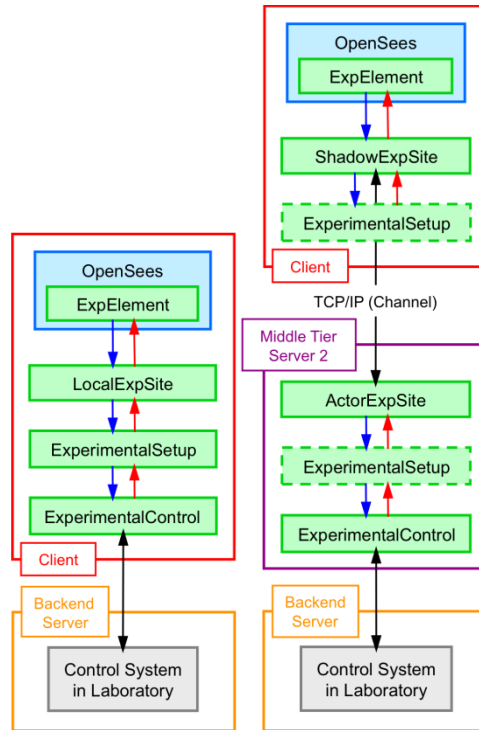
Figure 4.1 OpenFresco Local and Distributed Architectures (Schellenberg 2008)

In the left figure, representing the local architecture, the finite element software is the Open System for Earthquake Engineering Simulation (OpenSees 2012). Both OpenSees processes (blue box) and OpenFresco processes (green boxes) are executed in a single computer, the client, and communicate with the control system in the laboratory, the backend server. The OpenFresco "ExpElement" is contained within OpenSees which instructs OpenSees to interact with OpenFresco for the nominated element. "LocalExperimentalSite" manages communications. "ExperimentalSetup" transforms between experimental element degrees of freedom in OpenFresco and actuator degrees of freedom in the laboratory. Then "ExperimentalControl" interfaces with the control and data acquisition system in the laboratory. In the right figure, representing the distributed architecture, "ExperimentalSetup" is shown in a dashed box since it can be located on the client or the server side. The TCP/IP Channel connects the Client in one laboratory to the Middle Tier Server and Backend Server in another laboratory. The Site is split into "ShadowExpSite" and "ActorExpSite," one in each laboratory. This allows for the data storage and communication methods for distributed testing.

The laboratory at *nees@Berkeley* uses xPC-target experimental control. OpenSees and OpenFresco run on the xPC host computer. This is depicted in the center of Figure 4.2 below.
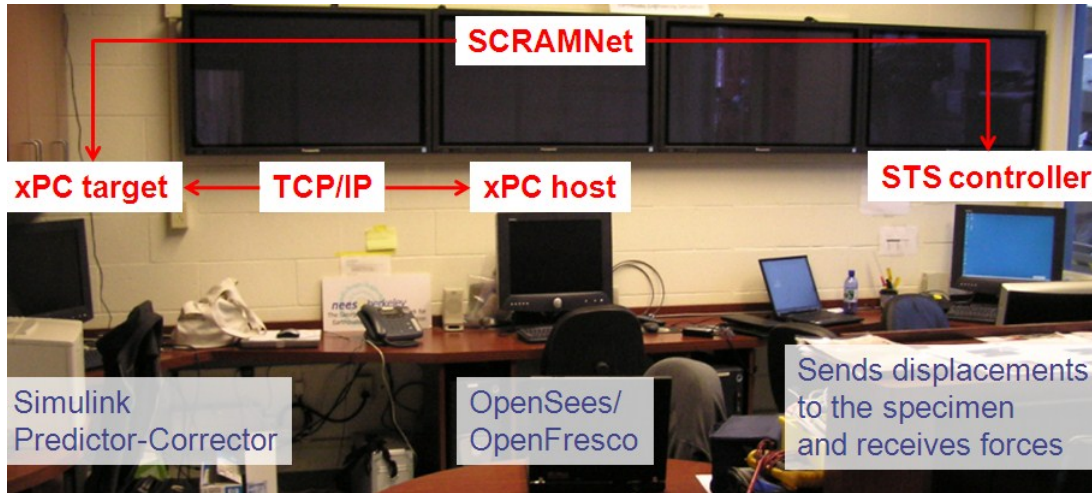
Figure 4.2 UCB Hybrid Simulation Laboratory

A Simulink predictor-corrector model is created on the xPC host PC using Matlab, Simulink, and Stateflow (Mathworks 2012). It is compiled onto the xPC target PC, which is a real-time data processor. Communication between the xPC host and target PCs occurs over a TCP/IP connection. The predictor-corrector algorithm generates command signals at a 1/1024 s. time step, required by the controller. The xPC target has a shared-memory real-time communications network with the Structural Test Systems (STS) Controller (MTS 2003), provided by MTS Systems Corp. This network is called SCRAMNet (Systran 2000), and it updates its memory every 1/1024 s. A SCRAMNet card is installed on each computer. This card holds a local copy of saved memory which is shared over the SCRAMNet high-speed, serial ring network. The STS Controller is a digital control system which links to the servo-valves, actuators, and laboratory specimens. It uses a closed-loop Proportional, Integral, Derivative, Feedforward (PIDF) control for the actuators. Additionally, it performs digital to analog (D/A) and analog to digital (A/D) conversions, as well as filtering. It receives measured data from the physical specimen.

During the hybrid simulation, the finite element model produces a target displacement when the time integration algorithm has converged. This occurs on the xPC host computer. Depending on the complexity of the model and the numerical integration scheme used, this can occur at an unpredictable rate. A simulation time step is selected by the user to ensure that the finite element model produces a target displacement within that time step. For instance, in a real-time simulation, if the earthquake ground motion time step is 0.02 s. (dt_{int}), a simulation time step would also be selected as 0.02 s. (dt_{sim}). Alternatively, a larger simulation time step could be chosen. A simulation time step of 0.04 s. would result in a hybrid simulation two times slower than real time. This could be necessary for a number of reasons: (1) A large finite element model may be slow to converge to a target displacement; (2) If an implicit integration method is used, the simulation time step would need to accommodate iterations; (3) In a distributed hybrid simulation, a larger simulation time step accommodates network delay as displacement commands are sent over the internet from the finite element model to the physical specimen. Meanwhile, the servo-hydraulic control system requires a command at 1/1024 s. intervals, selected by the manufacturer to ensure stability and good response of the servo-hydraulic control loop and the actuators. The predictor-corrector algorithm, running on the xPC

34

target computer, extrapolates past target displacement data points to generate predicted displacements at the required rate needed by the servo-hydraulic control system until the finite element model can provide the next displacement value (Mosqueda 2005). Below, Figure 4.3 shows a displacement time plot which illustrates the predictor-corrector algorithm behavior compared with a ramp hold procedure.
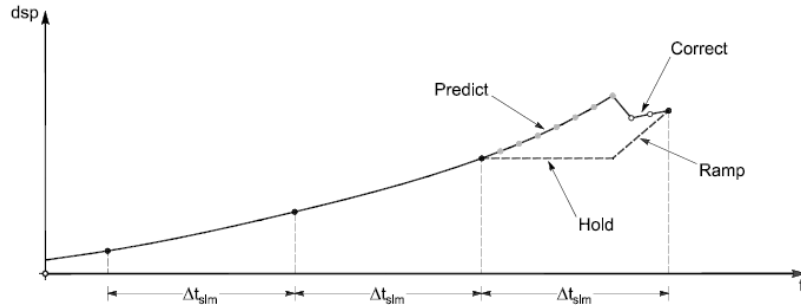
Figure 4.3 Predictor Corrector Algorithm (Mosqueda 2003)

At the end of each simulation time step (Δt_{sim}) interval, the target displacement from the finite element model has been successfully commanded to the specimen. The predictions are an extrapolation of these past points, sent to the controller every 1/1024 s. The finite element model must send the next target displacement before 60% of dt_{sim} elapses to leave sufficient time for correction. If the next target displacement is too slow, the actuator driving the physical specimen slows down. If the next target displacement is not received before 80% of dt_{sim} elapses, the actuator stops and holds. Slow-downs, and especially holds, should be avoided as much as possible in a physical test.

Schellenberg (2008) created predictor-corrector models for hybrid simulation. Schellenberg's HybridControllerD3D3.mdl model, available in the OpenFresco repository (OpenFresco\trunk\SRC\experimentalControl\Simulink\RTActualTestModels\SCRAMNet-xPCTarget-STS), was the basis for Lai's (2012) Simulink model for braced frame tests, HybridControllerD3D3_ Vconst_rec100Hz.mdl. Lai used the same actuator that was employed for the squat wall tests, and found the best performance by commanding displacements at a constant velocity. Lai's model was modified for use with the squat shear wall hybrid simulation tests. D3D3 indicates that this model is based on interpolation of the three prior displacements using third-order Lagrange polynomials during both the prediction and correction phases (Schellenberg 2008). The algorithm ensured that the displacement commands are C_0-continuous.

4.3   MODIFICATIONS TO ENABLE USE OF ENCODER

In order to use an encoder instead of a LVDT for displacement control feedback at the *nees@Berkeley* Laboratory, MTS Systems Corp. (Eden Prairie, MN) modified the STS Controller application. They created parallel displacement control feedback channels dedicated to the encoder, constructed in a similar way to the LVDT displacement control feedback channels. This permitted displacement control using the encoder when operating the actuator from the STS Controller graphical user interface (GUI) on the controller PC. By using the STS Controller GUI, displacements were commanded and fed back from the encoder.

35

Further modifications were necessary to conduct hybrid simulation using the encoder displacement feedback. First, the predictor-corrector model had to be able to access the encoder commands and feedbacks from the STS Controller.   MTS Systems Corp. modified the SCRAMNet memory map to allow for these communications. Lai's Simulink model for braced frame tests, HybridControllerD3D3_Vconst_rec100Hz.mdl, was modified for use with the encoder. The new model is called HybridControllerE3E3_Vconst.mdl and has been uploaded to the OpenFresco repository. The initializeSimulation.m file that works with the Simulink model was modified to increase the size of the User Datagram Protocol (UDP) to include new encoder commands and to add two extra partitions for the encoder input from SCRAMNet and output to SCRAMNet.

4.3.1   Encoder Test with Actuator on Laboratory Floor

Before using the encoder to feedback specimen displacements, its performance was compared to the performance of a LVDT by monitoring actuator displacements directly. The actuator was disconnected from the strong wall and placed on the laboratory floor. Both a LVDT and the encoder measured the motion of the actuator clevis relative to the actuator body. The test setup is shown below in Figure 4.4.
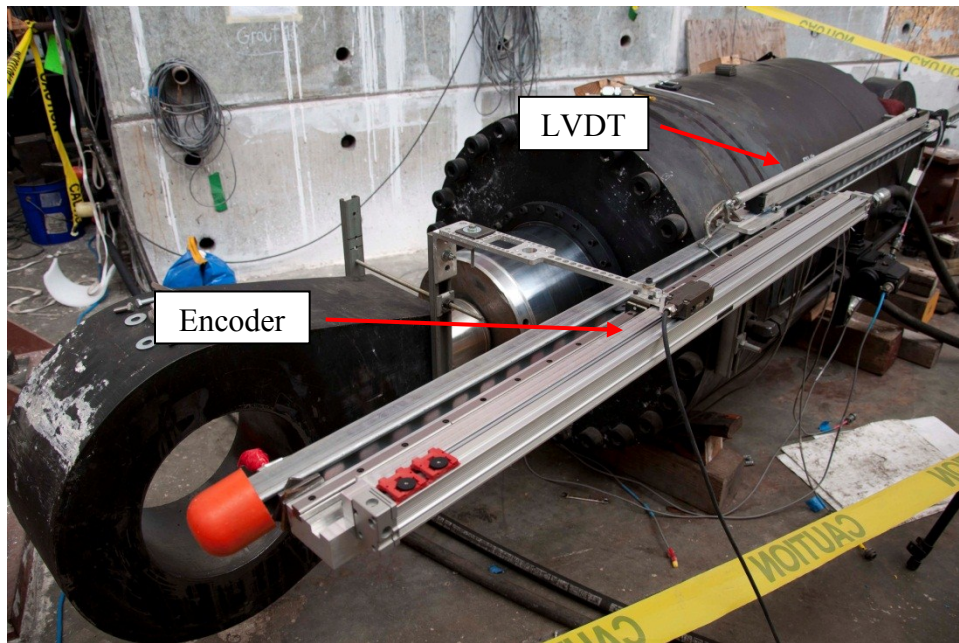
Figure 4.4: Test Encoder using Actuator on the Floor

First, the LVDT was used for the displacement feedback and the encoder displacements were recorded.   Then the encoder was used for the displacement feedback and the LVDT displacements were recorded. A constant velocity triangle motion was used for these tests since the actuator clevises were known to have a small amount of slip. In the previous test of a steel braced frame using the same actuator, Lai (2012) found improved results in a hybrid simulation by moving the specimen using a constant velocity.

Another recognized problem was that the Moog 72-103 servovalve, rated at 60 gal/min (227 L/min), was underperforming considerably. The flow at peak velocity was computed to be about 30 times less than the rated flow with no load. MTS Corp. suggested rewiring the cable connected to the servovalve in series instead of in parallel. The actuator was controlled using the LVDT with the parallel connection and then the series connection. The series connection improved performance. Then, the actuator was controlled using the encoder with the series connection wiring. A triangle displacement motion with a 1 in (2.54 cm) amplitude was commanded for these 3 cases. Velocities of 0.08 in/s (2.032 mm/s) and 0.24 in/s (6.096 mm/s) were tested. The comparisons of displacement errors between command and feedback displacements for each velocity are shown in Figure 4.5 and Figure 4.6 below.
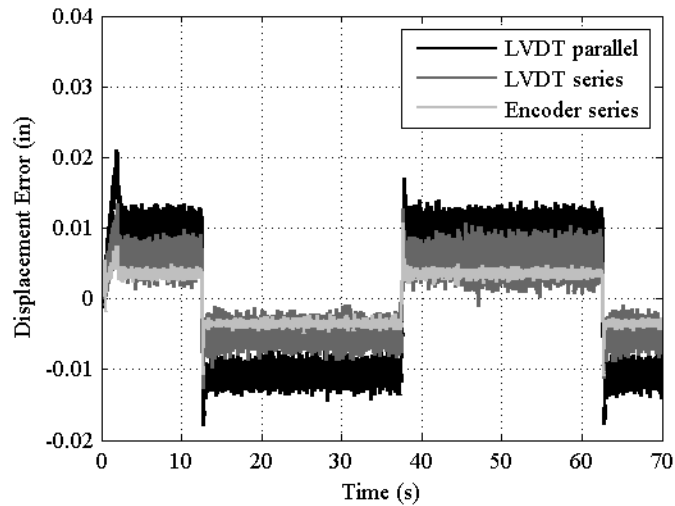
Figure 4.5: Displacement Error at Velocity=0.08 in/s
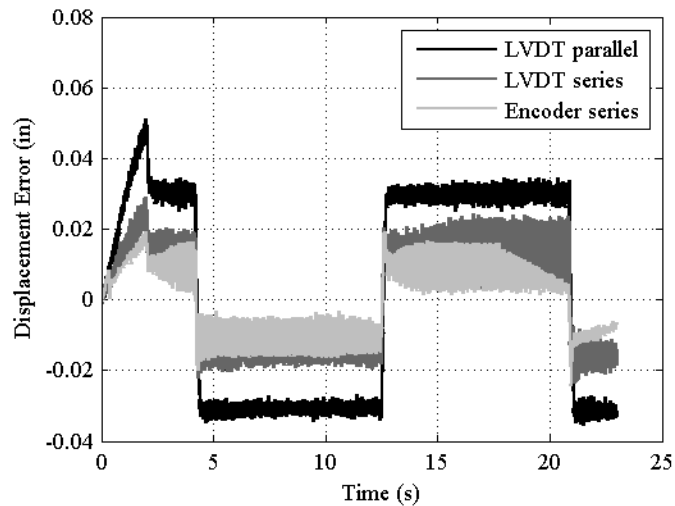
Figure 4.6: Displacement Error at Velocity=0.24 in/s

37

It is clear from these plots that the performance of the encoder is superior to that of the LVDT in terms of minimizing displacement errors between command and feedback displacements. It is also evident that the error plots contain spikes. These occur when the actuator changes directions and the clevises slip. Commanding displacements to the specimen with a constant velocity approach minimizes the error. After rewiring the cable, the P gain was left unchanged. The gains used are summarized in Table 4.1.

Table 4.1: PIDF Gains

Parameter	Gain
Proportional (V/V)	200
Integral (1/sec)	0
Integral Authority (%FS)	10
Derivative (sec)	0
Feedforward (sec)	0

Ultimately, the squat shear walls were tested at a velocity of 0.01 in/s (0.254 mm/s). This had not been determined at the time of testing the encoder. There is data from tests with a triangle displacement motion with a 1 in (2.54 cm) amplitude and velocity of 0.015 in/s (0.381 mm/s) for the LVDT wired in parallel and the encoder wired in series. This gives a better indication of the level of errors between command and feedback displacements at a velocity close to the actual testing velocity. This is shown in Figure 4.7.
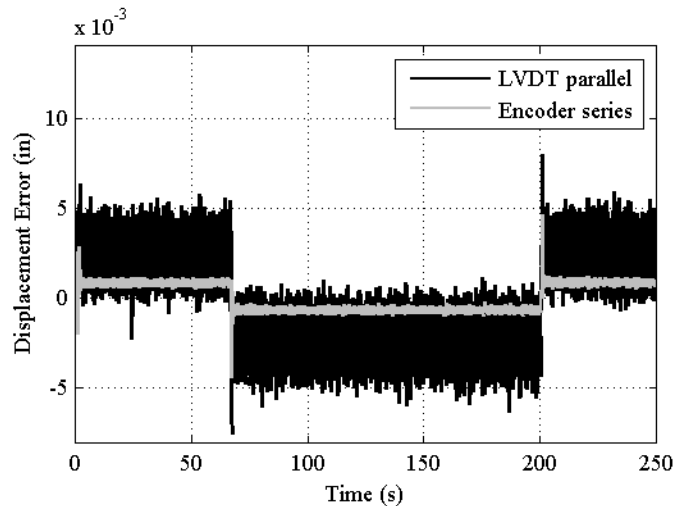
Figure 4.7: Displacement Error at Velocity=0.015 in/s

4.3.2 Encoder Test using Old Braced Frame Specimen

After confirming that the encoder worked to feedback displacements of the actuator directly, with the actuator placed on the laboratory floor, the encoder was tested in three new configurations. First, the LVDT and then the encoder controlled the actuator displacements directly (actuator now connected to strong wall but feedback instruments positioned as shown in Figure 4.4) while the actuator pushed the top of the first story of the braced frame specimen

38

(cable wired in series from this point forward). Second, a stiff reference frame was installed next to the braced frame specimen. The encoder was mounted on this frame and fed back braced frame column displacements via a long pole. This is the configuration shown below in Figure 4.8. Third, the encoder measured between the reference frame and the beam at the top of the first story of the braced frame via a connection designed for use with the squat shear wall hybrid simulations. A flexible steel plate connected the encoder to the specimen. This allowed for vertical motion but restrained any horizontal motion. A slider (a linear guide block on a rail) accommodated any out of plane movement and a 360 degree swivel accommodated any torsion of the specimen. The baseplate of the slider was attached to a small I-beam clamped to the top of the braced frame's beam. This was done because the reference frame was taller than the braced frame's beam, and the encoder needed a reference point at the same height. This attachment is shown in Figure 4.9. For the data presented in each of these cases, a triangle displacement motion with a 0.3 in (7.62 mm) amplitude was commanded at a velocity of 0.015 in/s.
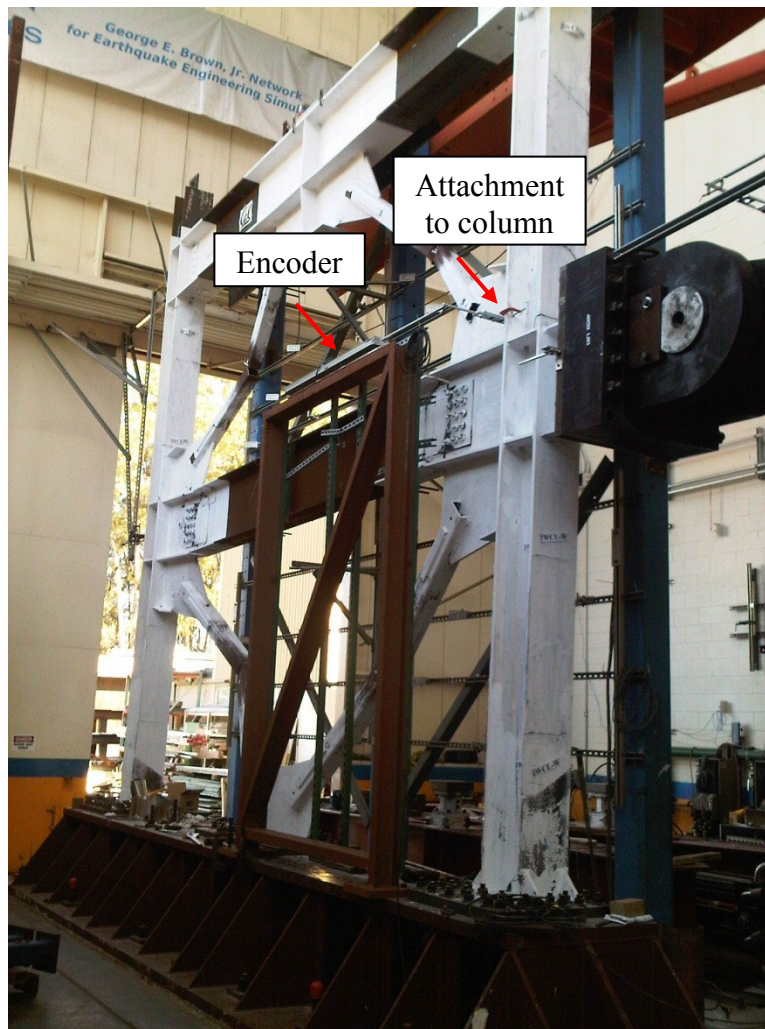
Figure 4.8: Test Encoder with Braced Frame

Figure 4.9: Encoder Attachment

The comparison of errors from the LVDT and errors from the encoder controlling displacements from the actuator body while the actuator pushed the braced frame are shown in Figure 4.10.
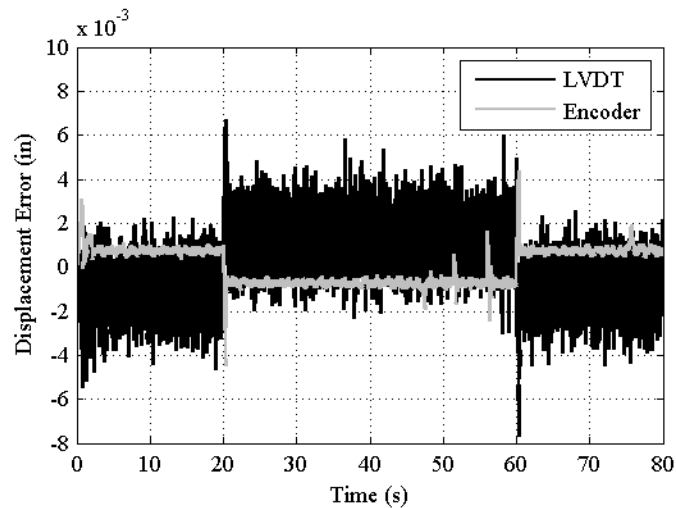
Figure 4.10: LVDT vs Encoder Displacement Errors while Controlling Actuator

Next, the encoder controlled the actuator by measuring from the reference frame to the braced frame's column. After confirming that the encoder performed well, the final setup was tested. The encoder controlled the actuator by measuring from the reference frame to the braced frame's beam using the flexible steel plate and slider connection. This was successful as well, so the same reaction frame and encoder connection would be used for the squat shear wall tests.

40

After confirming that the Simulink model worked well for a hybrid simulation using a simulated experimental element, a hybrid simulation was run with the braced frame specimen. When this also worked successfully, the hybrid setup was ready for the squat shear wall specimens.

5   Hybrid Simulation Tests of Squat Walls

5.1   INTRODUCTION

The hybrid simulation tests involved application of varying levels of a ground motion excitation to a simplified hybrid model of a typical nuclear facility structure. This hybrid model was a combination of a physical squat shear wall specimen with a computer model (the representation of the mass of a Candu Reactor). Implementing the mass in the numerical model allowed for the tested wall's dynamic motion to match that of the entire structure without physically adding mass to the wall. Numerically modeling the remaining lateral force resisting system of the building (the other shear walls) was considered. However, this approach was determined to be too risky because the outcome of the simulation depended on the accurate estimate of the stiffness of the numerically modeled walls. If the analytically modeled walls were stiffer than the physical specimen, they would not fail and would take all the force when the specimen began to soften. Alternatively, if the analytical walls were softer than the physical specimen, they would fail too early and overload the specimen.

Two nominally identical squat reinforced concrete shear walls, referred to as Wall 1 and Wall 2, were tested at the *nees@Berkeley* laboratory using hybrid simulation of a ground motion. The shear wall specimens were 8 in (20.3 cm) thick models of a prototype 36 in (0.9 m) thick structural wall typically found in nuclear facility structures. The 1999 Kocaeli, Turkey ground motion was selected as the input for the hybrid simulation tests. The Wall 1 hybrid simulation test sequence was conducted by increasing the intensity level of this applied ground motion from an operational basis earthquake (OBE), to a DBE, and to a beyond design basis earthquake (BDBE), followed by a DBE aftershock. The Wall 2 hybrid simulation test sequence was conducted by applying an OBE, a BDBE, and then two DBE aftershocks. After the ground motion sequences were applied to Wall 1 and Wall 2, the walls had lost most of their strength. Therefore, it was not safe to perform further ground motion simulations. Instead, the walls were broken using quasi-static single-cyclic motions to displacements of +/-1 in (+/-2.54 cm) and then +/-1.5 in (+/-3.81 cm).

Since the shear walls of interest in this study are very stiff, a small increment in displacement corresponds to a large increment in force. Thus, conventional displacement control hybrid simulation is very difficult, or even impossible, to use in this scenario. If the specimen is extremely stiff, the required displacement increment to achieve a reasonable-size force increment may become so small that it is on the order of the tolerance that the laboratory system can control. Stiff squat shear walls have not been previously studied dynamically at large scale because it is difficult to conduct a displacement-controlled test. This problem was overcome by using a very high precision displacement encoder to feedback displacements in the PID loop.

5.2 WALL GEOMETRY

The two shear walls at Berkeley were designed to be nominally identical to one of the University at Buffalo cyclic test specimens. The wall elevation and reinforcing bar layout are shown in Figure 5.1. The walls had 0.67% horizontal and vertical wall reinforcement ratios with #4 reinforcing bars placed in two curtains at 7 in (17.8 cm) on center. The shear wall specimens were 10 ft (3 m) long, 5 ft, 4-1/8 in. (1.6 m) tall to the height of the actuator axis (aspect ratio 0.53), and 8 in. (20.3 cm) thick. The walls were placed on tall foundations in order to accommodate the height of the actuator in the existing test setup at the *nees@Berkeley* laboratory.
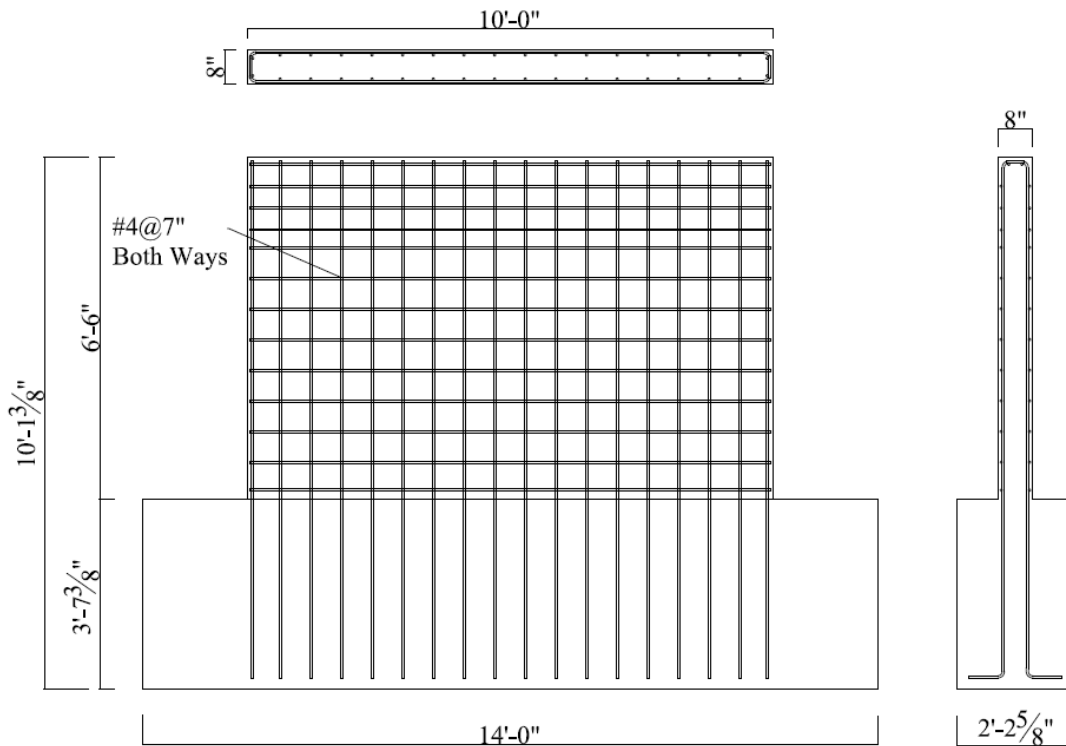
Figure 5.1: Wall Elevation and Reinforcement

The foundation elevation and reinforcing bar layout are shown in Figure 5.2. The foundations were 14 ft (4.27 m) long, 3 ft 7-3/8 in. (1.10 m) tall, and 2 ft, 2-5/8 in. (0.68 m) deep.

43
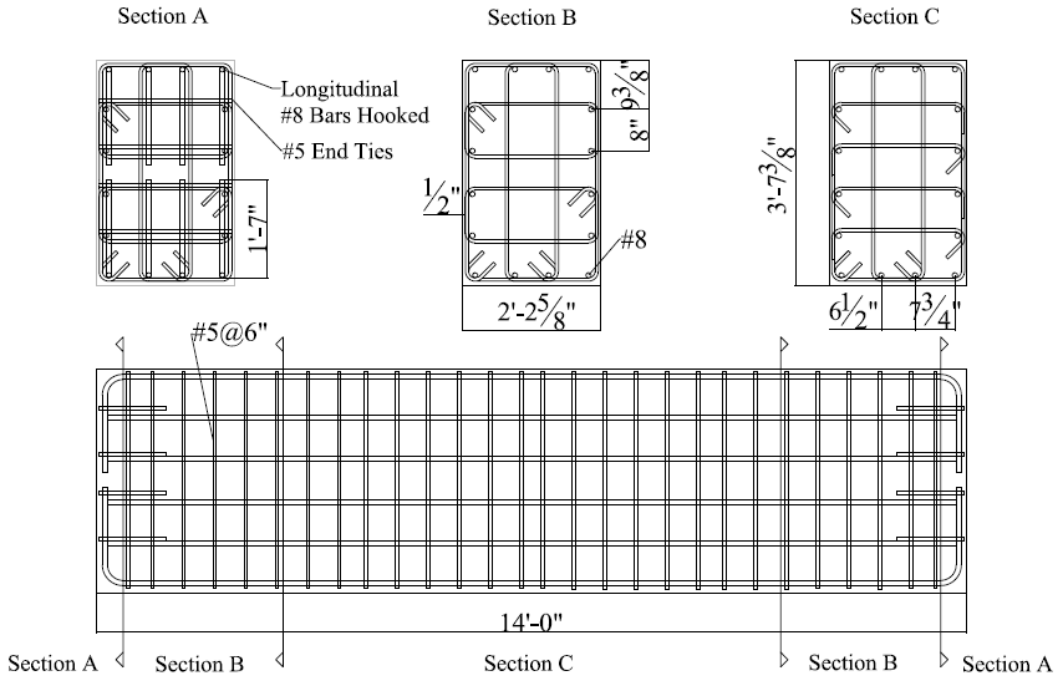
Figure 5.2: Foundation Elevation and Reinforcement

5.3   MATERIAL PROPERTIES

Table 5.1 summarizes the specified and measured strengths of the reinforcing steel bars and the concrete mixes. All of the #4 reinforcing bars for the walls came from the same batch of ASTM standard A706 reinforcing steel, produced at Tamco Steel Mini Mill. Three of these #4 bars were tested, and the average yield and ultimate strengths are reported. The concrete mix, produced by Right Away Redy Mix, Inc., was specified to replicate the mix used by Terzic (2009). This mix was designed by Caltrans engineers and the details can be found in Appendix A. The concrete for the foundations for both Walls 1 and 2 was poured on February 24, 2011. Then the surfaces of the foundations were roughened, and the concrete for both walls was poured on March 1, 2011. Though the same concrete mix was specified for the foundations and the walls, Right Away Redy Mix, Inc. added almost double the specified amount of ADVA 140 water reducing admixture to the foundations mix. Then the company failed to add any of the WRDA 64 water reducing admixture and enough of the ADVA 140 water reducing admixture to the mix used for the walls. This resulted in a reduced strength of the walls in comparison to the foundations. The average compressive strength of three concrete test cylinders is reported in Table 5.1 for measurements made on the day of the Wall 1 test (at 199 days) and on the day of the Wall 2 test (at 288 days). The concrete compressive strength over time is plotted in Appendix A. Also, the full stress-strain behavior and the splitting tensile strengths for cylinders tested on the days of the hybrid simulations are shown in Appendix A.

44

Table 5.1: Wall Specified and Actual Strengths

Material	Specified MPa (ksi)		Wall 1 Measured MPa (ksi)		Wall 2 Measured MPa (ksi)	
	Yield	Ultimate	Yield	Ultimate	Yield	Ultimate
Steel	413.7 (60)	551.6 (80)	464.0 (67.3)	632.9 (91.8)	464.0 (67.3)	632.9 (91.8)
	Wall	Foundation	Wall	Foundation	Wall	Foundation
Concrete	34.5 (5.0)	34.5 (5.0)	35.5 (5.15)	51.2 (7.43)	37.3 (5.41)	52.4 (7.59)

5.4 HYBRID MODEL AND GROUND MOTION

The numerical portion of the hybrid model was a large mass, modeled using OpenSees (OpenSees 2012) and OpenFresco (OpenFresco 2012). The mass was selected so the hybrid model has a 0.14 s natural vibration period at the start of the simulation. This vibration period is typical for nuclear facility structures, and is based on a model of a Candu Reactor created by Yin-Nan Huang (Huang and Whittaker 2008, Huang et al. 2009). The site for the nuclear facility structure considered for the hybrid simulation tests was a Western US rock site at Diablo Canyon Nuclear Power Plant in San Luis Obispo County, CA. Huang and Whittaker obtained the DBE spectrum for this site from the Nuclear Regulatory Commission (NRC). They matched 30 ground motions to the DBE spectrum over a wide range of periods using seed motions from the PEER NGA Database (PEER 2012). Since the fundamental period of the hybrid model elongates as the shear wall specimen is damaged during the hybrid simulation test, a ground motion was selected from their 30 motion set that best matched the DBE spectrum in the 0.14 s to 0.3 s range of periods. This motion was the 1999 Kocaeli, Turkey earthquake, shown in Figure 5.3.
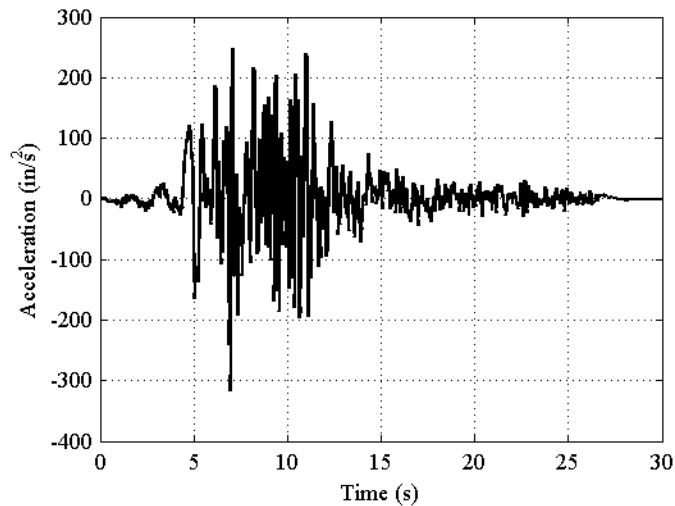
Figure 5.3: 1999 Kocaeli, Turkey Ground Motion

This ground motion was used as the base motion for the hybrid simulation tests and was further scaled to operational-level and design-level expected behaviors of a nuclear facility structure. Since nuclear facility structures are designed to remain "essentially elastic" in a DBE event, they

45

should remain elastic under a service level motion (operational basis earthquake) and possibly yield only marginally in a DBE. For the hybrid simulation tests, scaling factors applied to the Kocaeli base motion were selected to attain specific target behaviors in three levels of motion: an OBE, a DBE, and a BDBE. The OBE motion was designed so the wall would reach about 1/3 of its yield force. The DBE level motion targeted the wall reaching about 2/3 of its yield force. Then the BDBE was scaled to be an extremely large event that would enable investigation of the post-peak-strength behavior of the walls. This was selected to be 3 times larger than the DBE.

Prior to the hybrid simulation tests at *nees@Berkeley*, a quasi-static cyclic test of a nominally identical squat wall specimen was performed at University at Buffalo (Rocks et al. 2011). A yield force of 1500 kN (337.2 kips) was observed in the Buffalo test. Using this information, a single-degree-of-freedom (SDOF) oscillator bilinear model was developed in OpenSees to determine earthquake scaling factors that would achieve desired wall behavior. Table 5.2 shows the scaling factors for each ground motion (GM) level, which were applied to the Kocaeli base motion.

Table 5.2: Ground Motion Scaling Factors

GM Level	Scaling Factor	PGA (g)
OBE	0.053	0.043
DBE	0.14	0.12
BDBE	0.42	0.35

The test sequences for Wall 1 and 2 are summarized in Table 5.3. No vertical load was applied to the specimens. Walls 1 and 2 first experienced the OBE motion, since both walls were assumed to have been in service. Following the OBE motion, Wall 1 experienced a ground motion with a scaling factor of 0.11 (DBE 0.11), but the wall achieved less than the targeted 1/3 of its yield force for the DBE. Hence, the scaling factor of the DBE motion was increased to 0.14, as reported in Table 5.2, and resulted in Wall 1 reaching the desired force. This 0.14 scaling factor was used for all remaining DBE and DBE aftershock motions. Following the OBE, Wall 2 experienced the largest BDBE motion and then two DBE aftershocks, to investigate how well it survived strong aftershocks after a very large event.

Table 5.3: Ground Motion Test Sequences

Wall 1	Wall 2
OBE	OBE
DBE 0.11	BDBE
DBE	DBE Aftershock 1
BDBE	DBE Aftershock 2
DBE Aftershock 1	

5.5   INTEGRATION ALGORITHM

The OpenSees SDOF oscillator model was used to determine the appropriate integration algorithm and analysis time step. The ground motion time step is 0.01 s. The Newmark explicit method and the implicit Newmark Average Acceleration Method ($\gamma=0.5$, $\beta=0.25$) were both tested. First, the analytical time step was also set to 0.01 s, so the simulation was running in real

time. The explicit and implicit methods gave different displacement time history results for the 0.01 s analytical time step. For an analytical time step of 0.001 s, the explicit and implicit methods agreed. This was considered to be a close approximation to the true solution. Both the explicit and implicit methods, using a time step of 0.005 s (2 times slower than real time), were reasonably close to the true solution. An explicit method is better suited for hybrid simulation since it avoids iterations. Iterations on a physical specimen must be performed carefully since the intermediate steps affect the physical specimen's behavior. These analytical tests used the bilinear material, Steel01, in OpenSees. The sharp transition between the linear and nonlinear slopes in this material model contributed to some of the error. The actual hybrid simulation test, using a physical specimen that will lose stiffness gradually, will perform better. Thus, the explicit method with a time step of 0.005 s was selected for the hybrid simulation tests. The graph comparing a portion of the displacement time histories for explicit and implicit methods and varying time steps is shown in Figure 5.4.
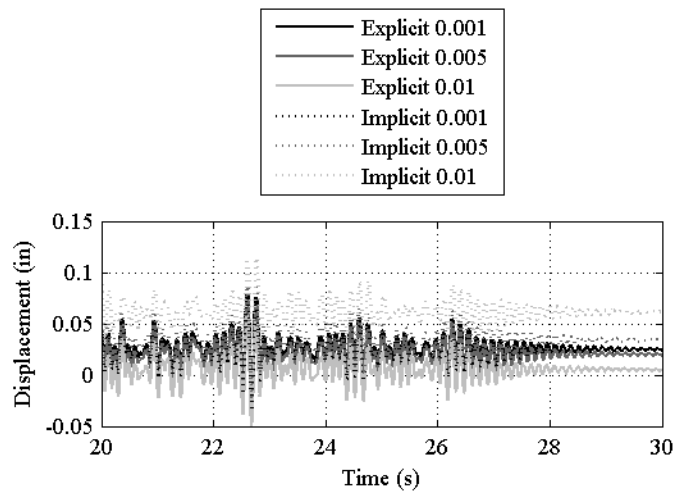
Figure 5.4: Comparison of Explicit and Implicit Methods

5.6   TEST SETUP

The laboratory test setup is shown in the drawing in Figure 5.5.
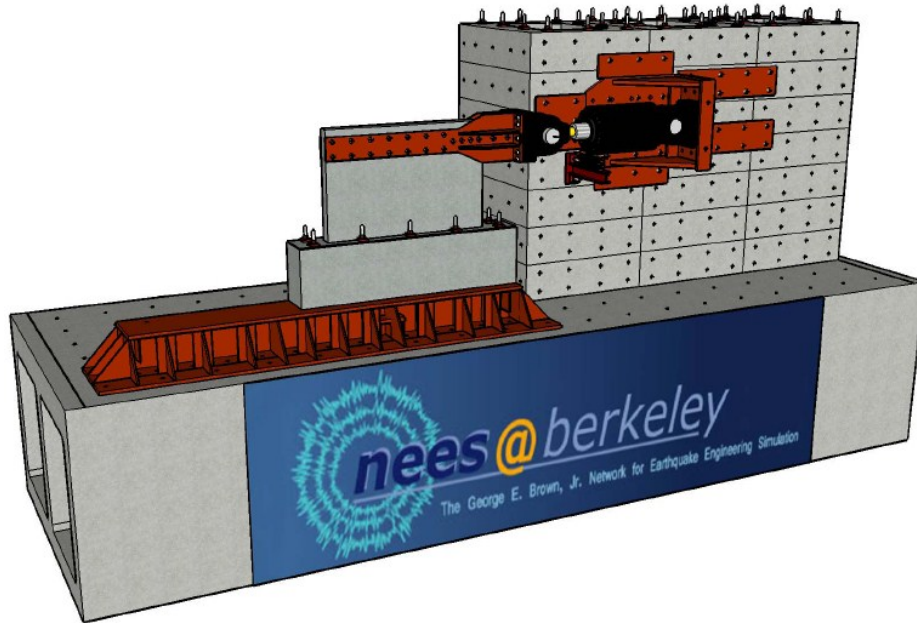
Figure 5.5: Global Sketch of Test Setup

The squat shear walls were tested using the existing setup from Lai's (2012) steel braced frame tests. Lai tested a two-story braced frame using two actuators mounted to the Reconfigurable Reaction Wall (RRW). The lower actuator was retained for the squat shear wall tests, which was attached to a stiff loading arm, designed to uniformly spread the actuator load across the top of the specimen. The actuator was first designed for the Caltrans research project (Astaneh-Asl and Ravat, 1998), and had a 1500 kip (6672 kN) capacity with +/-12 in (+/-30.5 cm) stroke. The clevises of the actuator slip slightly, so Lai performed hybrid simulation tests using a constant velocity displacement-controlled method at 0.002 in/s (0.005 cm/s). Each squat shear wall was attached to the steel floor beam, also used by Lai. The maximum shear capacity of the floor beam was calculated to be 900 kips, and the maximum uplift was calculated to be 600 kips (Lai 2012).

Photographs of Walls 1 and 2 are shown in Figure 5.6. The blue steel plate is used to distribute the load from the actuator (located on the right side of the wall) across the top of the wall. Testing a stiff specimen requires small displacement increments in order to have a smooth force response. Traditional displacement control strategies are inadequate for testing a stiff specimen because the displacement increments cannot be made small enough to avoid jumps in force. Typically, a LVDT is used for displacement feedback, but this instrument does not have the precision to control displacements below 0.001 in (25 microns). In order to test the stiff squat shear walls in this study, a Heidenhain LS 623 1140 mm (3.7 ft) high precision displacement encoder was implemented for displacement feedback in the PID loop. The encoder step resolution was 0.0004 in (10 microns). Before using the encoder for this study, it was tested, and its improved performance over a LVDT was validated (in Chapter 4). The encoder measured the displacements of the wall at the top center of the specimen with reference to a frame on the back of the wall. This stiff frame was embedded in the foundation of the specimen to eliminate the effect of any deformations at the interface between the specimen and the laboratory test floor.

In addition to traditional instrumentation including strain gages and Novotechnik potentiometers, Nikon Metrology K600 Krypton system targets were used on a portion of the front of the wall to monitor displacements of the wall surface. These targets are shown in Figure 5.6. For the Wall 2 test, a digital image correlation (DIC) technique was also used. A random pattern of black dots was drawn on the wall, and high resolution cameras were used to capture images of the changing pattern throughout the test. Finally, the VIC-2D software (Correlated Solutions 2009) was used to determine strain maps on the surface of the wall by tracking the motion of the pattern of dots throughout a sequence of images.
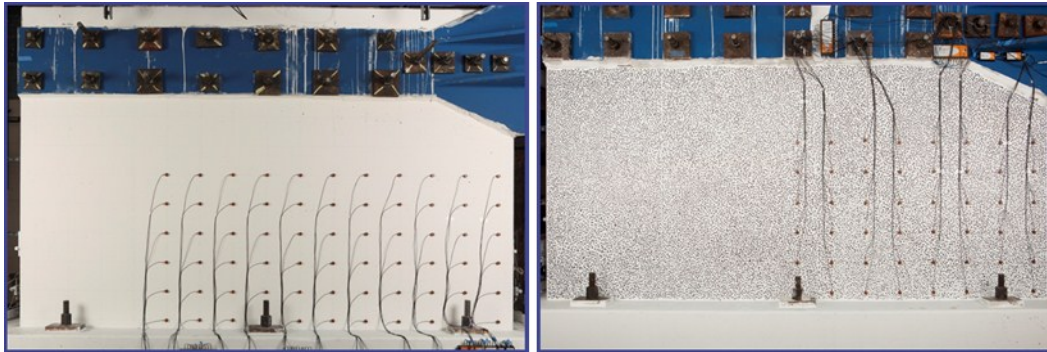
Figure 5.6: Wall 1 and Wall 2 Specimens

5.6.1 Novotechnik Displacement Potentiometers

A drawing of the Novotechnik instrumentation to capture wall displacements, flexure, and sliding is shown in Figure 5.7. In the side view of the wall, the Novotechniks mounted vertically are shown. Each attachment point to the wall has both horizontal and vertical instruments. For the purpose of wall displacement analysis, the sliding zone is defined as the 3 in (7.62 mm) narrow zone at the interface between the wall and its foundation. This zone includes the primary flexural crack along which sliding occurred, the first horizontal reinforcing bar, and a portion of the length where the vertical reinforcing bars acted as dowels on the sliding surface. The height of the sliding zone matched the attachment location of the first level of vertical and horizontal displacement measurement instruments. Pairs of vertically and horizontally positioned Novotechniks were installed at the left and the right edges of the wall at 3 in (7.62 cm), 9 in (22.86 cm), and 19 in (48.26 cm) above the foundation. At the lowest level, two vertical instruments are positioned. The average of their displacement was used to measure the vertical motion in the 3 inch (7.62 cm) region above the foundation. Two Novotechniks were attached to the point 3 in above the foundation, and positioned horizontally, to perform two-dimensional triangulation. Above these lowest instruments, a Novotechnik was positioned vertically to measure the relative motion between the lowest vertical instruments and a point 6 inches (15.24 cm) above. Two more Novotechniks were attached here horizontally for triangulation. Finally, one additional Novotechnik was positioned vertically to capture the relative motion in the next

49

10 inches (25.4 cm) above the previous instrument. Again, two more Novotechniks were attached horizontally for triangulation. This pattern was exactly replicated on the other side of the wall. On the non-actuator side of the wall, triangulation was also performed at the 64.125 in (1.63 m) height of the actuator. All reference frames were anchored to the foundation, so every Novotechnik instrument measured wall displacements relative to the foundation.
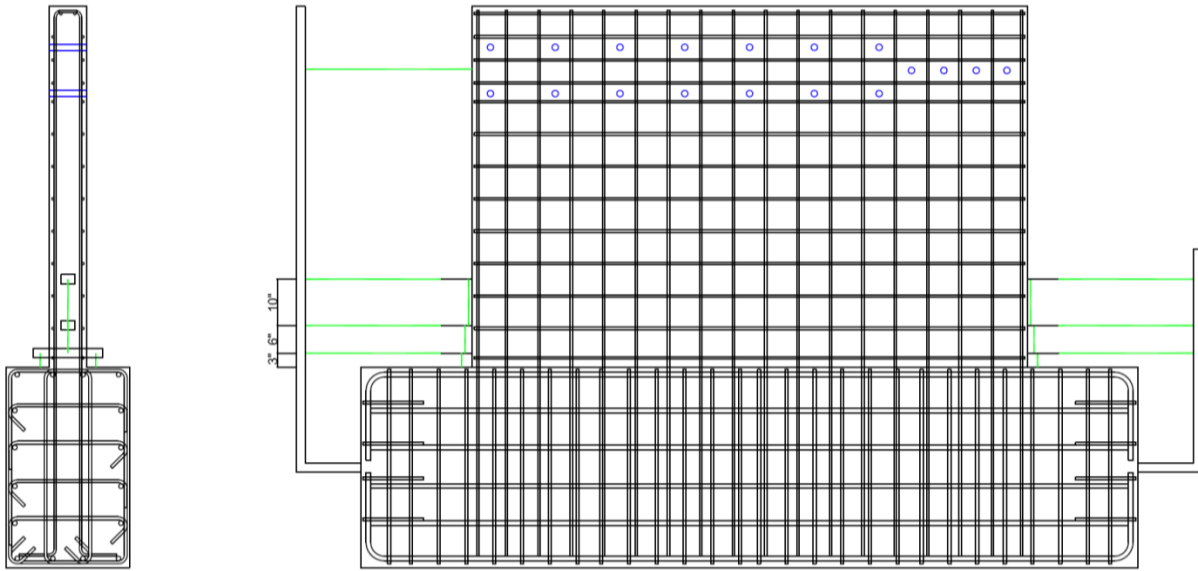
Figure 5.7: Novotechniks to Measure Wall Displacements, Flexure, and Sliding

In Figure 5.8 (a), a photograph shows the Novotechniks on the left side of the wall. The instrument wires are colored blue for better visibility. Here, the arrangement for two-dimensional triangulation is apparent. Similar instruments were located on the right side of the wall. The circled vertical instruments are shown in a close-up view in Figure 5.8 (b).
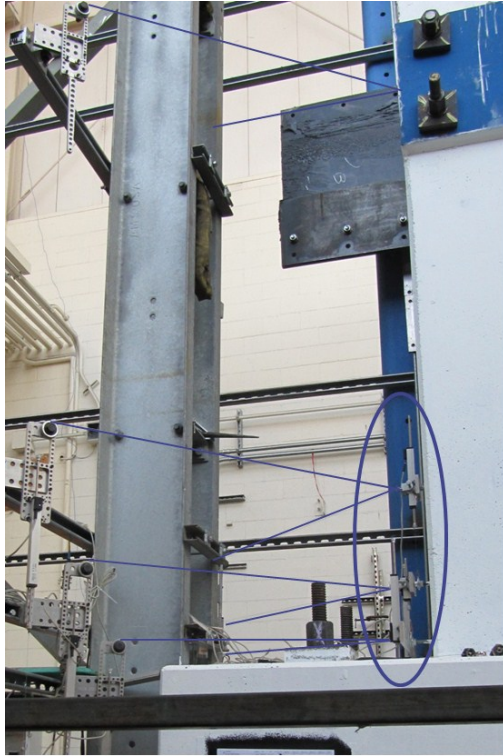
<div align="center">(a)   (b)</div>

Figure 5.8: Novotechnik Instruments for (a) Horizontal Motion and (b) Vertical Motion

A separate system of displacement potentiometers, arranged in a square pattern along the back of the wall, measured shear deformations. A drawing of these Novotechnik instruments to capture shear is shown in Figure 5.9. This drawing shows a rear view of the wall, so the actuator attaches on the left side. The Novotechniks were mounted to long rods with swivels on both ends. These were fastened to threaded rods embedded in the back of the wall with epoxy. The holes for these threaded rods were drilled after the walls were cast. The dimensions that the shear instruments measured were approximately 3 ft (0.914 m) x 3 ft squares. However, due to the positions of reinforcing bars in the wall, the threaded rods had to be shifted slightly. The far left side and far right side vertical instruments (6 inches or 15.24 cm from the left or right edges of the wall) contained four instruments each. These measured the bottom 3 inches from the foundation in the sliding zone. Then the next 6 inches, the next 10 inches, and the remaining 20 inches were measured vertically. These matched the heights of the vertical instruments on the short sides of the wall.
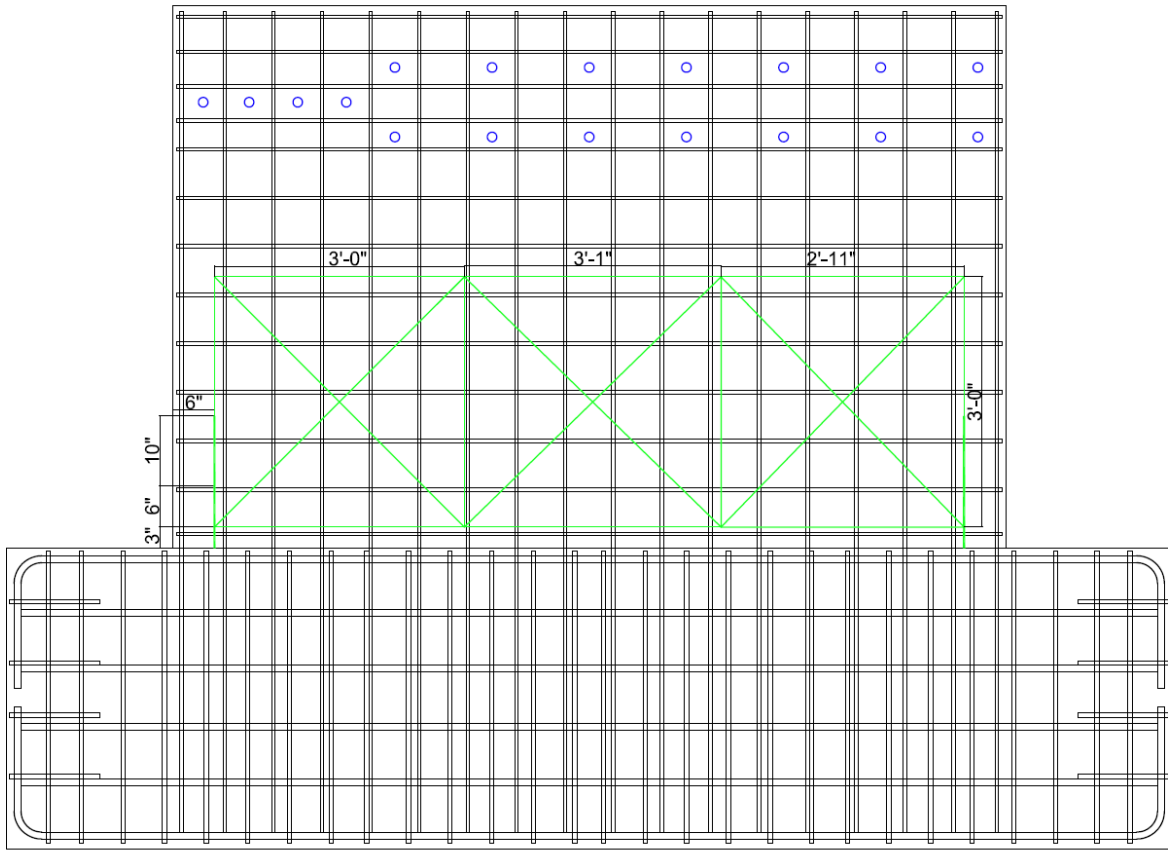
Figure 5.9: Novotechnik Instrumentation for Shear

A photograph of the shear instruments is shown in Figure 5.10.
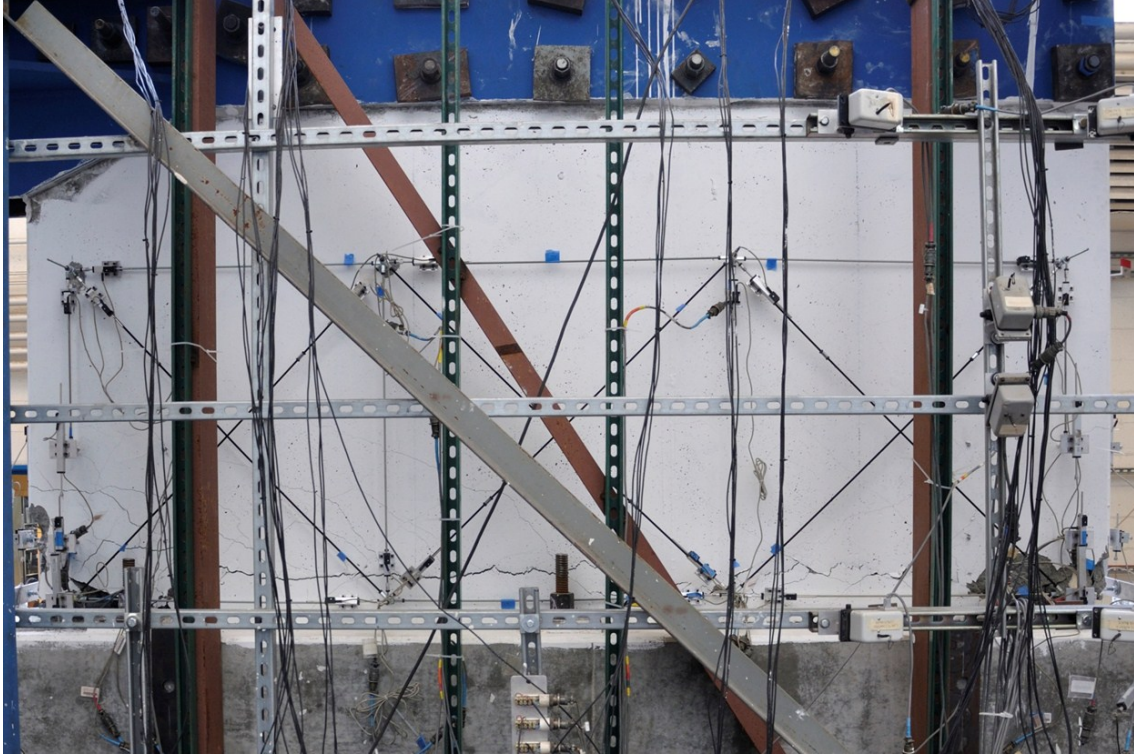
Figure 5.10: Novotechnik Instruments Shear

5.6.2 Strain Gage Instrumentation

A drawing of the strain gages on the vertical reinforcing bars is shown in Figure 5.11. This is the arrangement of gages, viewed from the front of the specimen. The gages are located on the rear curtain of reinforcing bars, except for any gages labeled "B," which are located on the front curtain.
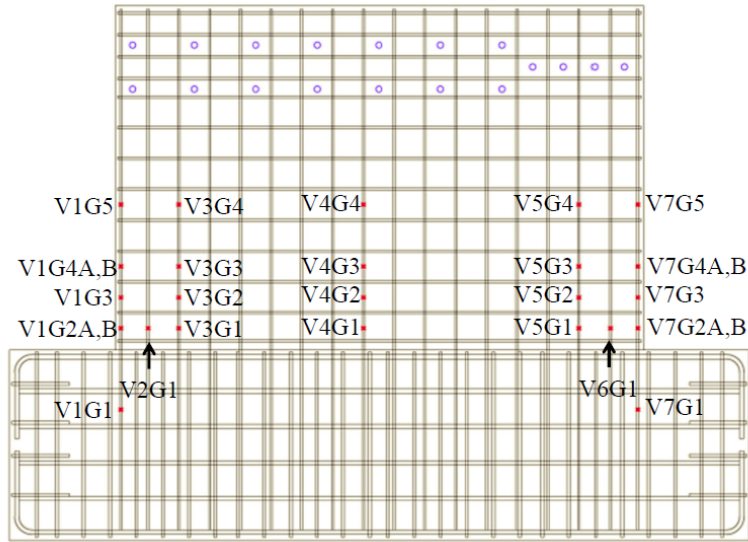
Figure 5.11: Strain Gages on Vertical Bars

A similar drawing of the strain gages on the horizontal reinforcing bars is shown in Figure 5.12. All horizontal reinforcing bars are located on the rear curtain.
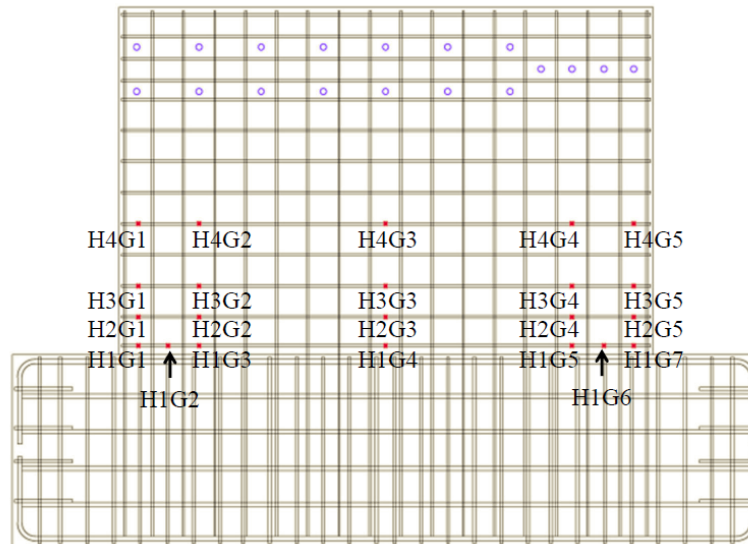
Figure 5.12: Strain Gages on Horizontal Bars

5.6.3 Krypton Instrumentation

The locations of the Krypton infrared LED targets are shown in Figure 5.13. The targets were hot glued to the specimen on an 8 inch (20.32 cm) x 7 inch (17.78 cm) grid. The Krypton K600 system tracked these targets using a camera unit that is composed of three individual cameras

and performed three-dimensional triangulation. A photograph of the K600 camera is shown in Figure 5.14.
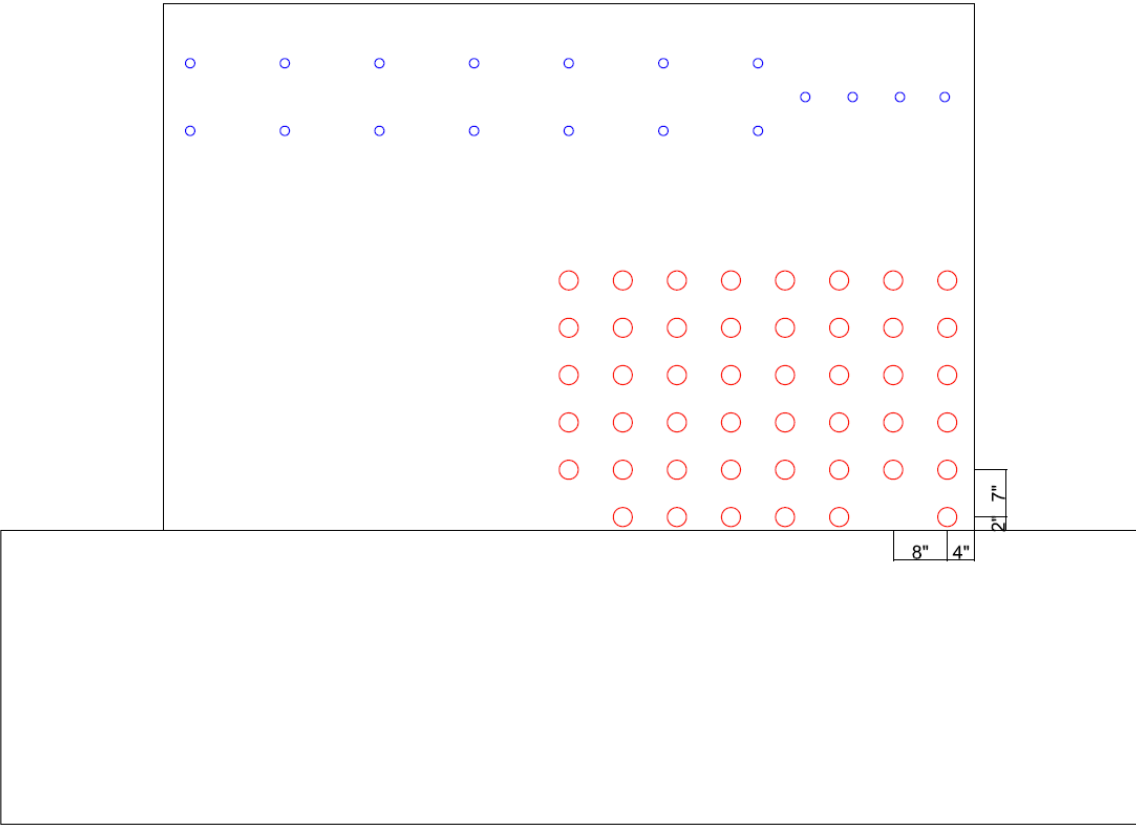
Figure 5.13: Krypton Target Locations

Figure 5.14: Krypton Camera

For these wall tests, the camera could only monitor targets on half of the test walls. Though there were extra LED targets mounted on the Wall 1 specimen, only the target locations shown in Figure 5.13 were used. There were space constraints in the lab such that the Krypton camera system could not be positioned further away from the specimen to capture a wider view. Even if more space was available, this would have compromised some accuracy. Though it is possible to use Krypton with two cameras, which would have allowed for a wider range of targets, a second camera was not available.

5.6.4   Digital Image Correlation

For the Wall 2 test, a Digital Image Correlation (DIC) technique was used. A random pattern of black dots was drawn on Wall 2 using a Sharpie pen, shown in Figure 5.15, and a high resolution 21 megapixel Canon 5D camera was used to photograph the pattern throughout the test. The length of the black marks was intended to be just larger than 1/8 in (3.2 mm), which corresponded to just larger than 5 pixels. An image correlation software, VIC-2D 2009 (Correlated Solutions 2009), was used to map strains by tracking the motion of the pattern of dots in a sequence of images.
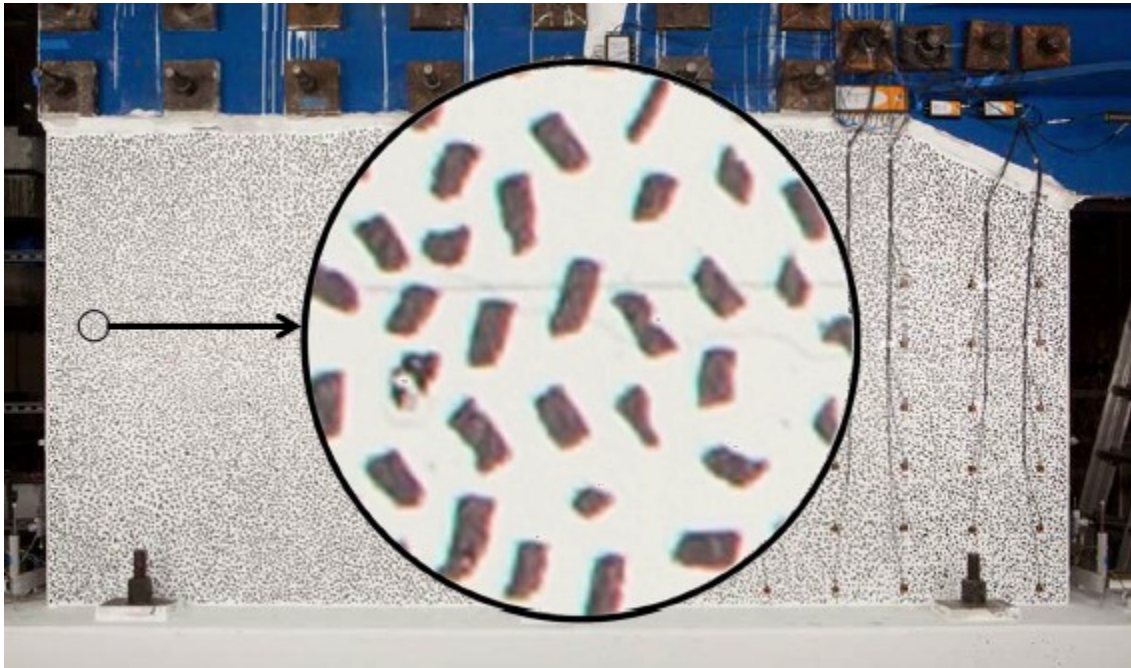
Figure 5.15: Spot Pattern on Wall 2 for DIC

5.6.5   Global Measurement Instruments

Figure 5.16 shows the instruments used to measure the global behavior of the test setup. Instruments in positions 1 and 2 determined the slip of the north and south sides of the east clevis. Similarly, instruments in positions 3 and 4 measured the slip of the north and south sides of the west clevis. Measurements from instruments 1 and 2 were averaged to determine the east slip (similarly 3 and 4 were averaged for the west slip). Hence, any out-of-plane rotation of the clevises could be assessed. Instrument 5 measured the slip of the base beam relative to the strong floor. Instrument 6 measured the slip of the foundation relative to the base beam. Enlarged views are shown for the instruments in positions 5, 7, 8, 9, and 10. These instruments were reused from the previous braced frame test (Lai 2012), and enlarged images showing the

positions of these five Novotechniks are courtesy of Lai. The reconfigurable reaction wall (RRW) that the actuator is mounted to is taller than shown in the global view in Figure 5.16. The RRW was cropped in the picture to focus attention on this test setup. The RRW is 25 feet (7.62 m) tall and 10 feet (3.05 m) deep. The Novotechniks mounted on this wall were located 9 inches (22.86 cm) from the left and right edges of the RRW and 1 inch (2.54 cm) above the base of the RRW (instruments 7 and 8) and 2 feet 1 inch (33.02 cm) below the top of the RRW (instruments 9 and 10). The motions of the RRW at the base and at actuator height were most relevant. The motion of the RRW was calculated at the 11 foot, 7 inch (3.53 m) actuator height using a linear relationship based on motion at the top of the RRW.
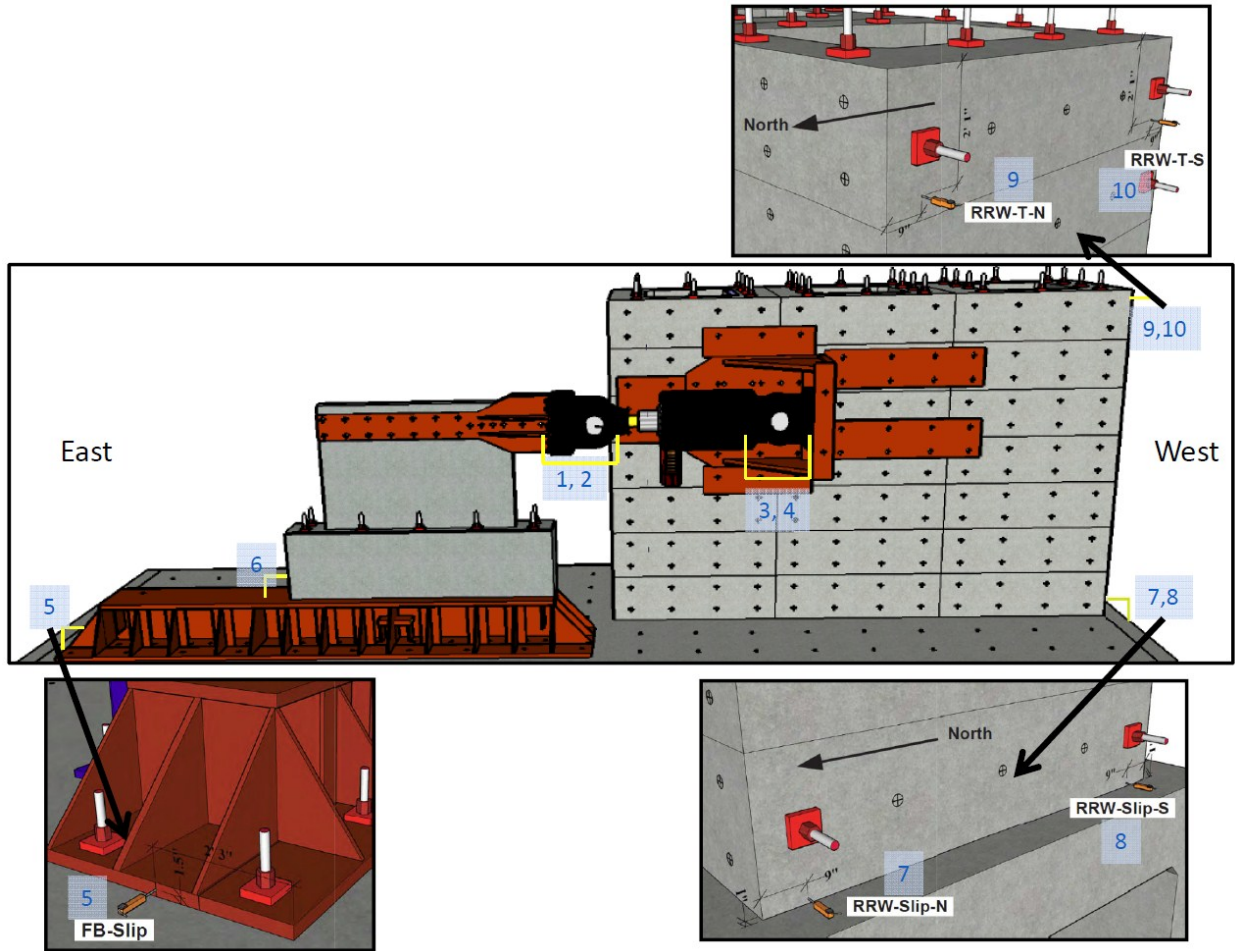
Figure 5.16: Global Measurements

5.7   WALL TEST PROCEDURES

A stiffness pre-test was performed on each wall specimen before the start of hybrid simulations. A very small saw-tooth displacement-controlled motion was imposed, with forces limited to +/-444.8 kN (+/-100 kips). Because of the high stiffnesses of the walls, the forces were initially very difficult to control and fluctuated within +/-444.8 kN (+/-100 kips). The stiffness of Wall 1 was approximated to be about 840.6 kN/mm (4800 kips/in). This value was used to determine

the mass in the numerical model required to achieve the fundamental vibration period of 0.14 s for the hybrid model.

Next, a free vibration pre-test was performed to assess the damping in the system due to errors in the control loop and to determine the appropriate velocity for the simulation. The forces were also maintained below +/-444.8 kN (+/-100 kips) for this test. Since the pins holding the clevises of the actuator were not perfectly machined, the clevises slipped slightly on load direction reversal. In order to limit control errors in this situation, the simulation was conducted using a slow constant actuator velocity model. With the selected velocity of 0.254 mm/s (0.01 in/s), the free vibration pre-test did not exhibit damping. Thus, 2% damping was implemented directly in the numerical model.

After the two pre-tests, the ground motion sequences were applied to each wall as described in Table 5.3. At the end of both simulation sequences, the walls had lost most of their strength, such that it was unsafe to perform further ground motion simulations. Instead, the walls were broken using quasi-static single-cyclic saw-tooth motions to +/-1 in (+/-2.54 cm) and then +/-1.5 in (+/-3.81 cm) peak displacements.

5.8   SUMMARY

This chapter summarized the wall designs, materials, and instrumentation. Additionally, it described the ground motion selected for the tests, the scaling factors applied to the ground motion, and the sequences of ground motions applied to the test specimens. Chapter 6 will provide and interpret the results from the hybrid simulation ground motion sequences applied to each wall.

6   Results and Discussion

6.1   INTRODUCTION

This chapter will first address the Wall 1 and Wall 2 behavior separately. Each wall will be described by its performance in the ground motions in the order that they were prescribed. Then the behavior of the two walls will be compared. The gain on the data acquisition system for the strain gages was accidentally set to a very high value for the Wall 1 test, so strain data was not available much beyond yield. For this reason, comparing strains between the two walls was not possible. The strain gages are analyzed to show the locations and the order that the gages yielded. An attempt is made to separate the wall displacements into shear, flexure, rotation in the 3 in sliding zone above the base, and base sliding components. This is challenging due to the small displacements for stiff specimens. The code equations introduced in Chapter 2 are evaluated for their ability to predict the behavior of Walls 1 and 2. Then the Wallace (2006) backbone curve for squat walls is assessed in comparison to the data observed in these experiments. Finally, the test setup response and the hybrid simulation errors are analyzed.

6.2   WALL 1 BEHAVIOR

Before subjecting Wall 1 to the hybrid simulations of the ground motions, pre-test stiffness and free vibration tests were performed. For the stiffness test, a very small saw-tooth displacement-controlled motion was commanded to the specimen. At first, the control system interlocks were set to limit the forces to +/-56.2 kips (+/-250 kN), which was half of the target force for the OBE motion. However, the high stiffness of the wall and the slip in the actuator clevises made the displacements (and thus the forces) difficult to control, so there were some spikes in the force. The force limit was reached in the first few trials, which automatically shut down the hydraulics, so the range of force limits was extended to +/-100 kips (+/-444.8 kN). The upper subplot in Figure 6.1 shows the displacement command and displacement feedback for the successful stiffness test. The displacement tracking was very poor when the actuator changed directions. Since the wall was very stiff, the displacements were very small. The actuator was changing directions after very little motion, and the errors constituted a large portion of the response. The fluctuations in the force feedback-time plot and the force-displacement response are shown in the lower two subplots of Figure 6.1.
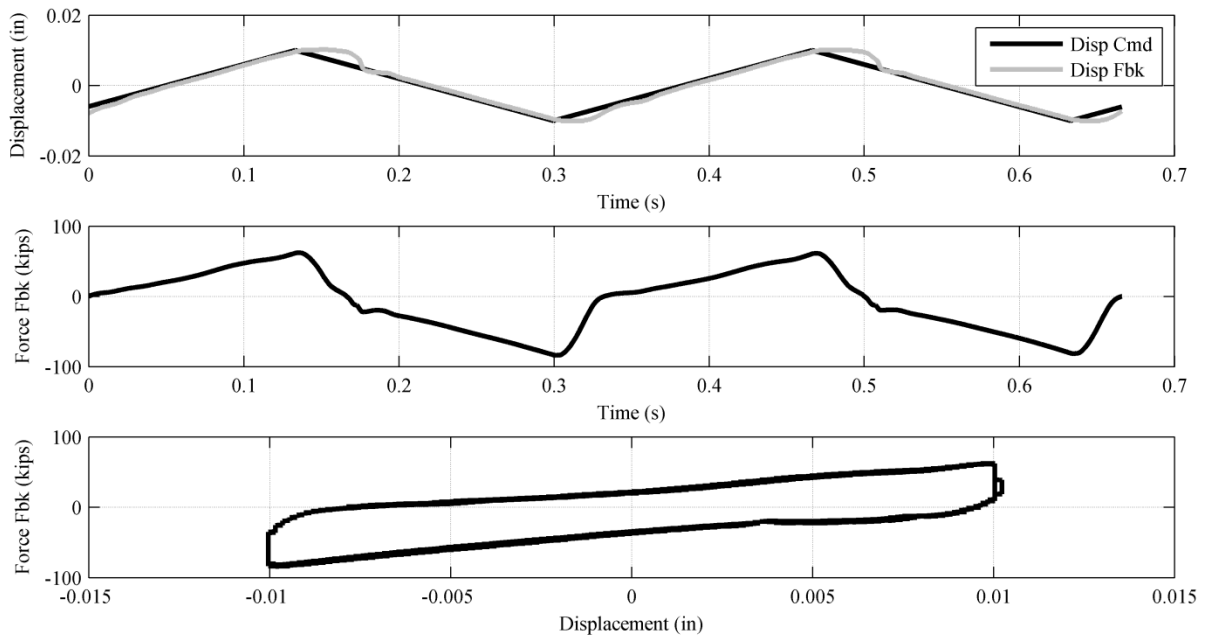
Figure 6.1: Wall 1 Stiffness Test

The stiffness of the wall was approximated from the force-displacement response plot. This was difficult because of the large amount of errors present. The stiffness was measured by using a best-fit line in the displacement range of -0.01 in to 0.003 in. The stiffness was determined to be approximately 4800 kips/in (840.6 kN/mm). This value was used in the hybrid model to calculate the mass necessary for the hybrid model to have a period of 0.14 s. The mass was 2.383 k-s^2/in. However, the stiffness was later shown to be underestimated significantly.

A free vibration test was performed to determine the simulation velocity and the damping in the numerical portion of the hybrid model. The forces were again limited to +/-100 kips (+/-444.8 kN). A constant velocity of 0.01 in/s (0.254 mm/s) was selected to drive the actuator. This resulted in approximately 0 damping due to errors in the control loop. Thus, 2% damping was implemented directly in the numerical model as mass-proportional damping.

A number of trials were necessary for a successful stiffness test and free vibration test. The free vibration test, in particular, required a few trials to choose the optimal velocity. These runs were assumed to be small enough to avoid affecting the integrity of the wall because it remained in the elastic range. Later it was discovered that these repeated small-force tests were rapidly reducing the wall stiffness. After the hybrid simulation test was completed and the data was inspected in detail, the recorded acceleration data from the free vibration tests revealed a much higher initial wall stiffness than estimated from Figure 6.1. The stiffness test was controlled directly from the laboratory control system, so the stiffness estimate was made based on the only available data (the force-displacement response plot). The free vibration test was executed using OpenSees and OpenFresco. The acceleration data was recorded in OpenSees, and the FFT of the acceleration data recorded during the first successful free vibration test revealed a frequency of 10.94 Hz. This corresponds to a period of 0.0914 s and a stiffness of 11,261 k/in. Thus, the force-displacement response plot in Figure 6.1 was not a good indication

of the actual wall stiffness. There were too many errors with slip in the clevises at those small displacements to accurately determine the stiffness from a best-fit line.

Following the completion of additional free vibration tests to decide the optimal constant velocity value and after the completion of the OBE hybrid simulation (all <100 kip runs), the wall stiffness already dropped to 3703 k/in. Thus, the 4800 k/in (840.6 kN/mm) stiffness used in the hybrid model to achieve an initial period of 0.14 s was appropriate for the condition of the wall at the time of the OBE hybrid simulation. However, the wall lost a very large amount of its stiffness in the pre-test runs.

After the pre-test stiffness and free vibration runs, some minor diagonal cracking was observed. These cracks extended from about mid-height on the east side of the specimen towards the lower west side of the specimen at about a 45 degree angle.

The hybrid simulation ground motion sequence for Wall 1 was OBE – DBE 0.11 – DBE – BDBE – DBE aftershock. The first attempt to reach 2/3 of the yield force for a DBE used a scaling factor of 0.11 and resulted in forces lower than those targeted. The scaling factor was increased to 0.14 and the DBE motion was repeated. After the ground motion sequence, the specimen was broken using cycles to 1 in (2.54 cm) and 1.5 in (3.81 cm). This decision was made based on the extent of damage following the DBE aftershock motion. Cycles were determined to be safer than a larger ground motion. The displacement feedback-time history for the total hybrid simulation sequence and the ductility-time history are shown in Figure 6.2. The yield displacement was determined to be 0.23 in. The force feedback-time history is shown in Figure 6.3. The asterisks (*) indicate the end of one ground motion and the start of the next.
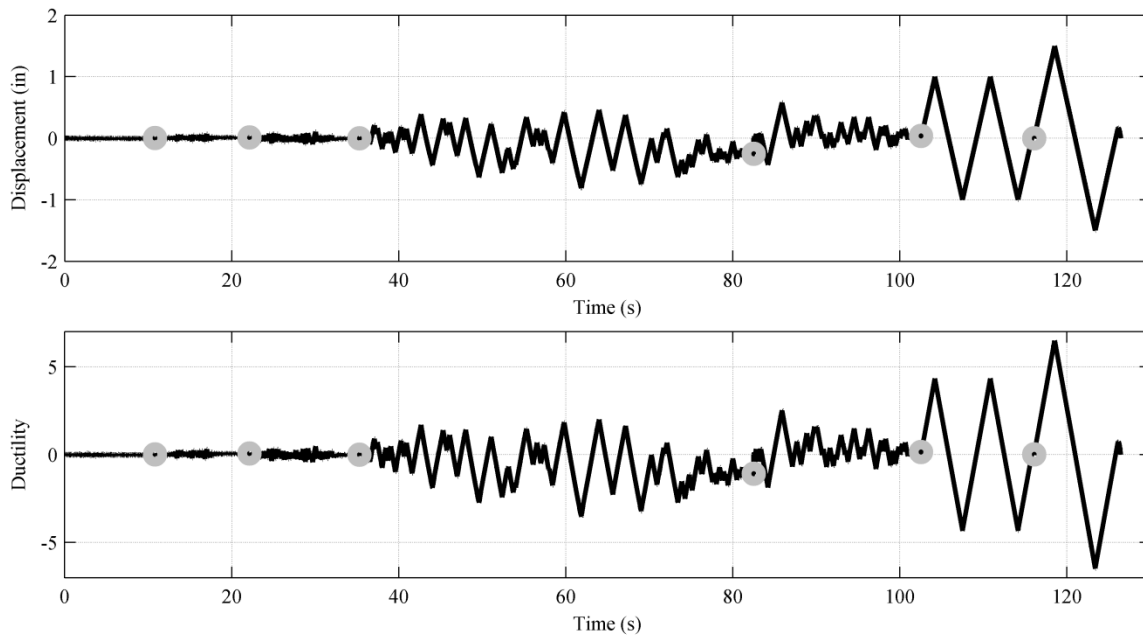
Figure 6.2: Wall 1 Displacement-Time and Ductility-Time Histories
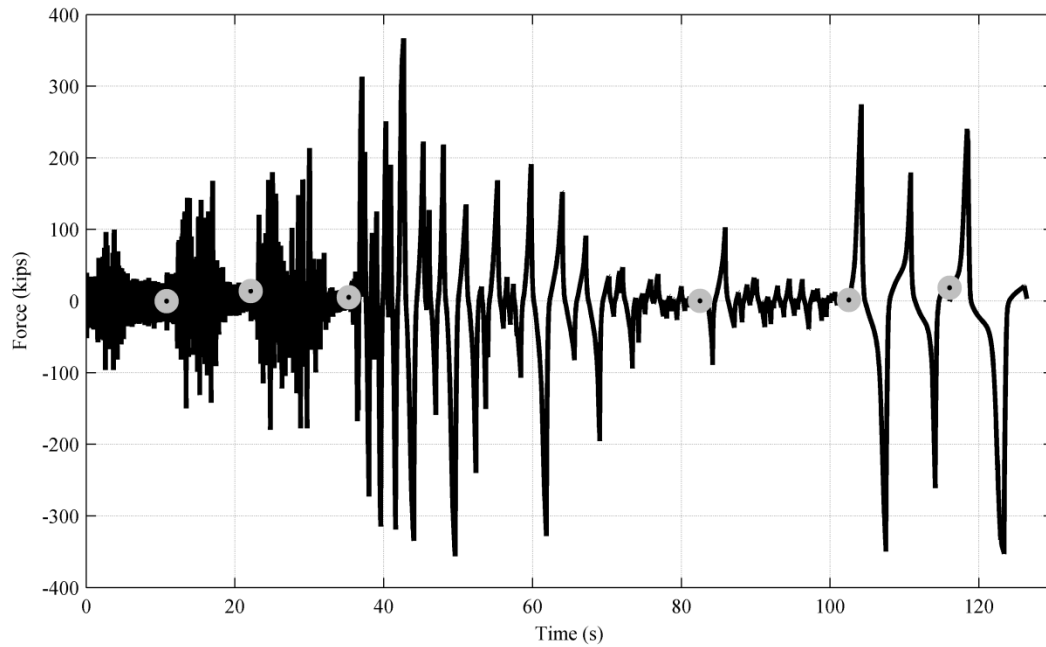
Figure 6.3: Wall 1 Force-Time Response History

Wall 1 was relatively undamaged until the BDBE motion, except for a few hairline shear and flexural cracks. Photographs of Wall 1 following the BDBE motion and both cyclic motions are shown in Figure 6.4. The cracks are enhanced in the images for better visibility.

(a)   (b)

(c)
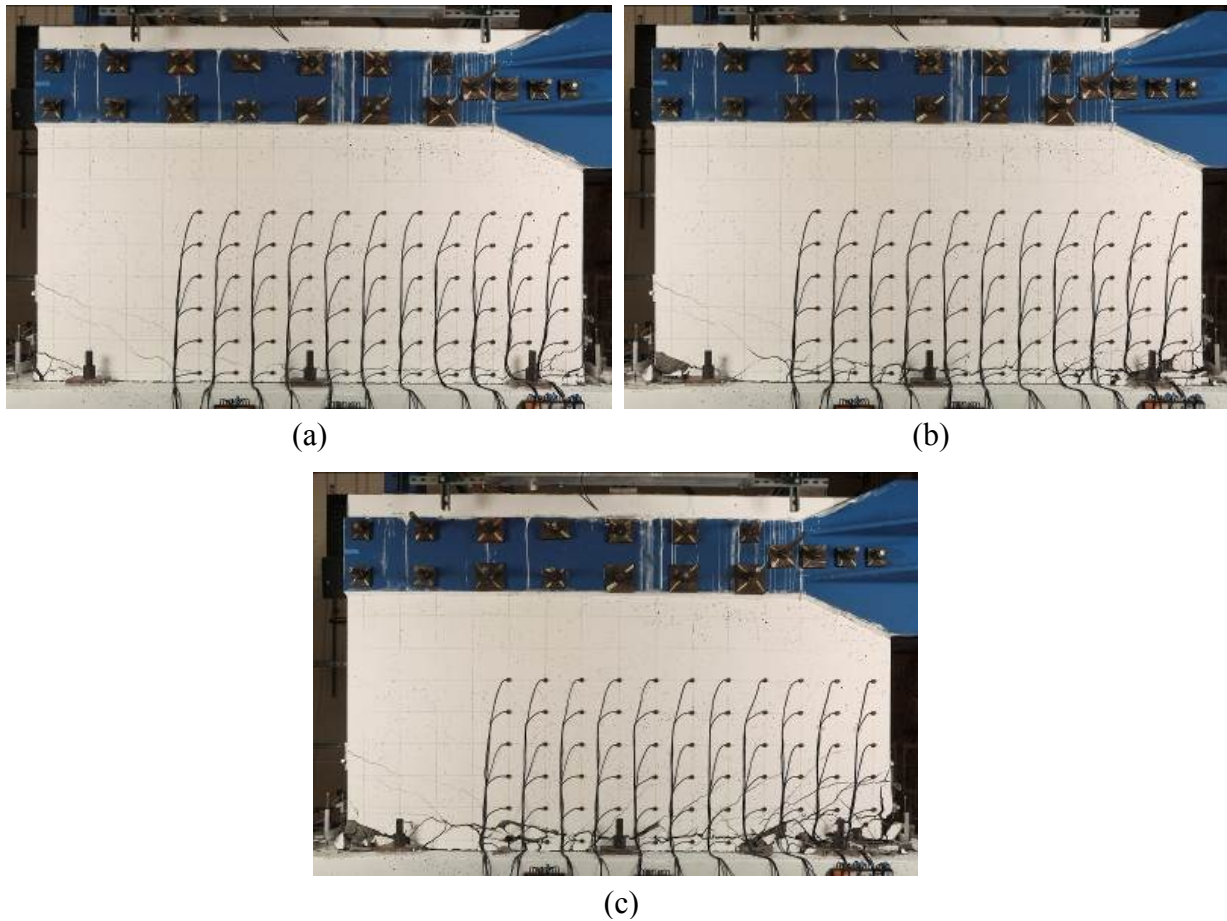
Figure 6.4: Wall 1 at (a) End of BDBE (b) End of Cycles to 1 in (c) End of Cycles to 1.5 in

6.2.1 OBE Motion

An OpenSees bilinear SDOF oscillator model was used to scale the ground motion for a target force of 1/3 of Buffalo's yield force (112.4 kips or 500 kN), representing a service level earthquake. Details of the simple model included a material model described by the measured 4800 k/in initial stiffness and the Buffalo yield force. The hardening branch of the material model used a stiffness that was 8% of the initial stiffness. The mass 2.383 k-s^2/in was used in the model so the elastic period was 0.14 s. This resulted in a ground motion scaling factor of 0.05263 for the OBE motion. The expected maximum displacement and force from the OpenSees model simulation were 0.023 in and 112.4 kips. The experimentally measured maximum displacement and force from Wall 1 were 0.029 in and 99.93 kips. The stiffness used in the SDOF oscillator model was 4800 kips/in, based on the Wall 1 stiffness pre-test. As mentioned in the previous section, after the OBE motion was imposed on Wall 1, the recorded acceleration data was used to determine the current stiffness. The FFT of the recorded acceleration showed a peak at 6.274 Hz. This represents a period of 0.1594 s. The stiffness was

calculated to be 3703 kips/in. Thus, the stiffness dropped significantly even after a very small ground motion, which did not produce much visible damage. The force-drift response from the OBE motion is shown in Figure 6.5. The displacement was recorded by the encoder and the force is the actuator load cell feedback.
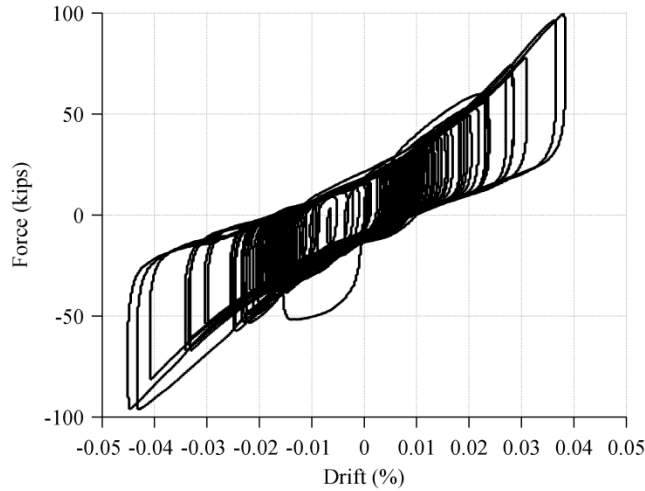
Figure 6.5: Wall 1 OBE Force-Drift Response

6.2.2 DBE 0.11 Motion

The OpenSees bilinear model was again used to scale the ground motion for the DBE run. The target force was 2/3 of Buffalo's yield force (224.8 kips or 1000 kN). The stiffness calculated at the end of the OBE motion was not performed until later. At the time of scaling the DBE motion, the stiffness was assumed not to have deviated much from the initial 4800 kips/in because the observed damage was so light. Using the same stiffness in the OpenSees bilinear model, the ground motion scaling value was determined to be 0.1052. The expected maximum displacement and force from the OpenSees model simulation were 0.047 in and 224.7 kips. The experimentally measured maximum displacement and force from Wall 1 were 0.074 in and 168.1 kips. The desired force was not achieved and the displacement was much larger than estimated because of the incorrect stiffness in the OpenSees model simulation. After the DBE 0.11 motion was imposed on Wall 1, the recorded acceleration data was used to determine the current stiffness. The FFT of the recorded acceleration showed a peak at 5.078 Hz. This corresponds to a period of 0.1969 s and a stiffness of 2426 kips/in. Again, the stiffness dropped significantly without much visible damage. Since the DBE 0.11 motion did not achieve the desired force, the motion was repeated with a larger scaling factor. The force-drift response from the DBE 0.11 motion is shown in Figure 6.6.

64
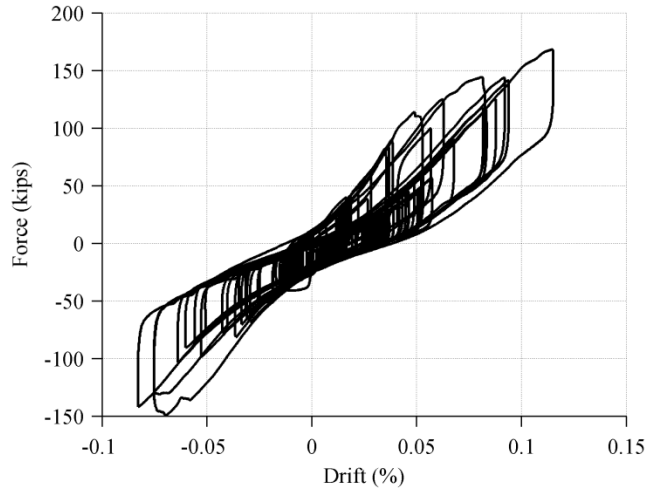
Figure 6.6: Wall 1 DBE 0.11 Force-Drift Response

6.2.3   DBE Motion

Since only 75% of the target force was achieved with the DBE 0.11 motion, the scaling was recalculated for a repeat run. The stiffness was updated to be 2426 kips/in in the OpenSees bilinear model.   Using the same scaling factor, 0.1052, the model predicted a maximum displacement of 0.11 in and a maximum force of 273.2 kips. This differed significantly from the measured displacement and force values. Therefore, the OpenSees bilinear model was no longer useful for determining scaling factors to achieve a desired force. A more complex model that considers the cracking point would be necessary. The DBE motion was now scaled directly by a factor of the target force/observed force.   The new scaling factor was 0.1407.   The experimentally measured maximum displacement and force from Wall 1 were 0.108 in and 213.7 kips. This was considered to be sufficiently close to the target force of 224.8 kips. After this motion, the FFT of the recorded acceleration showed a peak at 4.077 Hz. This corresponds to a period of 0.245 s and a stiffness of 1567 kips/in. Again, the stiffness dropped significantly without much visible damage. The force-drift response from the updated DBE motion is shown in Figure 6.7.

65
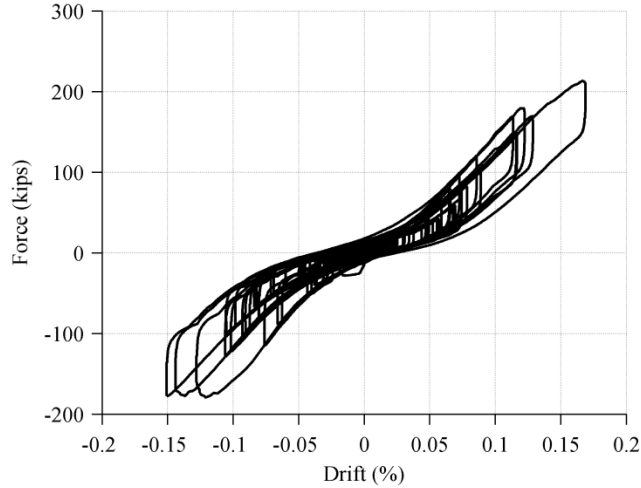
Figure 6.7: Wall 1 DBE Force-Drift Response

6.2.4 BDBE Motion

The purpose of the BDBE motion was to push the wall beyond its peak strength. Prior to this motion, Wall 1 was still relatively undamaged except for very minor diagonal cracking. The original plan called for scaling the BDBE motion as 2xDBE. However, after under-scaling the DBE motion initially with the factor of 0.11, the BDBE motion was scaled as 3xDBE to avoid any undershoot. This scaling factor was 0.4221. The experimentally measured maximum displacement and force from Wall 1 were 0.814 in and 368.2 kips. The FFT of the recorded acceleration showed a peak at 2.49 Hz. This corresponds to a period of 0.402 s and a stiffness of 583 kips/in. During the BDBE motion, the wall first experienced additional shear cracking. The approximately 45 degree cracks were well distributed along the length of the wall, indicating that the loading plate was distributing the load along the wall. These shear cracks are enhanced to be visible in Figure 6.8.
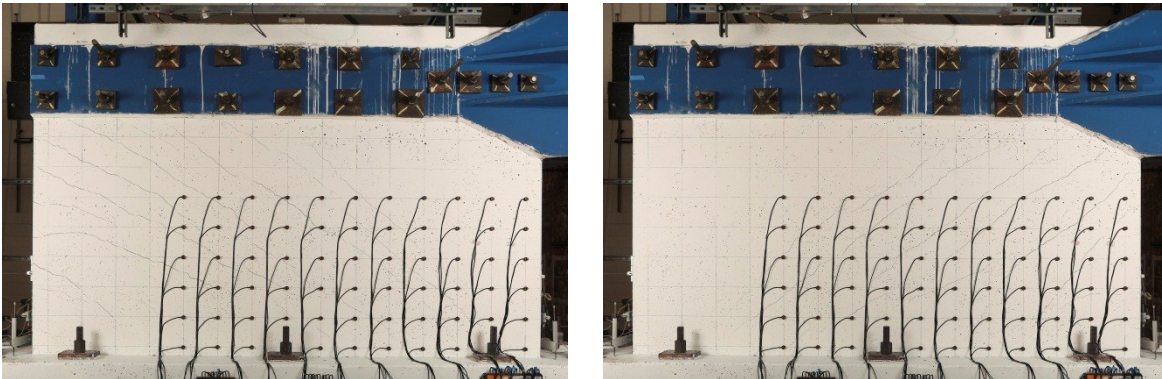
Figure 6.8: Wall 1 BDBE Shear Cracks

As the ground motion progressed, flexural cracks began developing in the lower corners of the wall, located at about 1/6 of the height of the wall from the base to the loading plate. These

cracks grew wider than the shear cracks and flexural response became more dominant. The wider flexural cracks are shown in Figure 6.9.
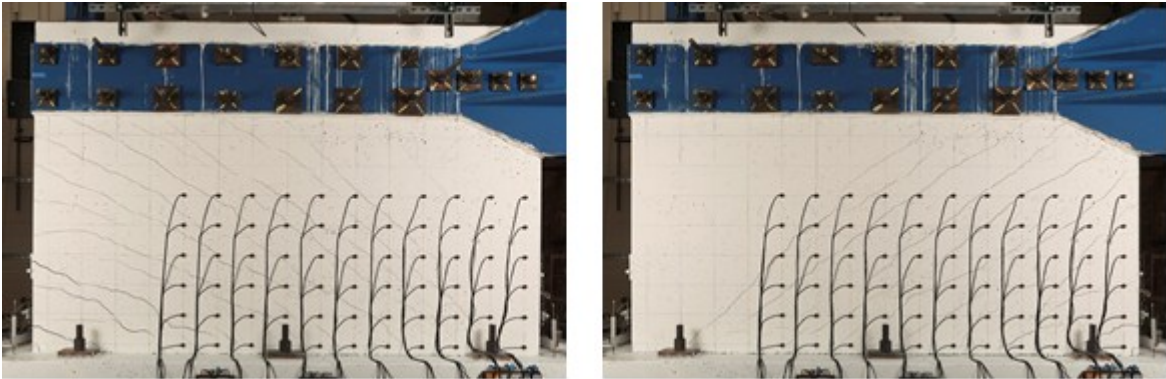
Figure 6.9: Wall 1 BDBE Shear and Flexural Cracks

The dominant flexural cracking was very brief since a crack developed from the lower corners of the wall and propagated across the entire base of the wall. The final failure mode was sliding shear. This crack along the base of the wall is evident in the right hand photo in Figure 6.10 and more visible in Figure 6.10. The flexural and shear cracking is still evident, but this is shown at the wall peak displacements. The wall slid along its base, and as it reached its peak displacement, the shear and especially the flexural cracks opened.
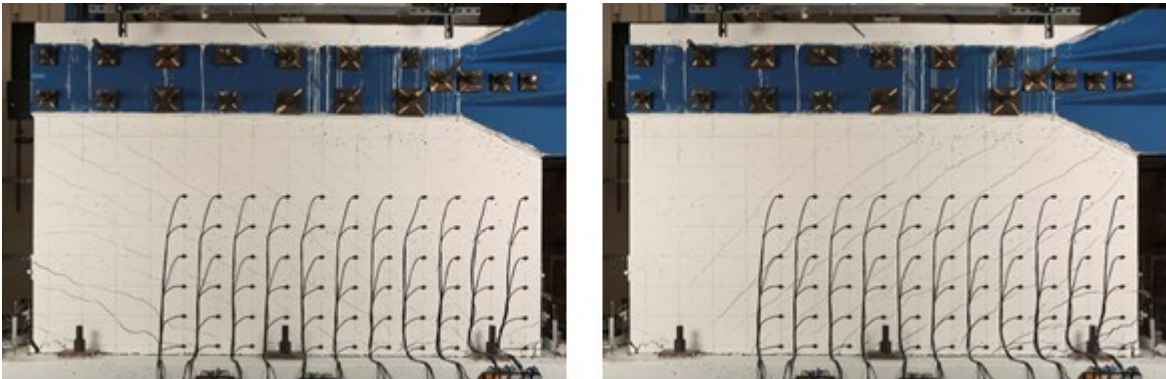
Figure 6.10: Wall 1 BDBE Sliding Shear

By the end of the BDBE motion, the wall was significantly damaged. A slightly smaller ground motion scaling would have been more appropriate, since very little wall strength remained for the upcoming DBE aftershock. The force-drift response from the BDBE motion is shown in Figure 6.11.
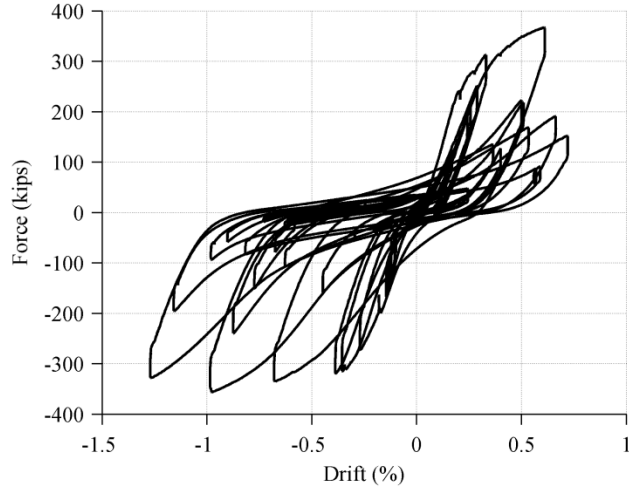
Figure 6.11: Wall 1 BDBE Force-Drift Response

The behavior of Wall 1 during the BDBE motion was asymmetric. In order to test whether this was a result of the ground motion or a problem with the test setup, the Wall 2 ground motions were prescribed in the opposite direction. Upon comparing the plots, the behavior was very similar. The conclusion was the ground motion was the reason for the asymmetry.

On the day of the Wall 1 test, the concrete compressive strength was 5145 psi. The maximum shear stress is defined as the peak lateral force divided by the wall cross sectional area (120 in x 8 in). This is expressed in terms of multiples of $\sqrt{f'}_c$, where f'$_c$ is defined in psi. The conversion to metric is $\sqrt{f'}_c$ psi = 1/12*$\sqrt{f'}_c$ MPa. The maximum shear stress achieved in the BDBE motion in the positive direction was $5.29\sqrt{f'_c}$ psi. The maximum shear stress in the negative direction was $-5.21\sqrt{f'_c}$ psi. The shear stress-drift plot is shown in Figure 6.12.
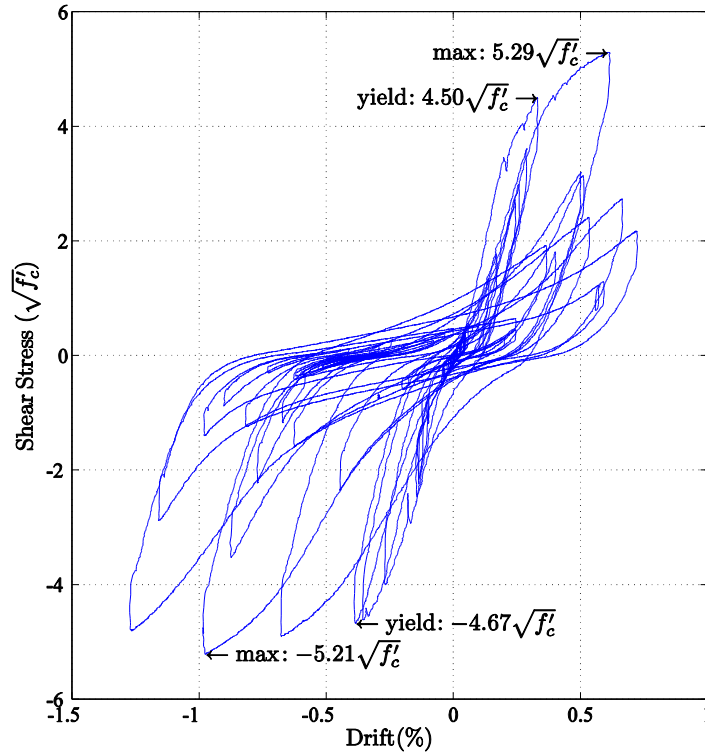
Figure 6.12: Wall 1 BDBE Shear Stress-Drift Response

The positive direction for Wall 1 is the actuator pulling the wall to the west. First, the wall yields in the positive direction at a shear stress of $4.50\sqrt{f'_c}$ psi at about 1.8 minutes. Then the wall yields in the negative direction at a shear stress of $-4.67\sqrt{f'_c}$ psi at about 6.3 minutes. The wall reaches its maximum force in the positive direction at about 7.4 min. Then the wall reaches its maximum force in the negative direction at about 14.3 minutes after two more loops.

Since Wall 1 was relatively undamaged before the BDBE motion, none of the strain gages yielded until this motion. The yield strain was assumed to be 0.002 in/in, and the locations of the strain gages and their names, first introduced in Section 5.6.2, are repeated below in Figure 6.13 and Figure 6.14, for convenience.

69
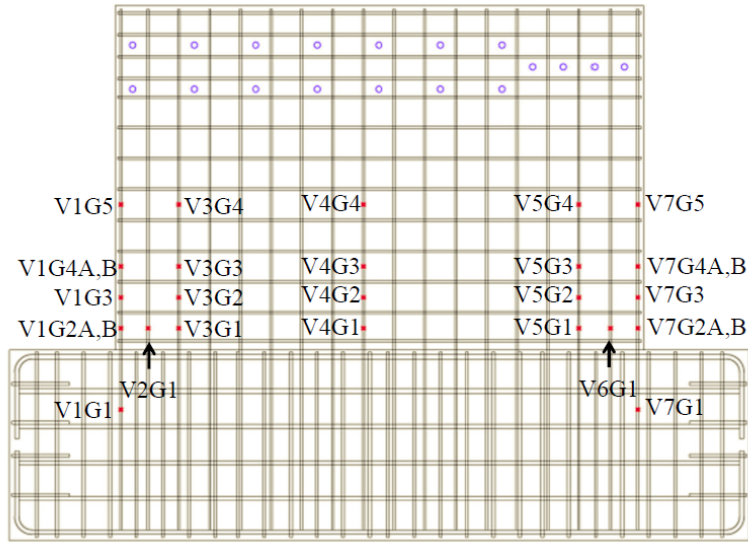
Figure 6.13: Strain Gages on Vertical Reinforcing Bars
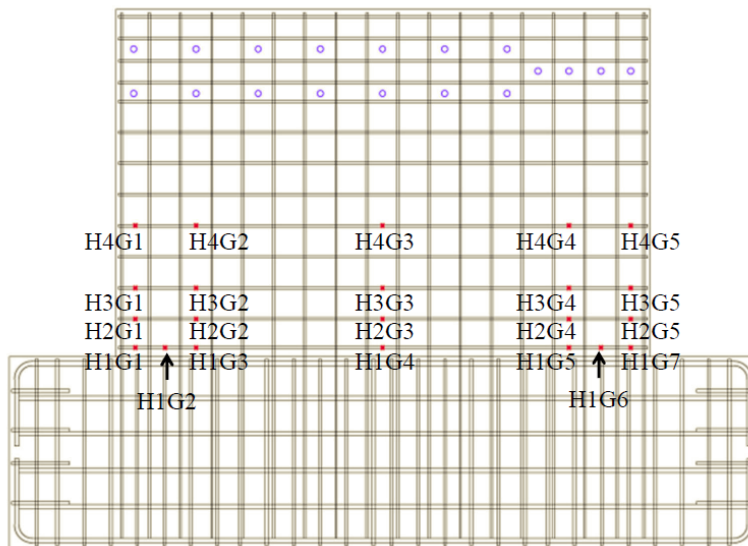
Figure 6.14: Strain Gages on Horizontal Reinforcing Bars

The first strain gages that yielded are shown in Figure 6.15. The force-drift response plot from the beginning of the ground motion to first yield is highlighted in red. The yielded strain gages are represented by blue *s on the plot, and they are listed in the order that they yielded. The diagrams of the walls on the right side show the strain gages on vertical reinforcing bars and on horizontal reinforcing bars. The black circles represent gages that did not work during the test. They were not working since the start of the tests, so possibly the strain gage was damaged

when the concrete was poured or the cable was damaged. The green circles represent the gages that have yielded.

In Figure 6.16, the force-drift response plot is shown for the strain gages that yielded from the time that Wall 1 yielded in the positive direction to the time that Wall 1 yield in the negative direction (in the global sense). In Figure 6.17, the strain gages are shown that yielded between the time Wall 1 yielded globally in the negative direction and Wall 1 achieved its maximum force in the positive direction. In Figure 6.18, the strain gages are shown that yielded between Wall 1 reaching maximum force in the positive direction and Wall 1 reaching maximum force in the negative direction. Finally, in Figure 6.19, the strain gages are shown that yielded from the time of Wall 1 maximum force in the negative direction to the end of the BDBE ground motion.
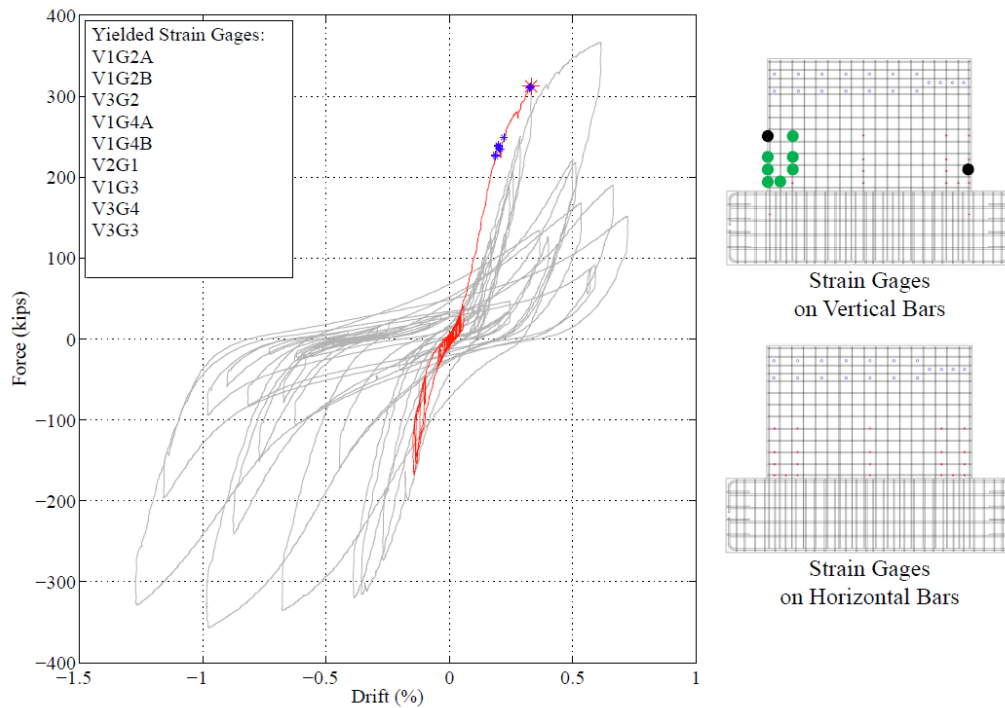
Figure 6.15: Yielded Strain Gages from Beginning of BDBE to Wall 1 First Yield
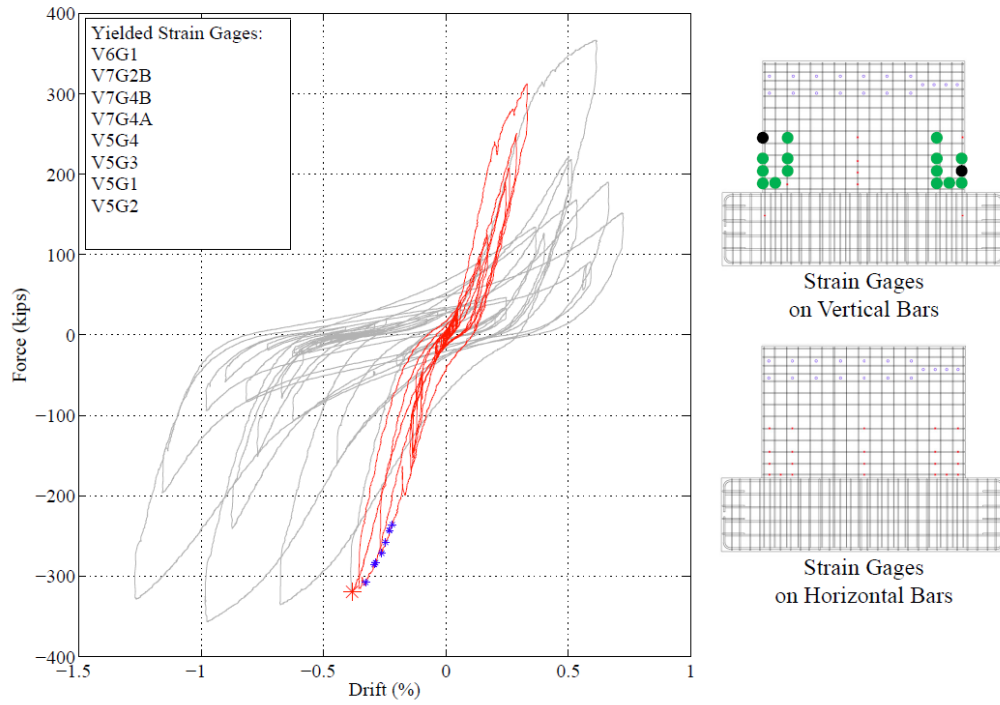
Figure 6.16: Yielded Strain Gages from Wall 1 Positive Yield to Wall 1 Negative Yield
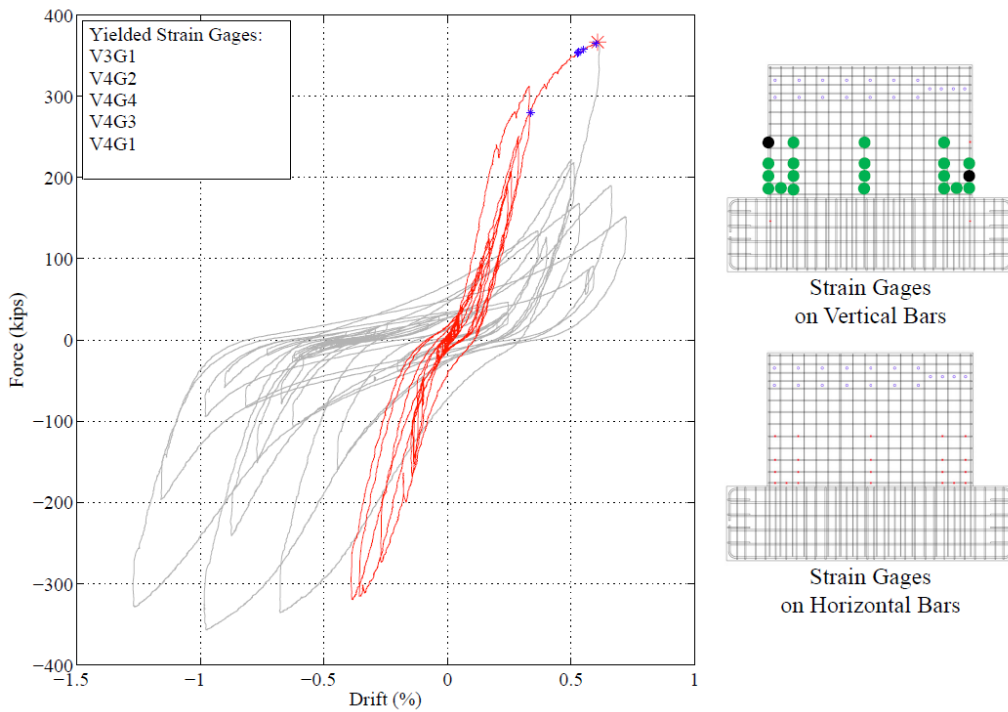
Figure 6.17: Yielded Strain Gages from Wall 1 Negative Yield to Max Positive Force
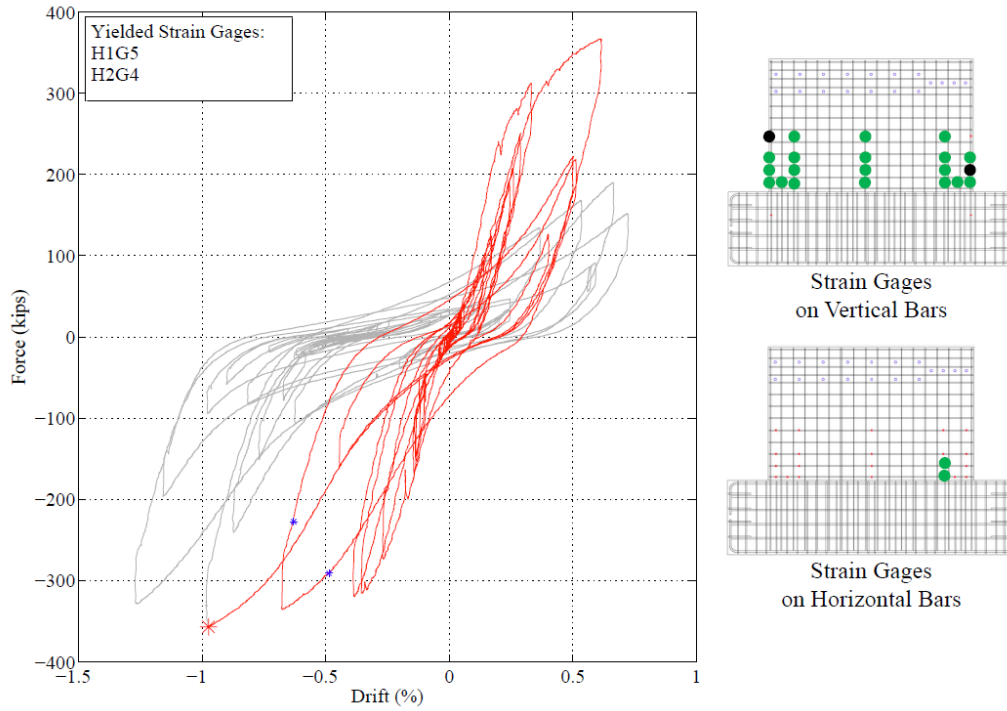
Figure 6.18: Yielded Strain Gages from Max Positive Force to Max Negative Force
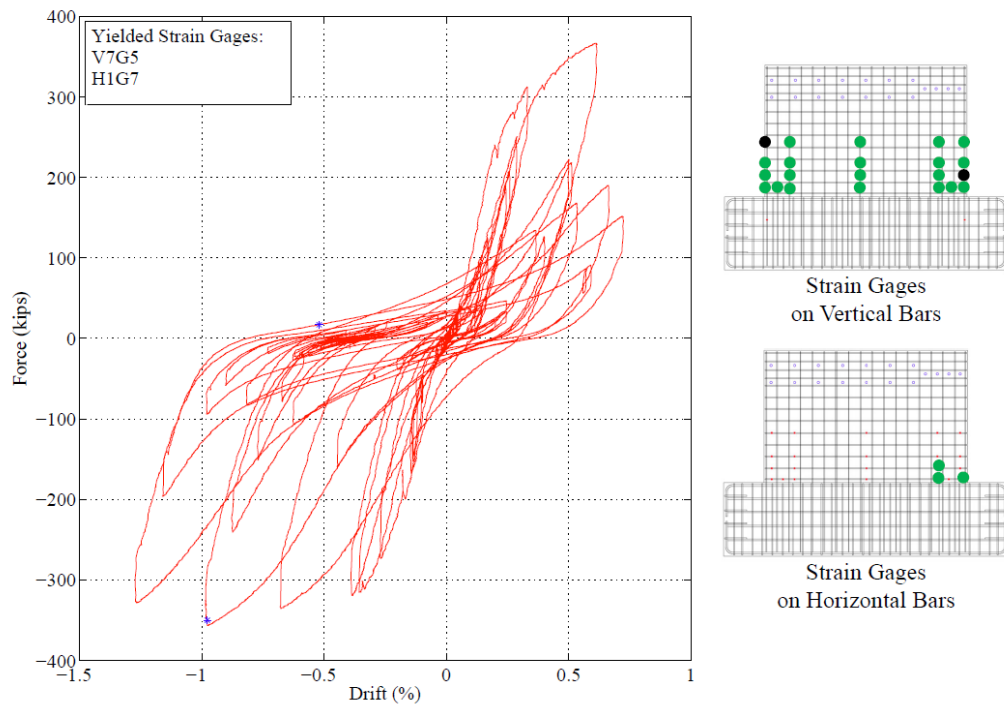
Figure 6.19: Yielded Strain Gages from Max Negative Force to End of BDBE

6.2.5 DBE Aftershock Motion

Wall 1 had lost most of its stiffness. It was sliding along its base and picking up force only after sliding enough to engage the dowel action. Before applying the DBE Aftershock motion, the wall was moved to zero the force, since there was a significant force offset after the BDBE. The experimentally measured maximum displacement and force from Wall 1 were 0.583 in and 102.1 kips. The FFT of the recorded acceleration showed a peak at 1.88 Hz. This corresponds to a period of 0.532 s and a stiffness of 333 kips/in. The force-drift response from the DBE Aftershock motion is shown in Figure 6.20. No additional strain gages yielded during the DBE Aftershock motion.
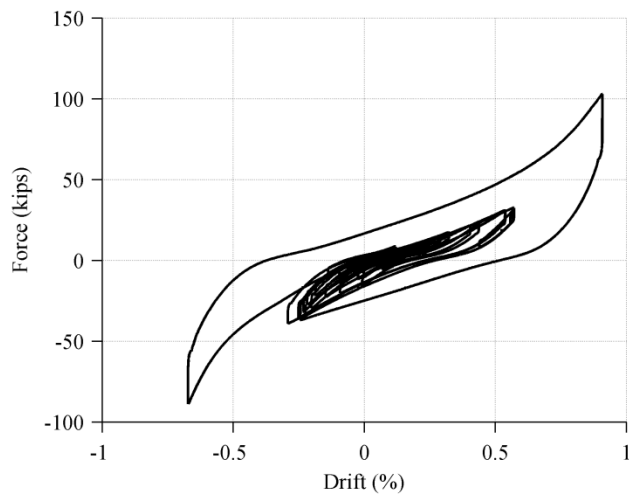
Figure 6.20: Wall 1 DBE Aftershock Force-Drift Response

6.2.6 Triangle Motions

The wall was very damaged after the DBE Aftershock motion, so triangle motions were determined to be the safest way to push Wall 1 to failure. First, Wall 1 was moved to zero the force. Then two quasi-static cyclic triangle motions to +/-1 in (+/-2.54 cm) were run using the function generator in the controller. Then the wall was moved to zero the force again, and one cycle to +/-1.5 in (+/-3.81 cm) was run. During this last cycle, two reinforcing bars were heard fracturing on each end of the wall. The force-drift response from triangle motions to +/-1 in (+/-2.54 cm) is shown in Figure 6.21.
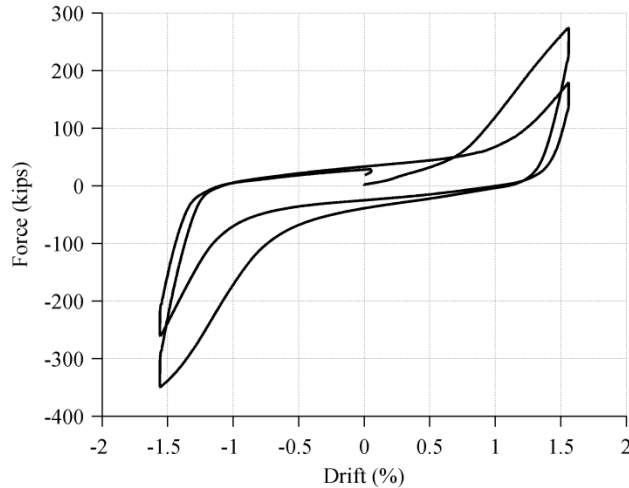
Figure 6.21: Wall 1 Triangle Motions to +/-1 in (+/-2.54 cm) Force-Drift Response

No additional strain gages yielded during the Triangle Motions to +/-1 in. The force-drift response from a triangle motion to +/-1.5 in (+/-3.81 cm) is shown in Figure 6.22.
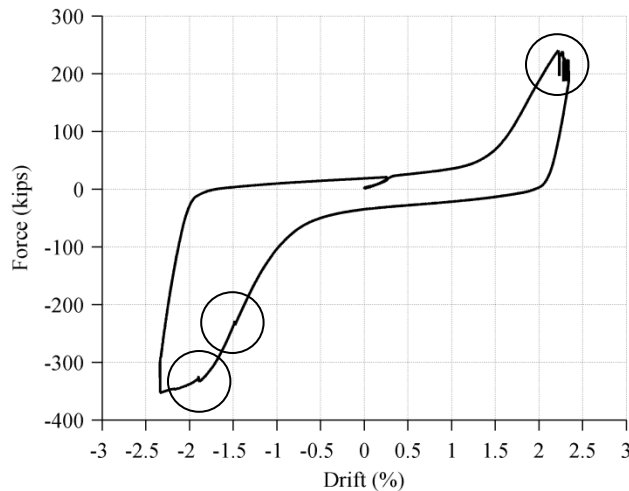
Figure 6.22: Wall 1 Triangle Motion to +/-1.5 in (+/-3.81 cm) Force-Drift Response

The fracture locations are evident in Figure 6.22 by the sudden force drops in the upper right hand side of the plot (circled). The fracture locations are also evident on the reversal of the load, but not as prominently (circled). During the Triangle Motion to +/-1.5 in, two more strain gages yielded. These gages are shown in the force-drift response plot and corresponding diagrams in Figure 6.23.
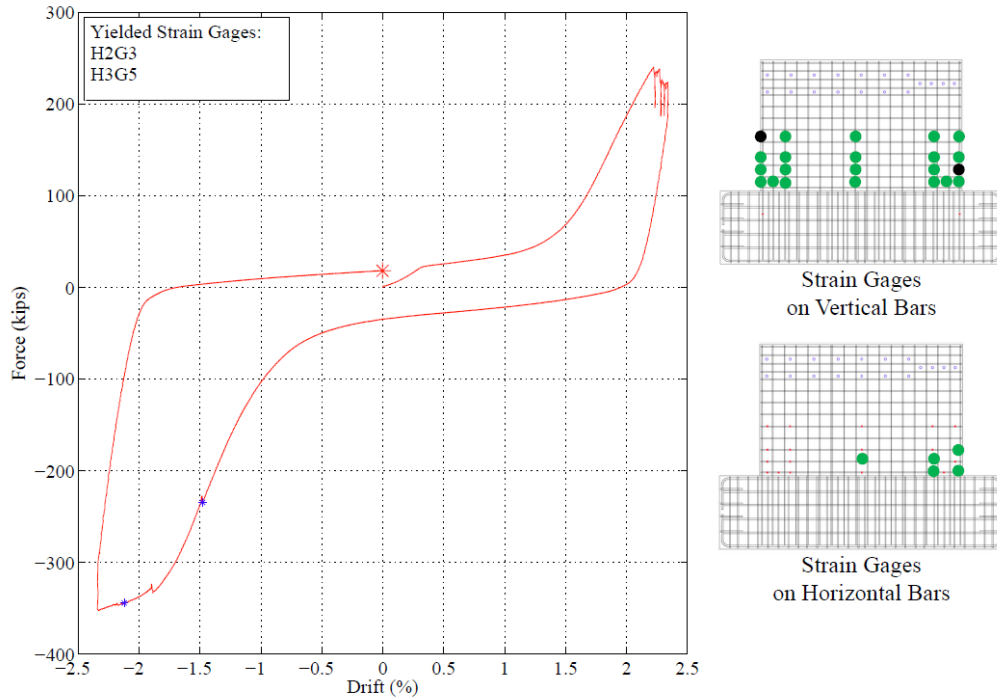
Figure 6.23: Strain Gages Yielded during the Triangle Motion to +/-1.5 in

6.2.7 Final Damage State

Figure 6.24 shows the final damage state of Wall 1 at the end of the tests. The east side and west side views are shown. The sliding plane is apparent across the length of the wall.

(a)   (b)
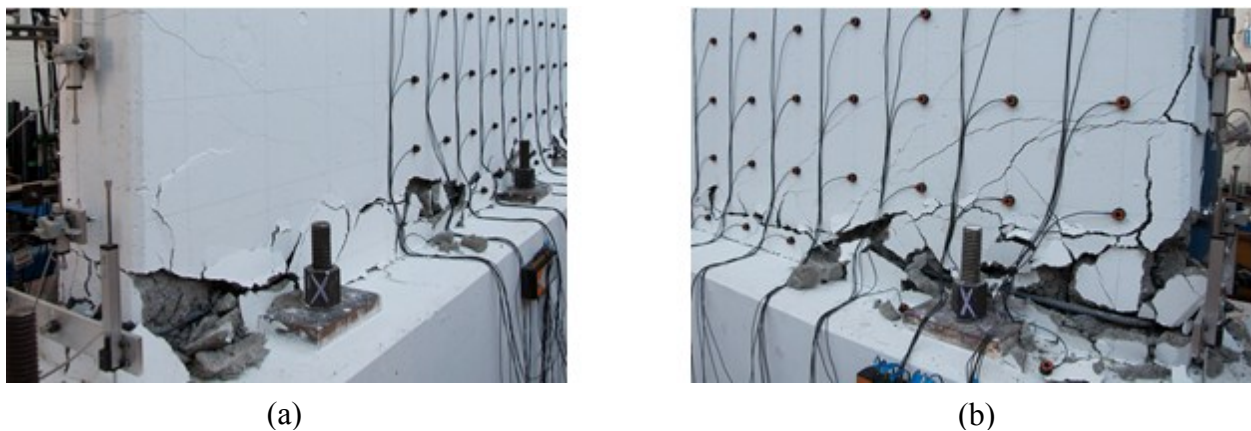
Figure 6.24: Wall 1 Damage State at End of Tests: (a) East Side (b) West Side

The loose broken concrete pieces were removed for a better view of the final state of the reinforcing bars. In Figure 6.25, the east side reinforcing bars remained mostly in-tact with

76

minor local buckling of the vertical bars below the lowest horizontal bar, but the west side bars displayed more local buckling of the vertical reinforcement and opening of hooks of the two lowest horizontal bars.

(a)   (b)
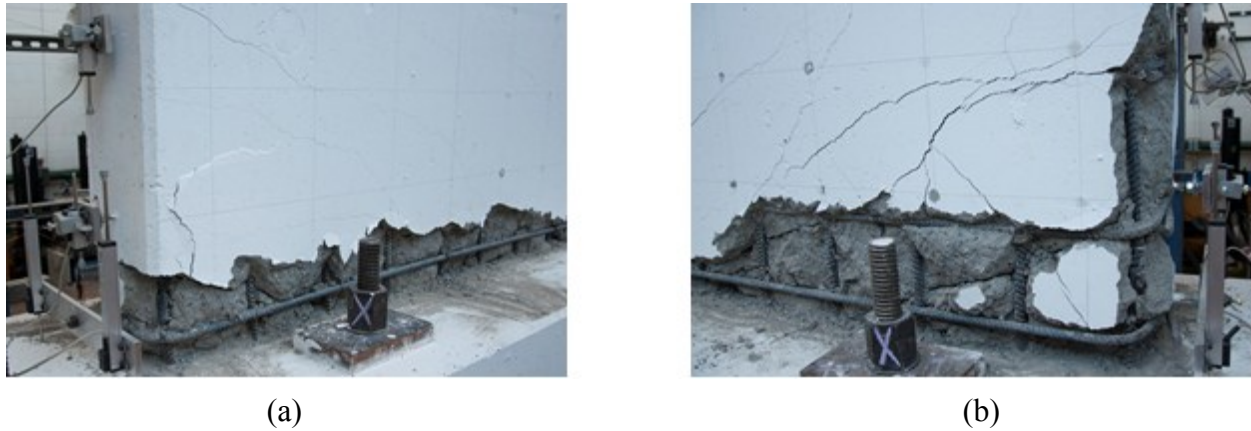
Figure 6.25: Wall 1 after Removing Broken Concrete Pieces (a) East Side (b) West Side

At the end of the Wall 1 test sequence, local buckling of the vertical wall reinforcement and opening of the hooks of the horizontal wall reinforcement induced by a combination of sliding and flexure was observed. The following pictures were taken after removing some of the broken concrete pieces for better visibility. Figure 6.26 (a) shows the rear view of the wall on the east side, where local buckling in the vertical bars is visible below the lowest horizontal bar. Figure 6.26 (b) shows the front view of the west side of the specimen, where local buckling is visible in the vertical bars from the base of the wall up to the height of the third horizontal bars. Since the hooks of the lowest two horizontal bars on the west side of the wall opened during the test, this allowed for a larger range of local buckling. Figure 6.26 (c) shows a closer view of the opening of the hooks of horizontal bars on the west side of the wall.
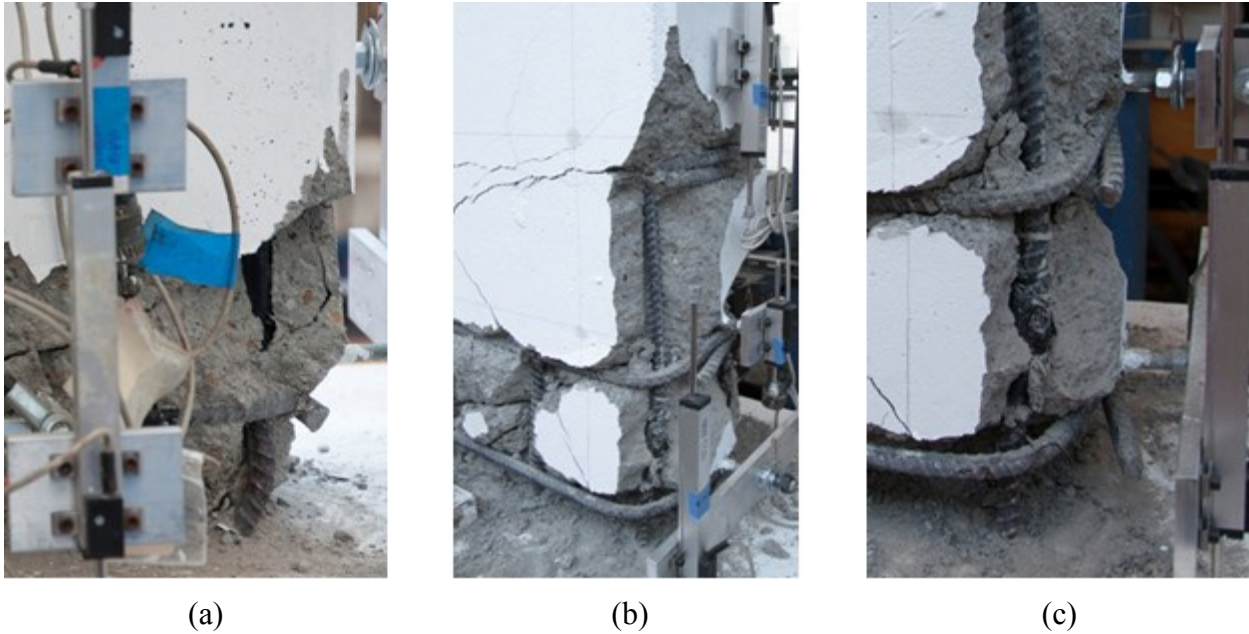
Figure 6.26: Wall 1 Local Buckling (a) Rear View of East Side of Wall (b) Front View of West Side of Wall (c) Opening of Hooks of Horizontal Bars on West Side of Wall 1

6.3 WALL 2 BEHAVIOR

Before subjecting Wall 2 to the hybrid simulations of the ground motions, pre-test stiffness and free vibration tests were performed, identical to those for Wall 1. For the stiffness test, a very small saw-tooth displacement-controlled motion was commanded to the specimen. The forces were limited to +/-56.2 kips (+/-250 kN), which was half of the target force for the OBE motion. However, the high stiffness of the wall made the forces difficult to control and there were some force spikes within +/-100 kips (+/-444.8 kN). The slip in the clevises of the actuator contributed to this. Limits were set on the controller to prevent excessive forces. It took a few trials to successfully perform a stiffness test without tripping the force limits. The force feedback-time and force-displacement responses from the successful stiffness test are shown in Figure 6.27.
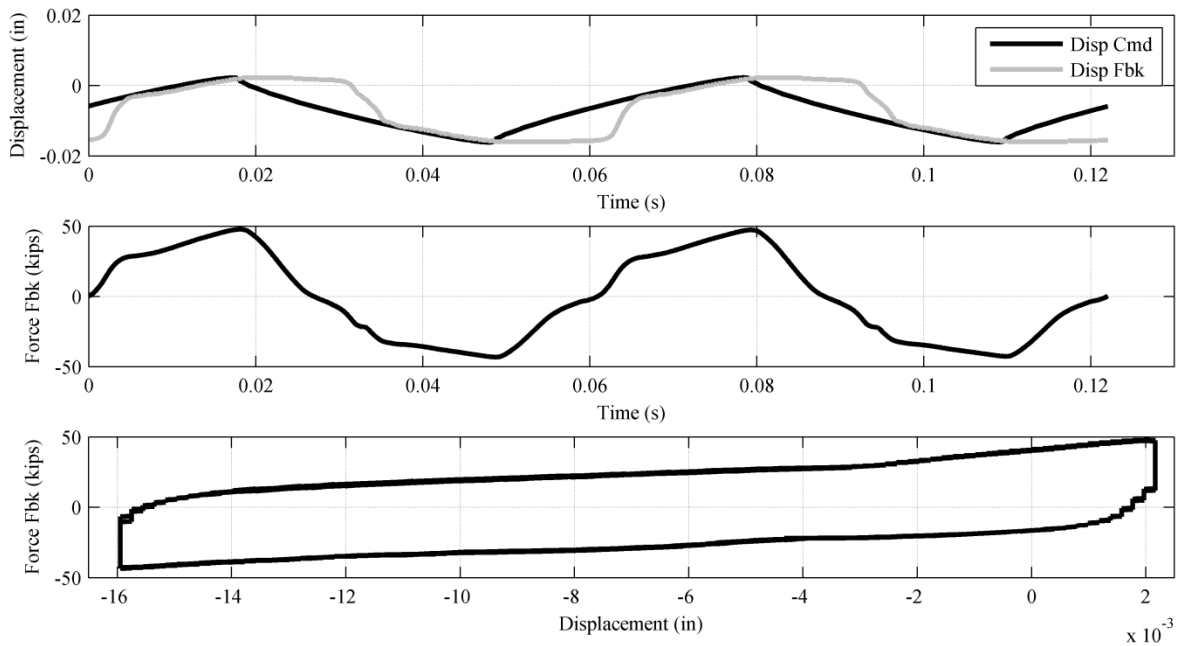
Figure 6.27: Wall 2 Stiffness Test

With such small displacements and slip in the clevises contributing to the response, it was very difficult to estimate the stiffness. The stiffness was determined to be approximately 3300 kips/in (577.9 kN/mm). As with Wall 1, this was later shown to be underestimated significantly.

As with Wall 1, a free vibration test was performed next to determine the simulation velocity and the damping in the numerical portion of the hybrid model. The 3300 kips/in (577.9 kN/mm) stiffness was used in the numerical free vibration model to determine the mass necessary for the model to have a period of 0.14 s. The forces were still limited to +/-100 kips (+/-444.8 kN). A constant velocity of 0.01 in/s (0.254 mm/s) was selected to drive the actuator. This resulted in just about 0 damping due to errors in the control loop. Thus, 2% damping was implemented directly in the numerical model as mass-proportional damping.

Before proceeding to the hybrid simulation tests, the mass in the numerical portion of the hybrid model was adjusted to be the same as the mass used for Wall 1. Even though the stiffness test for Wall 2 yielded a different value than the stiffness test for Wall 1, the stiffnesses of Wall 1 and Wall 2 after the free vibration test were assumed to be similar. In the cases of both walls, it took a number of trials for a successful stiffness test and free vibration test. For Wall 1, there were more trials of the free vibration test to determine the appropriate testing velocity. For Wall 2, there were more trials of the stiffness test because the force interlocks were tripped on the controller a number of times. With approximately the same number of pre-test runs for both walls, the stiffnesses at the time of the OBE hybrid simulation were assumed to be similar. The FFT of the acceleration data recorded in OpenSees for the first successful free vibration run had a peak at a frequency of 9.38 Hz. This corresponded to a period of 0.1067 s and a stiffness of 8263 k/in.

As with Wall 1, inspection of Wall 2 after these pre-tests revealed several hairline diagonal cracks. These cracks ran from about mid-height on the left side of the specimen towards the lower right side of the specimen at about a 45 degree angle.

79

The hybrid simulation ground motion sequence for Wall 2 was OBE – BDBE – DBE Aftershock 1 – DBE Aftershock 2. After the ground motion sequence, the specimen was broken using a cycle to each of 1 in (2.54 cm) and 1.5 in (3.81 cm). Cycles were determined to be safer than another ground motion at that level of damage. The displacement feedback-time history for the total hybrid simulation sequence and the ductility-time history are shown in Figure 6.28. The yield displacement was determined to be 0.17 in. The force feedback-time history is shown in Figure 6.29. The * indicate the end of one ground motion and the start of the next.
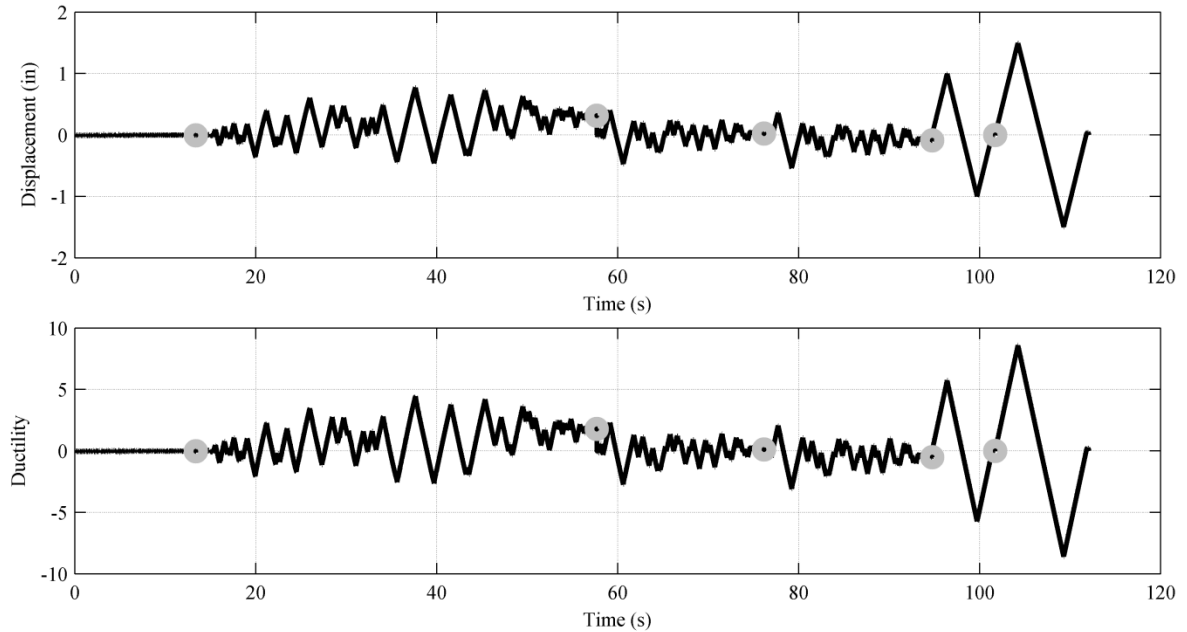
Figure 6.28: Wall 2 Displacement-Time and Ductility-Time Histories
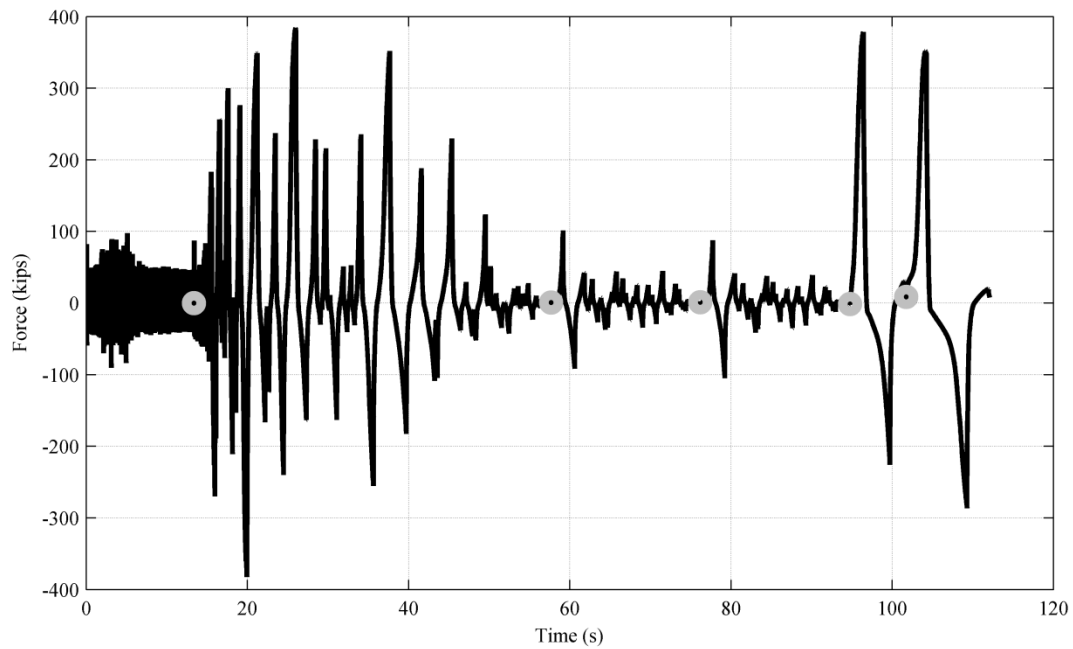
Figure 6.29: Wall 2 Force-Time Response History

Photographs of Wall 2 following the BDBE motion, both DBE Aftershock motions, and both cyclic motions are shown in Figure 6.30.

(a)

(b)

(c)

(d)

(e)
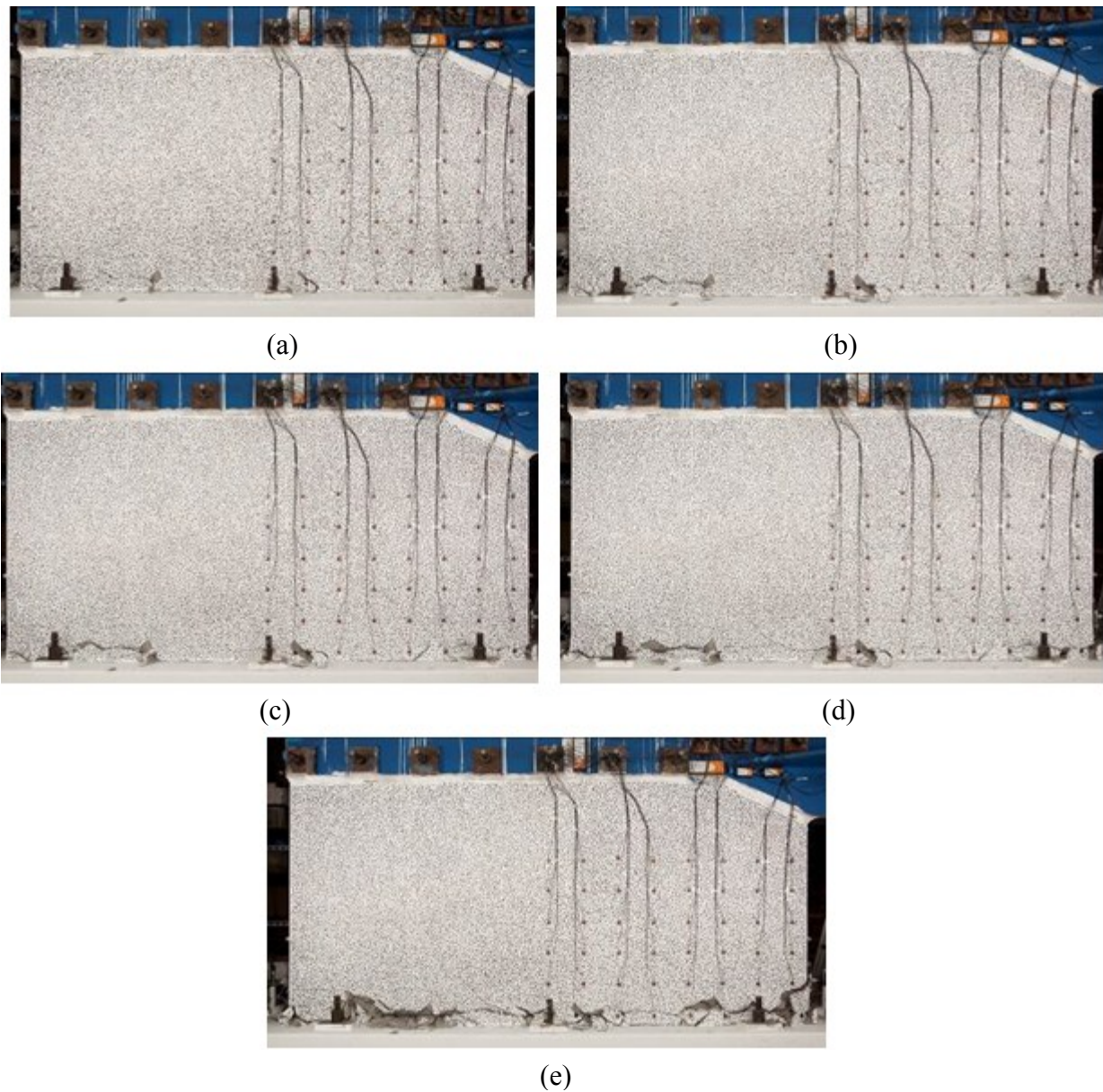
Figure 6.30: Wall 2 at (a) end of BDBE (b) end of DBE Aftershock 1 (c) end of DBE Aftershock 2 (d) end of cycle to 1 in (e) end of cycle to 1.5 in

6.3.1 OBE Motion

Since asymmetry in the force-displacement response behavior in Wall 1 was observed, the direction of the ground motion was reversed for the Wall 2 tests. By comparing the Wall 2 results to the Wall 1 results, the asymmetry was determined to be a result of the ground motion asymmetry and not an asymmetry in the test setup. The OBE for Wall 2 was the same as for Wall 1 and used the same scaling factor to reach 1/3 of the yield force, 112.4 kips (500 kN),

representing a service level earthquake. The ground motion scaling factor was 0.05263. The stiffness used in the numerical portion of the hybrid model was 4800 kips/in, as was used for Wall 1. The experimentally measured maximum displacement and force from Wall 2 were 0.029 in and 97.65 kips. After the OBE motion was imposed on Wall 2, the recorded acceleration data was used to determine the current stiffness. The FFT of the recorded acceleration showed a peak at 7.642 Hz. This represents a period of 0.1309 s. The stiffness was calculated to be 5490 kips/in. This can be compared directly to the stiffness of Wall 1 after the OBE motion, which was 3703 k/in. Wall 2 was stiffer than Wall 1 at this point in the test. This was a result of the pre-test runs which affected the walls stiffnesses much more than expected. The force-drift response from the OBE motion is shown in Figure 6.31. As with Wall 1, the displacement was recorded by the encoder and the force is the actuator load cell feedback.
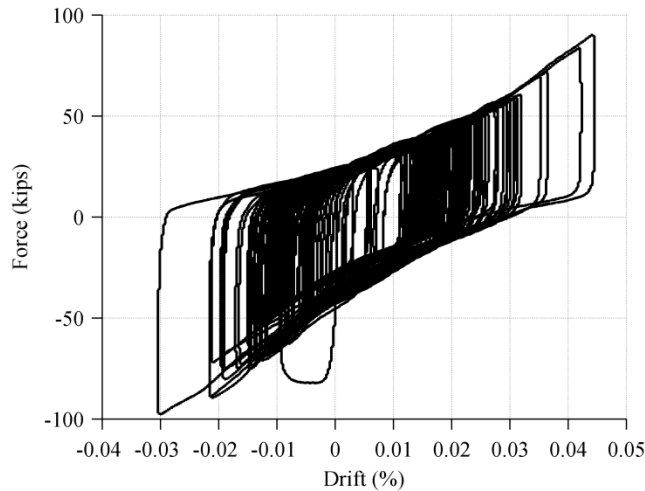
Figure 6.31: Wall 2 OBE Force-Drift Response

6.3.2 BDBE Motion

The purpose of the BDBE motion was to push the wall beyond its peak strength. Since the BDBE motion for Wall 1 was slightly larger than ideal, the scaling of the BDBE motion was reconsidered for Wall 2. However, Wall 2 was less damaged when it experienced the BDBE than Wall 1 (which had already experienced the DBE 0.11 and the appropriately scaled DBE), so Wall 2 would withstand the large motion better. The same ground motion scaling was maintained for Wall 2. This scaling factor was 0.4221. The experimentally measured maximum displacement and force from Wall 2 were 0.775 in and 384.4 kips. The FFT of the recorded acceleration showed a peak at 2.49 Hz. This corresponds to a period of 0.402 s and a stiffness of 583 kips/in. Coincidentally, this matches the stiffness of Wall 1 after experiencing the BDBE motion. After the BDBE motion, the actuator was moved to zero the force before the next hybrid simulation run.

During the BDBE motion, Wall 2 experienced similar behavior to Wall 1. The following three figures show ε_{yy} strains measured on the surface of the Wall 2 specimen during the BDBE simulation using high-resolution still image correlation (Correlated Solutions 2009). Figure 6.32 was recorded at the beginning of the BDBE simulation. Here, Wall 2 experienced additional

light shear cracking evident throughout the wall web along with some flexural cracks near the lower corners of the wall. The approximately 45 degree shear cracks were well distributed along the length of the wall, indicating that the loading plate was adequately distributing the load along the wall.

Figure 6.32: Wall 2 Shear and Flexural Cracking at Start of BDBE Motion

As the BDBE motion progressed, the flexural behavior mode became more dominant, as shown in Figure 6.33. These cracks are shown in the lower corner of the wall, located at approximately 1/6 and 1/3 of the height of the wall from the base to the loading plate.
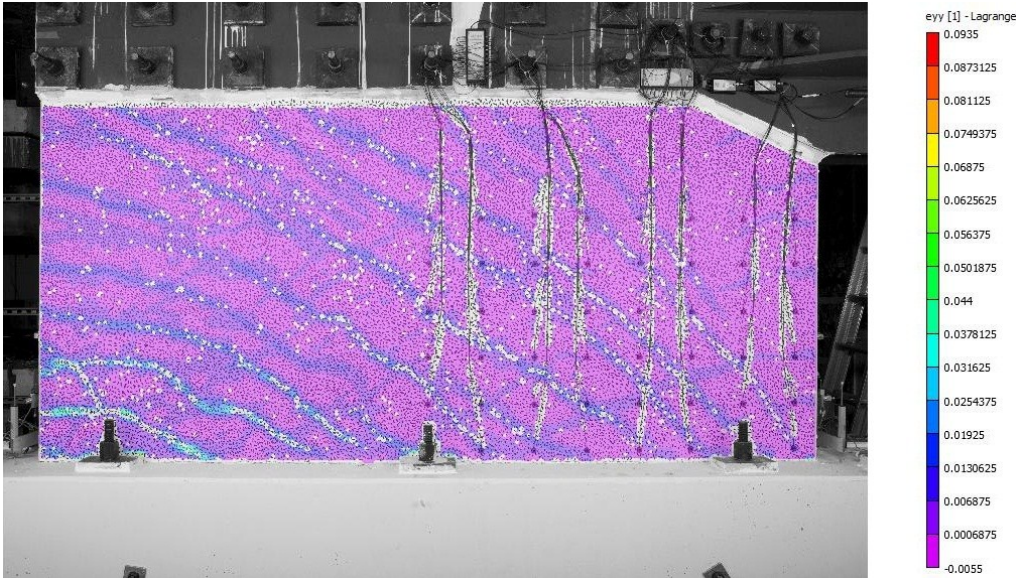
Figure 6.33: Wall 2 Development of Flexural Cracks during BDBE Motion

The dominant flexural cracking quickly gave way to a crack that developed from the lower corners of the wall and propagated across the entire base of the wall. The final failure mode was sliding shear along the base of the wall where it meets the foundation. This is shown in Figure 6.34. After the wall had slid to the point when the vertical reinforcement picked up some force in dowel action, the flexural cracks continued to develop. This is apparent in Figure 6.34 as well. The wall slid along its base, and as it reached its peak displacement, the shear and especially the flexural cracks opened.
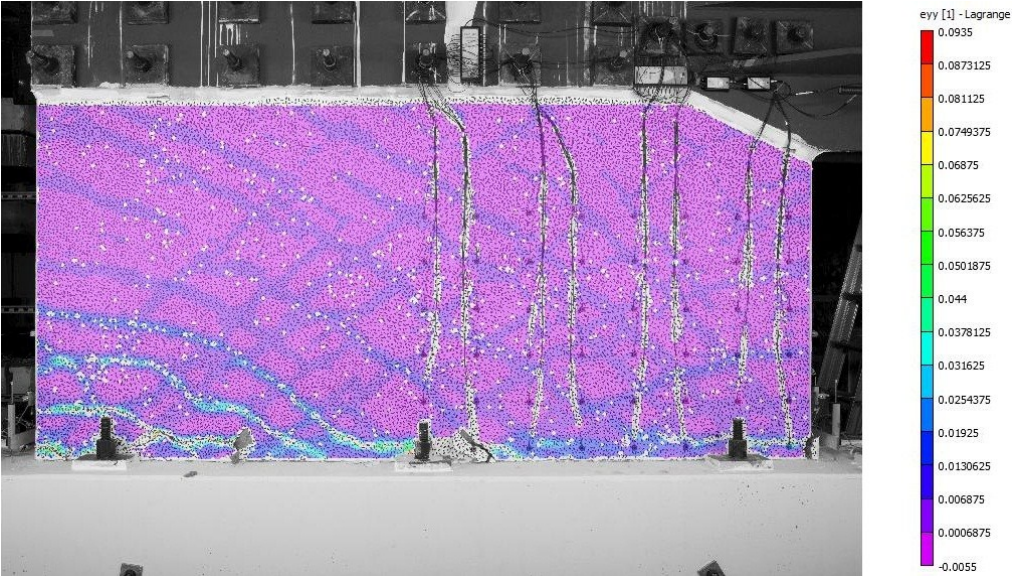
Figure 6.34: Wall 2 Continued Development of Flexural Cracking and Sliding during BDBE Motion

One of the Krypton targets toward the bottom center of the wall was attached to a piece of concrete that spalled off during this run, as seen in Figure 6.34. By the end of the BDBE motion, Wall 2 was significantly damaged. The force-drift response from the BDBE motion is shown in Figure 6.35.
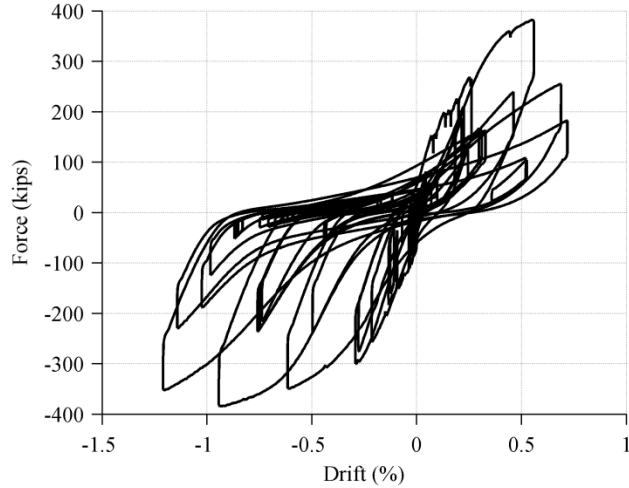
Figure 6.35: 42%-BDBE Force-Drift Response

On the day of the Wall 2 test, the concrete compressive strength was 5413 psi. The maximum shear stress achieved in the BDBE motion in the positive direction was $5.41\sqrt{f'_c}$ psi. The maximum shear stress in the negative direction was $-5.45\sqrt{f'_c}$ psi. The shear stress-drift plot is shown in Figure 6.36.
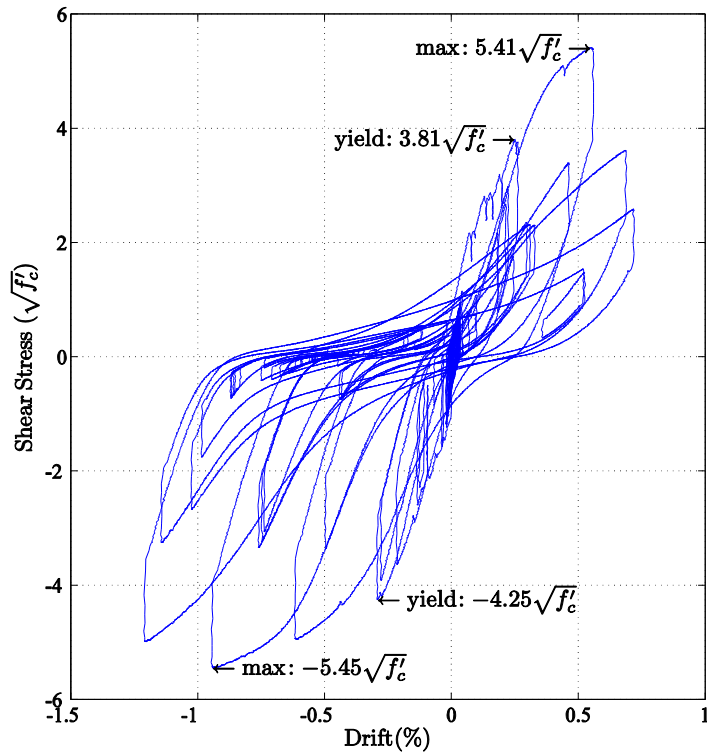
Figure 6.36: 42%-BDBE Shear Stress-Drift Response

The positive direction for Wall 2 is the actuator pushing the wall to the east. Wall 2 data is plotted with negated force and drift to facilitate comparison to Wall 1 plots. Wall 2 yields in the positive (actuator pushing) direction at about 2.6 minutes with a shear stress of $3.81\sqrt{f'_c}$ psi. Then the wall yields in the negative direction at about 4.2 minutes with a shear stress of $-4.25\sqrt{f'_c}$ psi. The wall reaches its maximum force in the positive direction at about 6.6 min. Then the wall reached its maximum force in the negative direction at about 12.6 minutes after two more loops.

Since Wall 2 was relatively undamaged before the BDBE motion, none of the strain gages yielded until this motion. The yield strain was again assumed to be 0.002 in/in, and the locations of the strain gages and their names were shown in Figure 6.13 and Figure 6.14. The first strain gages that yielded are shown in Figure 6.37. The force-drift response plot from the beginning of the ground motion to first yield is highlighted in red. The yielded strain gages are represented by blue *s on the plot, and they are listed in the order that they yielded. The diagrams of the walls on the right side show the strain gages on vertical reinforcing bars and on horizontal reinforcing bars. The black circles represent gages that did not work during the test. They were not working at the start of the tests, so possibly the strain gage was damaged when the concrete was poured or the cable was damaged. The green circles represent the gages that have yielded.

In Figure 6.38, the force-drift response plot is shown for the strain gages that yielded from the time that Wall 2 yielded (in a global sense) in the positive direction to the time Wall 2 yielded globally in the negative direction. In Figure 6.39, the strain gages are shown that yielded between Wall 2 yielding globally in the negative direction and Wall 2 achieving its maximum force in the positive direction. In Figure 6.40, the strain gages are shown that yielded between Wall 2 reaching maximum force in the positive direction and Wall 2 reaching maximum force in the negative direction. Here, strain gage V1G4C yielded. This was an extra gage that was accidentally placed between V1G4A and V1G5 on Wall 2 only. Finally, in Figure 6.41, the strain gages are shown that yielded between Wall 2 maximum force in the negative direction to the end of the BDBE ground motion.
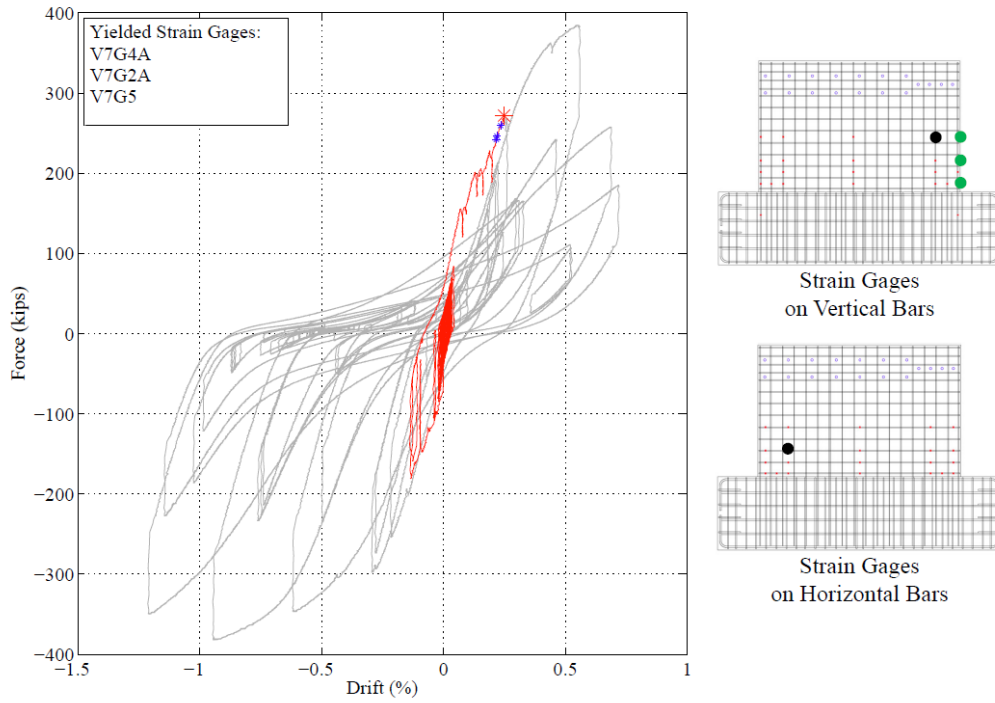
Figure 6.37: Yielded Strain Gages from Beginning of BDBE to Wall 2 First Yield
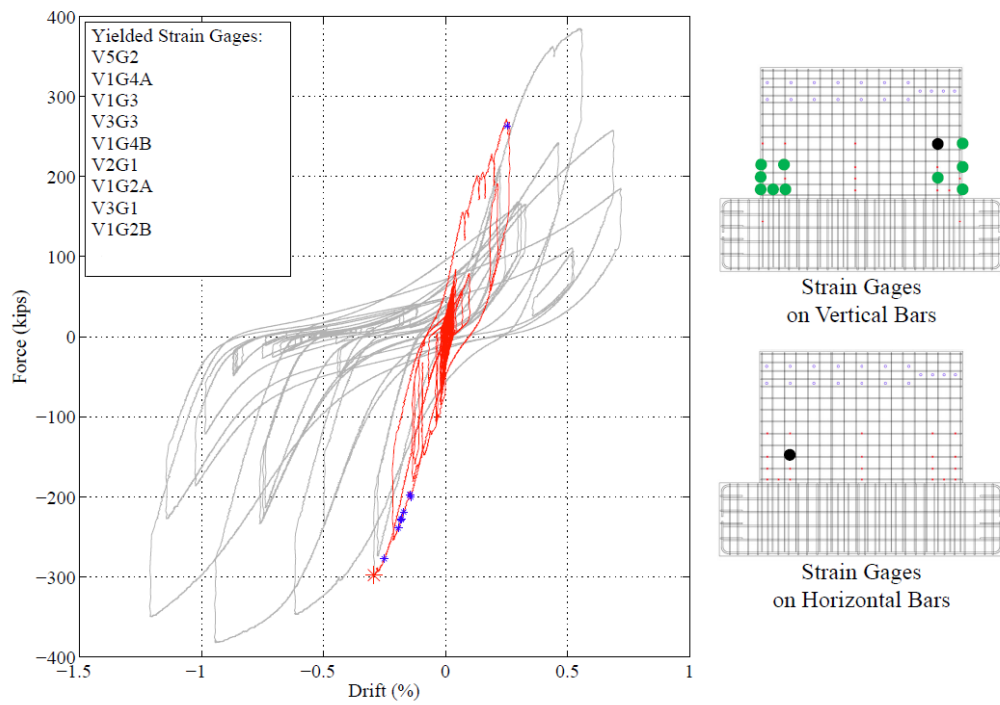
Figure 6.38: Yielded Strain Gages from Wall 1 Positive Yield to Wall 2 Negative Yield
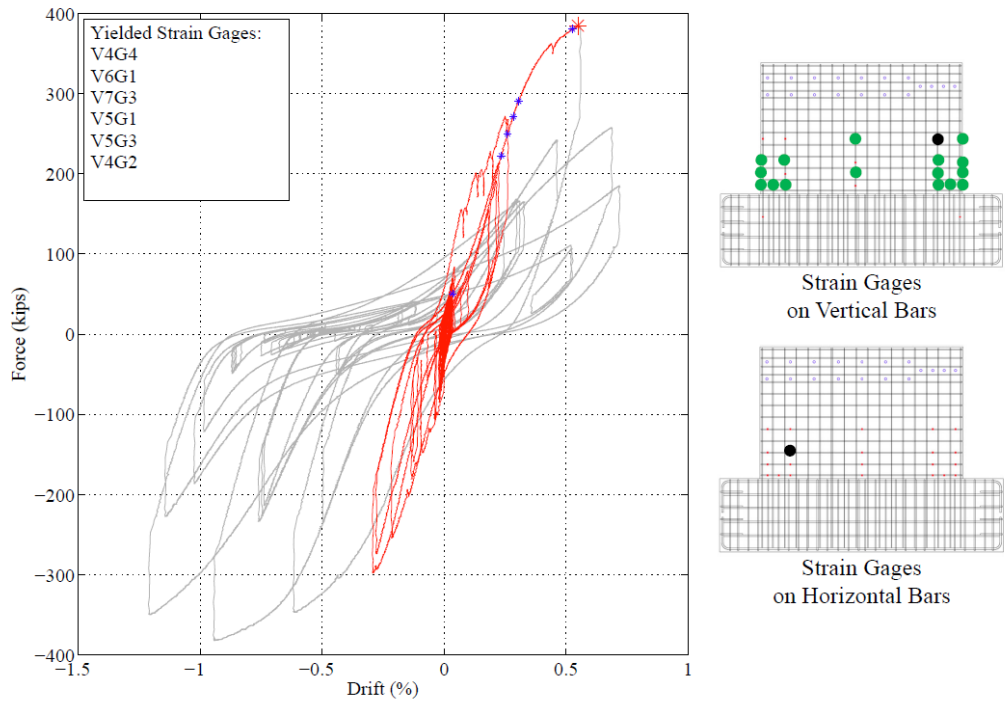
Figure 6.39: Yielded Strain Gages from Wall 2 Negative Yield to Max Positive Force
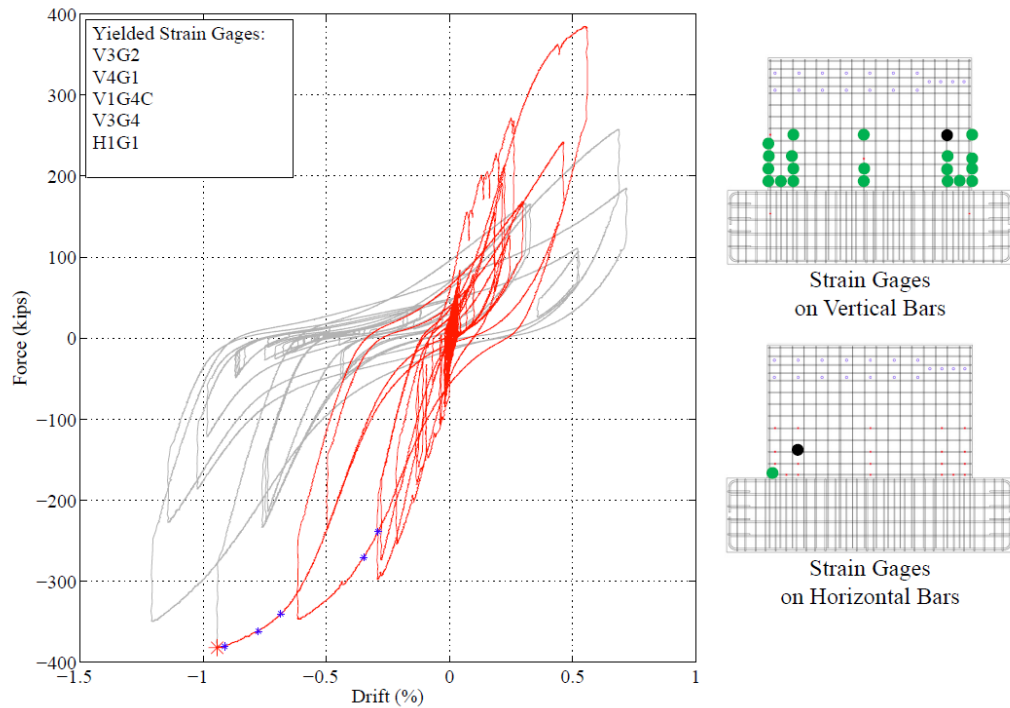
Figure 6.40: Yielded Strain Gages from Max Positive Force to Max Negative Force
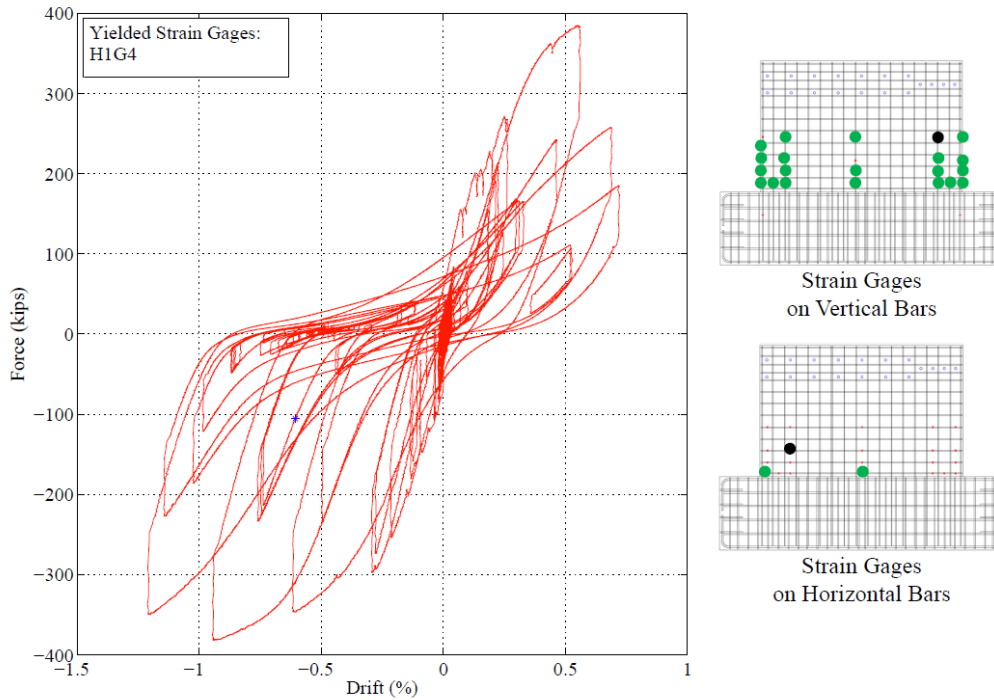
Figure 6.41: Yielded Strain Gages from Max Negative Force to End of BDBE

6.3.3 DBE Aftershock 1 Motion

The same DBE scaling that was used for Wall 1 was maintained for DBE Aftershock 1. This scaling value was 0.1407. The experimentally measured maximum displacement and force from Wall 2 were 0.474 in and 101.4 kips. The FFT of the recorded acceleration showed a peak at 1.855 Hz. This corresponds to a period of 0.694 s and a stiffness of 323.7 kips/in. Wall 2 was very damaged when it experienced this motion. The wall mostly slid along its base and picked up a little force at the extreme values of displacement. The force-drift response from the DBE Aftershock 1 motion is shown in Figure 6.42. No additional strain gages yielded during the DBE Aftershock 1 motion.
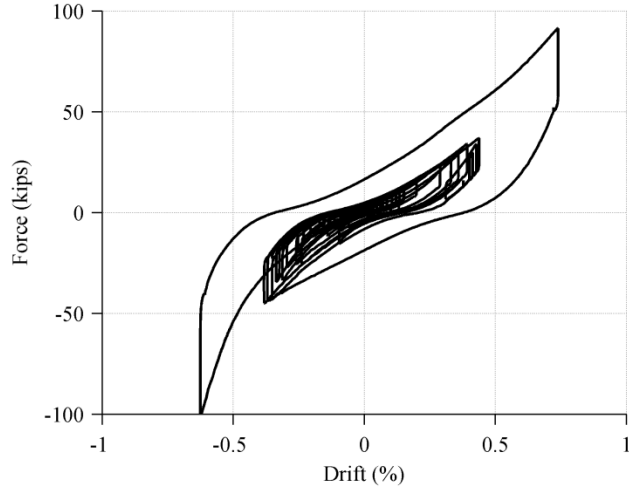
Figure 6.42: Wall 2 DBE Aftershock 1 Force-Drift Response

6.3.4   DBE Aftershock 2 Motion

This run was a repeat of the previous run.   The scaling factor remained 0.1407.   The experimentally measured maximum displacement and force from Wall 2 were 0.539 in and 104.6 kips.   The FFT of the recorded acceleration showed a peak at 1.44 Hz.   This corresponds to a period of 0.539 s and a stiffness of 195.1 kips/in.   Wall 2, again, slid along its base and picked up a little force at the extreme values of displacement.   The force-drift response from the repeated DBE Aftershock 2 motion is shown in Figure 6.43.   No additional strain gages yielded during the 14%-DBE Aftershock 2 motion.
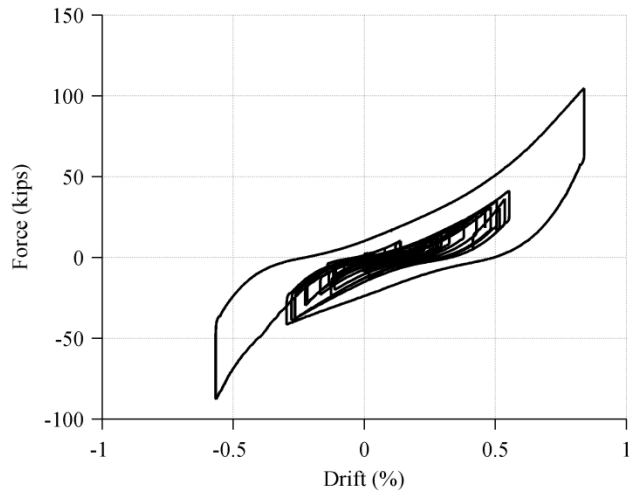
Figure 6.43: Wall 2 DBE Aftershock 2 Force-Drift Response

6.3.5   Triangle Motions

As with Wall 1, Wall 2 was too damaged to safely run another ground motion. One quasi-static cyclic triangle motion to +/-1 in (+/-2.54 cm) was run using the function generator in the controller. Then the wall was moved to zero the force, and one cycle to +/-1.5 in (+/-3.81 cm) was run. The force-drift response from the triangle motion to +/-1 in (+/-2.54 cm) is shown in Figure 6.44.
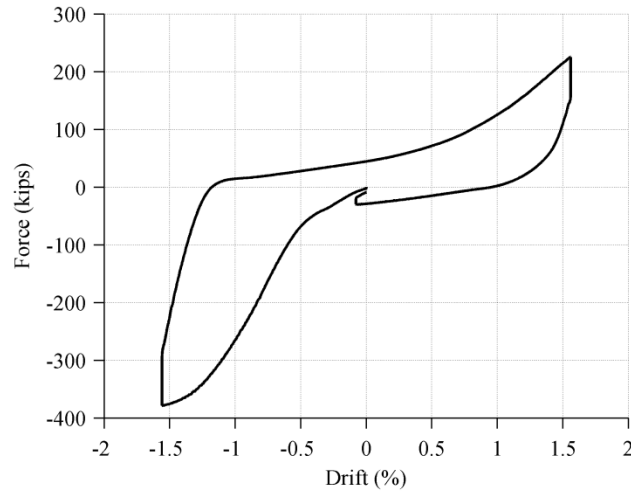
Figure 6.44: Wall 2 Triangle Motion to +/-1 in (+/-2.54 cm) Force-Drift Response

During the Triangle Motion to +/-1 in, three more strain gages yielded. These gages are shown in the Force-Drift response plot and corresponding diagrams in Figure 6.45.
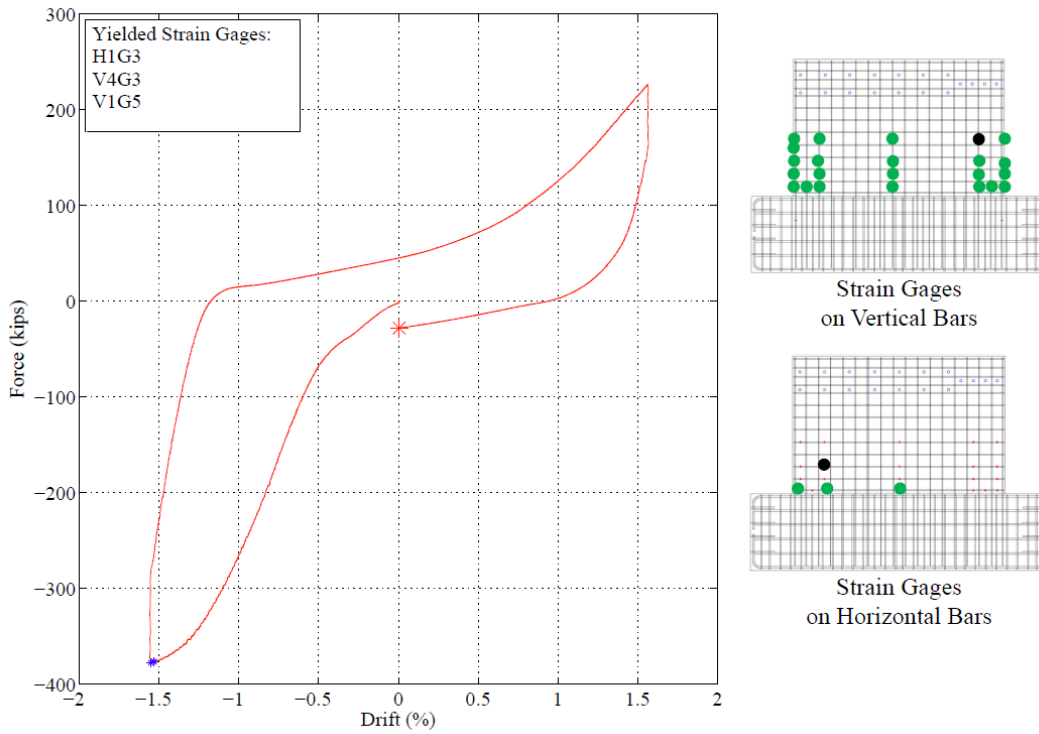
Figure 6.45: Strain Gages Yielded during the Triangle Motion to +/-1 in

The force-drift response from the triangle motion to +/-1.5 in (+/-3.81 cm) is shown in Figure 6.46.
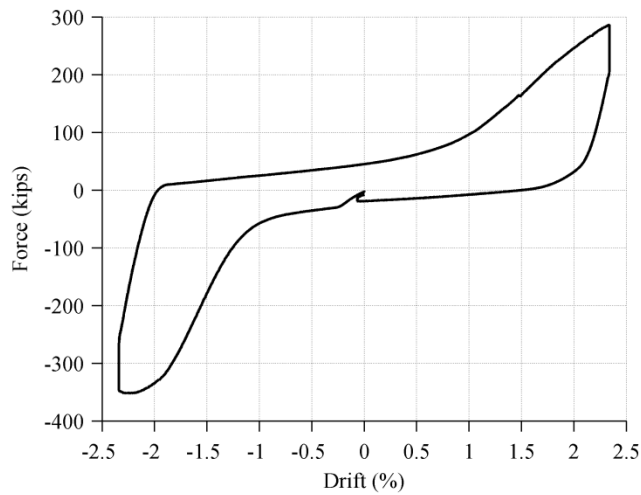
Figure 6.46: Wall 2 Triangle Motion to +/-1.5 in (+/-3.81 cm) Force-Drift Response

93

In Wall 2, there were no apparent rebar fractures, as were observed in Wall 1. During the triangle motion to +/-1.5 in, four more strain gages yielded. These gages are shown in the force-drift response plot and corresponding diagrams in Figure 6.47.
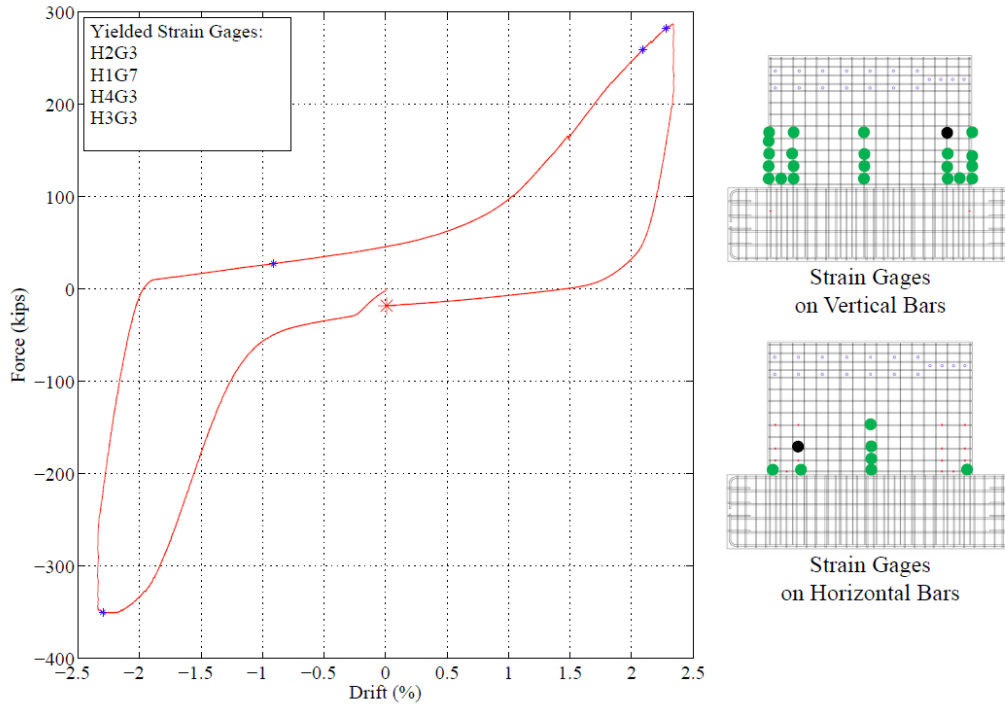
Figure 6.47: Strain Gages Yielded during the Triangle Motion to +/-1.5 in

6.3.6 Final Damage State

Figure 6.48 shows the final damage state of Wall 2 at the end of the tests. The east side view, the sliding plane, and the west side view are shown.

(a)	(b)	(c)
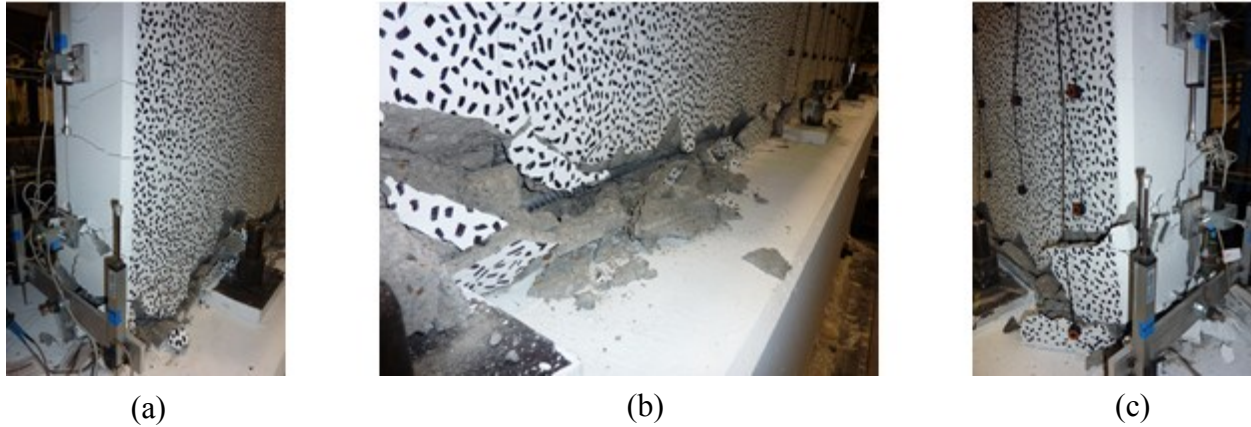
Figure 6.48: End of Wall 2 Test Sequence: (a) Shows Damage in East Corner (b) Shows Damage along Sliding Plane (c) Shows Damage in West Corner

The loose broken concrete pieces were removed for a better view of the final state of the reinforcing bars. In Figure 6.49, the east side reinforcing bars remained mostly in-tact, but the west side bars displayed some local buckling of the vertical reinforcement. Unlike Wall 1, the hooks of the horizontal wall reinforcement did not open.

(a)	(b)

Figure 6.49: Wall 2 Final Damage State after Removing Broken Concrete: (a) East Side (b) West Side

Figure 6.50 shows a close-up view of the hooks of the horizontal bars on the west side of the specimen. These remained closed at the end of the tests.

Figure 6.50: Wall 2 West Side Reinforcing Bars

6.4 WALL 1 AND WALL 2 COMPARISON

The force-drift response plots recorded during Wall 1 and Wall 2 hybrid simulations are shown in Figure 6.51. The responses are compared in Wall 2 simulation sequence (OBE, BDBE, DBE Aftershock, large displacement cycles). The peak force developed by Wall 1 was 367.1 kips (1633 kN) and that by Wall 2 was 384.4 kips (1710 kN). The nominal shear strength of the walls computed using ACI 318 Chapter 21.9 (ACI 2008) provisions is 666.6 kips (2965 kN). This is depicted as a black line in the BDBE subplot; evidently ACI 318 Chapter 21.9 provisions overestimate the observed wall strength by a significant margin. The response of both specimens to the selected ground motions was asymmetric. In order to confirm that this was the result of the nature of the ground motion and not an asymmetry in the test setup, the ground motion direction was reversed for the Wall 2 hybrid simulation by changing the algebraic sign of the acceleration array. To facilitate comparison between the walls, the first quadrant in the response plots corresponds to the actuator pulling Wall 1 and pushing Wall 2.
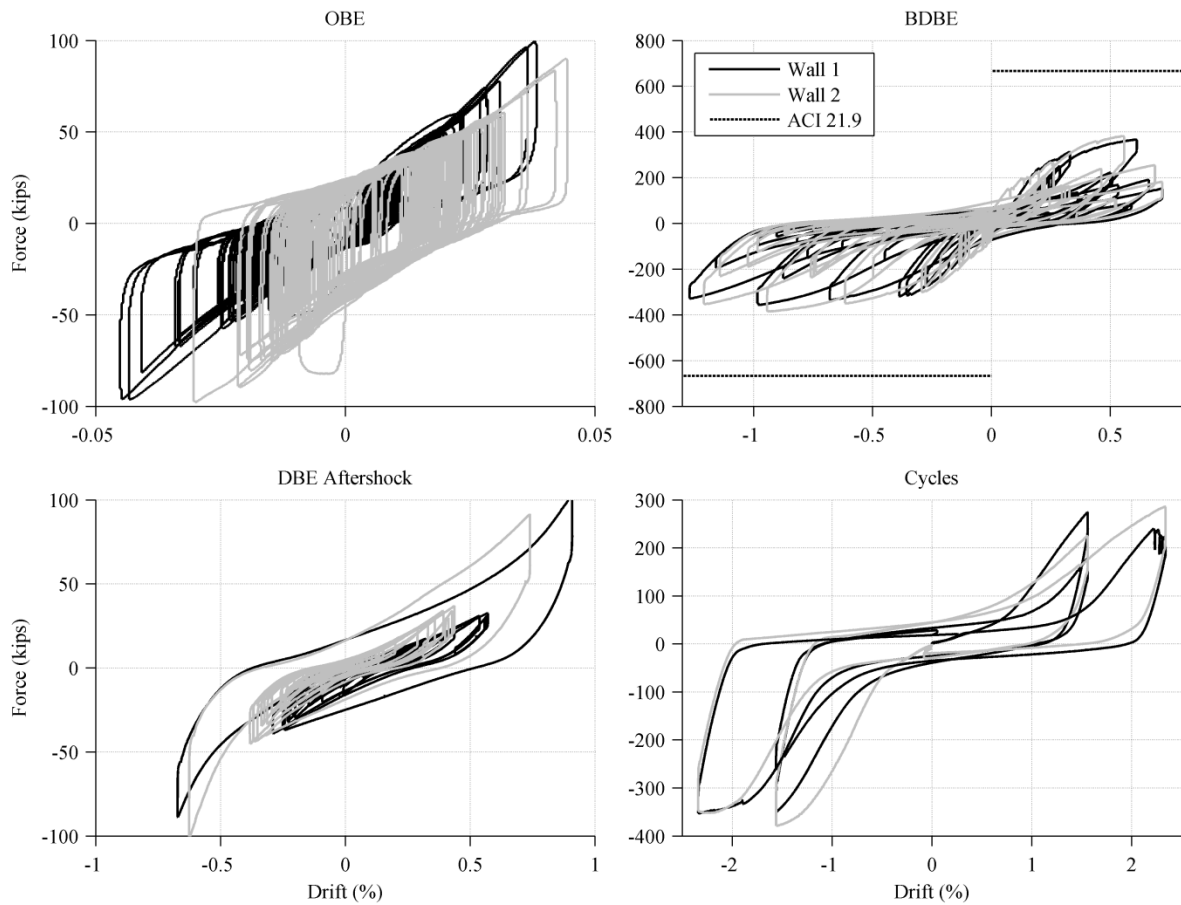
Figure 6.51: Wall 1 and Wall 2 Force-Drift Response Comparison for Ground Motion Test Sequence

The similarity between the plots of Wall 1 and Wall 2 suggests that the sequence of the ground motions does not significantly affect their force-drift global response. The plots in Figure 6.51 show a sudden drop in specimen resistance when the direction of the actuator motion changes (most evident in the BDBE motion). This is due to the slip in the actuator's clevises. When the actuator is pushing the specimen, the clevis gaps are closed. When direction of motion changes, first the clevis gaps must open and then the specimen begins to move. As the clevis gaps are opening, the force on the wall is decreasing yet the wall itself is not yet moving. The ground motions did not demand as much motion in the positive direction as in the negative direction (also most evident in the BDBE motion). When the cycles to +/-1 in (+/-2.54 cm) and +/-1.5 in (+/-3.81 cm) were applied, the walls slid along their bases and then began to pick up force again because the vertical wall reinforcement re-engaged in tension and the wall began to form a flexural force couple. This increase in force may not be realistic for a squat wall with a large structure above it. Since the experimental test setup did not constrain the top of the wall or impose vertical load, the wall was free to exhibit flexure after it slid to the point that dowels reengaged. The tensile strength of the wall was 432 kips using the nominal reinforcing bar yield strength and 509 kips using the measured reinforcing bar yield strength. 10% f'_cA_g was 494 kips. Thus, a vertical load of more than 10% f'_cA_g would likely have prevented the opening of

the crack at the wall-foundation interface along its entire length. This would have likely postponed sliding behavior.

The Wall 1 envelope connecting the peaks of its response to all ground motions and cycles is shown in Figure 6.52. The Wall 2 envelope connecting the peaks of its response to all ground motions and cycles is shown in Figure 6.53. Though these envelopes do capture the observed responses of the walls in the tests presented, they do show the increased forces after the start of sliding, which may not be realistic in a real-world application.
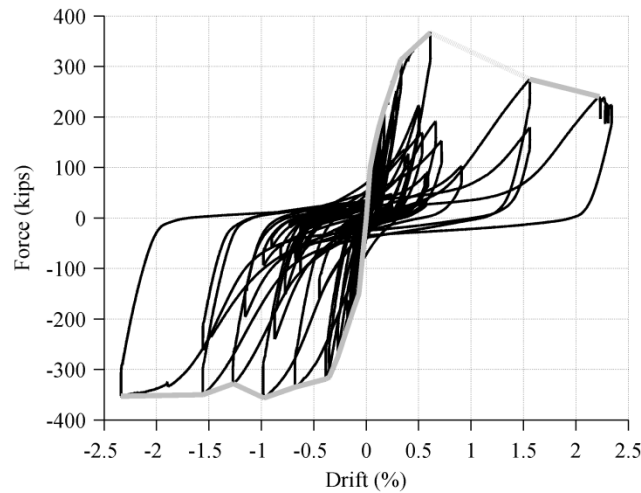
Figure 6.52: Wall 1 Force-Drift Response to Ground Motions and Cycles with Envelope
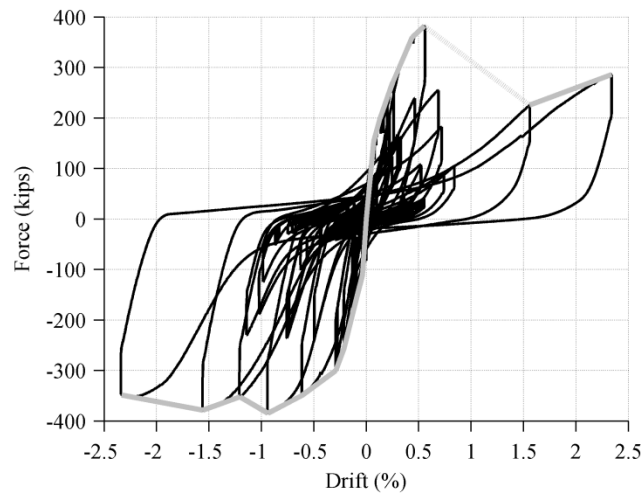
Figure 6.53: Wall 2 Force-Drift Response to Ground Motions and Cycles with Envelope

The ground motions were such that they did not demand as much motion in the positive direction as in the negative direction. When the cycles to 1 in and 1.5 in were applied, the walls began to pick up force again in the positive direction. The dotted lines on the positive side of the envelopes indicate a lack of data in that range of drifts, since the ground motions were not

98

demanding there. During the positive cycles, the peak forces in the positive direction were less than the peak forces in the negative direction. The positive side loses some strength after peak force, whereas the negative side maintains its peak force throughout the cyclic motions. This is due to the fact that the walls were more damaged on the positive side. The walls experienced first yield, first maximum force, and first sliding on the positive side. The force-drift response envelopes for Wall 1 and Wall 2 are shown in Figure 6.54. They are nearly identical.
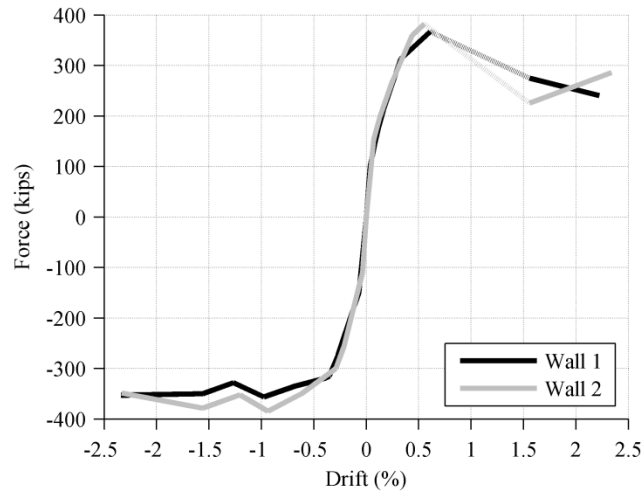
Figure 6.54: Comparison of Wall 1 and Wall 2 Force-Drift Response Envelopes

6.5   DRIFT CONTRIBUTIONS

The drift of the wall in each ground motion was decomposed into approximate contributions from shear, flexure, rotation in the sliding zone, and base sliding. Rotation in the sliding zone is defined as the inelastic flexure in the 3 in "sliding zone" above the base of the wall. Flexure is defined as the motion of the wall due to flexure above the 3 in sliding zone. This is mostly elastic. The interaction between these three major failure modes (grouping rotation in the sliding zone and flexure together) will be referred to as Flexural-Shear-Sliding (FSS) Interaction. The composition of each wall's motion in terms of these contributions was inspected at peak displacements. The methods for calculating each of these components are described below.

6.5.1   Drift Due to Shear and Flexural Deformations

The Novotechnik displacement transducers used to measure shear were located on the back of the wall, as shown in Figure 5.7 and repeated in Figure 6.55 below, for convenience.
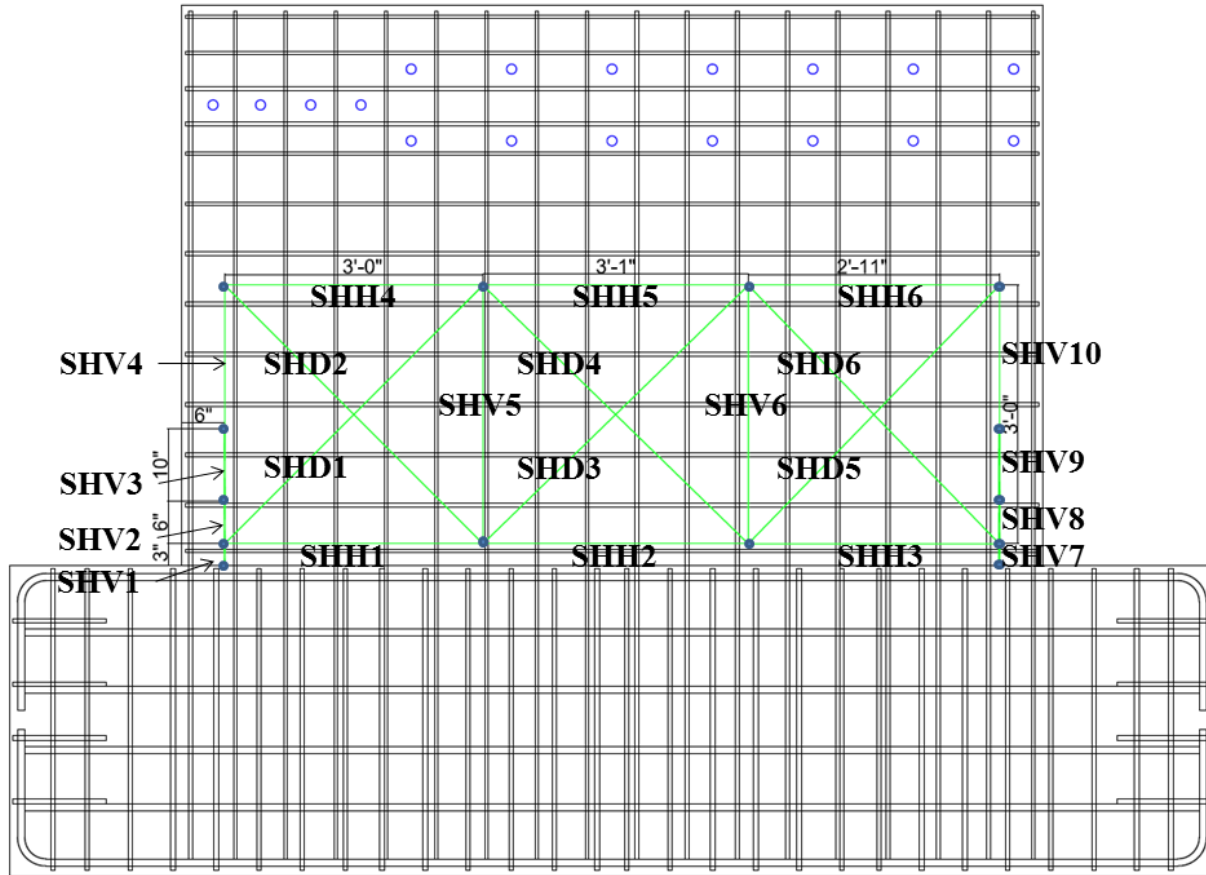
Figure 6.55: Novotechnik Instrumentation for Shear

The shear instruments were placed in three square arrangements horizontally. Each square arrangement has vertical, horizontal, and an X configuration of diagonal instruments. Each of these square arrangements will be referred to as a Shear-X configuration. Figure 6.55 shows the dimensions and instrument names. The squares were approximately 36 in by 36 in. The 36 in heights range from 3 in above the foundation to 39 in above the foundation. The bars holding the instruments were added to the wall after casting, so they had to be drilled and epoxied in place. Because of the placement of the vertical reinforcing bars in the wall, these holes had to be slightly staggered. Thus, the middle square is 37 in wide, and the right square is 35 in wide. The vertical instrument groups closest to the edges of the wall are composed of four instruments. SHV1 and SHV7 measure from 3 in above the foundation down to the foundation. Then SHV2 and SHV8 measure from 3 in above the foundation to 9 in above the foundation. SHV3 and SHV9 measure from 9 in above the foundation to 19 in above the foundation. These match the locations of the instruments measuring on the short sides of the wall, for comparison. Finally, SHV4 and SHV10 measure from 19 in above the foundation to 39 in above the foundation. All instruments except SHV1 and SHV7 participate in the shear calculations.

The shear was computed for each of these three Shear-X squares, according to recommendations by Massone and Wallace (2004). The diagram showing behavior measured by the diagonal instruments, excerpted from Massone and Wallace (2004), is shown in Figure 6.56.

100
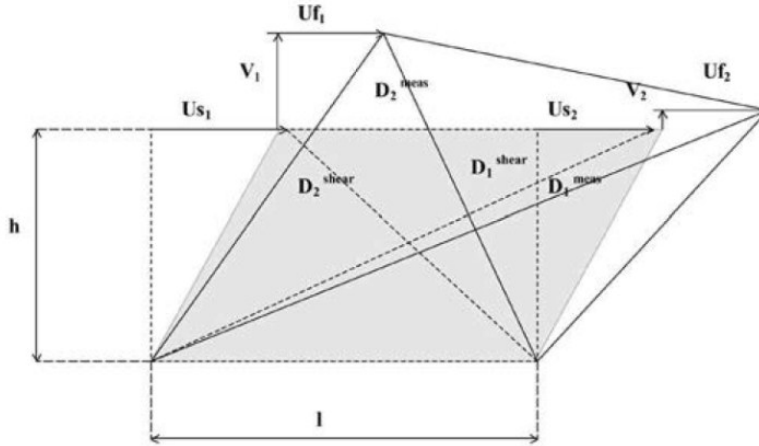
Figure 6.56: Determining Shear Displacements (Massone and Wallace, 2004)

The diagonal instruments measure D_1^{meas} and D_2^{meas}, as shown in Figure 6.56. The purely shear behavior of the concrete element is shaded grey, and the diagonal measurements corresponding to this purely shear behavior are shown as D_1^{shear} and D_2^{shear}. Because of the contribution of vertical motions, measured as V1 and V2, the diagonal instruments are measuring a combination of shear and flexural behavior. In order to isolate the lateral displacement resulting from the shear behavior, it is necessary to subtract this vertical motion. Massone and Wallace (2004) propose the following equation to calculate the total shear and flexural lateral displacement.

$$U_{total} = U_s + U_f = \frac{\sqrt{D_1^{meas^2} - (h + V_2)^2} - \sqrt{D_2^{meas^2} - (h + V_1)^2}}{2} \tag{6.1}$$

The flexural component of the displacement was calculated using the vertical instrument measurements V_1 and V_2 of each square set of instruments. First the rotation was computed as

$$\theta = \frac{V_1 - V_2}{l} \tag{6.2}$$

Then the flexural displacement at the actuator height was calculated as

$$U_f = (25.125 + \alpha h)\theta \tag{6.3}$$

where 25.125 in is the distance from the actuator to the top of the Shear-X configuration, and α is the relative distance from the top of the square to the centroid of rotation of the element. Based on the results of a parametric study, Massone and Wallace (2004) recommended using α=0.6. Then the flexural displacement was subtracted from U_{total} to obtain the shear displacement, U_s.

This procedure was applied to the data from Wall 1 and Wall 2. For each Shear-X configuration, the shear displacement that was calculated in this 36 in height was used to determine the shear strain, γ. Then the shear strain for the west, middle, and east Shear-Xs were averaged to determine an average shear strain across the length of the wall. Because the height of the Shear-X configuration of instruments only extended from 3 in to 39 in above the base of

101

the wall, there were no measurements available to calculate the shear strain from 39 in to the height of the actuator. Thus, the average shear strain across the length of the wall was assumed to remain constant up to the 64.125 in height of the actuator. The displacement due to shear at actuator level was calculated using this shear strain and the full 64.125 in height. For Wall 2, D_2^{shear} was not working for the right side Shear-X, so $-D_1^{shear}$ was used in the calculation in its place.

6.5.2   Drift Due to Rotation in the Sliding Zone

This is inelastic flexural behavior in the 3 in sliding zone above the base of the wall. Two vertical Novotechnik instruments were located on each end of the wall to measure the motion in this 3 in zone. The average vertical motion of the two instruments on the east side of the wall (V_1) and the average vertical motion of the two instruments on the west side of the wall (V_2) were computed. Then the rotation was computed using Equation 6.2. The drift due to this rotation was computed using

$$U_f = (61.125 + \alpha h)\theta \tag{6.4}$$

where 61.125 in is the distance from the actuator to the top of this 3 in sliding zone, α is the relative distance from the top of the sliding zone layer to the centroid of rotation of the zone, and h=3 in.

6.5.3   Drift Due to Base Sliding

Base sliding was determined using triangulation to compute the in-plane displacement at 3 in above the base on each side of the wall. These values were averaged. Since the instruments were showing readings prior to the known start of base sliding, it was determined that the instruments were picking up some motion from the flexural movement of the wall. In an attempt to correct for this, a line was fitted through the point 3 in above the base and the point 9 in above the base on each side of the wall. The angle of these lines to the vertical on each side of the wall was calculated, and the displacement due to this rotation at 3 in above the base was subtracted from the base sliding. This produced a more reasonable measure for the base sliding, but there is still some error since base sliding still appears to begin in these plots slightly too early. The values computed using this procedure are used in the plots of contributions to displacement in the next section.

In order to attempt to name a point the start of sliding in the BDBE motions, this procedure was used to calculate the base sliding in the Wall 1 DBE motion (just prior to the BDBE). Figure 6.57 shows the calculated base sliding vs. time for the Wall 1 DBE motion. It is known that sliding did not occur in the Wall 1 DBE motion, so the maximum of the absolute value of this calculated base sliding was considered the noise level. This value was 0.0044 in. When the calculated base sliding in the Wall 1 BDBE motion exceeded this noise level, this point was considered the start of sliding. Since Wall 2 experienced a BDBE following the OBE motion, the same information was not available. Since the same instruments were used for Wall

2, the noise level calculated was assumed to be consistent for Wall 2. When the Wall 2 calculated base sliding exceeded this same noise level, this was considered the start of sliding for Wall 2.
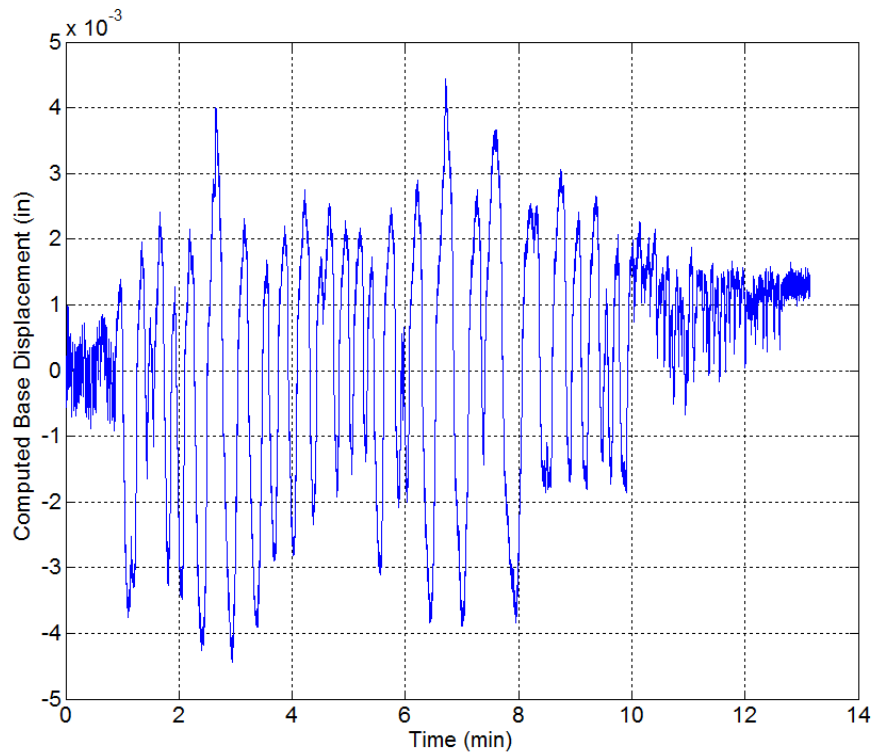
Figure 6.57: Wall 1 DBE Computed Base Displacement

Figure 6.58 shows the Wall 1 computed base displacement vs. time and shows the location that the computed base displacement exceeded the noise level. This occurred at 1.6 minutes.
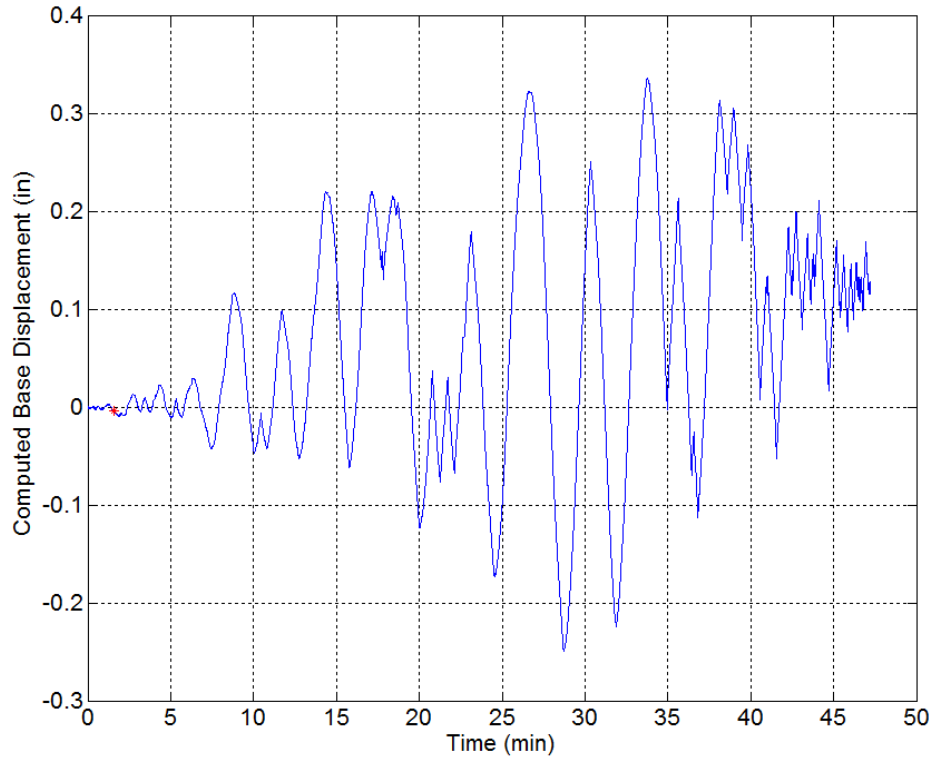
Figure 6.58: Wall 1 Start of Sliding

Though this procedure seems reasonable, the point on the force-drift response plot at 1.6 minutes does not correspond to a location that is sensible for sliding to start. This is shown in Figure 6.59, with the red star on the computed base displacement plot on the left and the corresponding location in the force-drift response plot on the right.
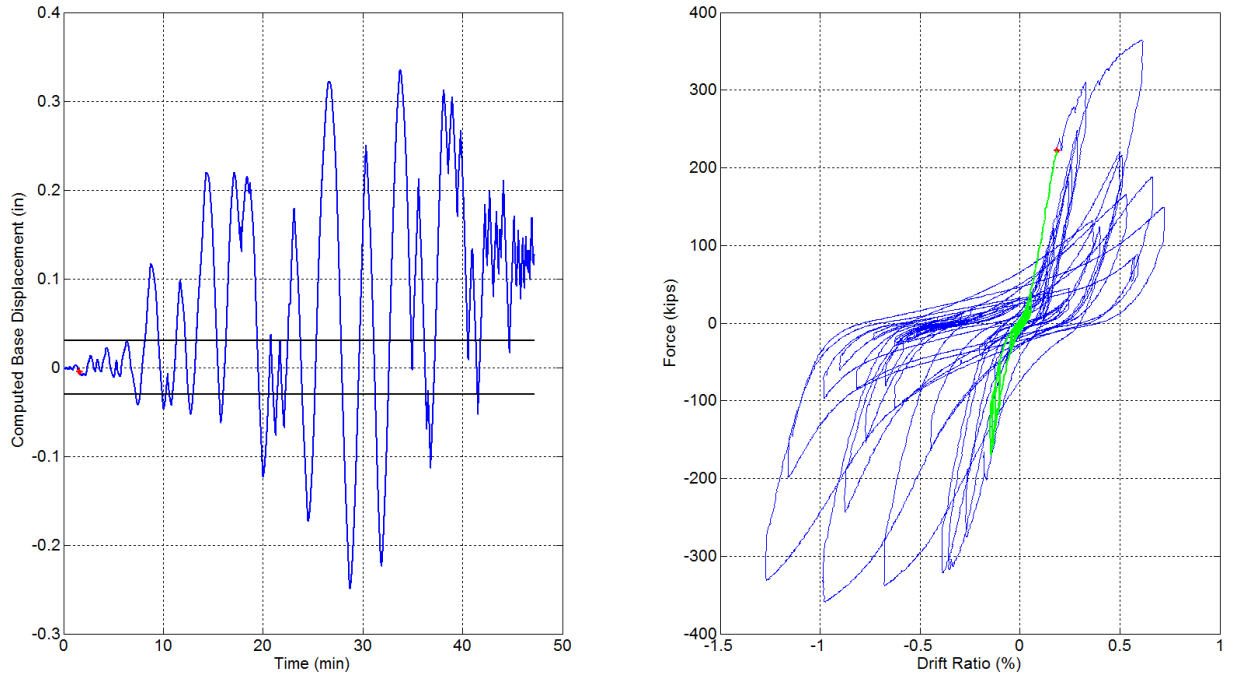
Figure 6.59: Sliding at 1.6 Minutes

The threshold for sliding must have been set too low. The black lines show a guess at a better "threshold" value of 0.03 in. Figure 6.60 shows a red star at a better guess for the start of sliding on the left and a more reasonable corresponding location in the force-drift response plot on the right.
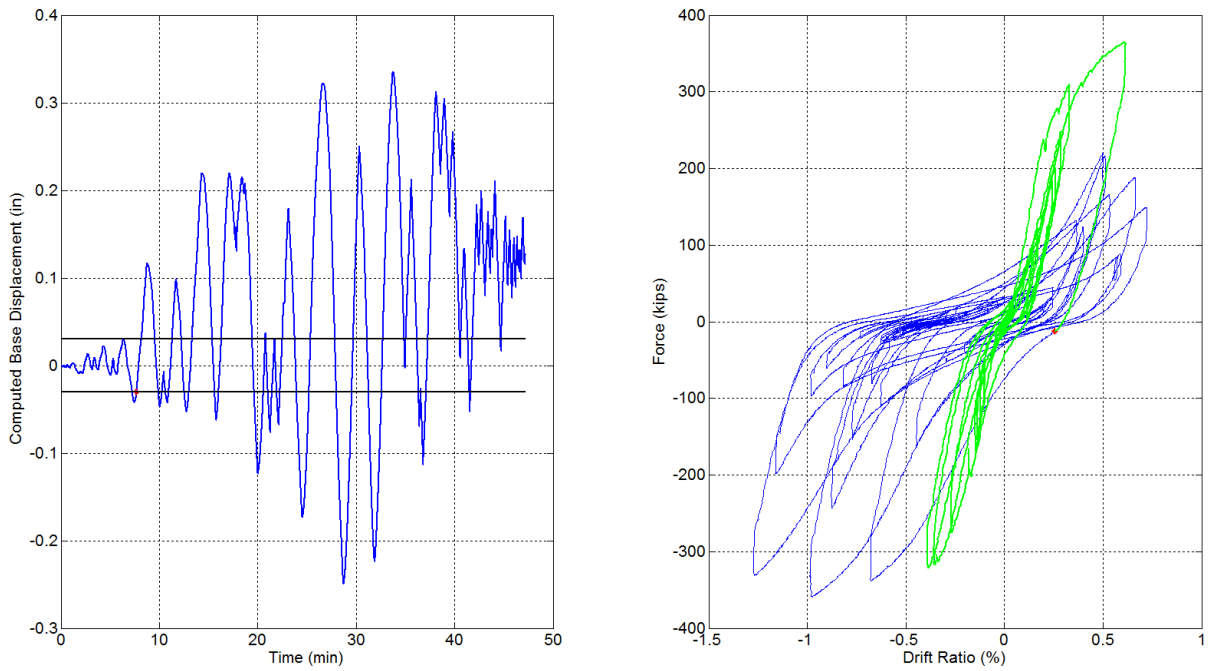
Figure 6.60: Estimate of Start of Sliding

105

However, it is not possible to justify the selection of this point. Since the flexure, shear, and sliding shear behavior are interacting, it is very difficult to isolate just one mode and determine when that mode begins to dominate.

6.5.4   Comparison of Wall 1 and Wall 2 Drift Contributions

The displacement contributions were investigated at peak displacements. In the upper two subplots of the following figures, ductility vs. time is plotted, and the peak displacements selected to assess displacement contributions are circled. Points of increasing ductility were selected. The positive points correspond to the actuator pulling Wall 1 and pushing Wall 2. The lower two subplots show contributions to total drift vs. time. Each of these plots corresponds to the ductility vs. time plot directly above it. The contributions to displacement are only sampled at the circled points, so the vertical lines in the contributions to total drift vs. time plots indicate where the data was sampled. It is important to note that between sampled points, the contributions to total drift are linearly interpolated. This is not a reflection of the actual behavior between these two points, but helps for visualization of the trend of contributions over time for increasing ductility. As mentioned in Section 6.5.1, one of the shear instruments was not working for Wall 2, so this introduced some error in computing the displacement contributions for shear in Wall 2.

The behavior in the Wall 1 DBE Motion is shown in Figure 6.61 below. There is about 20% of the drift contribution unaccounted for, but this is due to difficulty in measuring extremely small displacements. The plots erroneously show a small portion of sliding shear. There is some error due to the arcing of the instruments measuring the sliding shear, such that they picked up some motion before sliding actually began. These instruments measured lateral displacements using triangulation at 3 in above the base of the wall. However, as the wall flexed, the arcing of the wall was recorded as sliding. A correction was applied, but there is a small amount of error remaining. Here, shear is most dominant, especially in the positive actuator pulling direction. There is slightly more flexure in the negative actuator pushing direction. When the actuator is pushing, the wall tended to rotate about its east corner, at the far side opposite the actuator. When the actuator is pulling back, the wall tends to shear more easily.
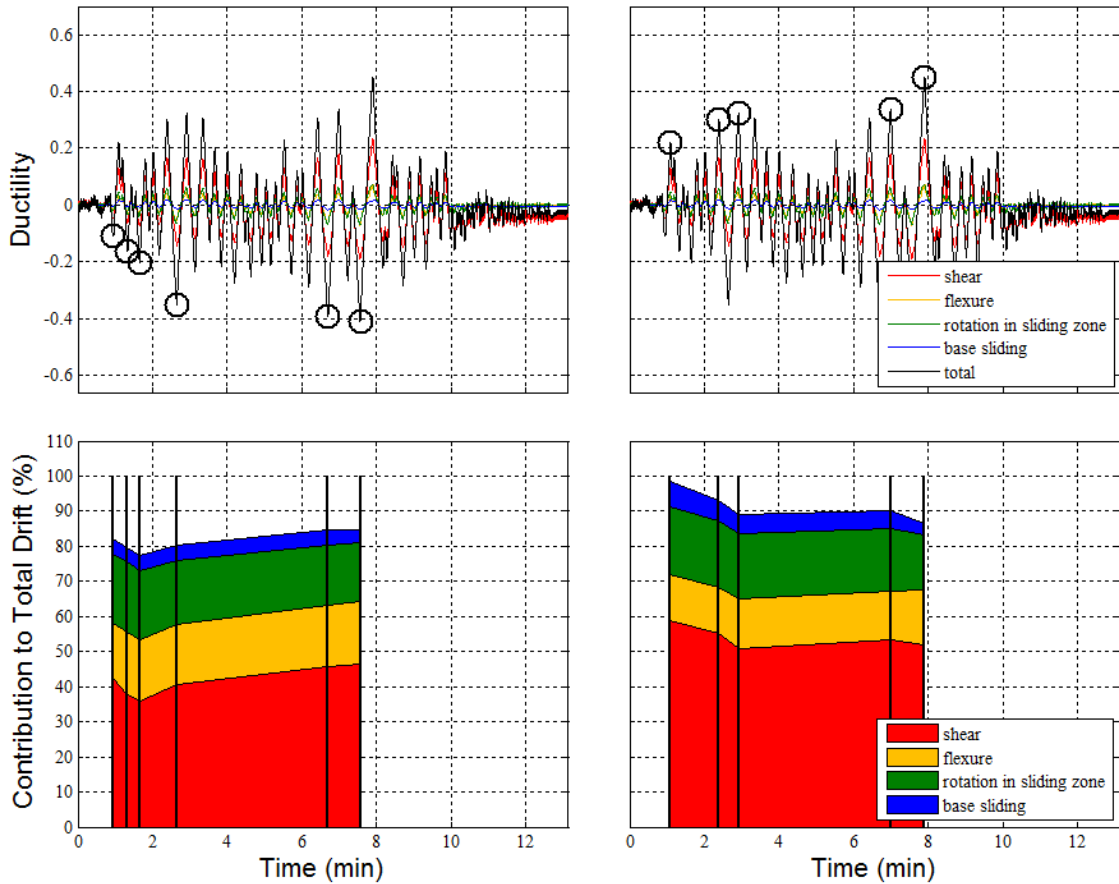
Figure 6.61: Wall 1 DBE Drift Contributions for Selected Increasing Ductilities

Wall 1 and Wall 2 behaved similarly in the BDBE motion, shown in Figure 6.62 and Figure 6.63 below. For the Wall 1 BDBE motion, there is about 15% error due to unaccounted for displacements at the beginning of the ground motion, which reduces to about 5% as the motion progresses. The greater error at the beginning of the motion is due to more error in measuring small displacements. First the negative direction when the actuator is pushing the wall will be discussed. The shear and flexural modes each make up about equal portions of the drift at the beginning of the ground motion. Within the flexural contribution, approximately half is due to rotation in the sliding zone about half due to rotation above the sliding zone. As the ground motion progresses, the flexural contributions remain mostly unchanged, but the shear contribution decreases, and the sliding shear contribution increases to about the same amount as the flexural contribution. Since these displacement contributions were sampled at the peak displacements, it is reasonable that the flexural contribution remains so significant. As the wall slides to its maximum displacement, the dowels begin to engage, and the wall picks up flexure at its peak. Additionally, with the actuator pushing, the wall tended to rotate about its east corner, at the far side opposite the actuator. The final response was nearly 1/3 due to each of shear, flexure, and sliding. For the positive direction when the actuator is pulling the wall, the shear mode dominates the displacement contribution at the beginning of the ground motion, with some flexural contribution. The shear contribution decreases as the ground motion progresses and the

flexural contribution decreases a small amount. The sliding shear increases to dominate the behavior. The amount of shear contribution remains consistently larger than when the actuator is pushing the wall. When the actuator pulled the wall back, it slid easily along its base, so there was less flexural behavior and more shear behavior.

For the Wall 2 BDBE motion, there is about 20% error due to unaccounted for displacements at the beginning of the ground motion. In the positive direction, the contributions are overestimated as the ground motion progresses. This is due to one of the shear instruments not working. Similar to Wall 1, sliding appears to contribute too early due to arcing of the instruments measuring the sliding. In the negative direction when the actuator is pulling the wall, the shear and flexural modes make up about equal portions of the drift at the beginning of the ground motion. As the ground motion progresses, the flexural contributions remain fairly constant. The portions due to rotation in the sliding zone and flexure above the sliding zone remaining about equal. As the ground motion progresses, the shear contribution decreases slightly, and the sliding shear contribution increases, such that the final response was nearly 1/3 due to each of shear, flexure, and sliding (as was with Wall 1). In the positive direction when the actuator is pushing the wall, it is difficult to draw many conclusions due to the large error introduced by the shear instrument that was not working.
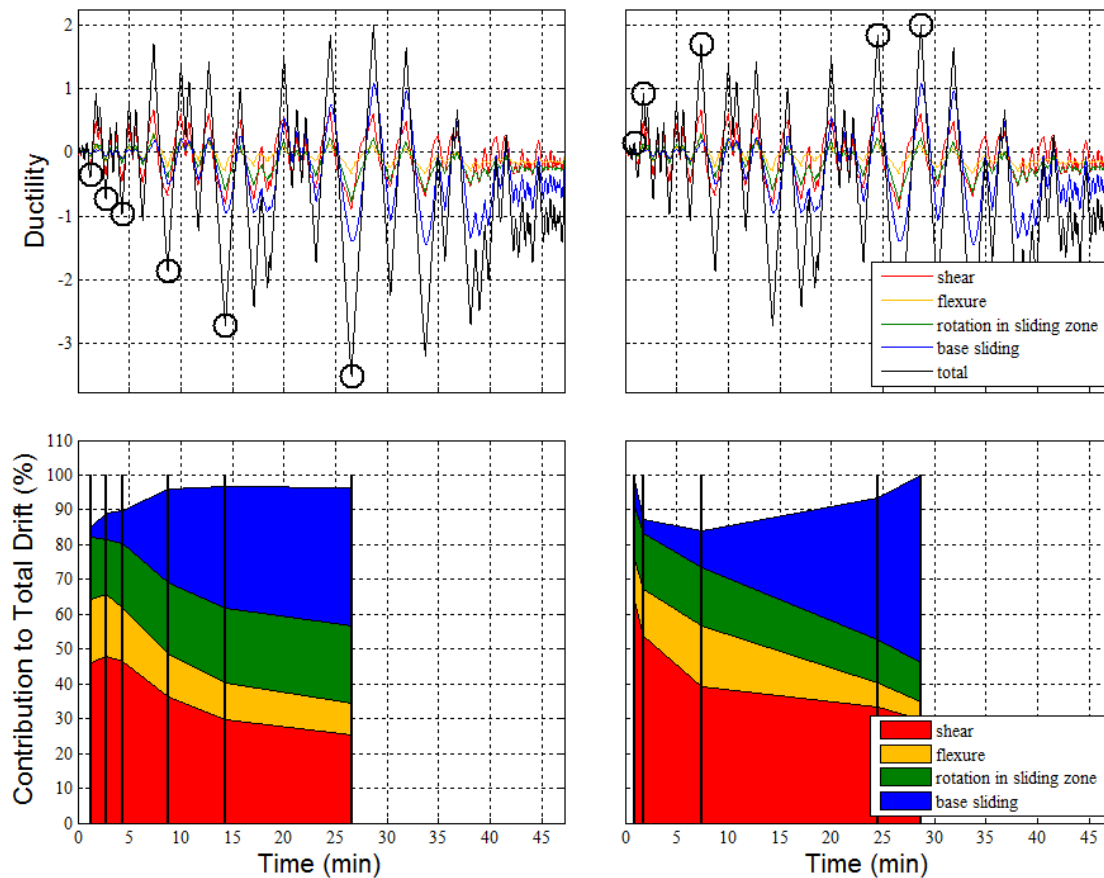
Figure 6.62: Wall 1 BDBE Drift Contributions for Selected Increasing Ductilities
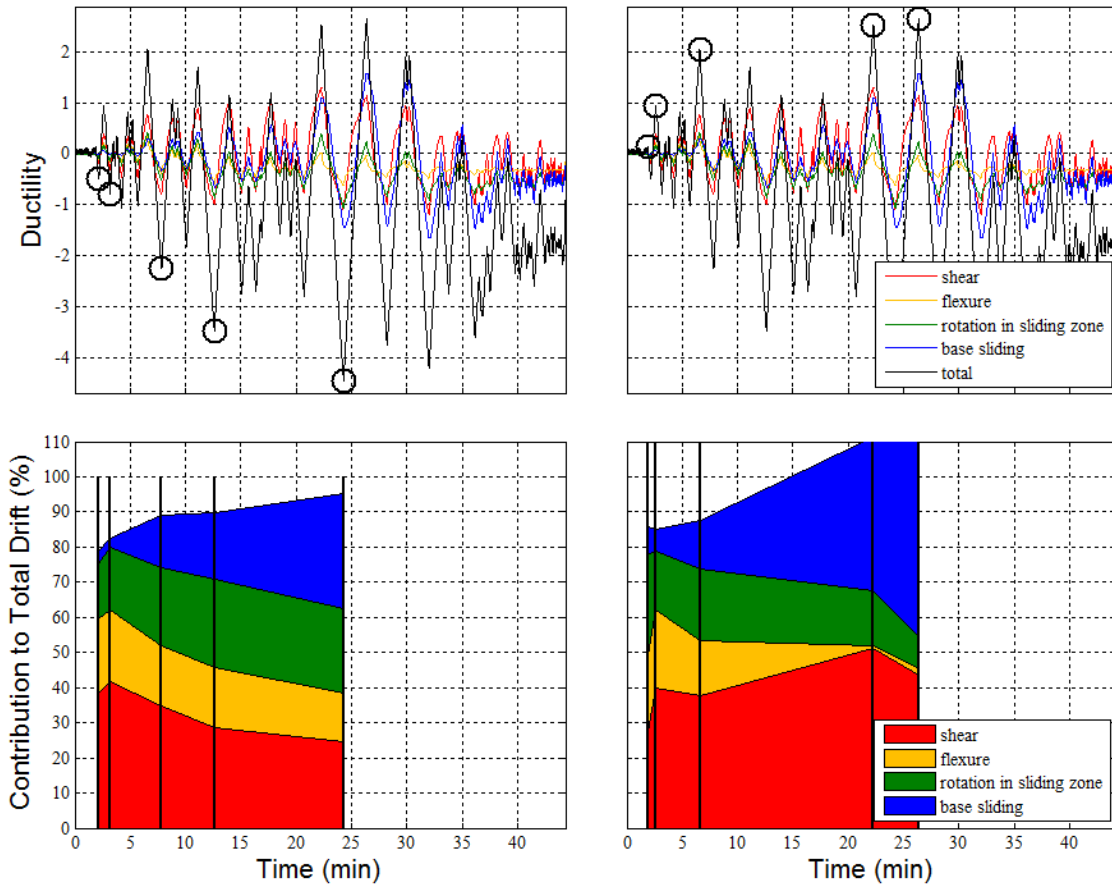
Figure 6.63: Wall 2 BDBE Drift Contributions for Selected Increasing Ductilities

In the BDBE motions of both walls, there was more flexure seen on the west side of the wall when the actuator was pushing. This is positive side of the displacement contribution plots. This is consistent with the damage observed. Both walls experienced more local buckling of bars on west side of specimen despite reversed ground motions. A likely explanation for this is the actuator pushing the wall tended to cause more rigid body motion about the toe of the wall on the east side, but the actuator pulling the wall caused the wall to slide back more smoothly. Every time the actuator pushed the wall, the west side of the wall experienced more vertical motion. Then upon load reversal, these bars were elongated and buckled more. This contributed to opening of horizontal hooks on Wall 1 because these elongated vertical bars buckling pushed the hooks open.

Wall 1 and Wall 2 also behaved similarly in the DBE Aftershock 1 motions, shown in Figure 6.64 and Figure 6.65 below. There is more uniform behavior with the actuator pushing and pulling in the DBE aftershocks. This is reasonable since the walls were very damaged and they were mostly sliding. Here, the flexural components are smaller on the west sides of the walls (positive displacement contributions). This makes sense because the DBE aftershock motions were not very demanding on the walls. They were mostly sliding and not picking up much force. In fact, since the vertical bars on the west sides of the specimens had elongated

109

more, they allowed for much more sliding in the positive displacement contributions. The sliding components are clearly larger in the positive side plots.
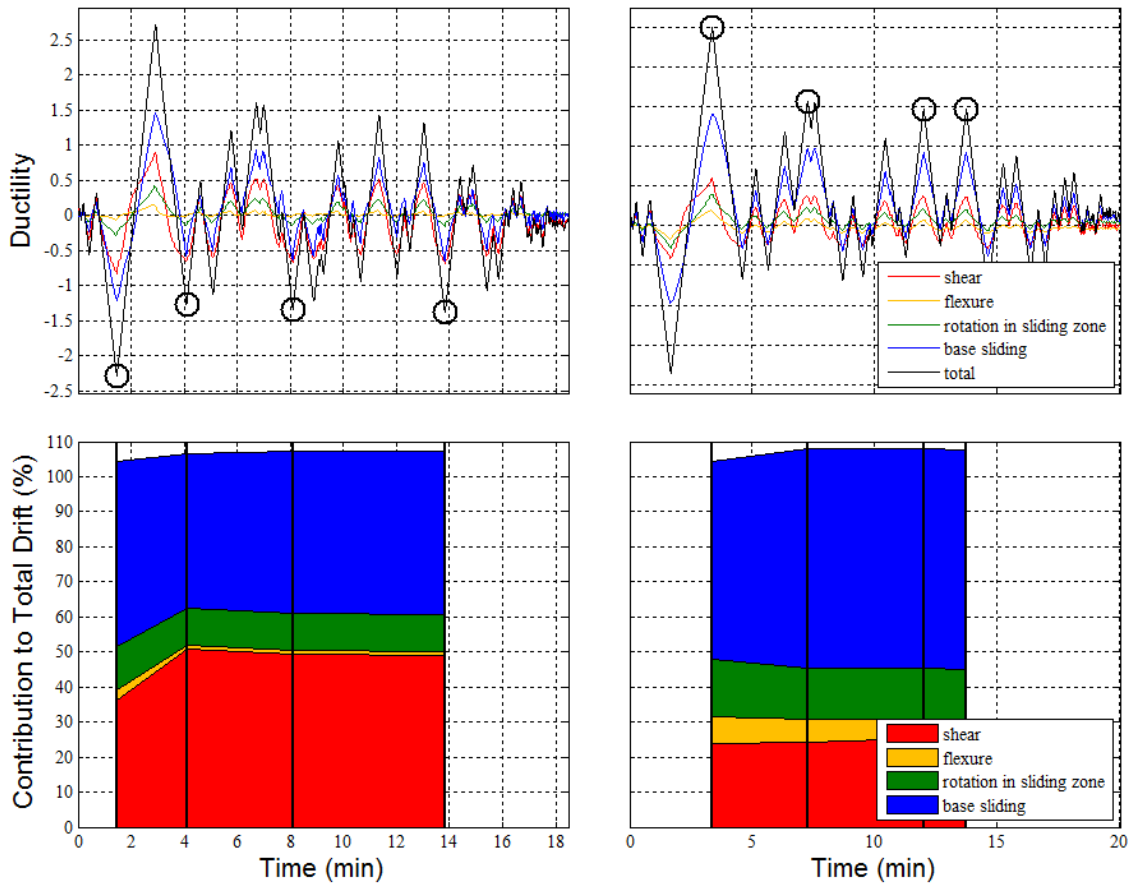
Figure 6.64: Wall 1 DBE Aftershock 1 Drift Contributions for Selected Increasing Ductilities
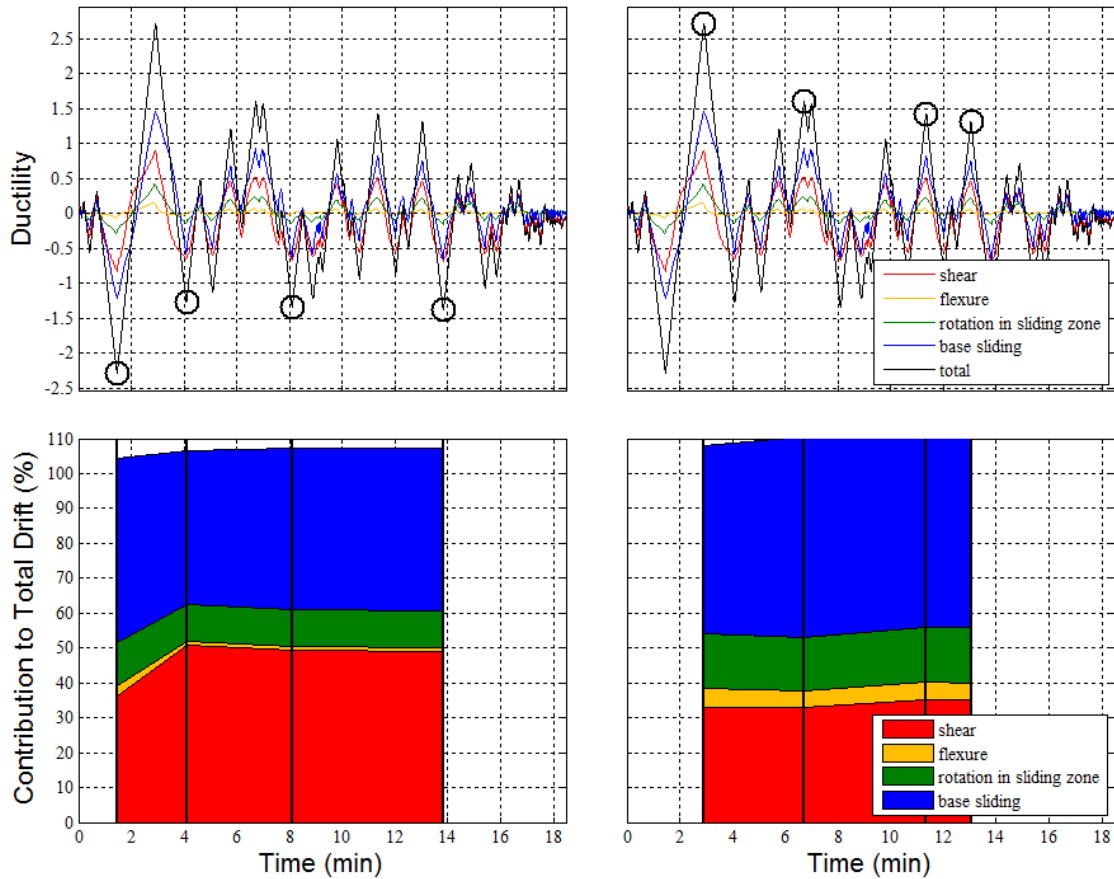
Figure 6.65: Wall 2 DBE Aftershock 1 Drift Contributions for Selected Increasing Ductilities

6.6   EXPECTED STRENGTHS BASED ON CODE EQUATIONS

The peak shear strength observed in the wall tests was 367.1 kips for Wall 1 and 384.4 kips for Wall 2. The peak shear strength was calculated using code equations by ACI 318-08 Ch 11.6, Ch 11.9, and Ch 21.9 and using equations proposed by Barda (1977), ASCE 43-05, Wood (1990), and Gulec (2009). These equations are all given in Section 2.6. For each of these equations, Figure 6.66 shows the predicted strengths for Wall 1 and Wall 2 using measured material properties and the predicted strengths using nominal material properties. Figure 6.67 shows the same information as the ratio of predicted to measured shear strengths.

111
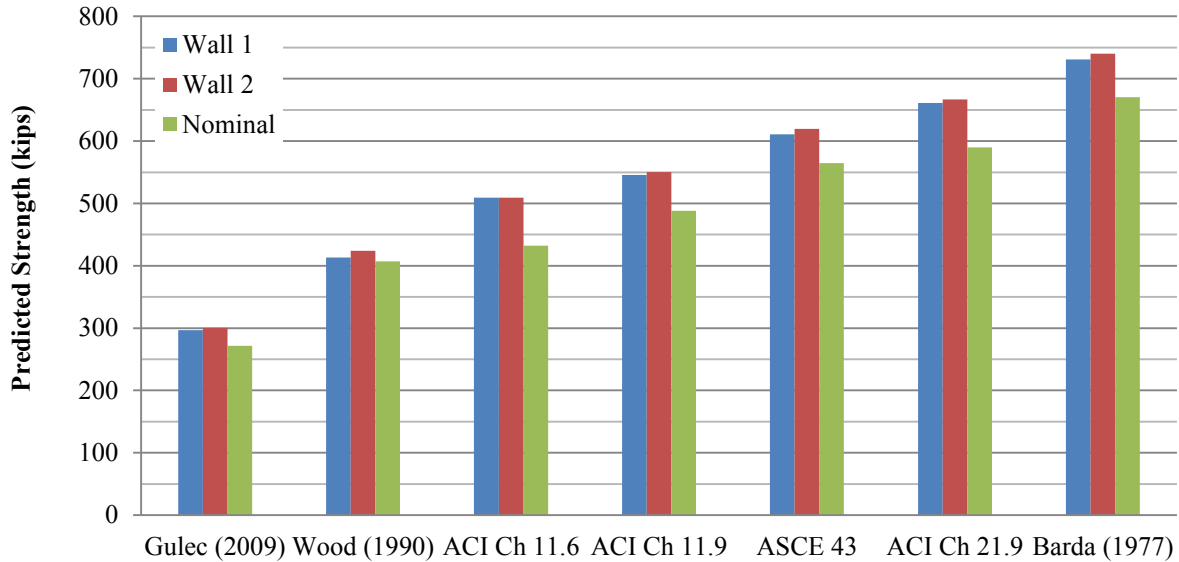
Figure 6.66: Predicted Peak Shear Strength using Code Equations
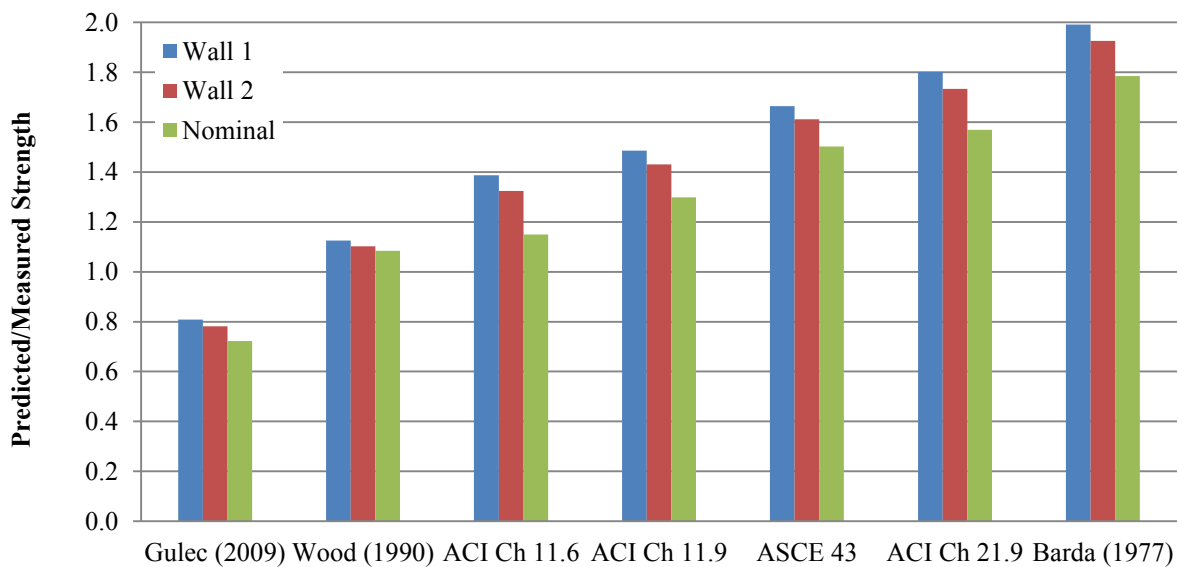
Figure 6.67: Ratio of Predicted to Measured Peak Shear Strength for Code Equations

The lower bound of Wood's (1990) equation, with shear stress $6\sqrt{f'_c}$, provides the best estimate of the actual peak shear strength observed in the Wall 1 and Wall 2 tests. This equation also was the best fit for the walls in the Gulec database as discussed in Section 2.6.8. Her equation predicted a peak shear strength of 413 kips for Wall 1, 424 kips for Wall 2, and 407 kips using nominal material properties. ACI Ch 11.6 provides the next closest estimate with the shear friction model; it predicted a value of 509 kips for Wall 1 and Wall 2 and a value of 432 kips using nominal material properties. This is significant because sliding shear was the ultimate failure mode, so the shear friction captured the peak strength well. However, the code states that

the shear friction model oversimplifies the actual behavior by artificially increasing the coefficient of friction and assuming that all of the shear resistance comes from friction between the crack faces. The coefficient of friction used in this model was based on finding a number that agreed well with test results. Gulec (2009) is the only equation that underpredicts the peak strength. ACI Ch 11.9, ACI Ch 21.9, and Barda (1977) all significantly overpredicted the peak shear strength. ACI Ch 21.9 gave a peak shear strength of 661 kips for Wall 1, 667 kips for Wall 2, and 590 kips using nominal material properties. Barda (1977) overpredicted the peak strength by nearly two times; however, his equation was based on tests of walls with large flanges, so this is expected.

The peak sliding shear strength will be taken as the 509 kip value given using the ACI Ch 11.6 shear friction model.

The peak flexural strength was calculated using the ACI method and found to be 420.5 kips for Wall 1 and 421.9 kips for Wall 2. ACI gives the initial stiffness as $0.8EI$, so the Wall 1 predicted initial flexural stiffness is 42870 k/in and the Wall 2 predicted initial flexural stiffness is 43972 k/in. Since the values are so similar for Wall 1 and Wall 2, the Wall 1 envelope will be used. Figure 6.68 shows the ACI Ch 21 prediction for peak strength, the peak sliding shear, the flexural envelope calculated using the ACI method, and Wood's estimate for peak shear. The Wallace (2006) backbone curve for shear walls applied to the Wall 1 data is also shown, both with using the ACI Ch 21 equation for V_n, as recommended, and with using Wood's equation for V_n, which estimated the peak strength of the walls much more closely. The details of the Wallace backbone curve model are described in Section 2.4.3.
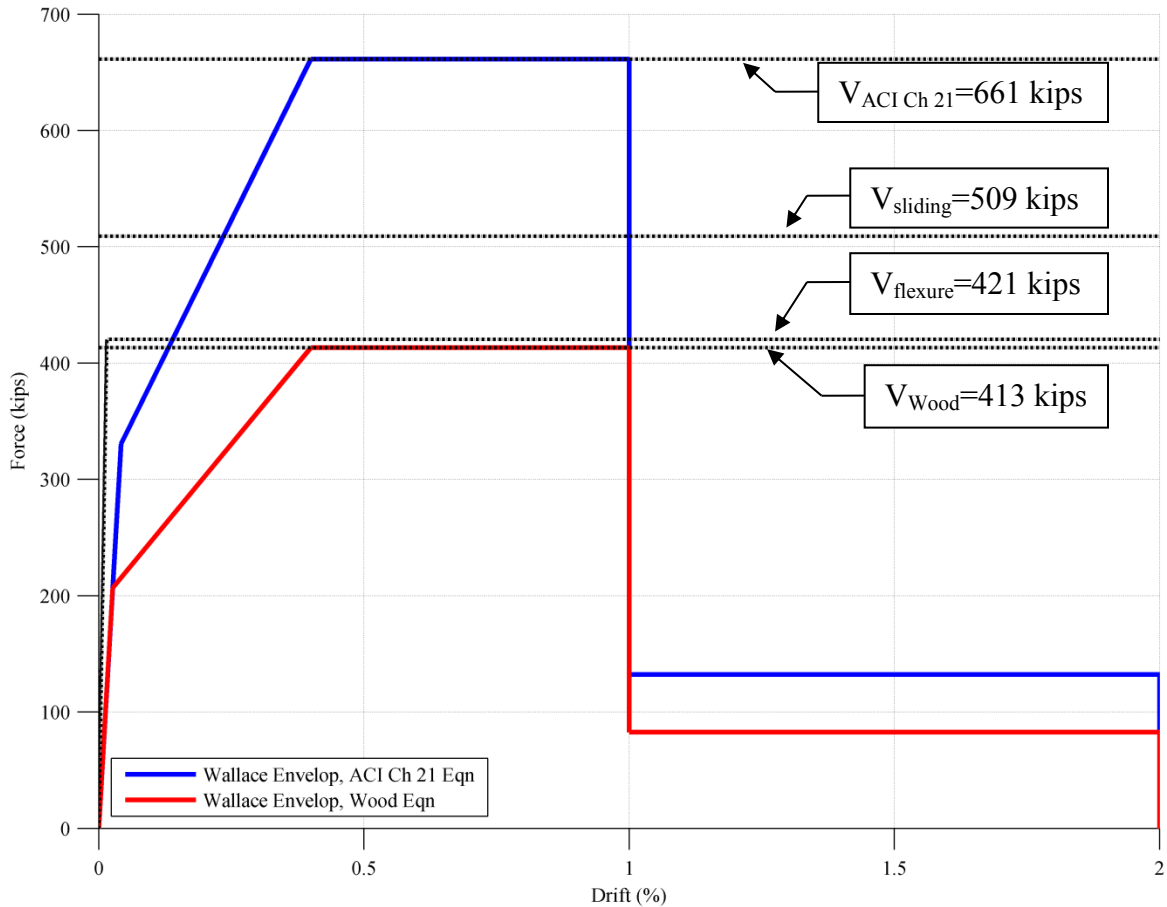
Figure 6.68: Predicted Strengths and Wallace (2006) Backbone Curve

The shear strength envelope, V_{Wood}, and the sliding envelope, $V_{sliding}$, deteriorate with increasing drift ratio. The rate of deterioration and final degraded strengths will be assessed from the test data.   The Wallace Envelope using the ACI Ch 21 equation overestimates the response significantly.   The walls data peak strength is less than Wood's predictive equation.   In the subsequent plots, Wallace's envelope will be drawn using Wood's predicted peak strength.

The Wallace recommended backbone curve using the ACI Ch 21 equation for peak strength is plotted with the Wall 1 force-drift response in Figure 6.69. The Wallace backbone curve using Wood's equation for peak strength is plotted with the Wall 1 data in Figure 6.70. The initial stiffness is taken as the shear stiffness, equal to $0.4*E_c$, as recommended. In order to compare the Wallace backbone curve to the measured data without the effect of the clevis slip, the Wallace backbone curve is offset by 0.03% drift (approximately the clevis slip in the OBE motions).

114
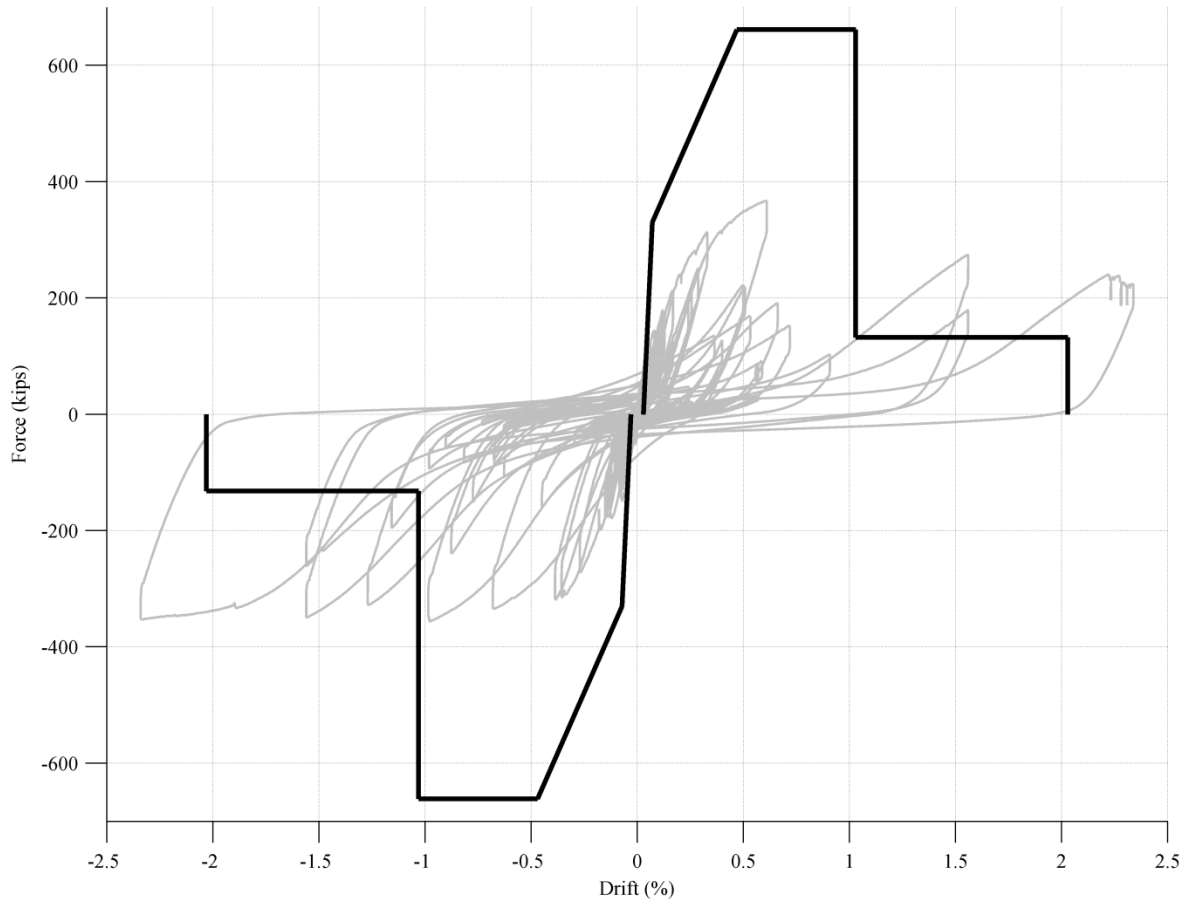
Figure 6.69: Wallace Backbone Curve using ACI Ch 21's Equation for Peak Strength
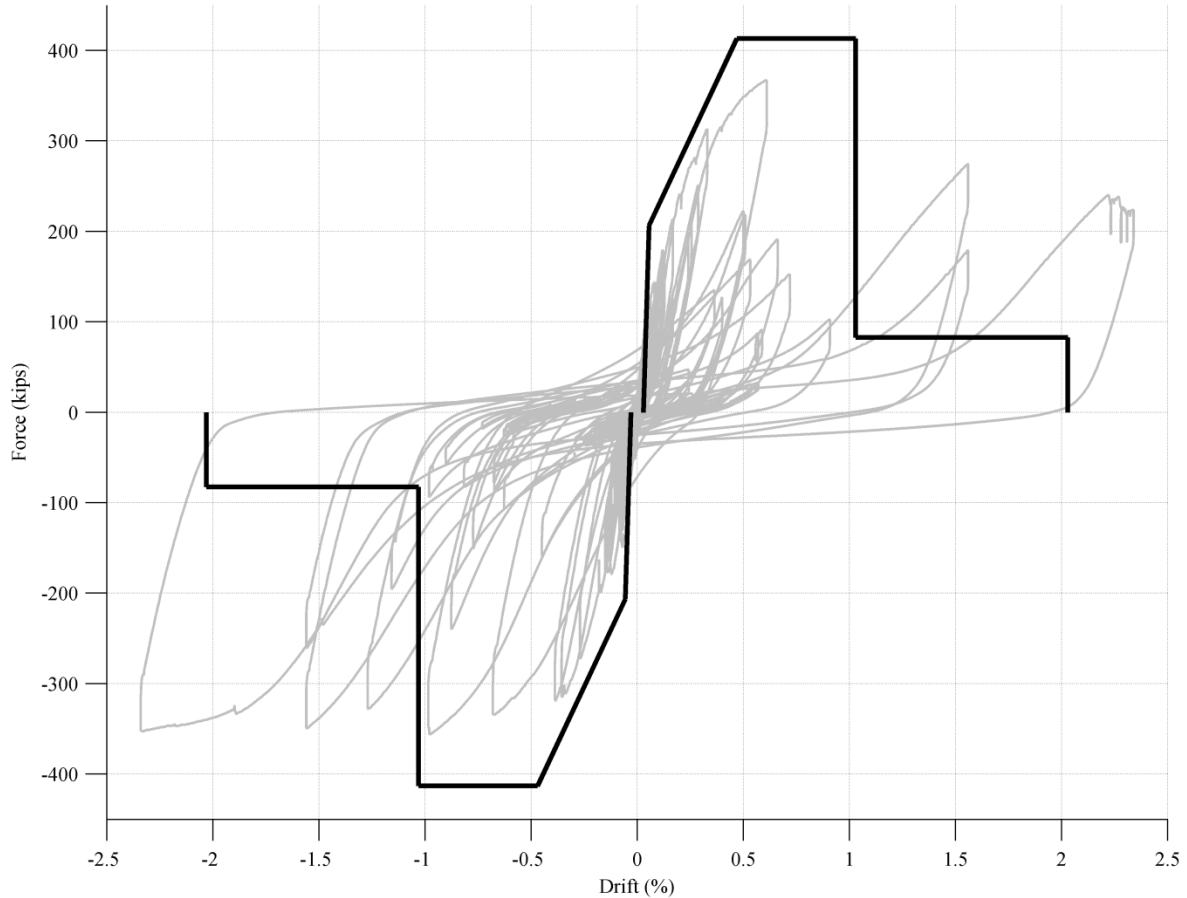
Figure 6.70: Wallace Backbone Curve using Wood's Equation for Peak Strength

The Wallace envelop using ACI Ch 21 for peak strength significantly overestimates the data, but the envelop using Wood's equation provides a decent fit. However, the initial stiffness recommended by Wallace is higher than observed experimentally. 30% of Wallace's recommended stiffness provides a good fit to the data. Thus, the shear stiffness is $0.3*0.4*E_c$. The plot from Figure 6.70 is repeated below in Figure 6.71 with the modification to the initial stiffness in the Wallace backbone curve. Also, Wallace's point B is slightly modified to better fit the experimental data. Instead of 0.4% drift, it is moved to 0.44% drift.
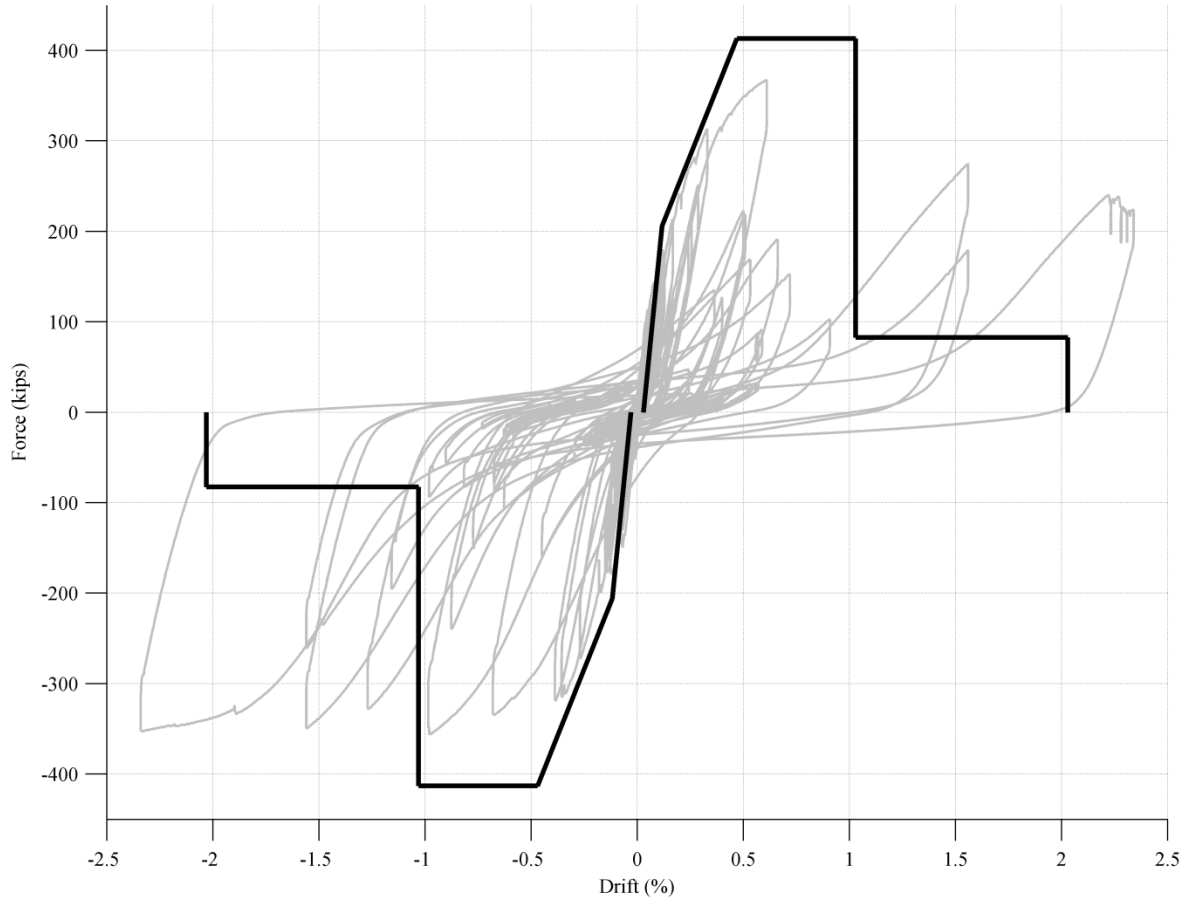
Figure 6.71: Wallace Backbone Curve using 30% of Initial Stiffness

This modification provides a good estimate to the initial data. The "essentially elastic" range of data is estimated as the range of stiffnesses from the initial stiffness to the stiffness connecting the origin and Wallace's point B. This range is shown in Figure 6.72. The second stiffness is proposed to be 0.4*initial stiffness. The proposed "essentially elastic" range is from initial stiffness, $0.3*0.4*E_c$, to second stiffness, $0.4*(0.3*0.4*E_c)$.
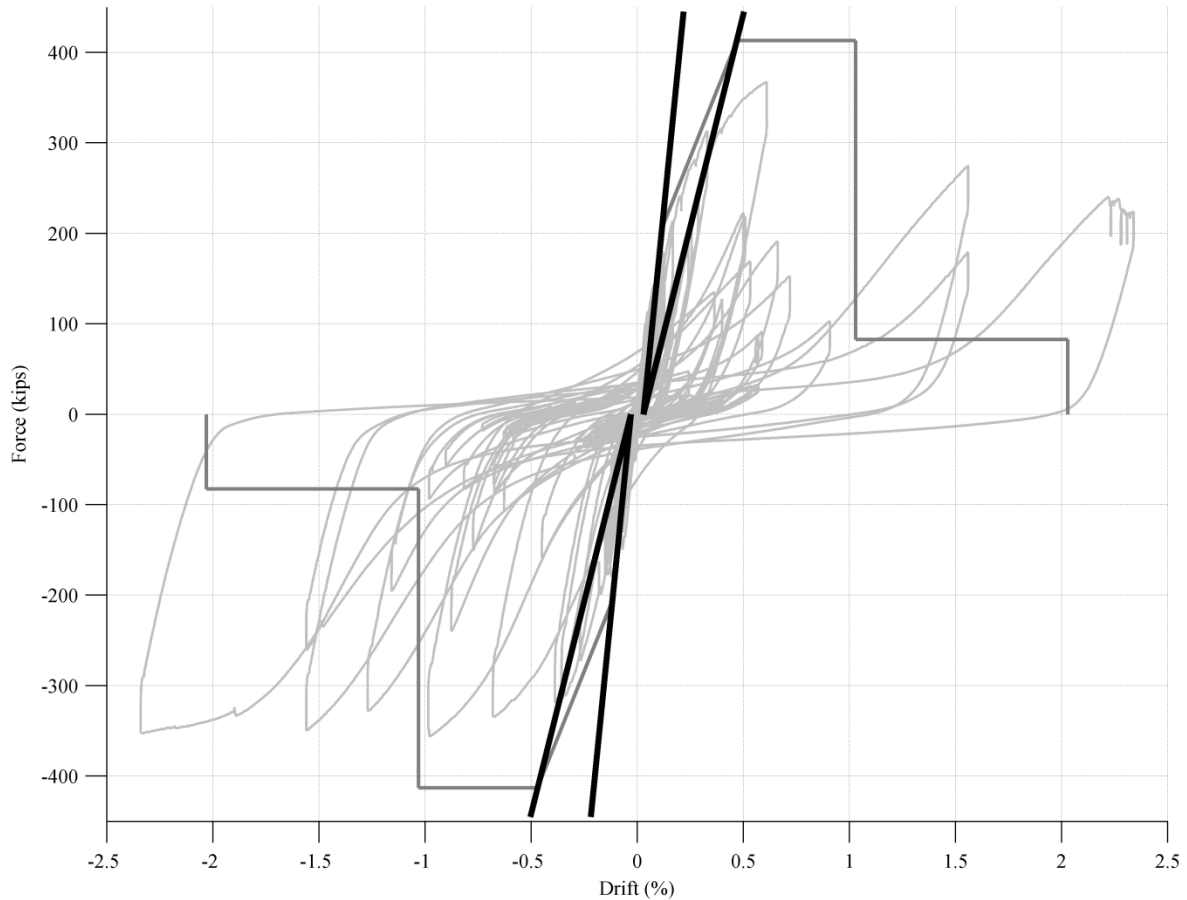
Figure 6.72: "Essentially Elastic" Region and Wallace Backbone Curve using 30% of Initial Stiffness

Ideally, the point where the wall rapidly began to lose strength would be identified and better reflected in the Wallace backbone curve. However, there is not enough data to make this judgment. The ground motion caused different demands on the wall on the positive and negative sides, so it is difficult to choose a point with certainty. The residual strength shown by the Wallace curve does seem to approximate the sliding strength well. As the wall slid in the later cycles, it maintained a low force level throughout most of the motion. Then the wall picked up some force at the peaks when the aggregate interlock and dowel action were re-engaged. This increase in force after sliding was addressed above as a behavior that is not representative of what would be seen in a wall in an actual building. The top of the wall would not be free to rotate as the wall flexes since the weight of a building above the wall would constrain it.

In the envelope responses in Figure 6.52 and Figure 6.53, solid lines are shown in the positive direction up to the end of the ground motion cycles. Then the lines are dotted from approximately 0.6% drift to 1.5% drift before they become solid again. Because the ground motion was not as demanding in the positive direction than in the negative direction, there is a lack of data in the dotted section of the envelopes. When the walls were pushed to cycles of 1 in and 1.5 in, the envelopes can be drawn again for that range. In this range of cycles, the walls

picked up force again, but did not reach their peak force a second time. In the negative direction, however, Wall 1 and Wall 2 reach peak strength at about 1% drift and maintain that strength throughout the remainder of the ground motion runs and cyclic runs. Figure 6.73 shows the Wallace and Wall 1 and Wall 2 envelopes with the Wall 1 BDBE motion displacement contributions. Figure 6.74 shows the Wallace and Wall 1 and Wall 2 envelopes with the Wall 2 BDBE motion displacement contributions.
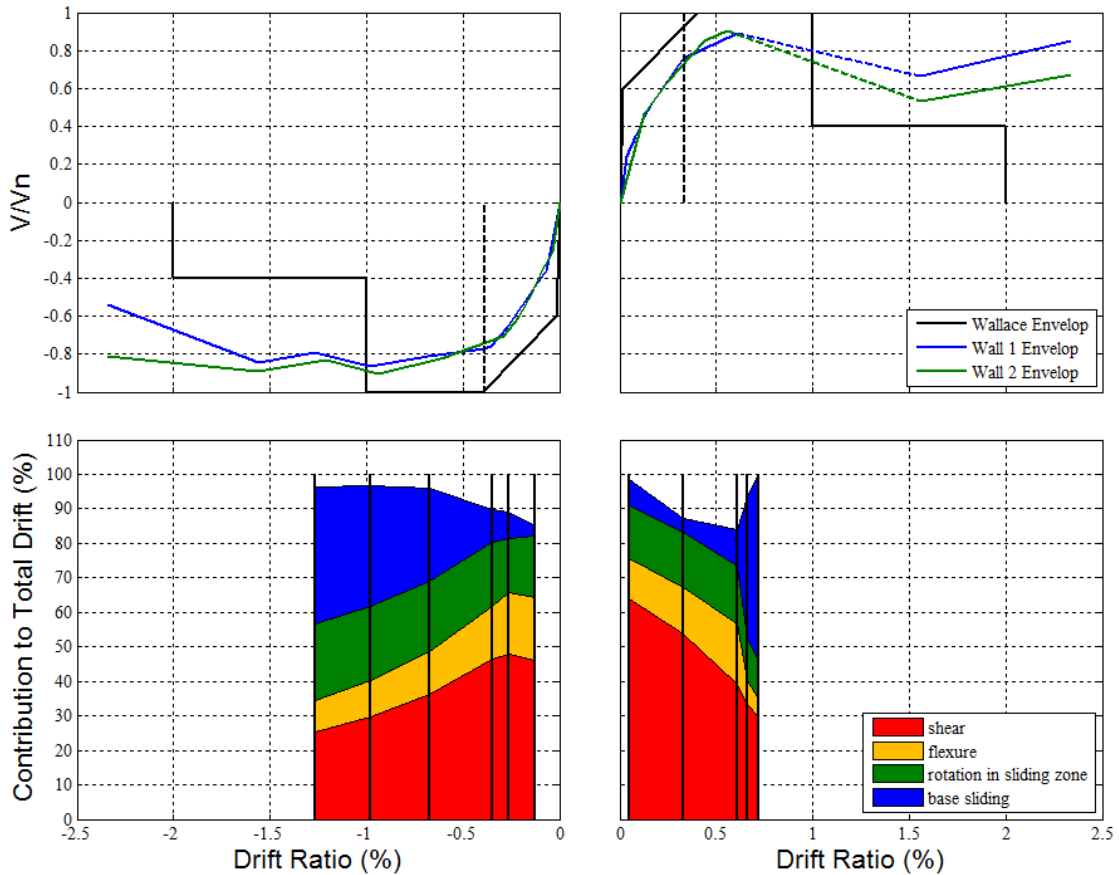
Figure 6.73: Envelope Response with Contributions to Drift from Wall 1 BDBE
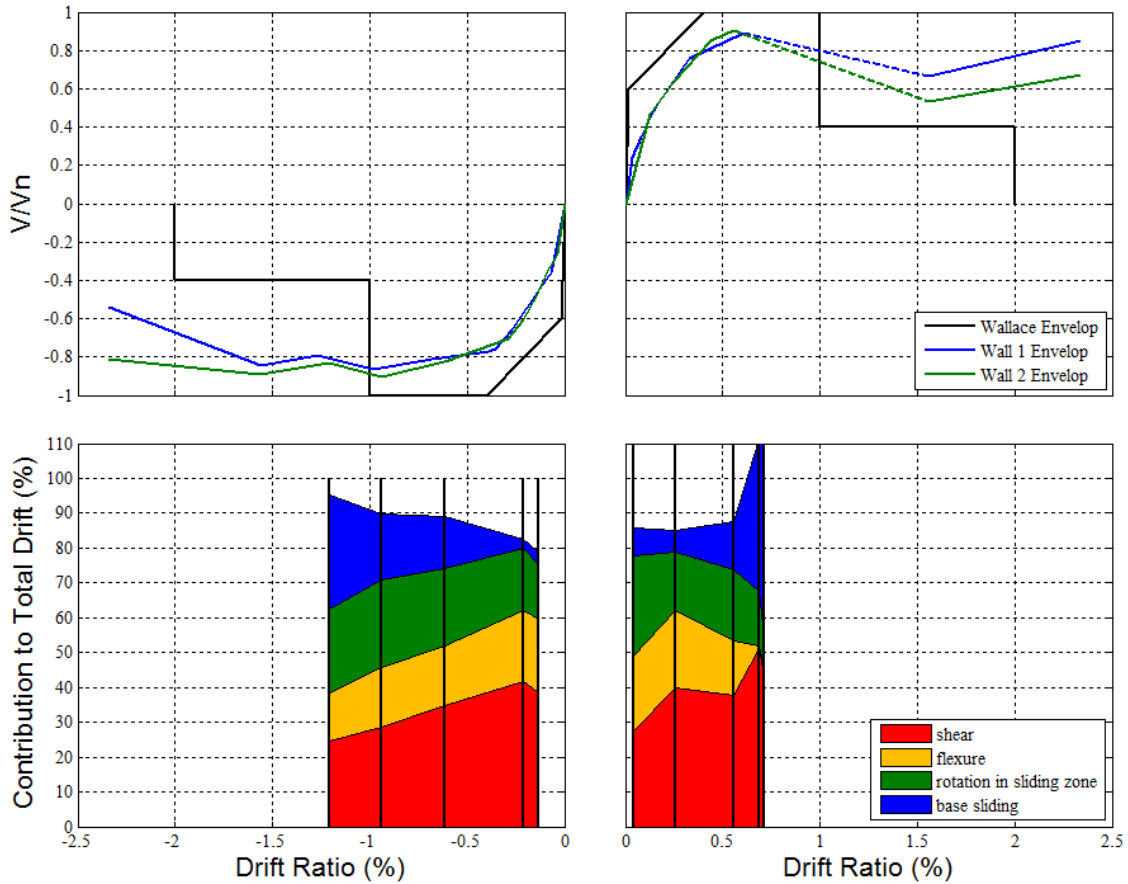
Figure 6.74: Envelope Response with Contributions to Drift from Wall 2 BDBE

6.7   TEST SETUP RESPONSE

Novotechniks measured slips and deformations in the test setup as described in Section 5.6. These included slips in the clevises of the actuator, slips between the steel base beam and the strong floor, slips between the foundation and the steel base beam, slips at the base of the reconfigurable reaction wall (RRW), and deformations at the top of the RRW. During the Wall 1 tests, only the slips on the NE and NW sides of the actuator clevises were measured. This is not as robust as when slips were measured on all sides of the actuator clevises for the Wall 2 tests. When the gaps in the clevis opened and closed (movement in the east and west directions), there was motion in the north and south directions also. This contributed to some out-of-plane motion of the wall since the actuator was not pushing uniformly upon load reversals.

Additionally, during the Wall 1 tests, the deformations of the top of the RRW were not monitored, but the slip on the north and south sides of the base of the RRW was monitored. For the Wall 2 tests, the deformations of the top of the RRW were measured on the north and south sides. As mentioned in Section 5.6, the motion of the RRW was calculated at the 11 foot, 7 inch (3.53 m) actuator height using a linear relationship based on motion at the top of the RRW. This is what will be displayed in the figures below. The slips for the BDBE motions for both walls will be presented here and the slips for the other smaller ground motions will be included in

120

Appendix B. The clevis slips were on the order of 10^-2, whereas all other slips were on the order of 10^-3 in or 10^-4 in. Figure 6.75 shows the slips for the Wall 1 BDBE motion.
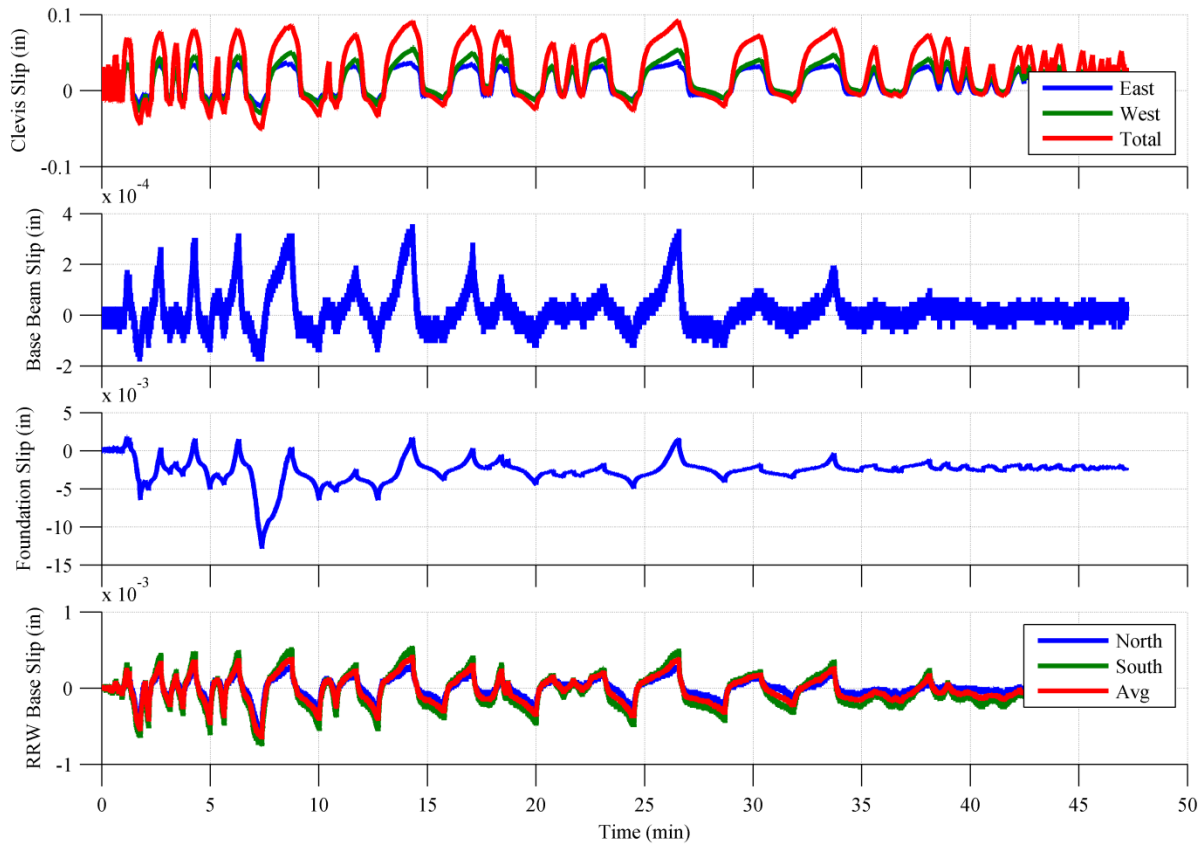
Figure 6.75: Wall 1 BDBE Test Setup Slips

Figure 6.76 shows the slips in the clevises for the Wall 2 BDBE motion, and Figure 6.77 shows the slips in the rest of the test setup for the Wall 2 motion. The total average clevis slip is as much as 7 times larger than the deformation of the RRW at the actuator level. The other slips are negligible in comparison.
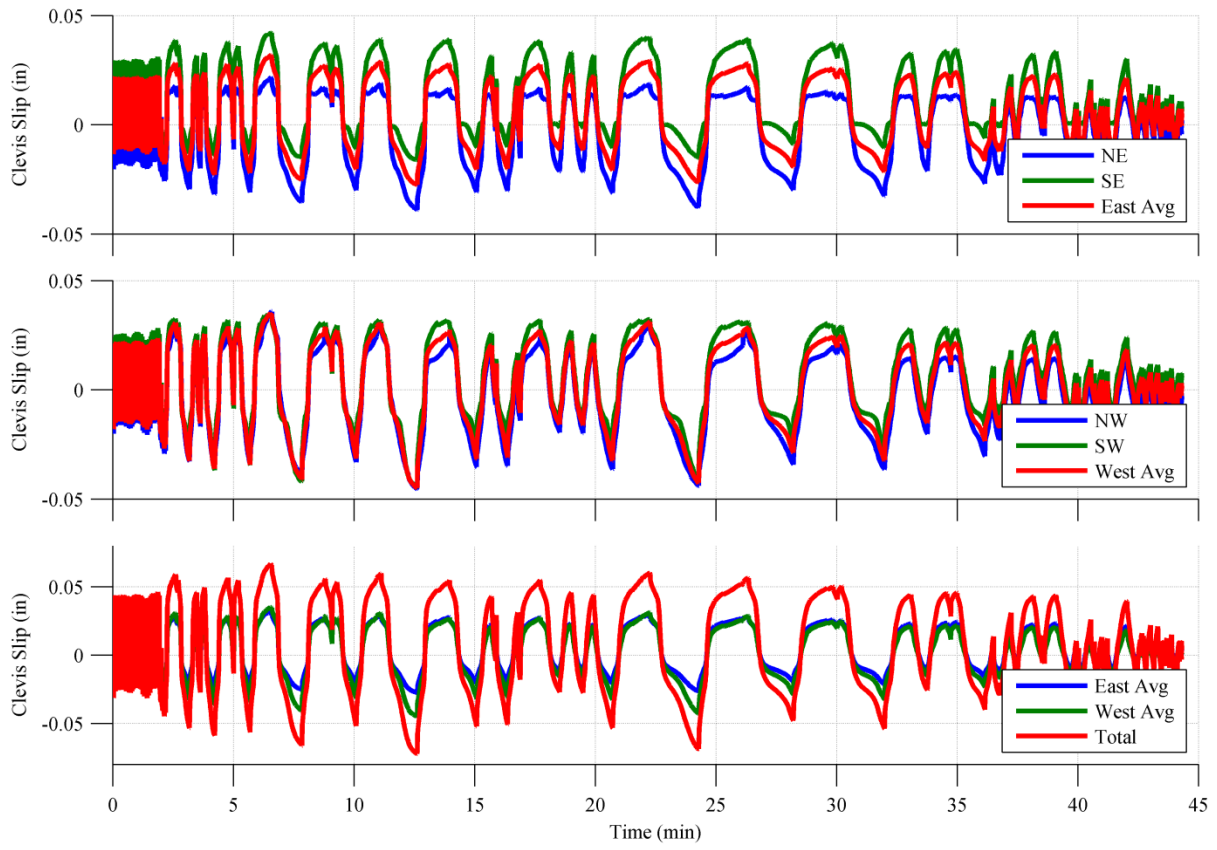
Figure 6.76: Wall 2 BDBE Clevis Slips
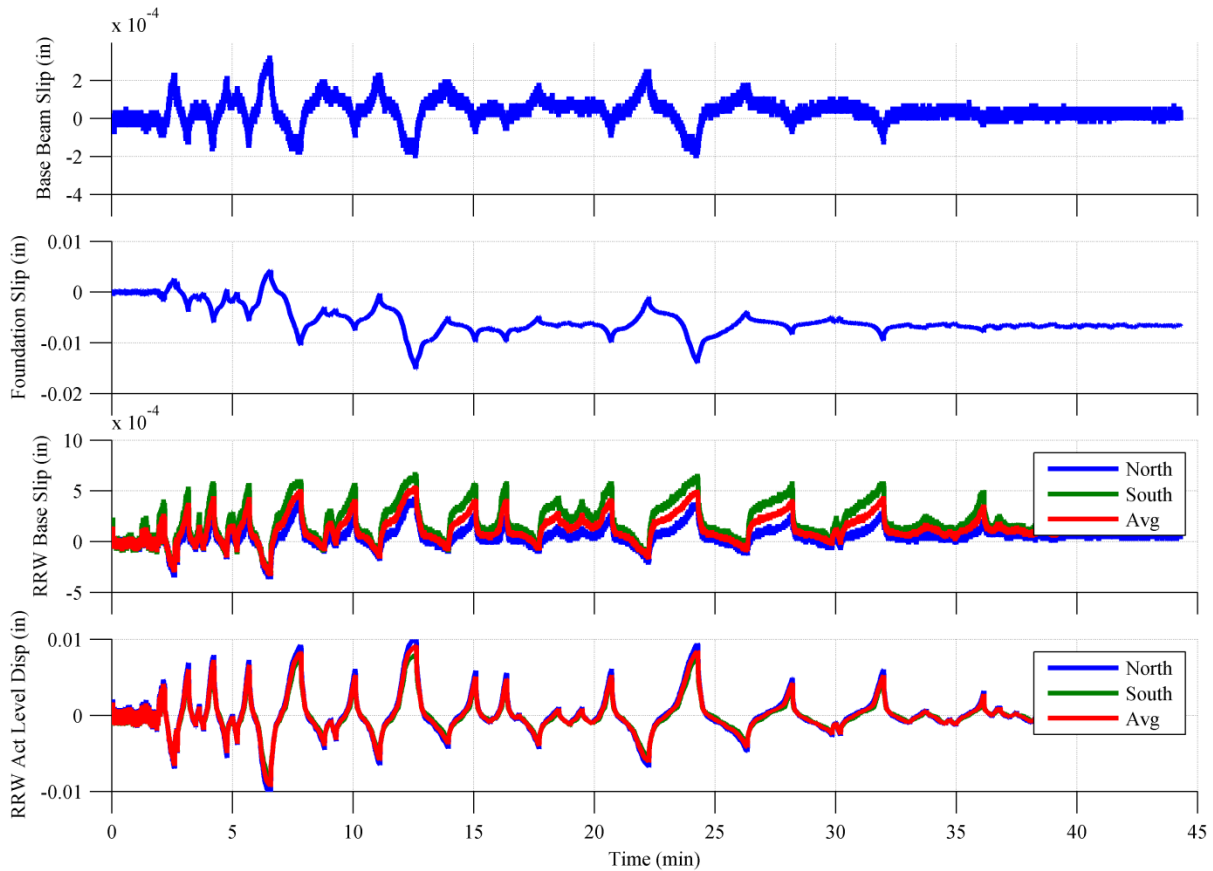
Figure 6.77: Wall 2 BDBE Test Setup Slips

As mentioned above, the slips in the clevises were not uniform, so the walls experienced some out-of-plane motion.   The Wall 1 BDBE Motion in-plane and out-of-plane displacements measured using triangulation at points along the height of the east side of the wall are shown in Figure 6.78 and in Figure 6.79 for points along the west side of the wall. The displacements measured on the west side of the wall do not have measurements at actuator height, since the actuator was attached to the west side. The positive in-plane displacements are the actuator pulling the wall to the west; the positive out-of-plane displacements are the wall moving to the north. The residual displacements were in-plane to the east. The east side of the wall was moving out-of-plane to the north, and the west side of the wall was moving out-of-plane to the south. There was a slight twisting behavior.
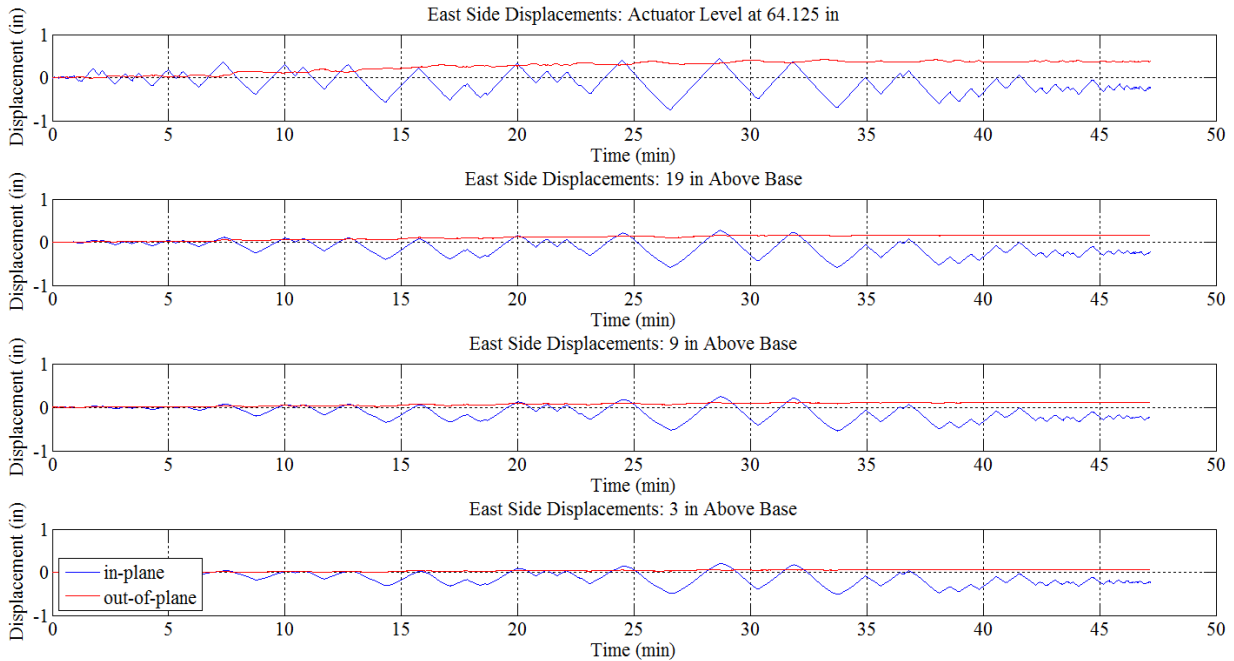
Figure 6.78: Wall 1 East Side Displacements
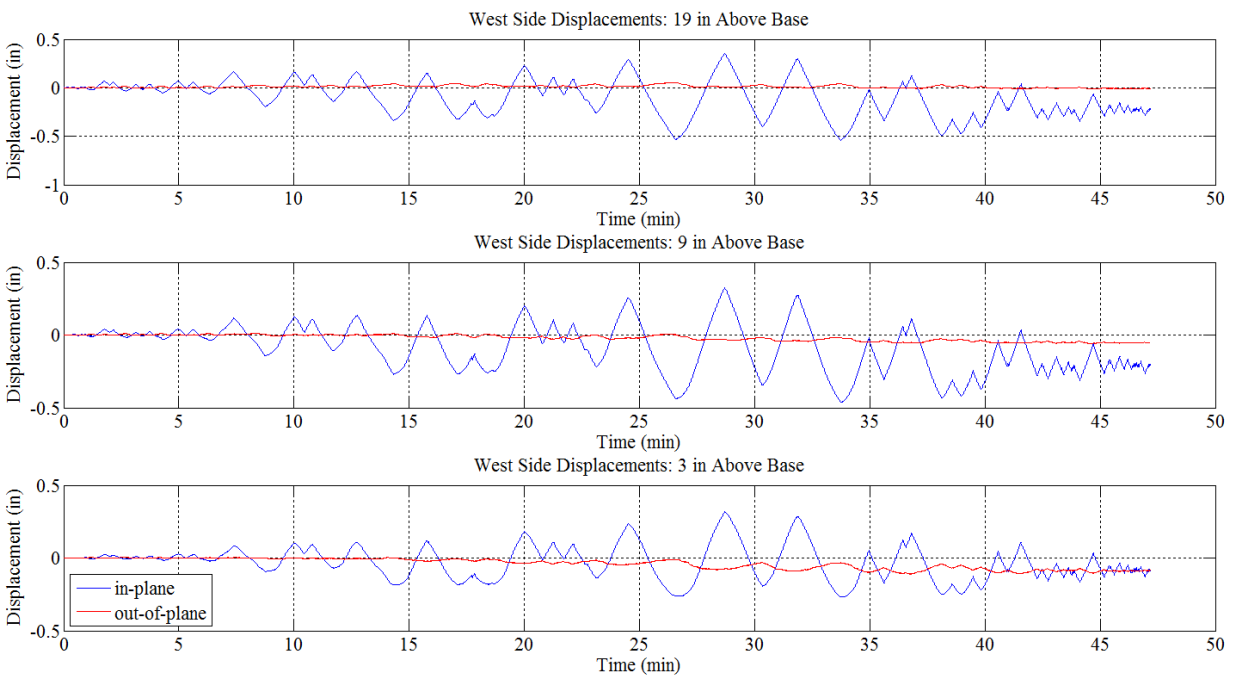
Figure 6.79: Wall 1 West Side Displacements

The corresponding plots for the Wall 2 BDBE Motion are shown in Figure 6.80 and Figure 6.81. Opposite behavior is observed for Wall 2 compared to Wall 1 since the ground motion sign was reversed. The positive in-plane displacements are the actuator pulling the wall to the west; the

124

positive out-of-plane displacements are the wall moving to the north. The residual displacements were in-plane to the west. The east side of the wall was moving very slightly out-of-plane to the north, and the west side of the wall was moving very slightly out-of-plane to the south. There was a slight twisting behavior, but less than during the Wall 1 BDBE motion. This can be explained by Wall 2 being less damaged at the time of this motion, so it retained more stiffness to resist out-of-plane motion. Appendix C shows similar in-plane and out-of-plane displacements for the remaining ground motion runs.
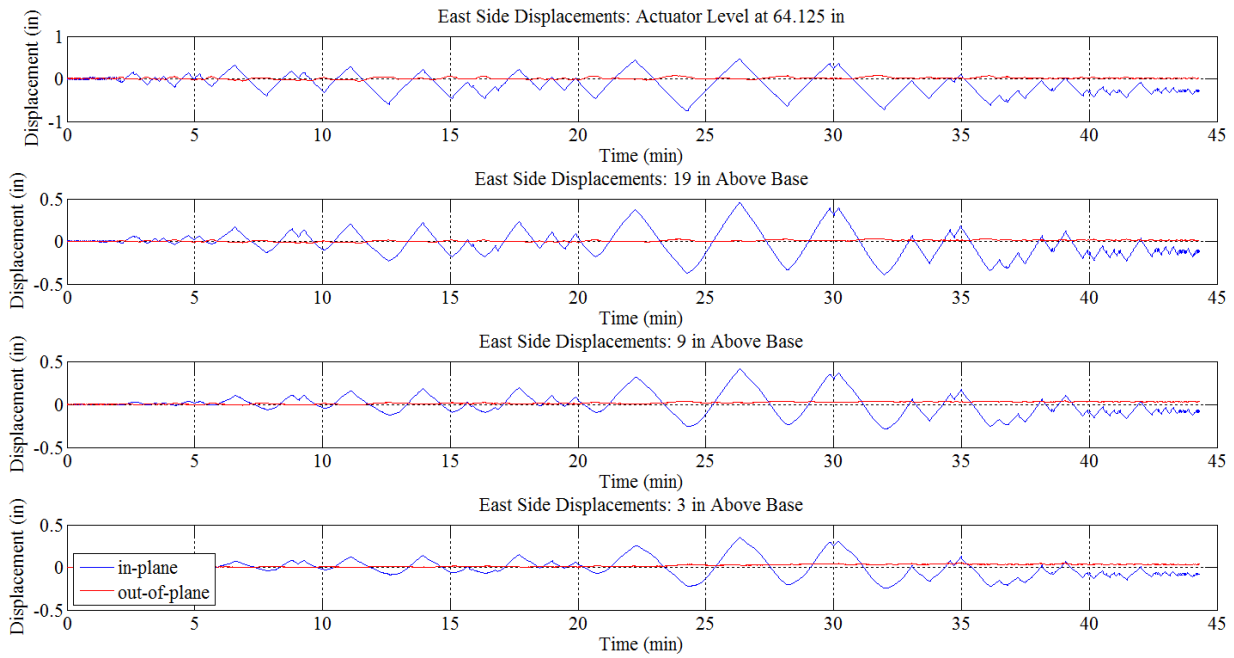
Figure 6.80: Wall 2 East Side Displacements
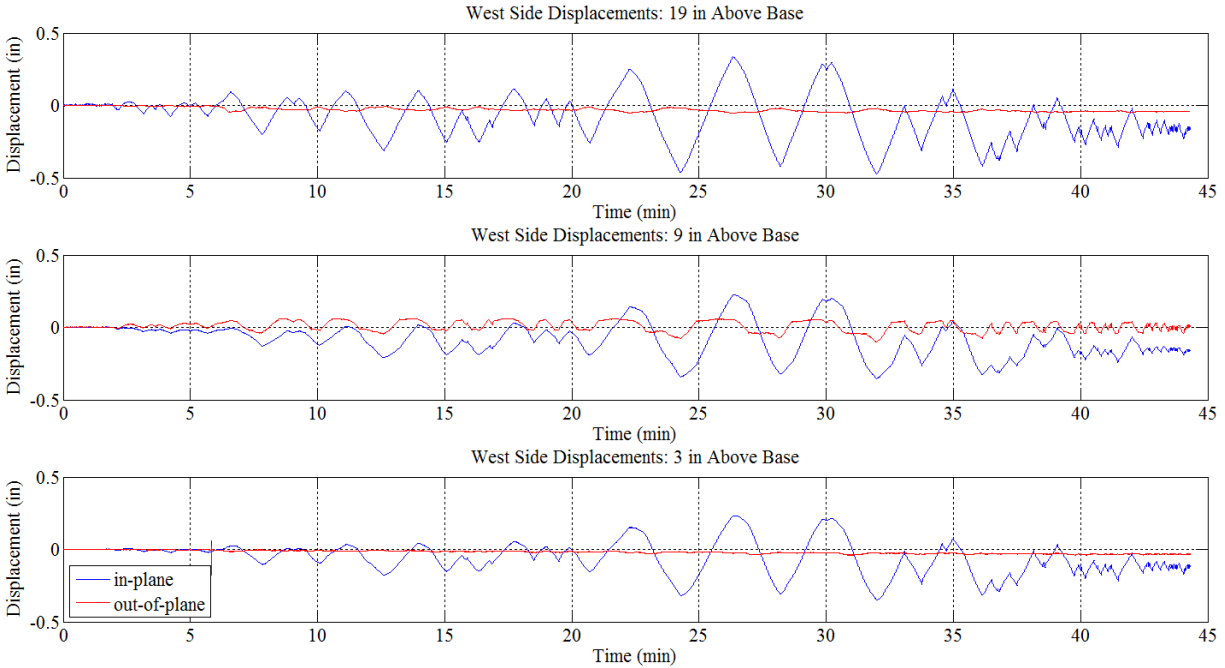
Figure 6.81: Wall 2 West Side Displacements

6.8   HYBRID   SIMULATION   ERRORS   IN   SERVO-HYDRAULIC   CONTROL SYSTEM

Since all measurements were made relative to the foundation, the clevis slips and other smaller slips in the test setup did not distort the measurements of the wall responses. However, the clevis slip did introduce hybrid simulation errors since the actuator was not able to produce the exact commanded displacements. Hybrid simulation error in the servo-hydraulic control system is investigated as the difference between the command and feedback displacements, since ideally the actuator should be able to produce the displacements commanded to it.

The majority of the errors occurred when the actuator changed directions. For instance, if the actuator was pushing the wall, the gaps in the clevises would be closed. When the actuator changed directions, first it pulled the clevis gaps open, and then the wall began to move. This behavior is evident in all of the force-drift response plots. For example, the Wall 1 DBE Aftershock 1 force-drift response plot is repeated below in Figure 6.82, with this behavior circled. As the displacement reached a peak value and then changed directions, the force was seen to drop suddenly over no displacement increment. This is because the clevis gaps were either opening or closing, but the wall itself was not yet moving.

126
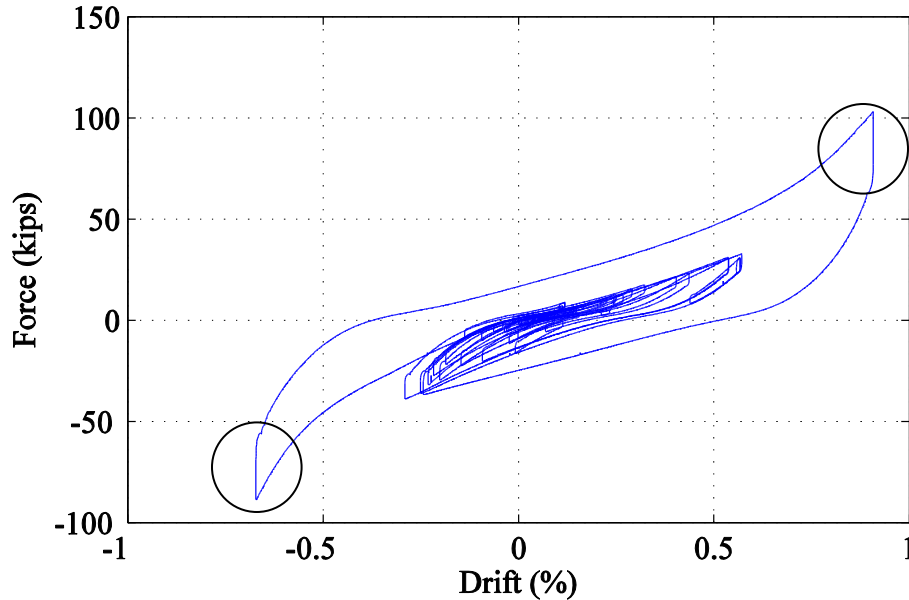
Figure 6.82: DBE Aftershock 1 Force-Drift Response

Using the constant velocity model for hybrid simulation minimized errors as much as possible. The clevises slipped when the actuator changed directions, but they remained stable when the actuator was moving at a constant velocity. The tracking between command and feedback displacements at constant velocity was good. Figure 6.83 shows the displacement tracking and corresponding error for the Wall 1 BDBE motion, and Figure 6.84 shows the displacement tracking and corresponding error for the Wall 2 BDBE motion. The maximum displacement error in the BDBE motion was 0.010 in for Wall 1 and 0.013 in for Wall 2. This is equivalent for approximately 1.18% of the maximum displacement for Wall 1 and 1.61% for Wall 2. The displacement tracking and error plots use the same sign convention for both Wall 1 and Wall 2. Positive is when the actuator is pulling the wall. The displacements are generally increasing for Wall 1 and generally decreasing for Wall 2, because the ground motion for Wall 2 was negated compared to Wall 1. The error is slightly higher when the actuator is pushing than pulling. Additionally, the error spikes significantly every time the actuator changes directions, as addressed above.
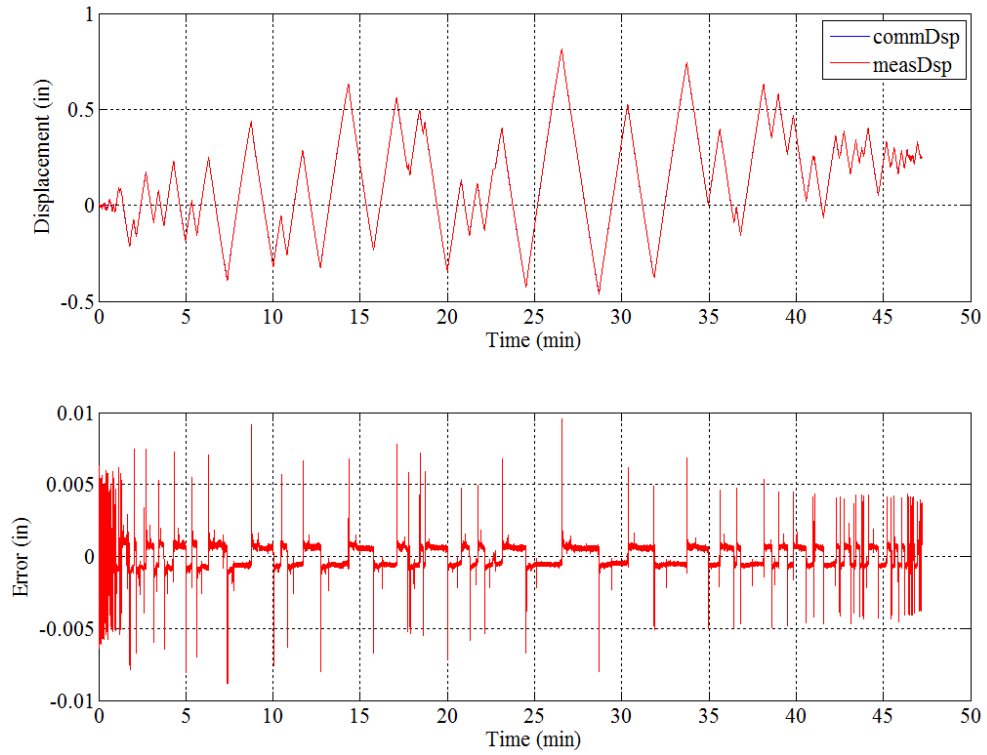
Figure 6.83: Displacement Tracking for Wall 1 BDBE motion
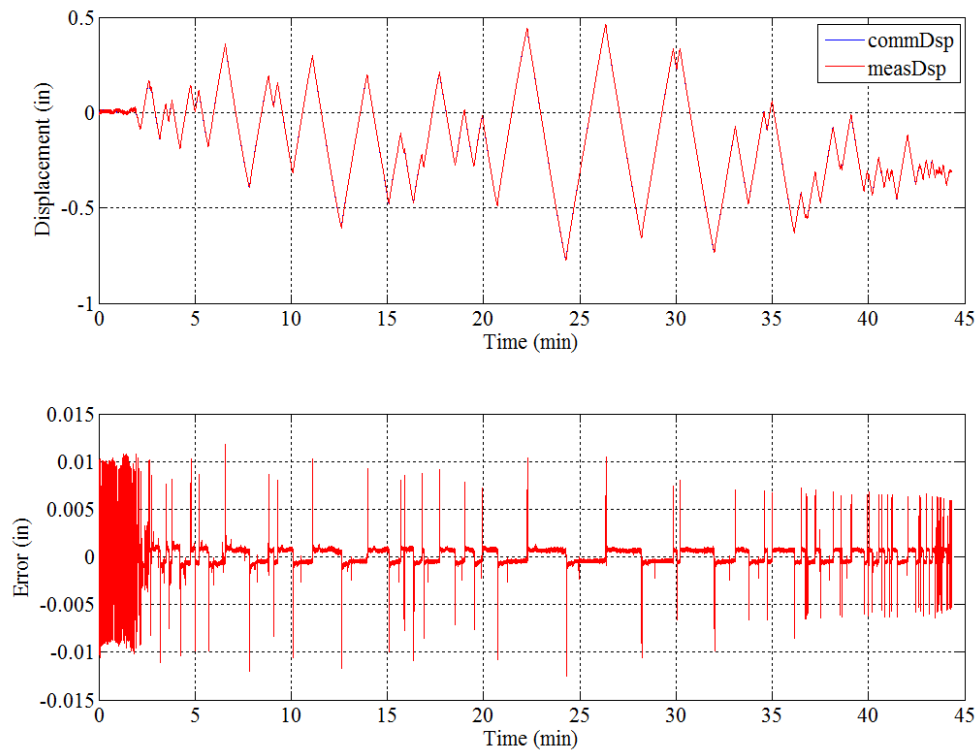
Figure 6.84: Displacement Tracking for Wall 2 BDBE motion

128

Synchronization subspace plots, developed by Mercan (Mercan 2007), show the actuator measured displacement vs. the actuator commanded displacement. Perfect tracking would be a line at a 45 degree angle, where measured and commanded displacements are exactly equal. The corresponding tracking indicator plots, also developed by Mercan (Mercan 2007), measure the accumulation of area enclosed in the hysteresis loops of the synchronization subspace plots. Figure 6.85 shows the Mercan plots for Wall 1, and Figure 6.86 shows the Mercan plots for Wall 2. In both cases, the synchronization subspace plots are showing very good behavior, and the measured and command displacements match well. The tracking indicator is decreasing, so the displacement response is lagging slightly and energy dissipation is negative. The energy dissipation is still quite small and the servo-hydraulic control system performed well.
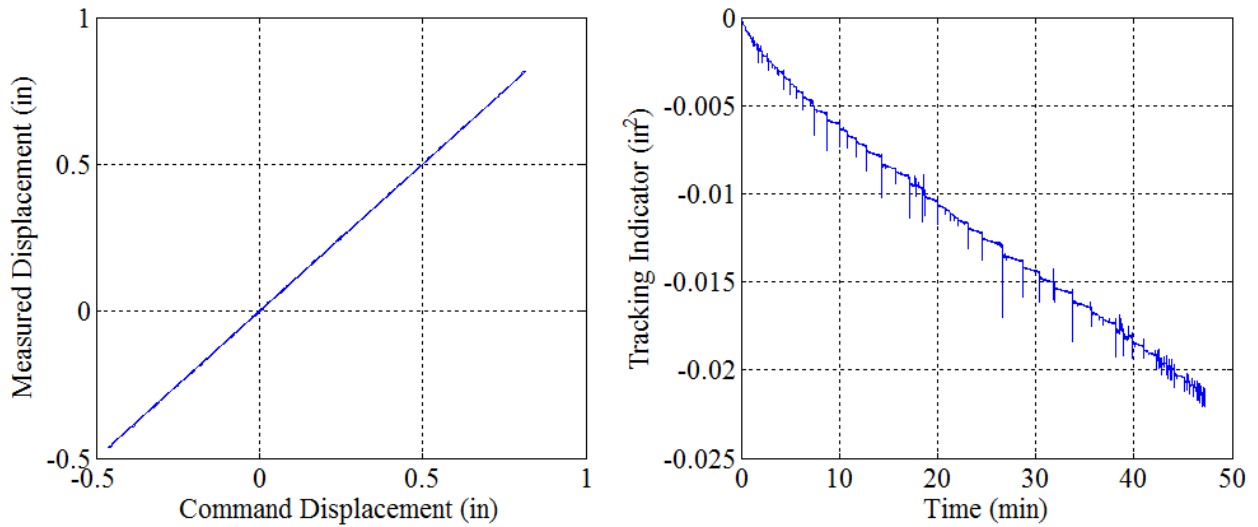
Figure 6.85: Wall 1 Mercan Plots
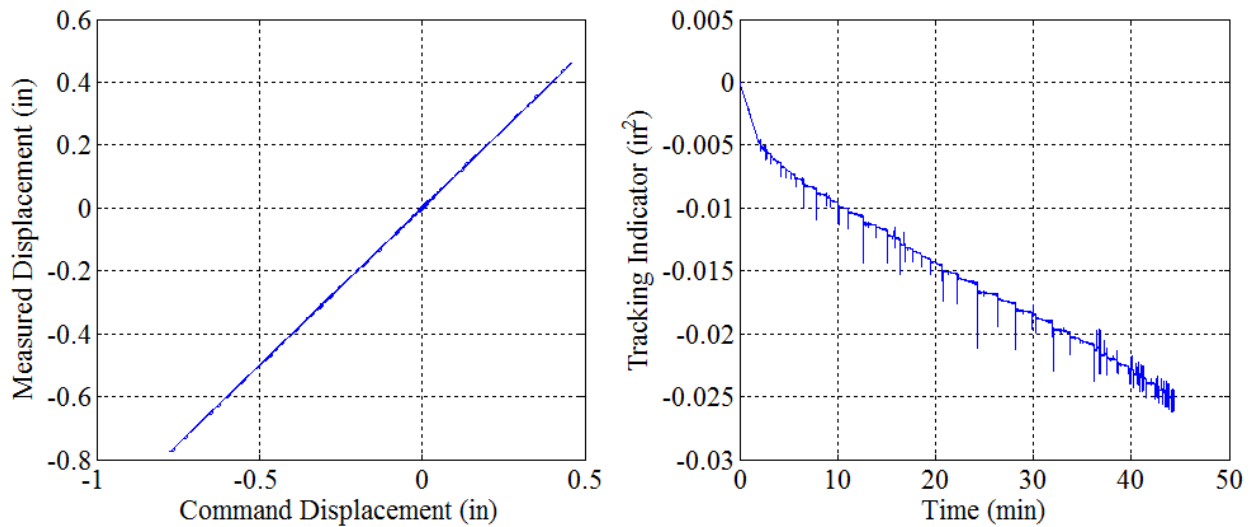
Figure 6.86: Wall 2 Mercan Plots

129

6.9   SUMMARY

The results from the two squat shear wall tests were presented in this chapter. The responses of Wall 1 and Wall 2 were addressed separately and then compared. The wall displacements were separated into components of shear flexure, rotation in the sliding zone, and base sliding. The percentage contribution of each component was analyzed. This was successful to understand the general trends, but there was significant error due to measurements of small displacements for stiff specimens. The code equations from Chapter 2 were evaluated for their ability to predict the peak shear strength of the walls. Generally, the equations significantly overestimated the observed responses. Wood's (1990) equation provided the closest fit to the observed data. The Wallace (2006) backbone curve was evaluated, and recommendations were made for adjusting the initial stiffness of this relation. Recommendations were also made for a definition of the "essentially elastic" range. Finally, the test setup response and hybrid simulation errors were presented.

7 Comparison of Ground Motion Hybrid Simulations to Quasi-static Cyclic Results

7.1 INTRODUCTION

This short chapter focuses on comparing the global behavior of Wall 1 and Wall 2, tested at Berkeley in hybrid simulation of their seismic response, to the nominally identical wall tested at Buffalo using quasi-static cycles. Following an introduction to the testing program at Buffalo, the global force-drift response behavior of the walls is compared. Then, the adequacy of code equations for predicting peak shear strengths and the recommended provisions for initial stiffnesses for modeling purposes are evaluated.

7.2 BUFFALO SPECIMENS

At University at Buffalo, 12 squat walls with varying aspect ratios and reinforcement ratios were tested using quasi-static cyclic loading patterns. One of the walls was identical in design to the walls tested at Berkeley. This provided an opportunity to directly compare the two data sets and judge whether quasi-static cyclic testing adequately captured the ground motion sequence response.

The Buffalo Wall had the following properties: aspect ratio of 0.54, 0.67% horizontal and vertical reinforcement, concrete compressive strength of 7800 psi (53.8 MPa), and reinforcing bar yield stress of 63 ksi (434.4 MPa). The test setup is shown in Figure 7.1. The loading protocol, shown in Table 7.1, was commanded to the specimen at a loading rate of 0.004 in/s (0.102 mm/s) (Rocks et al. 2011). No vertical load was applied to the Buffalo wall.
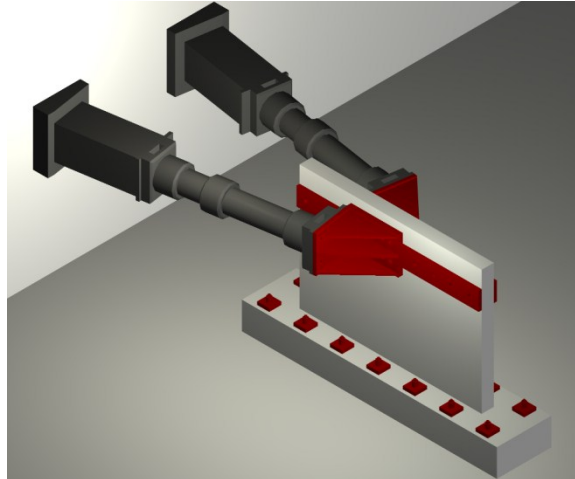
Figure 7.1: University at Buffalo Test Setup (Luna 2012)

Table 7.1: Buffalo Loading Protocol

Load Step	Peak Deformation cm (in)	Number of Cycles
LS1	0.089 (0.035)	3
LS2	0.178 (0.07)	2
LS3	0.254 (0.1)	2
LS4	0.381 (0.15)	2
LS5	0.508 (0.2)	2
LS6	0.635 (0.25)	2
LS7	0.762 (0.3)	2
LS8	1.016 (0.4)	2
LS9	1.270 (0.5)	2
LS10	1.905 (0.75)	2
LS11	2.540 (1)	2
LS12	3.810 (1.5)	2
LS13	5.080 (2)	2

Photographs of the Buffalo Wall at the first peak of load steps 11, 12, and 13 are shown in Figure 7.2.

(a)   (b)

(c)
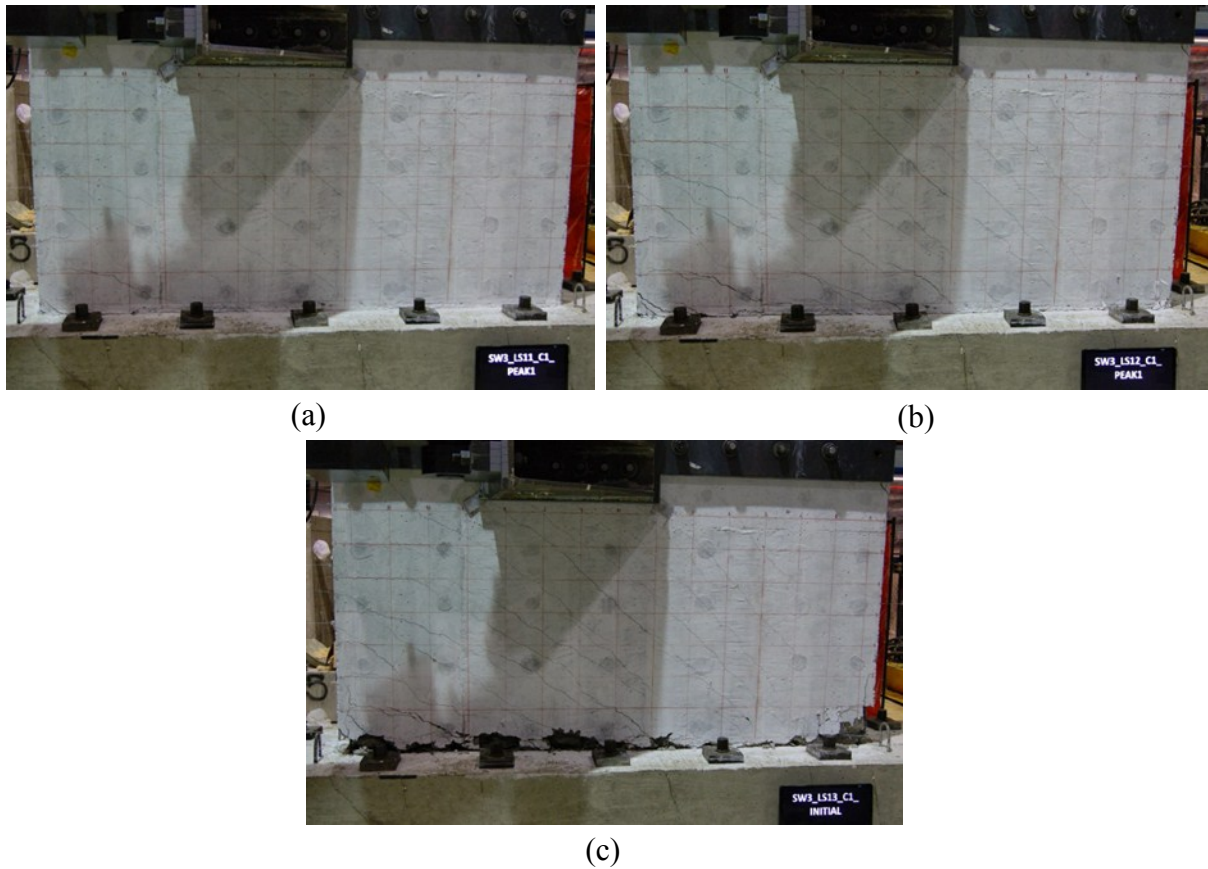
Figure 7.2: Buffalo Wall at First Peak of (a) LS 11, (b) LS 12, and (c) LS 13

The cracking pattern very closely resembled the cracking pattern observed in the Berkeley walls. In Figure 7.2 (a), the wall exhibited shear cracking and some flexural cracking toward the lower edge of the wall. In (b), the cracks widened and the flexural cracks had become more dominant. Sliding has also begun along the base of the wall. In (c), the wall experienced extensive damage due to sliding, and much of the concrete along the base of the wall was lost.

7.3   COMPARISON OF THE BERKELEY AND BUFFALO WALLS

In order to compare the cracking patterns, the photograph of the Buffalo Wall at the first peak of load step 12 is repeated in Figure 7.3 along with the Berkeley Wall 1 at the end of the BDBE ground motion.

| (a) | (b) |
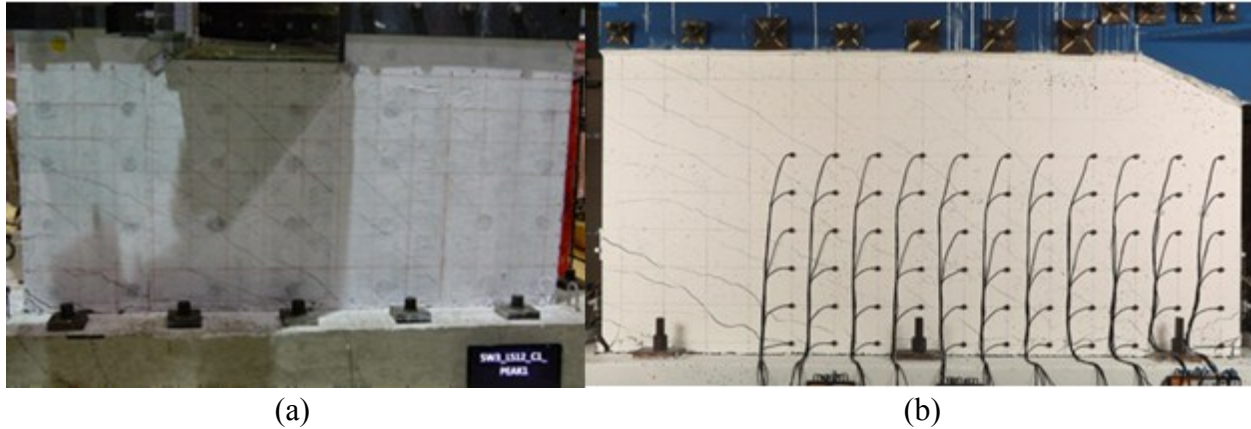
Figure 7.3: (a) Buffalo Wall at First Peak of LS 12 and (b) Berkeley Wall 1 at End of BDBE Motion

It is important to recognize that the cracks in the Berkeley Wall 1 were enhanced using edge detection for better visibility, so the pictures in Figure 7.3 serve only to compare the crack pattern, not the crack widths. Also, the walls had experienced different motions and different total displacements, so it is difficult to make a direct comparison at a specific point. Regardless, Figure 7.3 displays a remarkable similarity in the locations of the shear cracks (both spacing and angle), and in the locations of the flexural cracks and their severity, relative to the shear cracks. Furthermore, the crack patterns between Berkeley Wall 1 and Wall 2 were also very similar, so there is consistency between the three walls. This is a visual indication that the quasi-static cyclic test captured the behavior observed in the ground motion sequences.

The final cycles experienced by the Buffalo Wall were +/- 2 in in load step 13. The maximum cycles experienced by both of the Berkeley walls were to +/- 1.5 in, consistent with the Buffalo wall load step 12. Table 7.2 investigates the total displacement that each of the walls experienced. In the case of the Berkeley walls, these total displacements excluded the pre-test stiffness and free vibration runs, which were all very small displacements.

Table 7.2: Cumulative Displacements Experienced by Each of the Walls

	Wall 1	Wall 2			Buffalo
End of BDBE	49.0 in	34.4 in		LS11 Peak 1	23.2 in
				LS 11 End	30.2 in
End of GM	60.9 in	56.5 in		LS 12 Peak 1	31.7 in
				LS 12 End	42.2 in
End of Cycles	75.3 in	66.7 in		LS 13 Peak 1	44.2 in
				LS 13 End	58.2 in

It is difficult to directly match to the Buffalo load steps the end of the Berkeley BDBE, the end of the Berkeley ground motions (GM), and the end of the Berkeley Cycles. Berkeley Wall 1 experienced a greater displacement than Berkeley Wall 2, partly because the DBE motion was originally scaled too small and then repeated with the larger scaling. The discrepancy in the end of BDBE displacements was also because Wall 2 experienced its BDBE earlier in the ground motion sequence than Wall 1. The end of the Berkeley Wall 2 BDBE motion approximately matched the displacement of Buffalo LS 12 Peak 1; the end of the Berkeley Wall 1 BDBE

motion approximately matched the displacement of Buffalo LS 12 End. The end of the Berkeley ground motions approximately matched the displacement of Buffalo LS 13 End. When the Buffalo Wall had been pushed to +/-2 in, the Berkeley walls had not yet experienced half of that displacement; however, the Berkeley walls had experienced many more smaller cycles, so they had similar total displacements. Finally, the end of the Berkeley wall cycles showed more displacement than the Buffalo wall had experienced.

Figure 7.4 shows the force-deformation response of the three walls, with the shear strength normalized by the product of wall area and $\sqrt{f'_c}$ vs. drift. The Berkeley OBE motions are compared to Buffalo Load Steps 1-2. The DBE motion for Wall 1 (Wall 2 did not experience this motion) is compared to Load Steps 3-6. The Berkeley BDBE motions are compared to Load Steps 7-11. Finally, the DBE Aftershocks and Cycles are compared to Load Step 12.
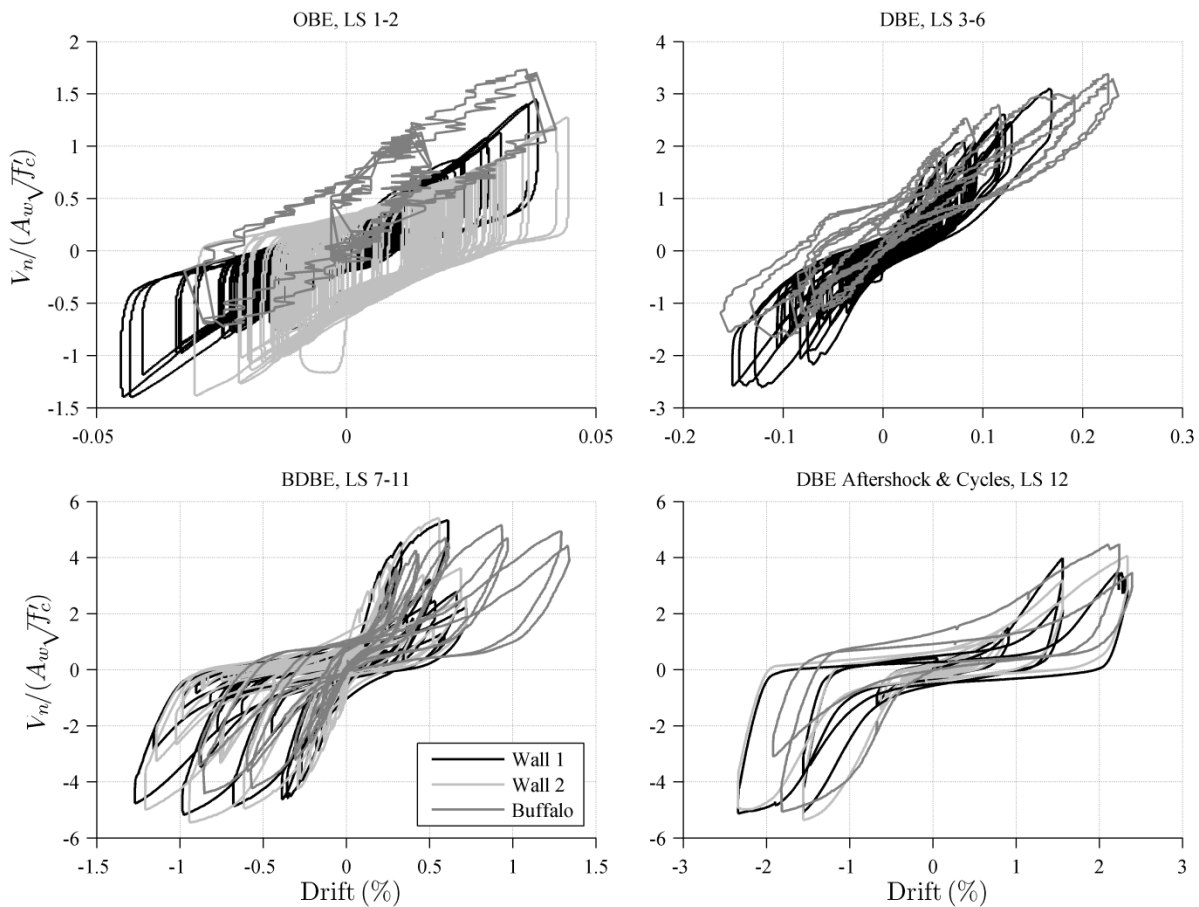
Figure 7.4: Normalized Shear Strength vs. Drift Response for Berkeley Walls 1 and 2 and the Buffalo Wall

The BDBE comparison of shear strength normalized by the product of wall area and $\sqrt{f'_c}$ vs. drift is repeated in Figure 7.5 for better viewing.
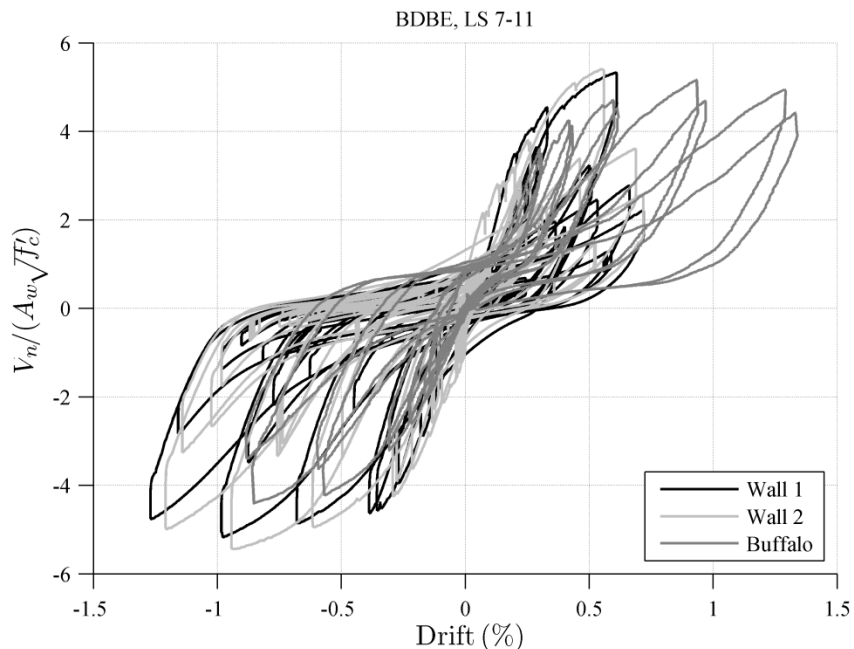
Figure 7.5: Berkeley BDBE Compared to Buffalo LS 7-11 Normalized Shear Strength vs. Drift Response

The Buffalo Wall did not show the asymmetry that was displayed by the Berkeley specimens in the ground motion sequence response simulations. Thus, the Buffalo Wall achieved a slightly larger drift in the positive direction and a drift comparable to the Berkeley walls in the negative direction. The Buffalo Wall experienced higher peak strengths than the Berkeley walls, but it also had a larger concrete compressive strength, so its normalized shear strength was slightly lower than that of the Berkeley walls. The Buffalo Wall hysteresis showed more pinching than that of the Berkeley walls. This is likely a result of greater slip in the Berkeley actuator clevises. In general, the three walls showed very similar force-deformation global behavior and a similar failure mode sequences.

Table 7.3 summarizes the yield and maximum displacements and forces for each wall in each direction. The positive direction corresponds to the positive direction in Figure 7.4.

Table 7.3: Summary of Berkeley and Buffalo Displacements and Forces at Key Points

	direction	yield disp (in)	yield drift (%)	yield force (kips)	yield shear stress (ksi)	disp at max force (in)	drift at max force (%)	max force (kips)	max shear stress (psi)
Wall 1	+	0.21	0.33	312.2	4.53√f'c	0.39	0.61	366.4	5.32√f'c
	-	-0.25	-0.39	-319.6	-4.64√f'c	-0.62	-0.97	-356.9	-5.18√f'c
Wall 2	+	0.16	0.25	271.9	3.85√f'c	0.35	0.55	384.7	5.45√f'c
	-	-0.19	-0.30	-297.7	-4.21√f'c	-0.61	-0.95	-382.1	-5.41√f'c
Buffalo	+	0.29	0.45	330.9	3.90√f'c	0.49	0.75	380.9	4.49√f'c
	-	-0.3	-0.46	-340.6	-4.02√f'c	-1.36	-2.09	-468.2	-5.52√f'c

136

Table 7.4 summarizes the stiffnesses (K) for the Berkeley and Buffalo Walls. The Wall 1 and Wall 2 measured initial stiffnesses were determined using the acceleration data recorded in the first successful free vibration tests.

Table 7.4: Summary of Stiffnesses, K

	Measured Initial K (kip/in)	Theoretical "uncracked" (kip/in)	ASCE 43-05 "cracked" (kips/in)	Secant K at peak resistance + (kip/in)	Secant K at peak resistance - (kip/in)	Secant+/ ASCE 43	Secant-/ ASCE 43
Wall 1	11261	17280	8640	939	576	0.11	0.07
Wall 2	8263	17724	8862	1099	626	0.12	0.07
Buffalo	10000	20805	10403	777	344	0.07	0.03

Table 7.5 summarizes the secant stiffnesses at increasing shear stresses, expressed as multiples of $\sqrt{f'c}$ psi, for the positive and negative directions of each wall. Figure 7.6 shows a plot of the stiffness vs. shear stress, expressed as a multiple of $\sqrt{f'c}$ psi, for the average values for each wall.

Table 7.5: Secant Stiffnesses at Increasing Shear Stresses (psi)

	Wall 1 +	Wall 1 -	Wall 2 +	Wall 2 -	Buffalo +	Buffalo -
Theoretical	17280	17280	17724	17724	20805	20805
Initial	11261	11261	8263	8263	10000	10000
$\sqrt{f'c}$	2971	3081	2082	3721	4965	2540
$2\sqrt{f'c}$	2496	3024	1973	1963	3388	1751
$3\sqrt{f'c}$	1856	1839	1919	1705	1897	1367
$4\sqrt{f'c}$	1481	1498	1441	1432	1207	997
$5\sqrt{f'c}$	1031	634	1203	742	697	365
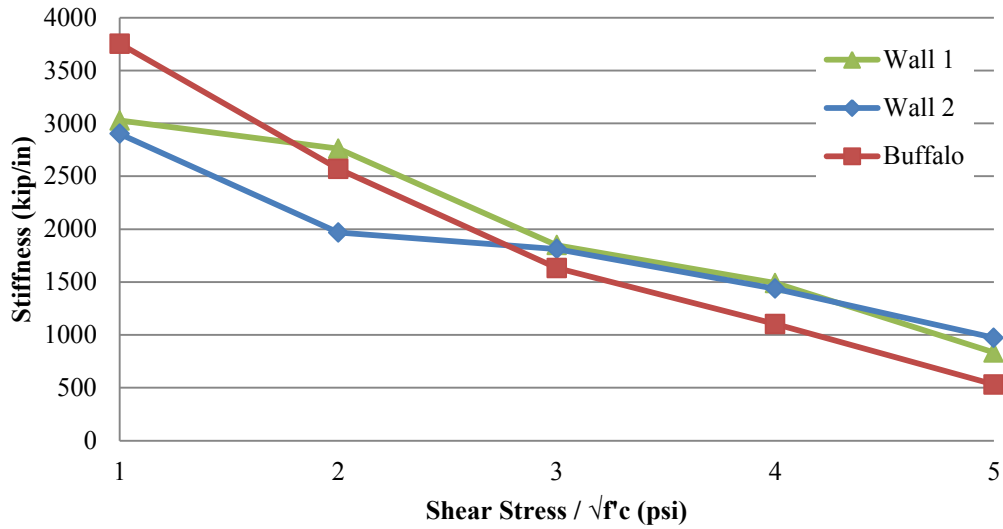
Figure 7.6: Stiffness vs. Shear Stress (Expressed as Multiple of √f'c)

These stiffnesses are normalized by the modified initial stiffness of 30% of the Wallace recommended value (now G=0.3*0.4*E_c) in Figure 7.7.
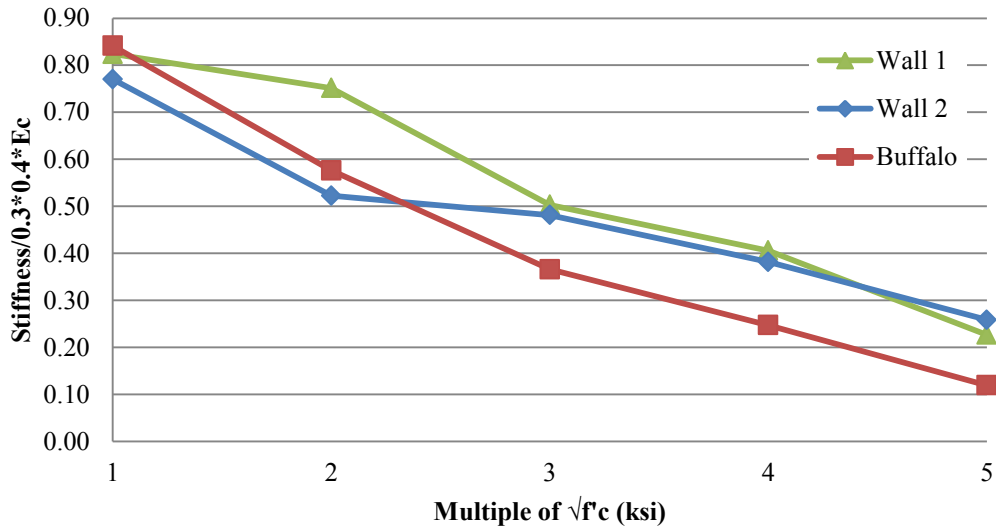
Figure 7.7: Normalized Stiffness vs. Shear Stress (Expressed as Multiple of √f'c)

Figure 7.8 shows the process of selecting values for calculating the strength degradation ratios. V1 is taken as the shear strength at peak force. V2 is taken as the shear strength at the next excursion to the displacement corresponding to peak force. V3 and V4 are the shear strengths at the following two excursions to that displacement.   Table 7.6 summarizes the strength degradation ratios for each wall in both the positive and negative directions. The average values for each wall are plotted in Figure 7.9.
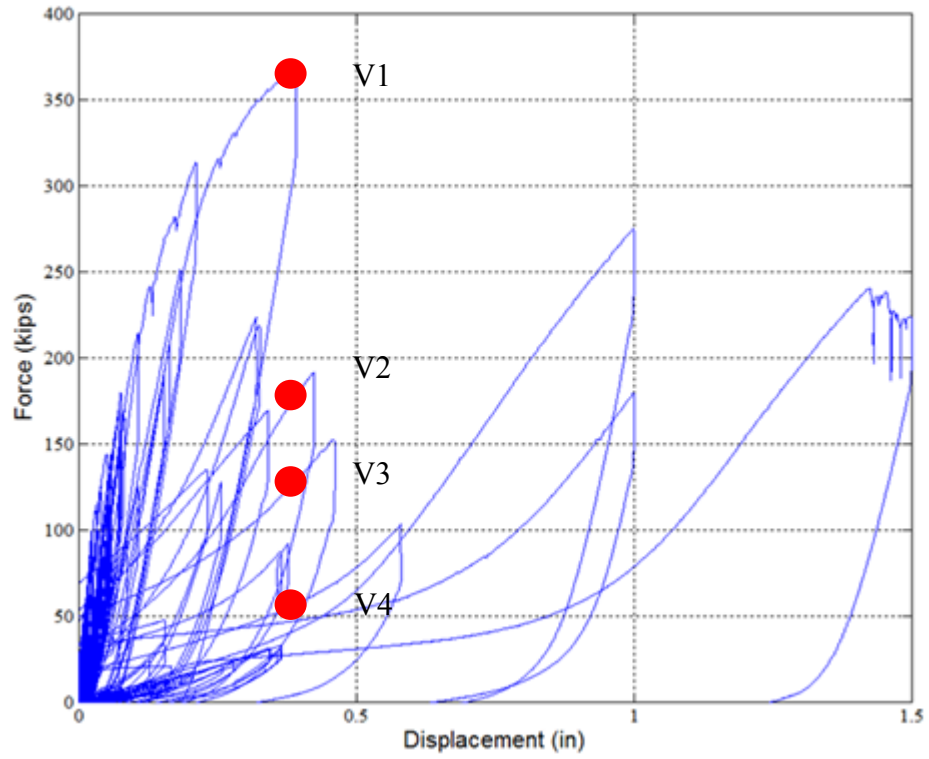
Figure 7.8: Selecting Values for Strength Degradation Calculation

Table 7.6: Strength Degradation Ratio for Each Wall and Each Direction

Specimen	V2/V1	V3/V1	V4/V1
Wall 1 +	0.49	0.35	0.15
Wall 1 -	0.65	0.34	0.26
Wall 2 +	0.59	0.39	0.18
Wall 2 -	0.73	0.40	0.36
Buffalo +	0.86	0.72	0.51
Buffalo -	0.60	0.42	0.13
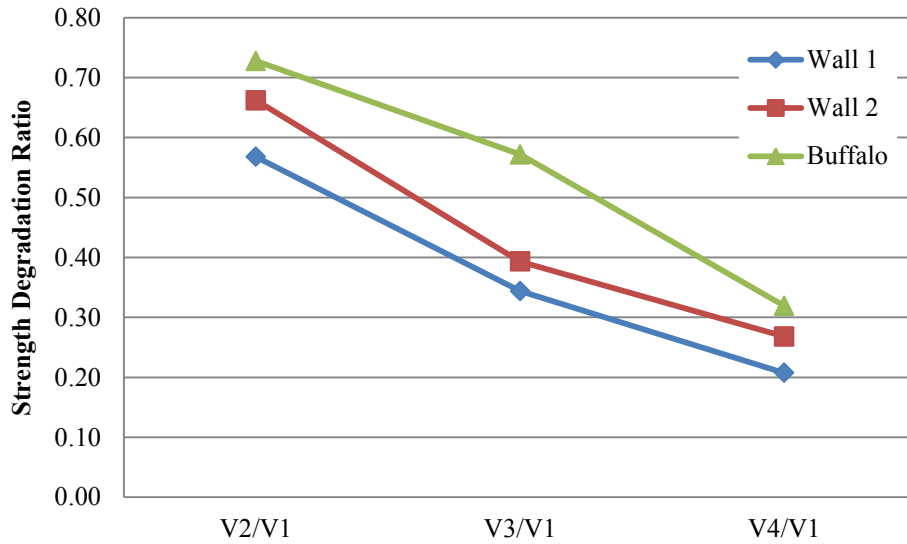
Figure 7.9: Average Strength Degradation for Each Wall

7.4   COMPARISON OF CODE EQUATIONS

Supplementing the comparisons in Chapter 6 of the predicted vs. measured strength of Wall 1 and Wall 2 using various code equations, Figure 7.10 shows the same data including the Buffalo wall.
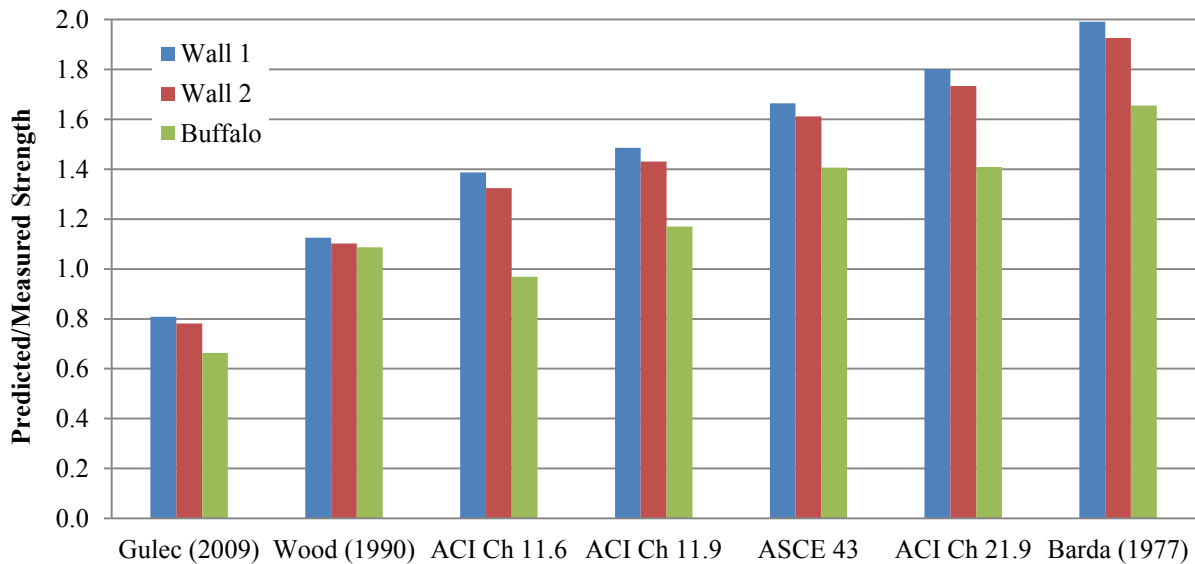
Figure 7.10: Ratio of Predicted to Measured Strengths for Code Equations

ACI Ch 11.6 made the best prediction of the strength of the Buffalo wall. Then Wood (1990) made the next best estimate for the Buffalo wall. The yield stress of the reinforcing bars in the Buffalo wall was 63 ksi; the yield stress of the reinforcing bars in the Berkeley walls were 70.7 ksi. As reviewed previously, Buffalo had a higher concrete compressive strength and thus achieved a larger peak force of 468 kips. Berkeley Wall 1 achieved a maximum of 367 kips, and Berkeley Wall 2 achieved a maximum of 384 kips. In general, the code equations predicted the strength of the Buffalo wall better than the Berkeley walls.

In Figure 7.11, the Wallace Envelope with the modified initial slope (30% of Wallace's recommendation) is shown along with the envelopes for the Wall 1, Wall 2, and Buffalo Wall responses. Since the Wallace Envelope is using Wood's equation for the Wall 1 peak strength, it slightly underestimates the Buffalo response.
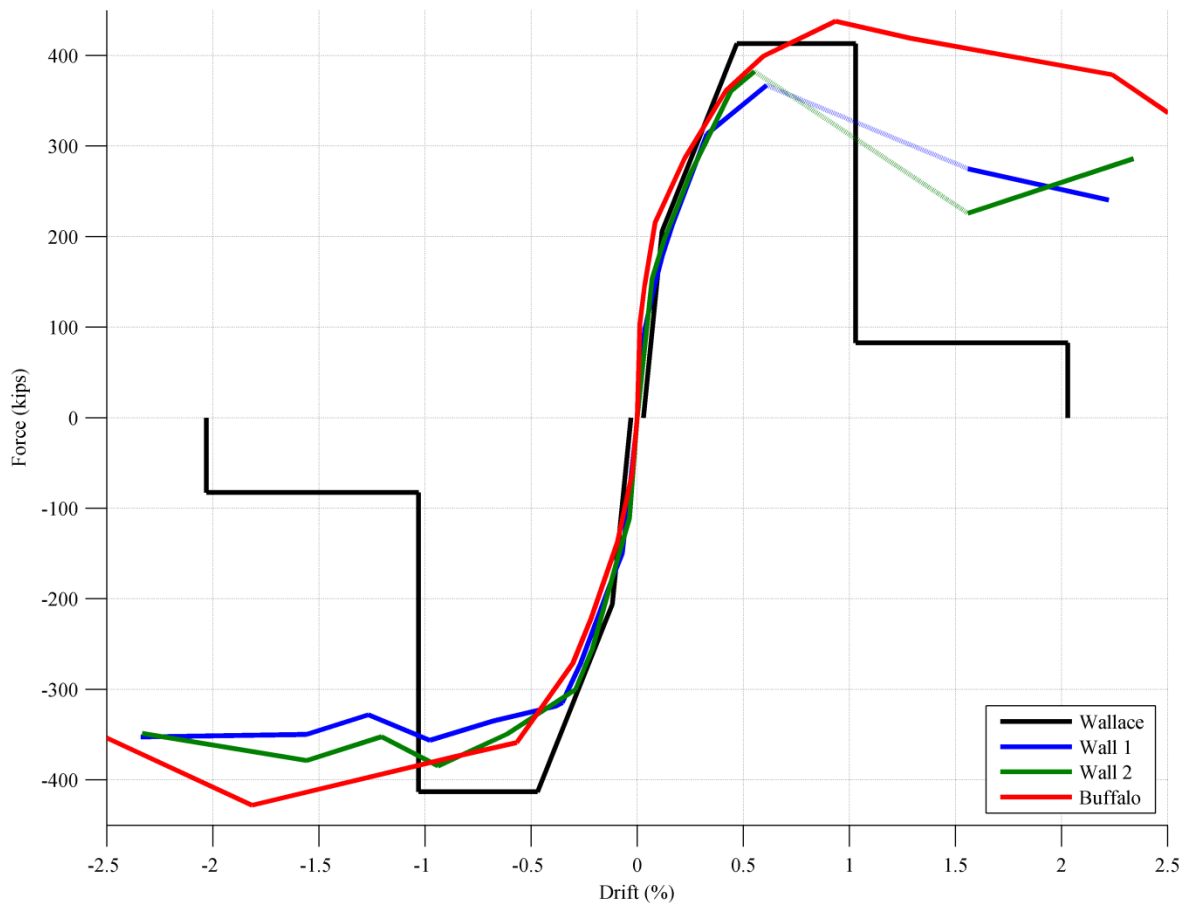
Figure 7.11: Wallace and Walls Envelopes

In Figure 7.12, the Wallace Envelope is shown with dotted lines resembling ASCE 43 LS-C, LS-B, and LS-A and the ASCE41 immediate occupancy (IO), life safety (LS), and collapse prevention (CP) drift limits. LS-C and IO have drift limit 0.4 (shown as 0.43 because of correction for base slip); LS-B has drift limit 0.6; LS-A and LS have drift limit 0.75; CP has drift limit 1. The LS-C and IO limit occurs just after the yield point of all of the walls. It is the only limit state remaining in the essentially elastic range. The LS-B and LS-A/LS limits occur prior

141

to peak strength for all of the walls in the negative direction, but they occur after the peak strength for Wall 1 and Wall 2 in the positive direction. Since this is due to the nature of the ground motion demand, a conclusion cannot be made about the implications of this. If the ground motion was stronger in the positive direction, Wall 1 and Wall 2 are likely to have behaved in a manner reflecting their behavior in the negative direction. At the LS-B and LS-A/LS limits, the Buffalo wall has yet to reach peak strength in the positive direction. Then, the CP limit occurs just after the walls reach peak strength, but significant strength degradation has not occurred. However, the CP limit is not applicable to nuclear facility walls.
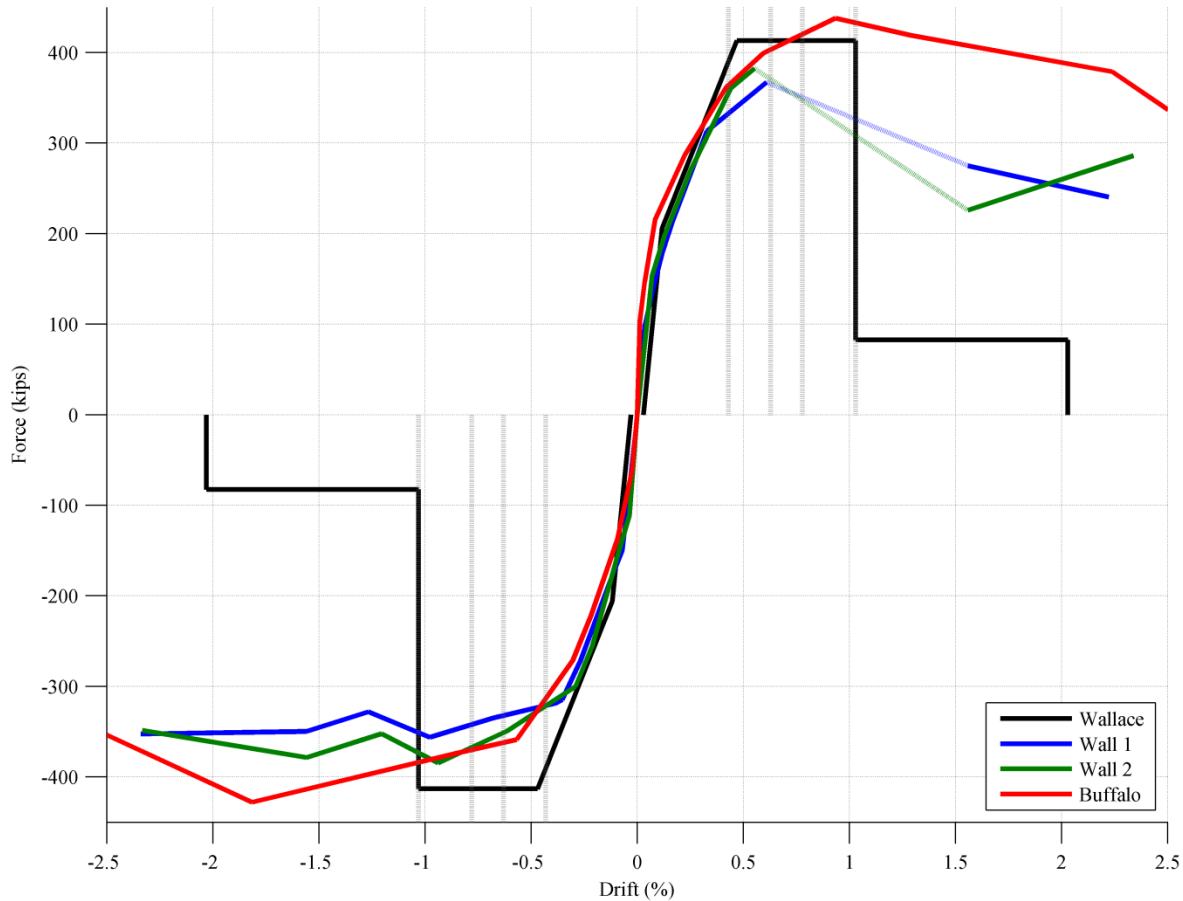
Figure 7.12: Envelopes with IO, LS, and CP

7.5   SUMMARY

The comparison of global responses between the Berkeley walls and the nominally identical Buffalo wall showed that the responses were very similar, and the quasi-static test was adequate to represent the global behavior of the squat shear walls in ground motion sequences. A comparison of local behavior was not possible in this study. The gain on the data acquisition system was set too high for the Berkeley Wall 1 test, so the strain gages were saturated at low strains. This did not allow for local strain comparisons beyond comparing when the gages

yielded, as shown in Chapter 6. The Buffalo wall strain gages were not placed in the same locations at for the Berkeley walls, so this comparison did not yield useful information.

The ability of code equations to predict the observed responses of the walls was analyzed. Wood's (1990) equation provided a very close estimate for all of the walls. The code-recommended initial stiffness values were also evaluated. This will be the subject of future research since it was very difficult to characterize the initial stiffness of the walls. The initial stiffnesses reported for Walls 1 and 2 were measured during the first successful free vibration tests. The walls had already experienced some amount of damage in the stiffness tests runs and the unsuccessful free vibration runs. Furthermore, it is very likely that microcracks were present in the walls prior to testing, which resulted from moving the walls into position for testing in the laboratory. Data for wall strength degradation was also presented and occurred quite rapidly for all of the walls in just four excursions to the displacement corresponding to peak force. Finally, the wall envelope responses for all three walls were compared to the modified Wallace (2006) backbone curve, as discussed in Chapter 6. With proposed modifications, the initial stiffness is well characterized for the three walls tested. Future studies will focus on better understanding the behavior of post-peak shear strength. The information from these three wall tests is not sufficient to draw conclusions about displacement capacities.

8 Analytical Modeling

8.1 DESCRIPTION OF OPENSEES ELEMENT

The OpenSees Flexure-Shear Interaction Displacement-Based Beam-Column Element, developed by Massone et al. (2006), was implemented and compared to the observed wall responses in the Berkeley hybrid simulations and the Buffalo cyclic test. In its current implementation, this element is monotonic.

The analytical model implemented is based on a Multiple-Vertical-Line-Element (MVLE) model, which is similar to a two-dimensional macroscopic fiber model. The MVLE model of a shear wall is composed of elements positioned vertically along the height of the wall. Each element is defined by a series of strips, as shown in Figure 8.1, and a concrete and a steel fiber are created within each strip. The fiber areas correspond to the tributary area of each of those materials in the strip. Then, an area of horizontal reinforcement is assigned to each element. The natural discretization of strips is based on the locations of vertical reinforcement in the wall. The natural discretization of elements is based on the locations of horizontal reinforcement in the wall.
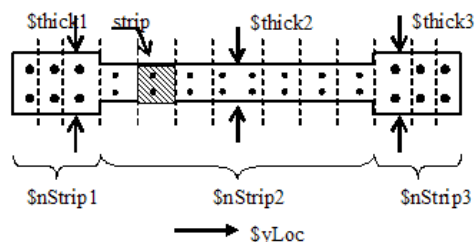

**Figure 8.1: Strips and Fibers within MVLE Cross Section (Massone et al. 2006)**

The MVLE is shown in Figure 8.2, excerpted from Massone et al. (2006). The top and bottom of the MVLE are rigid beams, which are connected by macrofibers. The center of rotation of the element is located at a distance ch from the bottom of the element. A single average value of curvature is assigned to each element and concentrated at this center of rotation. Also, a horizontal spring, representing the shear response, is located at the center of rotation. The original MVLEM had shear and flexural responses uncoupled, but in the Massone et al. (2006) implementation, shear and flexure interact at the fiber level. This interaction is modeled by a

shear spring assigned to each macrofiber, so each macrofiber acts like a reinforced concrete panel element. Figure 8.3 shows the modified MVLE, excerpted from Massone et al. (2009).
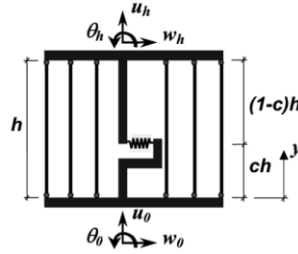
Figure 8.2: MVLE (Massone et al. 2006)
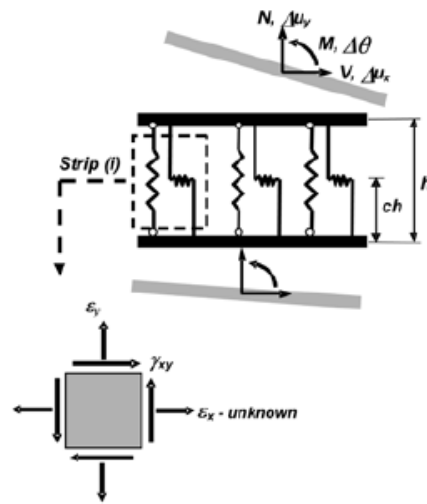
**Figure 8.3: Modified MVLE with Shear-Flexure Interaction (Massone et al. 2009)**

The six degrees of freedom at the ends of the element (ux, uy, and θ) are used to find the strains in each macrofiber. The model assumes that plane sections remain plane, and there is zero resultant transverse normal stress (σ_x=0) in each strip. This is problematic for squat walls, especially near the boundaries (top and bottom of the wall). Assuming zero resultant transverse normal strain (ε_x=0) in those areas is more appropriate. Massone et al. (2006) compared the model results (with zero transverse normal stress) to an alternate implementation of the model with zero transverse normal strain for the case of squat walls. Massone et al. (2009) conducted an experimental program with wall segments having shear span-depth ratios of 0.5 and 0.44, and neither implementation (zero transverse stress or zero transverse strain) represented the experimental behavior adequately. Zero transverse stress underestimated the experimental results; zero transverse strain overestimated the experimental results. Thus, with the current implementation of this model, with zero transverse normal stress, the numerical analysis is expected to underestimate the actual force-drift response behavior of the walls.

8.2   MATERIAL MODELS

The uniaxial material models used for the fibers were Concrete06 and ReinforcingSteel. These were chosen because they were able to match the stress-strain behavior of the concrete cylinder tests and the steel coupon tests very closely.

8.2.1   Concrete

Concrete06, shown in Figure 8.4, is similar to the Concrete01, 02, and 03 models, but it also implements the Thorenfeldt-base curve for the concrete compressive behavior. Two parameters associated with this curve are n, the compressive shape factor, and k, the post-peak compressive shape factor. The tensile portion of the curve is represented by the tension stiffening equation of Belarbi and Hsu (1994). This introduces the parameter b1 as an exponent in their equation. Parameters alpha1 and alpha2 are used in the definition of the unloading and reloading paths of the material.
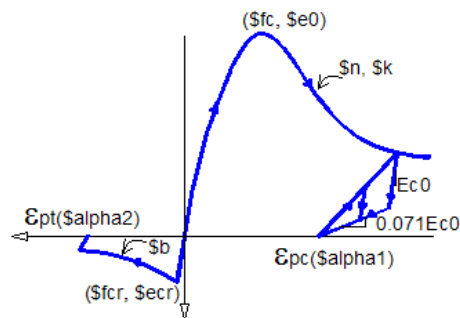
Figure 8.4: Concrete06 Material (OpenSees 2012)

The input parameters for the Concrete06 materials are summarized in the following command line, and then described along with the units (if any) that will be used in the following table.

uniaxialMaterial Concrete06 $tag $fc $e0 $n $k $alpha1 $ft $et $b1 $alpha2

Parameters n, k, b1, alpha1, and alpha2 are described above. fc is the concrete compressive strength, e0 is the strain at peak compressive strength, ft is the tensile strength, and et is the strain at peak tensile strength.

The parameters for the material model, summarized in Table 8.1, were determined by matching the material stress-strain curve to the average stress-strain curve from the concrete cylinder tests as closely as possible. The strain was not measured for the Buffalo concrete cylinder tests, so the value for e0 was assumed.

Table 8.1: Concrete06 Material Properties

	fc	e0	n	k	alpha1	Ft	et	b1	alpha2
Wall 1	-5.145	-0.003	2	1	0.32	0.538	0.00008	4	0.08
Wall 2	-5.413	-0.0029	2	1	0.32	0.552	0.00008	4	0.08
Buffalo	-7.8	*-0.003	2	1	0.32	0.662	0.00008	4	0.08

*did not measure the strain, so assumed this value

8.2.2   Steel

The ReinforcingSteel material, shown in Figure 8.5, is given in engineering stress and strain. By transforming from engineering stress to natural stress and accounting for changes in bar area, the same backbone curve is used for both tension and compression.
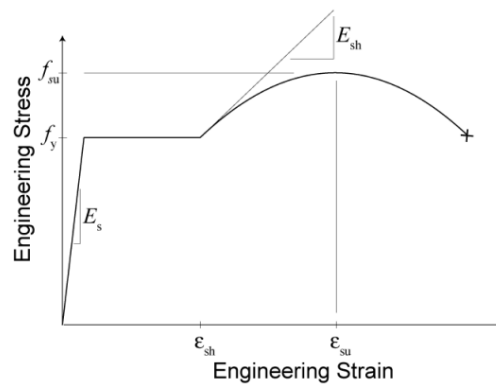
Figure 8.5: ReinforcingSteel Material (OpenSees 2012)

The input parameters for the reinforcing steel material are summarized in the command line, and then described along with the units (if any) that will be used in the following table.

uniaxialMaterial ReinforcingSteel $tag $fy $fu $Es $Esh $esh $eult

fy is the yield stress in tension, fu is the ultimate stress in tension, Es is the initial elastic tangent, Esh is the tangent at initial strain hardening, esh is the strain corresponding to initial strain hardening, and eult is the strain at peak stress.

Each of these parameters is summarized in Table 8.2. For the Berkeley walls, the values of the reinforcing steel parameters are selected based on coupon test results by Terzic (2009). She used the same steel reinforcing bars as those used in the squat shear wall hybrid simulation tests. The parameters for the Buffalo wall were determined from their reinforcing bar coupon tests and matched the material stress-strain curve to the average stress-strain curve from the reinforcing bar tests as closely as possible.

147

**Table 8.2: ReinforcingSteel Material Properties**

	fy	fu	Es	Esh	esh	eult
Wall 1	70.7	120	29000	725	0.01	0.12
Wall 2	70.7	120	29000	725	0.01	0.12
Buffalo	63	87	29000	725	0.003	0.07

## 8.3   IMPLEMENTATION OF FLEXURE-SHEAR INTERACTION ELEMENT

For the Berkeley and Buffalo analytical models, 18 strips were created, corresponding to the number of vertical reinforcing bars along the length of the wall. All thicknesses were a uniform 8 in, since the walls are rectangular. Each strip contains a steel and concrete fiber, corresponding to the tributary area of each of those materials in the strip. The wall was defined using 10 vertical elements, corresponding to the number of horizontal reinforcing bars.

As discussed in Section 6.5.1, the parameter α was defined as the relative distance from the top of the square to the centroid of rotation of the element. Massone and Wallace (2004) recommended α=0.6. Here, the center of rotation factor, c, is defined as the relative distance from the bottom of the element to the center of rotation, so c is taken as 0.4.

When Massone et al. (2009) reported the modeled monotonic force-displacement response compared to results from cyclic tests of laboratory specimens, they plotted the numerical model results only until the point of post-peak force degradation. They reported that the degradation behavior of the model after reaching peak force was very sensitive to the number of elements used in the wall model definition. However, the behavior of the model up to peak force was insensitive to the selected element discretization. The results for the Berkeley and Buffalo walls are displayed in the same manner. Figure 8.6 compares the Berkeley Wall 1 hybrid simulation results with the results obtained using the numerical model; Figure 8.7 shows the Berkeley Wall 2 results; Figure 8.8 shows the Buffalo wall results.
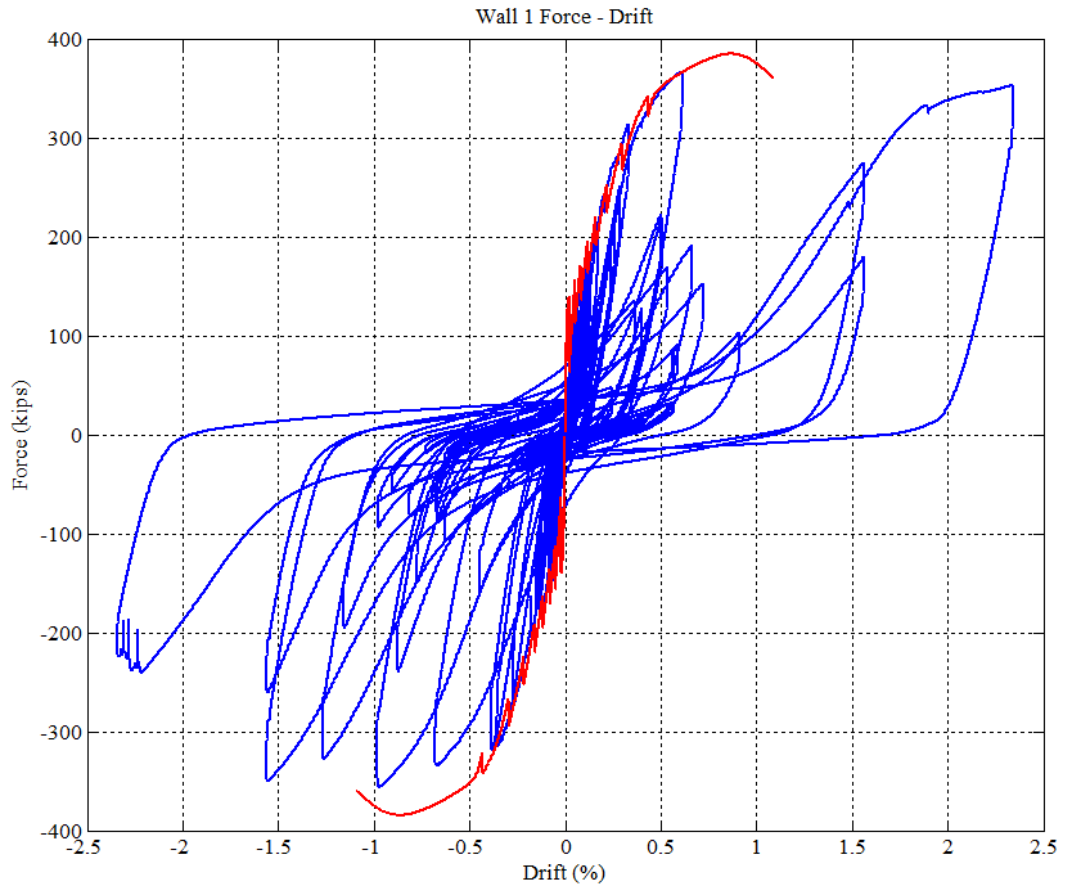
Figure 8.6: Berkeley Wall 1 Test Results Compared to Flexure-Shear Interaction Model
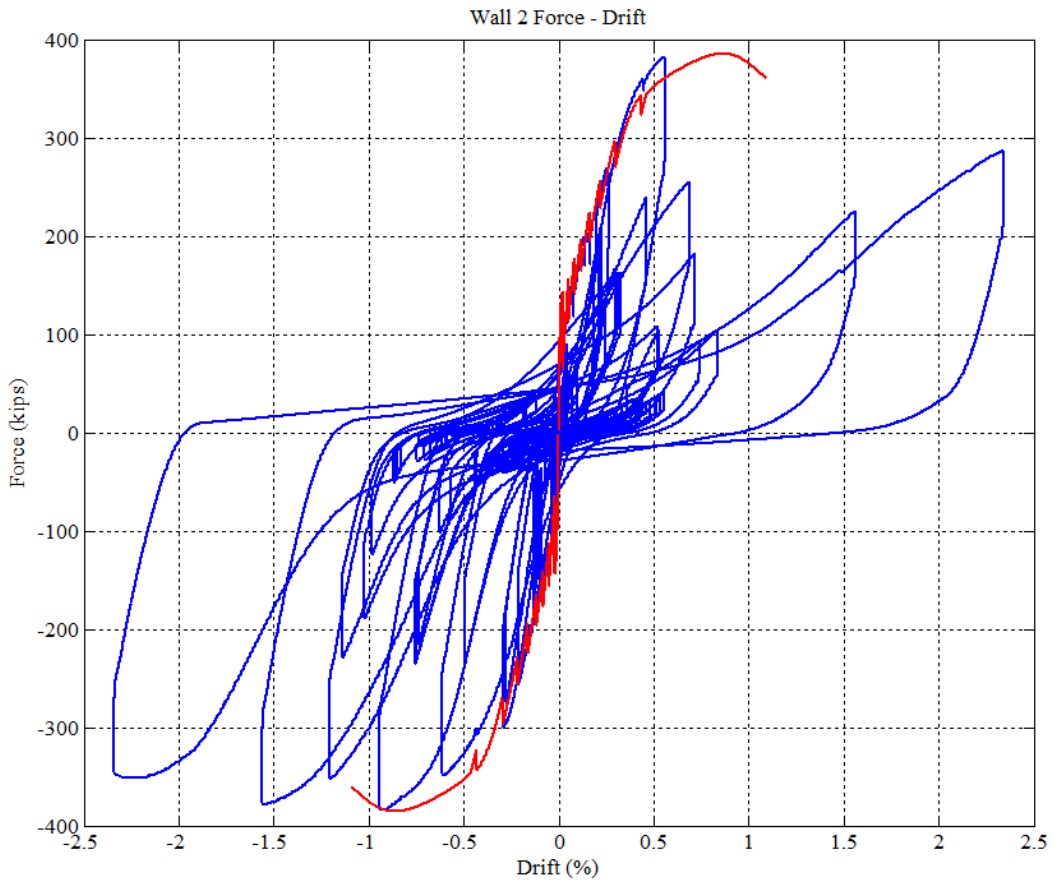
Figure 8.7: Berkeley Wall 2 Test Results Compared to Flexure-Shear Interaction Model
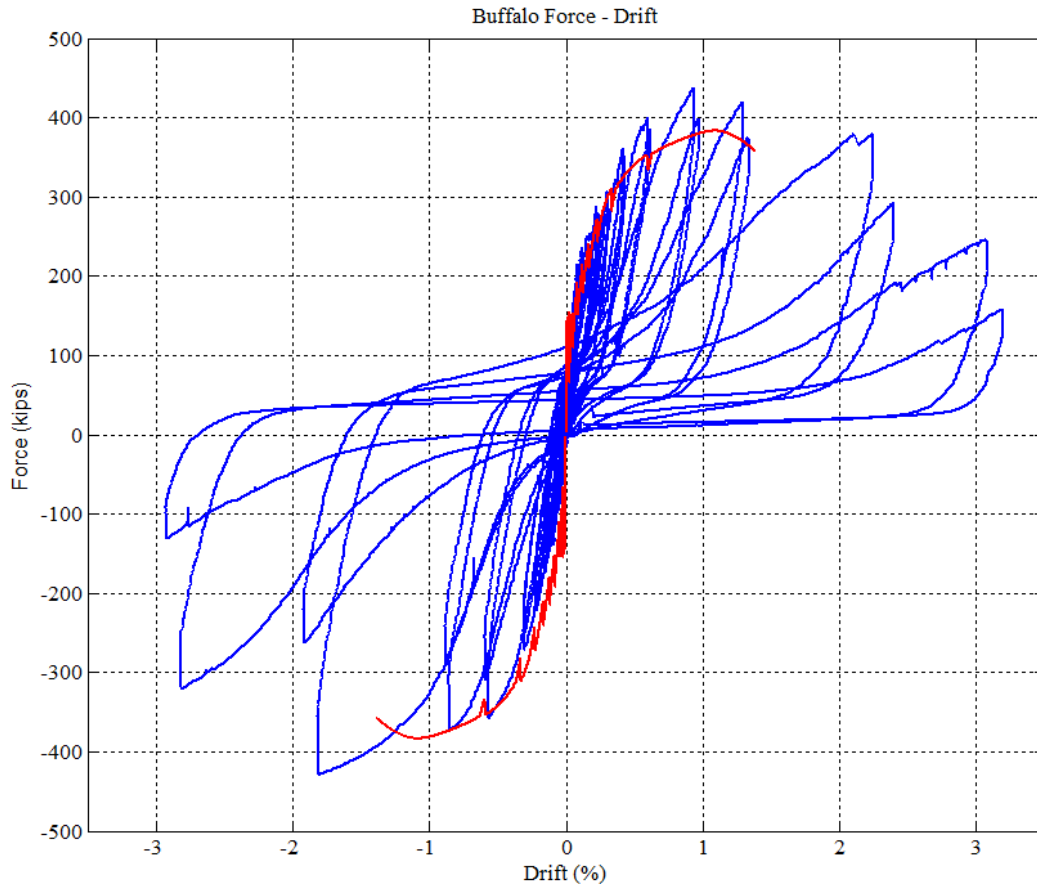
Figure 8.8: Buffalo Test Results Compared to Flexure-Shear Interaction Model

The zero transverse stress model assumption was expected to underestimate the experimental results. However, this was not observed in Berkeley Wall 1. The model matched the Berkeley Wall 1 behavior fairly closely until peak strength. Perhaps the model did not underestimate the Berkeley Wall 1 response because Wall 1 lost much of its strength when it experienced many cycles at low drift. Berkeley Wall 2 did not experience as many cycles at low drift, so it reached a higher peak force, and the model slightly underestimated its behavior, as expected. The Buffalo wall experienced the fewest cycles at low drift of the three walls, and as expected, the model underestimated its response. In all cases, the model adequately predicted the initial stiffness and the stiffness post-cracking.

8.4   EFFECT OF VERTICAL LOAD

Since no vertical load was applied to the walls in the hybrid simulation tests, the vertical load added to the Massone model was the 5.375 kips weight of the concrete. In order to investigate the response of the model to higher vertical loads, the Wall 1 model was implemented with 5%, 10%, and 15% $f'_c A_g$. The value, c, in the model remained 0.4 for the 5% and 10% $f'_c A_g$ runs. The 15% $f'_c A_g$ run did not converge with c=0.4, but successfully converged with c=0.2. That is what is reported in Figure 8.9. The original model force-drift ratio response with the weight of

the concrete alone is plotted with the responses using 5%, 10%, and 15% f'$_c$A$_g$. The analysis was stopped at the same displacement for all of the runs.
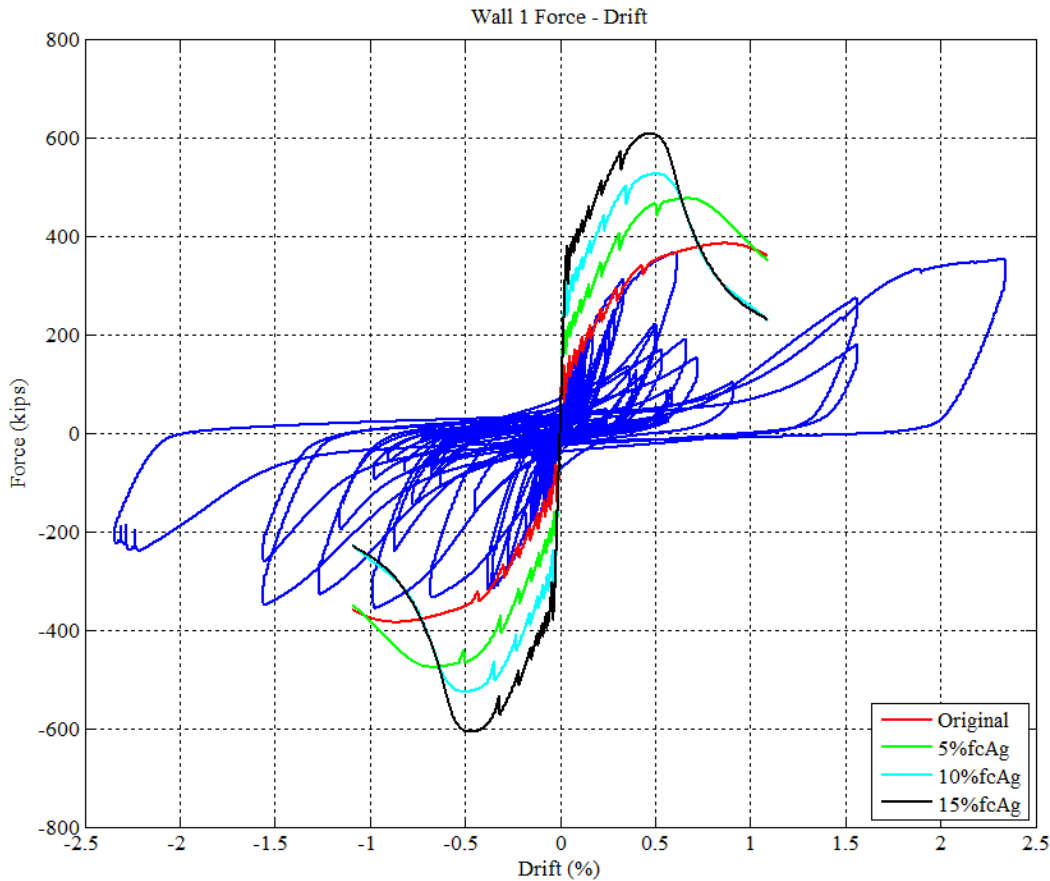
**Figure 8.9: Effect of Varying Vertical Load**

The peak horizontal load capacity increases with increasing vertical load. The ductility capacity appears to decrease with increasing vertical load because the peak displacement is attained at a smaller drift. The stiffness of the wall in the "essentially elastic" region increases, due to the lack of deformation in the very small drift range and a buildup of shear force within that small displacement. Once the wall moves, the tangent stiffness seems to be similar for all of the runs. The values of the initial and tangent stiffnesses are highly dependent on the modeling parameters. These should be further verified with continued studies.

8.5   SUMMARY

Massone's envelop predicted the behavior of the tested walls well up to peak strength, but there was significant uncertainty with modeling post-peak behavior. This is due to the shear or sliding shear (or some combination) behavior observed here. Hence, further research is required to improve models. Further investigation into walls in Gulec's database, in addition to future experimental work, will be important. The goal of this future research will be to develop

bending, shear, and sliding envelopes, reflecting the decay in strength of each failure mode, and their interactions. Examples of these possible interactions are sketched in Figure 8.10.
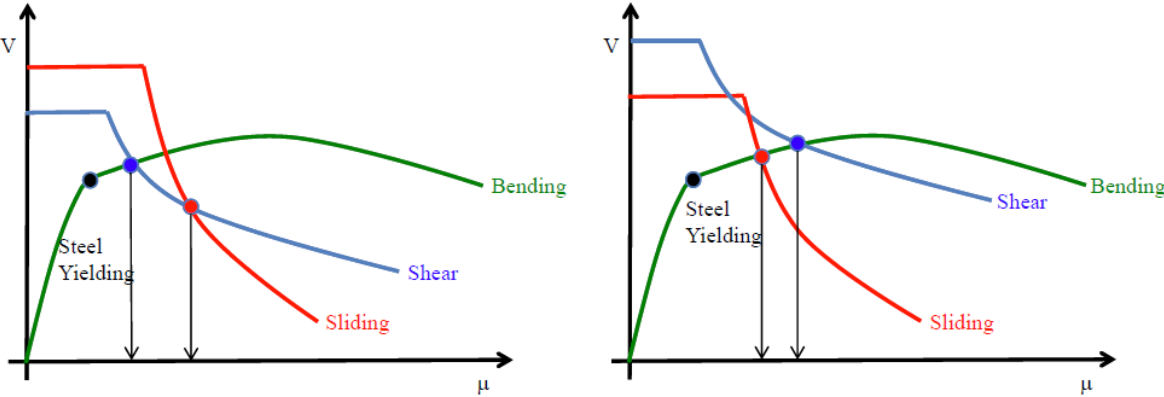
Figure 8.10: Flexure, Shear, Sliding Interaction

9 Conclusion

9.1 SUMMARY

Significant uncertainty exists concerning the strength and deformation capacities of low-aspect-ratio reinforced concrete shear walls, which commonly comprise the lateral-force-resisting system in nuclear and industrial structures. Knowledge about the strength and deformation capacities of these walls comes from test data. However, the stiff and brittle response of squat walls and laboratory testing constraints lead to a substantial scatter in this test data. Size effects associated with small scale models and quasi-static loading sequences contribute to uncertainties about squat wall behavior in ground motion excitations. Current building code equations tend to overpredict the peak shear strength capacity of squat shear walls, in some cases by a factor as large as 3, as shown by Gulec (2005) in his compilation of test data from 150 squat rectangular wall tests. Additionally, squat walls experience a complex interaction of flexure, shear, and sliding shear failure modes. Although design codes promote the ductile mechanism of flexural yielding, the geometry of squat walls prevents them from bending easily, and they instead tend to fail in shear and/or sliding shear. Both of these brittle failure modes are extremely undesirable because they cause rapid loss of strength and stiffness after very little deformation.

Squat walls in nuclear applications are especially problematic because these structures have a short natural vibration period, putting them in the acceleration sensitive range of a typical earthquake response spectrum. Here, any small amount of structural nonlinearity leads to a large increase in displacement ductilty demand (Chopra 2007). Additionally, the design provision of "essentially elastic" behavior in a design basis earthquake (DBE) for nuclear facility structures is not clearly defined, which is especially problematic for squat walls with small displacement capacities, since they cannot meet a large displacement ductility demand. Thus, it is important to quantify force and displacement ductility capacities of squat walls in order to clearly define the term "essentially elastic," and thereby ensure that squat walls meet this criterion.

Most tests of squat shear walls have used small-scale specimens either excited by a shaking table or by a quasi-static load sequence. The advantage of hybrid simulation over these traditional methods includes incorporation of ground motion input with a large-scale test. Furthermore, it comprises a combined numerical and physical model. In hybrid simulation tests performed at the *nees@Berkeley* laboratory, the hybrid model consisted of a large-scale squat shear wall paired with a numerically modeled mass to achieve a natural period that was representative of a nuclear facility structure. Physically placing this large a mass on a shaking table or quasi-static test specimen would not be possible.

The high stiffness of the squat walls in these structures poses a challenge for hybrid simulation using conventional displacement control strategies. In order to perform a hybrid

simulation test with a stiff squat shear wall, a review of displacement, force, and switch (from force to displacement) control hybrid simulation methods was conducted. Ultimately, a displacement control method using a high precision displacement encoder was selected and verified for use in this study. This approach proved to be an effective tool for a large-scale hybrid test of a stiff specimen because the encoder provided small enough displacement feedback increments to ensure a smooth force response. This new method is useful for addressing the shortcomings with understanding the dynamic behavior of stiff specimens, and will be used for future tests at the *nees@Berkeley* laboratory.

Following verification of the hybrid simulation encoder control method, two nominally identical walls were tested in hybrid simulation of their seismic response at the *nees@Berkeley* laboratory and exposed to different sequences of the same ground motion. The responses of the walls were then compared to evaluate the effect of ground motion sequence. Wall 1 was tested with a sequence of increasing levels of ground motion, followed by a DBE-level aftershock. Wall 2 was tested with a large initial BDBE ground motion, followed by two DBE-level aftershocks. No vertical load was applied to either of the specimens. Both walls initially experienced flexure and shear deformations. However, as the displacement demands grew, the flexural cracks from each end of the wall joined to form a continuous crack along the interface between the wall and its foundation. Sliding in the narrow zone surrounding this crack initiated and grew to dominate the response of the seismic walls. The eventual failure mode of both tests specimens was sliding shear. Comparison of the force-drift responses of both walls showed great similarity, indicating that significantly different sequences of ground motion intensities do not result in a significantly different force-deformation response of squat shear walls nor do they affect the failure mode sequence for these walls. Wall 2 achieved slightly higher force levels than Wall 1 due to its relatively smaller amount of damage when it experienced the largest BDBE ground motion.

A third nominally identical wall model was tested at The State University of New York at Buffalo using a quasi-static loading sequence (Rocks et al. 2011). The wall tested at Buffalo experienced a very similar sequence of failure modes compared to both of the Berkeley walls. The global force-deformation response behavior was also comparable, which showed that the quasi-static cyclic test is adequate (at least in a global sense) to predict the response of squat shear walls to a sequence of ground motion events. Due to unavailability of strain gage data post-yield for Wall 1 and a different strain gage placement scheme at Buffalo, local behavior comparisons were not possible beyond photographic evidence of similar cracking patterns.

Wood (1990) proposed the equation, $6\sqrt{f'_c}$, for the lower bound peak shear stress of squat walls. This equation provided the closest estimate (though as an upper bound) to the observed peak shear stresses in the walls: Wall 1 peak shear stress was $5.32\sqrt{f'_c}$ psi; Wall 2 peak shear stress was $5.45\sqrt{f'_c}$ psi; the Buffalo wall's peak shear stress was $5.52\sqrt{f'_c}$ psi. These results were consistent with Gulec's (2005) database of rectangular walls, where Wood's equation also provided the best fit. Other design equations, including those given in ACI Chapter 21.7, Barda (1977), and ASCE 43-05 overpredicted the observed peak shear strengths in these tests. These results are also consistent with Gulec's observations. These equations are more appropriate for predicting peak shear strength of walls with barbells or flanges. The backbone curve proposed by Wallace (2006) for squat walls was evaluated in comparison to the walls in this study. Wallace recommended using $0.4*E_c$ for the uncracked initial shear stiffness and the ACI Chapter 21.7 equation to calculate the peak shear strength of the envelope. Wood's equation provided a better fit for peak shear strength of the squat walls tested in this study. Furthermore, the initial

155

stiffness of Wallace's backbone curve was significantly higher than observed. This study recommends applying an additional modification factor of 0.3 to Wallace's equation, and a definition of "essentially elastic" as the range from the modified initial stiffness, $0.3*0.4*E_c$, to second stiffness, $0.4*(0.3*0.4*E_c)$, as shown in Section 6.5. Two hybrid simulation wall tests did not provide sufficient data to model the degradation of shear and sliding shear envelopes. This was especially difficult to characterize because the 1999 Kocaeli, Turkey ground motion was more demanding in one direction than the other.

The flexure, shear, and sliding failure mode interaction in squat walls is complex. The monotonic flexure-shear interaction element in OpenSees, contributed by Massone (2009), was implemented and compared to results from the three wall tests. The OpenSees model closely matched the initial stiffness and enveloped the response from physical testing up to peak shear strength, but it was unable to capture post-peak response.

9.2 FUTURE WORK

In collaboration with the State University of New York at Buffalo and the University of Washington, test data from the Berkeley wall tests will be aggregated with test data from the squat wall tests at Buffalo to develop improved code equations for peak shear strength. The proposed initial stiffness and "essentially elastic" range will be evaluated with the other Buffalo test data in addition to the nominally identical wall discussed in Chapter 7. After comprehensive consideration of all of the wall tests, displacement capacity and strength degradation will be further addressed. The hybrid simulation data will be contributed to the modeling efforts at University of Washington. Further testing may be necessary to understand the complex interaction of failure modes.

Since nuclear facility structures generally carry a small amount of vertical load in relation to their load carrying capacities, vertical load was not imposed in the squat wall tests. Tall buildings tend to carry a higher amount of vertical load in relation to their capacities, so the two cases should be treated separately. Future investigations will consider the effect of vertical load on the squat wall response characteristics, including cracked stiffness, yield point, ultimate load, and deformation capacity.

Further hybrid simulation work will include continued investigations of the use of force and switch control for stiff specimens. After an adequate squat wall computational model is developed, a hybrid simulation with a more complex numerical model will be instructive, such as combining a whole system of walls modeled analytically with a physical specimen.

REFERENCES

American Concrete Institute (ACI) Committee 349-06, 2006. Code Requirements for Nuclear Safety Related Concrete Structures (ACI 349-06) and Commentary (ACI 349R-06), Farmington Hills, MI.

American Concrete Institute (ACI) Committee 318-08, 2008. Building Code Requirements for Structural Concrete and Commentary (ACI 318-08), Farmington Hills, MI.

American Concrete Institute (ACI) Innovation Task Group 1 and Collaborators (ACI ITG/T1.1-01), 2001. Acceptance Criteria for Moment Frames Based on Structural Testing, Farmington Hills, MI.

American Society of Civil Engineers (ASCE), 2010. Minimum Design Loads for Buildings and Other Structures (ASCE/SEI 7-10), Reston, VA.

American Society of Civil Engineers (ASCE), 2007. Seismic Design Criteria for Structures, Systems, and Components in Nuclear Facilities (ASCE/SEI 43-05), Reston, VA.

American Society of Civil Engineers (ASCE), 2007. Seismic Rehabilitation of Existing Buildings (ASCE/SEI 41-06), Reston, VA.

American Society of Civil Engineers (ASCE), 2007. Supplement No. 1, Seismic Rehabilitation of Existing Buildings (ASCE/SEI 41-06), Reston, VA.

Antebi, J., S. Utku, and R. J. Hansen, 1960. The Response of Shear Walls to Dynamic Loads, Department of Civil and Sanitary Engineering, Massachusetts Institute of Technology, Cambridge, MA.

Astaneh-Asl A. and S. Ravat, 1998. Cyclic Behavior and Seismic Design of Steel H-piles, *UCB/CEE-Steel-98/01*, Final Report to the California Department of Transportation.

Barda, F., J. M. Hanson, and W. G. Corley, 1976. Shear Strength of Low-Rise Walls with Boundary Elements, *ACI Symposium on Reinforced Concrete Structures in Seismic Zones*, Detroit, MI.

Benjamin, J. R., and Williams, H. A., 1954. Investigation of Shear Walls, Part 6 – Continued Experimental and Mathematical Studies of Reinforced Concrete Walled Bents under Static Shear Loading, *Technical Report No. 4*, Department of Civil Engineering, Stanford University, Stanford, CA.

Chopra, A., 2007. *Dynamics of Structures: Theory and Applications to Earthquake Engineering*. Prentice Hall, Upper Saddle River, NJ.

Correlated Solutions, 2009.VIC-2D. http://www.correlatedsolutions.com/index.php/products/vic-2d-2009.

Dermitzakis, S. N. and S. A. Mahin, 1985. Development of Substructuring Techniques for On-Line Computer Controlled Seismic Performance Testing, *Technical Report No. UCB/EERC-85/04*, Earthquake Engineering Research Center, University of California, Berkeley.

Elkhoraibi, T., and K. M. Mosalam, 2007. Generalized Hybrid Simulation Framework for Structural Systems Subjected to Seismic Loading, *PEER Report 2007/101*, University of California, Berkeley.

Elwood, K. et al., 2009. Update to ASCE/SEI 41 Concrete Provisions, *PEER Report 2009/021*, University of California, Berkeley.

Envirospace, 2011. Shear Wall in Finland's Nuclear Reactor in Olkiluoto. http://www.enviro-space.com/index.php?app=core&module=attach&section=attach&attach_rel_module=post&attach_id=51.

Farrar, C. R., and W. E. Baker, 1993. Experimental Assessment of Low-Aspect-Ratio, Reinforced Concrete Shear Wall Stiffness, *Earthquake Engineering and Structural Dynamics*, Vol. 22, 373-387.

Galletly, G. D., 1952. Behavior of Reinforced Concrete Walls under Static Load, Department of Civil and Sanitary Engineering, Massachusetts Institute of Technology, Cambridge, MA.

Gulec, C. K., 2005. Ultimate Shear Strength of Squat Rectangular Reinforced Concrete Walls. MS Thesis, Department of Civil, Structural and Environmental Engineering, State University of New York at Buffalo, Buffalo, NY.

Gulec, C. K., A. S. Whittaker, and B. Stojadinovic, 2008. Shear Strength of Squat Rectangular Reinforced Concrete Walls, *ACI Structural Journal*, Vol. 105, No. 4, 488-497.

Gulec, C. K., and A. S. Whittaker, 2009. Performanced-Based Assessment and Design of Squat Reinforced Concrete Shear Walls, *Technical Report MCEER-09-0010*, University at Buffalo, State University of New York at Buffalo, Buffalo, NY.

Huang, Y.N. and Whittaker, A. S., 2008. Performance Assessment of Conventional and Base-Isolated Nuclear Power Plants for Earthquake and Blast Loadings, *Technical Report MCEER-08-0019*, State University of New York at Buffalo, Buffalo, NY.

Huang, Y. N. et al., 2009. Assessment of Base-Isolated Nuclear Structures for Design and Beyond-Design Basis Earthquake Shaking, *Technical Report MCEER-09-0008*, State University of New York at Buffalo, Buffalo, NY.

Kim, H., 2009. Extending Hybrid Simulation Methods in OpenFresco Software Framework, *CE299 Report*, University of California, Berkeley.

Kim, Y., T. Kabeyasawa, T. Matsumori, and T. Kabeyasawa, 2007. Dynamic Collapse Analysis of the Six-Story Full-Scale Wall-Frame Tested at E-Defense, Proceedings of the 8th Pacific Conference On Earthquake Engineering (8PCEE), Singapore, Dec 5-7, 2007.

Lai, J. W., 2012. Experimental and Analytical Studies on the Seismic Behavior of Conventional and Hybrid Braced Frames, Dissertation, Department of Civil and Environmental Engineering, University of California, Berkeley, Berkeley, CA.

Luna, B., 2012. Seismic Response of Low Aspect Ratio Reinforced Concrete Shear Walls, Quake Summit, July 2012, Boston, MA.

Mahin, S. A. and M. Williams, 1981. Computer Controlled Seismic Performance Testing, Proceedings of the 2nd ASCE-EM D Specialty Conference on Dynamic Response of Structures, Atlanta, Georgia.

Massone, L. M. and J. W. Wallace, 2004. Load-Deformation Responses of Slender Reinforced Concrete Walls, *ACI Structural Journal*, Vol. 101, No. 1, 103-113.

Massone, L. M. K. Orakcal, and J. W. Wallace, 2006. Shear-Flexure Interaction for Structural Walls, *SP-236, ACI Special Publication – Deformation Capacity and Shear Strength of Reinforced Concrete Members Under Cyclic Loading ACI Structural Journal*, 127-150.

Massone, L. M., K. Orakcal, and J. W. Wallace, 2009. Modeling of Squat Structural Walls Controlled by Shear, *ACI Structural Journal*, Vol. 106, No. 5, 646-655.

Mathworks, 2012. MATLAB, Simulink, Stateflow, xPC Target, http://www.mathworks.com.

Mercan, O. and J. M. Ricles. 2007. Stability and Accuracy Analysis of Outer Loop Dynamics in Real-Time Pseudodynamic Testing of SDOF Systems, *Earthquake Engineering & Structural Dynamics* Vol. 36, No. 11, 1523-1543.

Mosqueda, G., B. Stojadinovic, and S. A. Mahin, 2005. Implementation and Accuracy of Continuous Hybrid Simulation with Geographically Distributed Substructures, *Technical Report UCB/EERC 2005-02*, Earthquake Engineering Research Center, University of California, Berkeley.

MTS, 2003. Model 793.00 System Software, User Information and Software Reference, MTS Systems Corporation.

Naze, P. A. and J. F. Sidaner, 2001. Presentation and Interpretation of SAFE Tests: Reinforced Concrete Walls Subjected to Shearing, *SMiRT 16*, August, Washington, DC.

Nakashima, M., et al., 1990. Integration Techniques for Substructure Pseudo Dynamic Test, Proceedings of the 4th US National Conference on Earthquake Engineering, Palm Springs, CA II, 515-524.

OpenFresco, 2012. Open Framework for Experimental Setup and Control. http://openfresco.neesforge.nees.org.

OpenSees, 2012. Open System for Earthquake Engineering Simulation. http://opensees.berkeley.edu.

Paulay, T., M. J. N. Priestley, and A. J. Synge, 1982. Ductility in Earthquake Resisting Squat Shearwalls, *ACI Journal*, Vol. 79, No. 4, 257-269.

PEER NGA Database, 2012. http://peer.berkeley.edu/peer_ground_motion_database.

Rocks, J. F., B. N. Luna, and A. S. Whittaker, 2011. Seismic Response of Low Aspect Ratio Reinforced Concrete Shear Walls, *SMiRT 21*, New Delhi, India.

Schellenberg, A., 2008. Advanced Implementation of Hybrid Simulation, *Ph.D. Thesis*, University of California, Berkeley.

Schellenberg, A. and S. Mahin, 2006. Application of an Experimental Software Framework to Hybrid Simulation of Structures through Collapse, *1st European Conference on Earthquake Engineering and Seismology*, Geneva, Switzerland.

Shing, P. B., and S. A. Mahin, 1983. Experimental Error Propagation in Pseudodynamic Testing, *Technical Report No. UCB/EERC-83/12*, Earthquake Engineering Research Center, University of California, Berkeley.

Shing, P. B., and S. A. Mahin, 1984. Pseudodynamic Test Method for Seismic Performance Evaluation: Theory and Implementation, *Technical Report No. UCB/EERC-84/01*, Earthquake Engineering Research Center, University of California, Berkeley.

Shing, P. B., M. T. Vannan, and E. Carter, 1991. Implicit Time Integration for Pseudodynamic Tests, *Earthquake Engineering and Structural Dynamics*, Vol. 20, 551-576.

Sozen, A. M., and J. P. Moehle, 1993. Stiffness of Reinforced Concrete Walls Resisting In-Plane Shear, *Technical Report No. EPRI TR-102731*, Electrical Power Research Institute, Palo Alto, CA.

Synge, A. J., 1980. Ductility of Squat Shear Walls, *Technical Report No. 80-8*, Department of Civil Engineering, University of Canterbury, Christchurch, New Zealand.

Takanashi, K., et al., 1975. Nonlinear Earthquake Response Analysis of Structures by a Computer-Actuator On-Line System, Bulletin of Earthquake Resistant Structure Research Center, Institute of Industrial Science, University of Tokyo, No. 8.

Terzic, V., 2009. Post-earthquake Traffic Capacity of Modern Bridges in California, *Ph.D. Thesis*, University of California, Berkeley.

Theon, B., UCB PC Simulation Simulink Model, MTS Systems.

Thewalt, C. R. and S. A. Mahin, 1987. Hybrid Solution Techniques for Generalized Pseudodynamic Testing, *Technical Report No. UCB/EERC-87/09*, Earthquake Engineering Research Center, University of California, Berkeley.

Thewalt, C. R. and S. A. Mahin, 1995, An Unconditionally Stable Hybrid Pseudodynamic Algorithm, *Earthquake Engineering and Structural Dynamics*, Vol. 24, pp 723-731.

Wallace, J. W., 2006. Lightly Reinforced Wall Segments, *New Information on the Seismic Performance of Existing Concrete Buildings Seminar Notes*, Earthquake Engineering Research Institute, Oakland, California.

Wood, S. L., 1990. Shear Strength of Low-Rise Reinforced Concrete Walls, *ACI Structural Journal*, Vol. 87, No. 1, 99-107.

Appendix A: Materials and Construction

A.1   MATERIALS

A.1.1 Wall Reinforcement

The reinforcing bars were made in a single batch with ASTM standard A706 reinforcing steel with a nominal yield strength of 60 ksi (413 MPa). The #4 reinforcing bars in the wall were tested for yield and ultimate strength. The testing was performed using standard testing procedures at a company named Testing Engineers. Three samples of #4 bars, each 3 ft long, were sent to the company for testing. The resulting yield and ultimate strengths are summarized in Table A.1.

Table A.1: Wall Reinforcement

	Bar 1	Bar 2	Bar 3	Average
Yield Strength (ksi)	66.5	68.5	67	67.3
Ultimate Strength (ksi)	91.5	92.5	91.5	91.8

A.1.2 Plain Concrete

The concrete mix was specified to replicate the mix used in Dr. Vesna Terzic's study "Post-earthquake Traffic Capacity of Modern Bridges in California." This mix was designed by Caltrans engineers to reach the 5000 psi (34.5 MPa) target compressive strength after about 60 days and maintain approximately that strength thereafter. The max aggregate size was 3/8 in. This mix was appropriate for the squat wall tests since the walls were tested a number of months after casting. The foundations were cast on February 24, 2011 and walls were cast on March 1, 2011. The first wall was tested on September 16, 2011 and the second wall was tested on December 14, 2011. The target concrete mix, the actual mix for the foundations, and the actual mix for the walls is shown in Table A.2. The Type A water reducer was WRDA 64 and the Type F water reducer was ADVA 140. The concrete ready mix company added nearly double the ADVA 140 water reducing admixture to the foundations mix. The concrete company failed to

add the WRDA 64 water reducing admixture and failed to add enough of the ADVA 140 water reducing admixture to the mix used for the walls, so they had a reduced strength.

Table A.2: Concrete Properties

		per yd^3						
	Slump (in)	Coarse Aggregate Weight (lb)	Fine Aggregate Weight (lb)	Cement (lb)	Fly Ash (lb)	Water (lb)	WRDA 64 (fl. oz.)	ADVA 140 (fl. oz.)
Target	6	1000	1965	529	176	300	21.2	56.4
Foundations	6	1010.5	2000	498.5	209.7	115.8	21.1	106.1
Walls	5/3.5	1000	2000	504	214	137	0	53

Prior to casting the foundations, a slump test was performed to check the mix. The slump was 6 in. as specified. After casting the foundations, the surfaces were roughened where the walls would be placed. Prior to casting of the walls, a slump test was performed and measured 5 in. At the end of pouring the walls, the slump test was repeated and measured 3.5 in. At the time of both castings, 12 in. tall x 6 in. diameter test cylinders were poured. Three cylinders were tested incrementally for compressive strength as the specimens aged. The foundation test cylinders had an average compressive strength of 5217 psi at 28 days, 7428 psi on the day of the first specimen test (at 204 days), and 7593 psi on the day of the second specimen test (at 293 days). The wall test cylinders had an average compressive strength of 3250 psi at 28 days, 5145 psi on the day of the first specimen test (at 199 days), and 5413 psi on the day of the second specimen test (at 288 days). By the first wall's testing date, they achieved a compressive strength of 5145 psi (at 199 days). Figure A.1 shows the development of average concrete strength over time for the foundation mix and the wall mix.
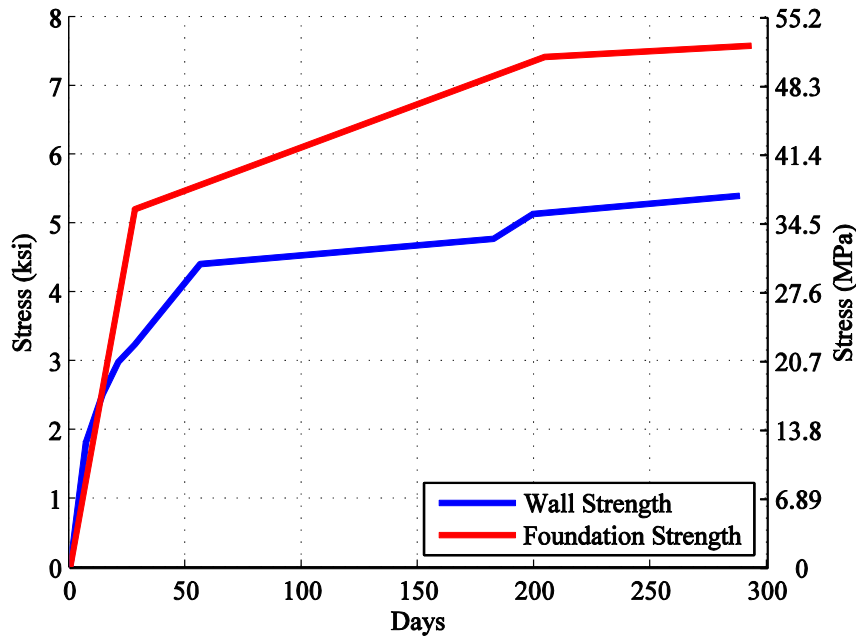
Figure A.1: Concrete Strength Development over Time

On the days of testing, three concrete cylinders from the foundations batch were tested for compressive strength. Three cylinders from the walls batch were tested for their full stress-strain behavior, and three cylinders from the walls batch were tested for their splitting tensile strength. Figure A.2 and Figure A.3 show the stress-strain behavior for the wall mix on the test day of Wall 1 and on the test day of Wall 2.
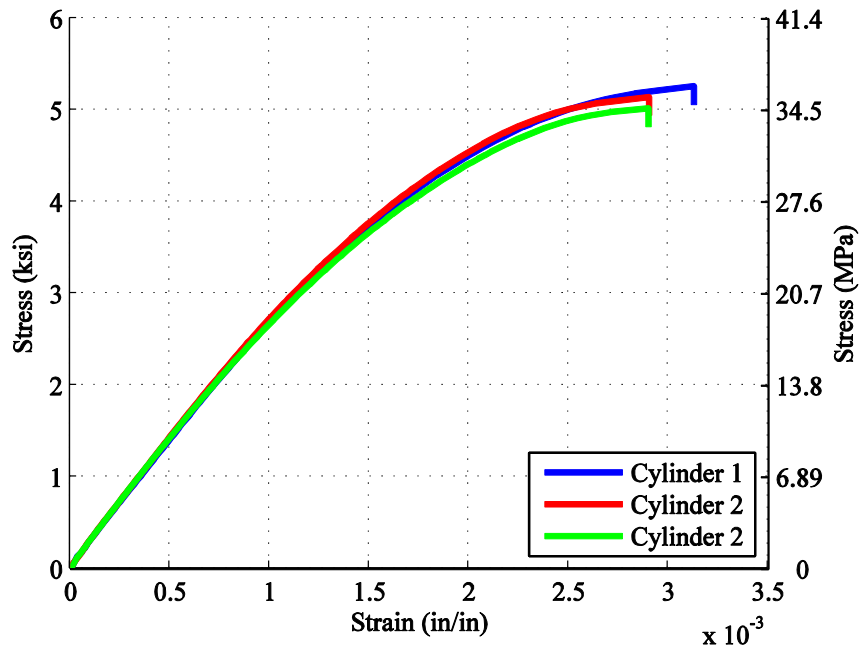
Figure A.2: Wall 1 Stress-Strain

164
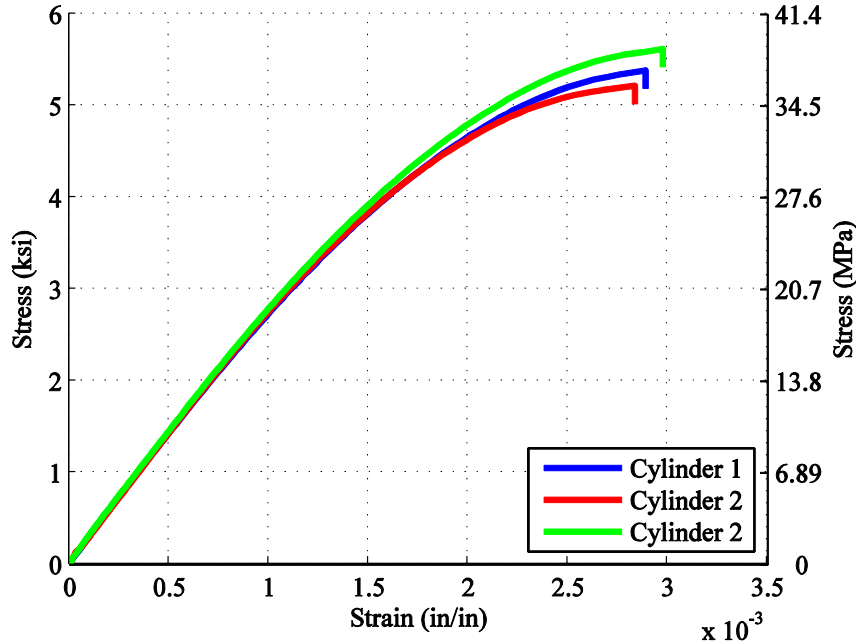
Figure A.3: Wall2 Stress-Strain

The average tensile strength of the concrete in the wall on the test day of Specimen 1 was 404 psi. The average tensile strength in the wall on the test day of Specimen 2 was 363 psi. The tensile strength of each cylinder for Wall 1 and Wall 2 is shown in Figure A.4.
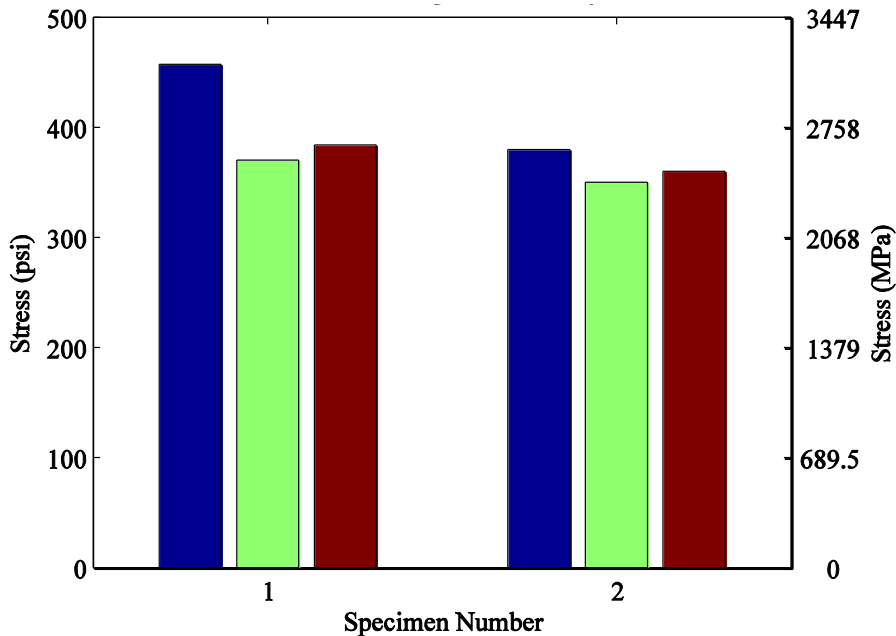
Figure A.4: Tensile Strength on Test Day

One of the cylinders tested for Wall 1 had a high tensile strength, 457 psi. This affected the average, so the Wall 1 cylinders had a higher tensile strength than the Wall 2 cylinders.

The average material properties for Wall 1 were calculated using the measured f'c=5145 psi on test day. The corresponding average strain is (ec)=0.003 in/in. The modulus of rupture (fr)=7.5*sqrt(f'c)=538 psi. The elastic modulus (Ec)=57000*sqrt(f'c)=4089 ksi. The shear modulus (G)=Ec/(2*(1+nu)) with nu=0.2. G=1704 ksi.

The average material properties for Wall 2 were calculated using the measured f'c=5413 psi on test day. The corresponding average strain is (ec)=0.003 in/in. The modulus of rupture (fr)=7.5*sqrt(f'c)=552 psi. The elastic modulus (Ec)=57000*sqrt(f'c)=4194 ksi. The shear modulus (G)=Ec/(2*(1+nu)) with nu=0.2. G=1747 ksi.

A.2   CONSTRUCTION OF SPECIMENS

YFLA-5 strain gages from Texas Measurements were used to instrument the reinforcing bars. These are high elongation, post yield gages, measuring up to 10-20% strain. Gage length is 5 mm, gage width is 2 mm, backing length is 12 mm, and backing width is 4 mm. The following pictures shown a gage mounted to the rebar. The lead wires from the gage are soldered to a terminal along with a heavy duty wire. This heavier wire is used so it will survive the concrete pour. Figure A.5 shows a strain gage mounted to the reinforcing bar with the heavy wire attached.

Figure A.5: Strain Gage

The strain gages were wrapped in mastic tape for their final protective layer, as shown in Figure A.6.

Figure A.6: Mastic Tape over Strain Gages

After all of the strain gages were attached, contractors were hired to assemble the reinforcing bar cages. First, they assembled the cages for both foundations, as shown in Figure A**.**7.

Figure A.7: Assembled Foundation Reinforcing Bar Cages

Then, they added the reinforcing bars for the walls, as shown in Figure A**.**8.

Figure A.8: Wall and Foundation Reinforcement

Next, the formwork was built around the foundations and the foundations were poured. This is shown in Figure A.9 and Figure A.10.

Figure A.9: Building Formwork

Figure A.10: Foundations Poured

The surface of the foundation below where the wall would be placed was left roughened. Then the wall formwork was built, as shown in Figure A.11, and the walls were poured.

Figure A.11: Walls Formwork

A forklift was hired to move the walls inside, shown in Figure A.12 and Figure A.13.

Figure A.12: Forklift Preparing to Move Wall

Figure A.13: Forklift Moving Wall

The foundations were too large to fit through the nearest laboratory door, so the forklift was used to drive the walls around the building. The foundations had to be angled to fit through the lab door, shown in Figure A.14.

Figure A.14: Bringing the Wall Inside the Laboratory

Then in Figure A**.**15, the crane was used to place the first specimen on the existing steel beam in the laboratory.

Figure A.15: Lowering the First Wall into the Testing Location

In Figure A**.**16, the loading plate was attached to the wall using the crane.

Figure A.16: Attaching Loading Plate to Wall

Appendix B: Test Setup Response

B.1   WALL 1 SLIPS

The Wall 1 slips for the BDBE motion were presented in the main body of the paper. The slips in each of the other ground motions are presented here. Figure B.1 shows the slips for the Wall 1 OBE motion.

173
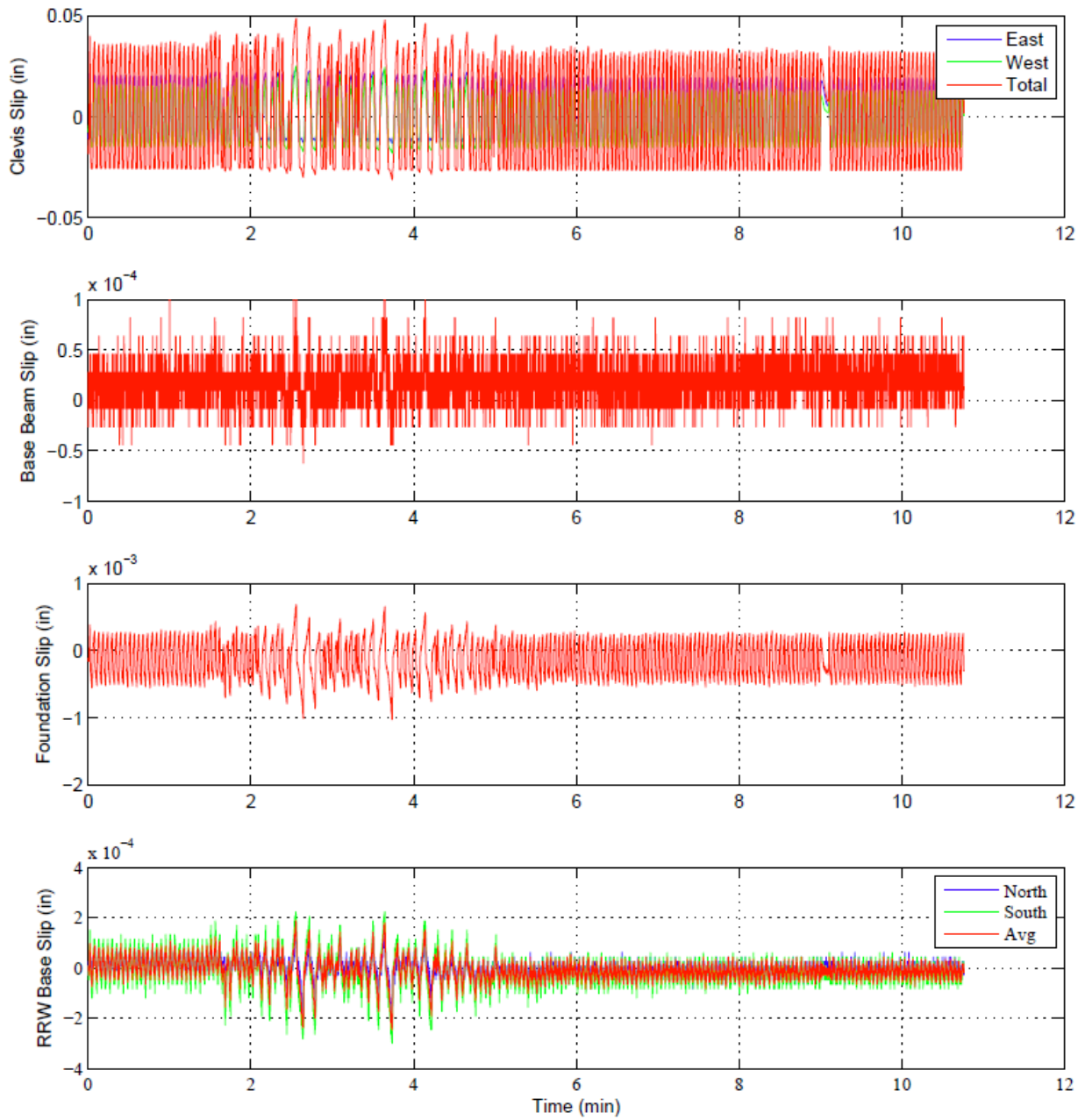
Figure B.1: Wall 1 OBE Test Setup Slips

Figure B.2 shows the slips for the Wall 1 DBE 0.11 motion.
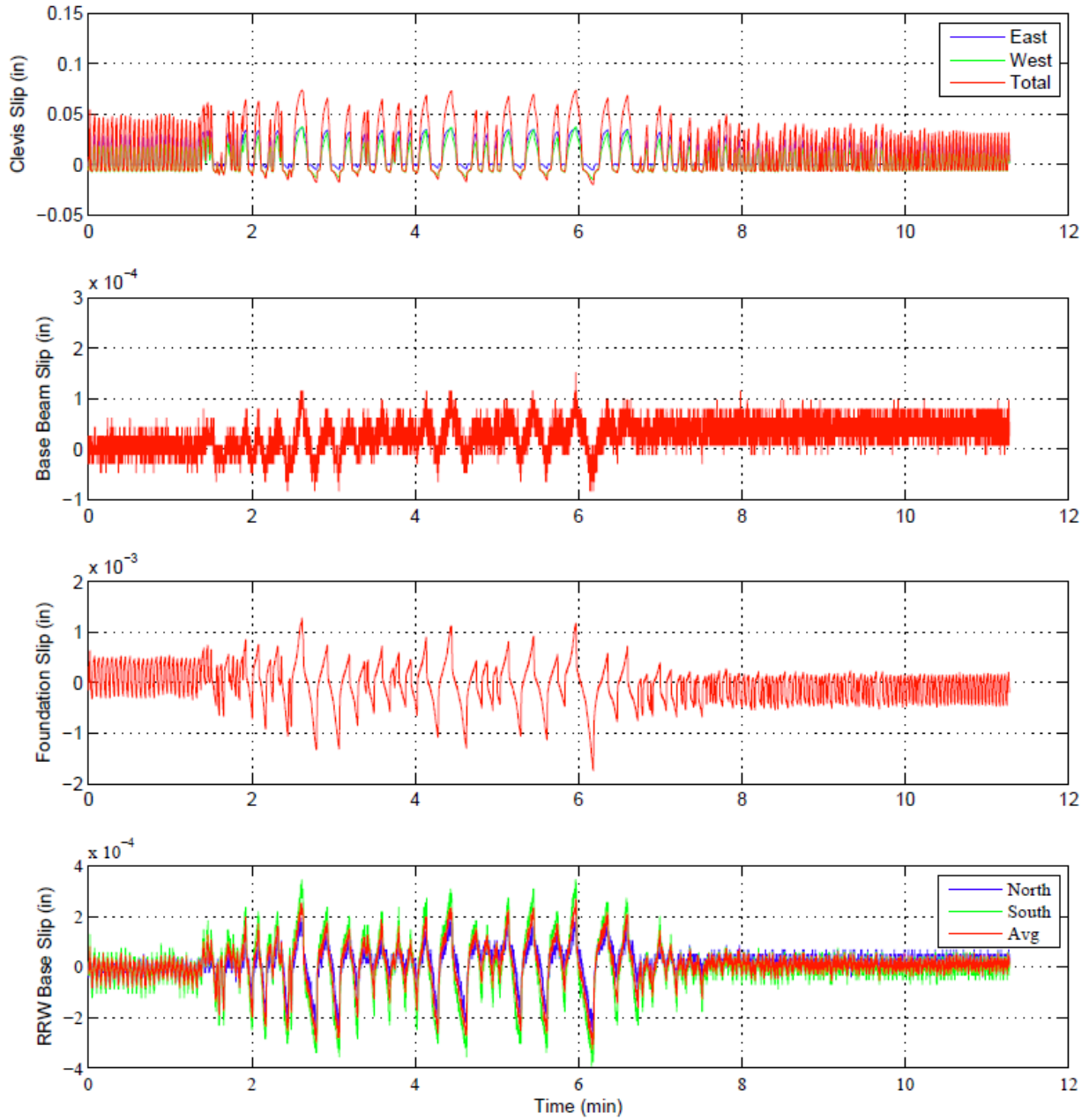
Figure B.2: Wall 1 DBE 0.11 Test Setup Slips

Figure B.3 shows the slips for the Wall 1 DBE motion.
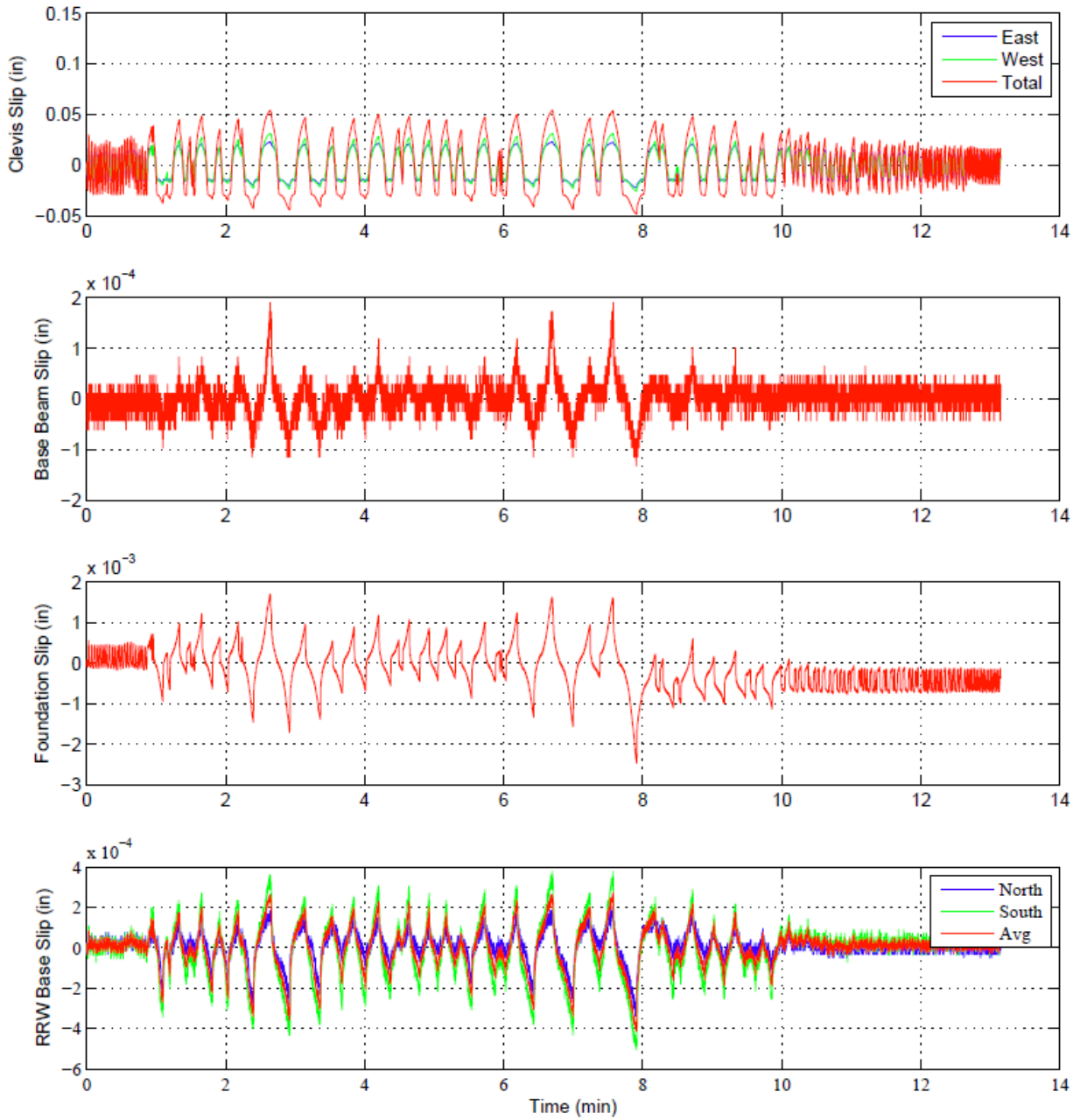
Figure B.3: Wall 1 DBE Test Setup Slips

Figure B.4 shows the slips for the Wall 1 DBE Aftershock motion.
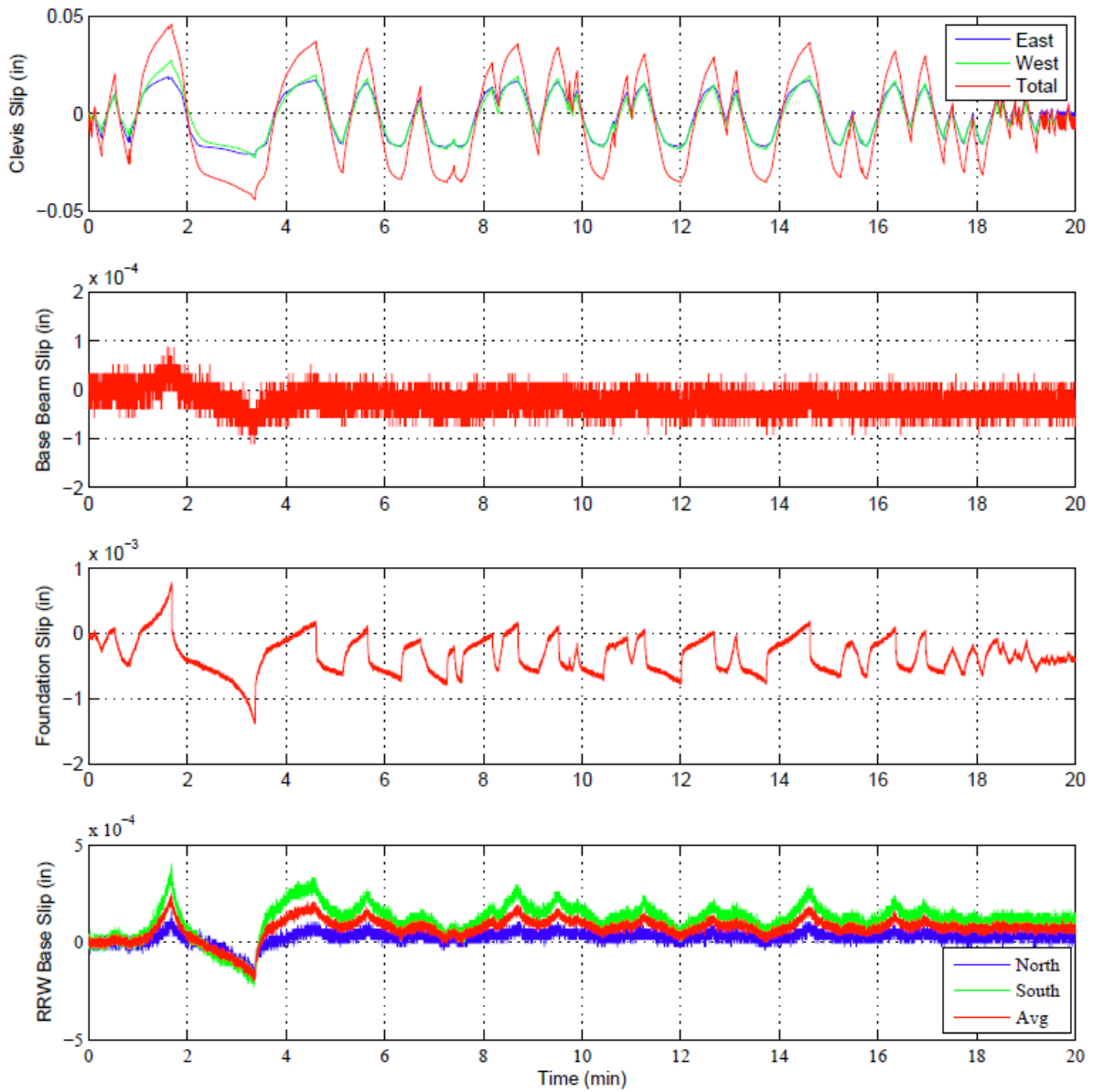
Figure B.4: Wall 1 DBE Aftershock Test Setup Slips

Figure B.5 shows the slips for the Wall 1 +/-1 in Triangle motion.
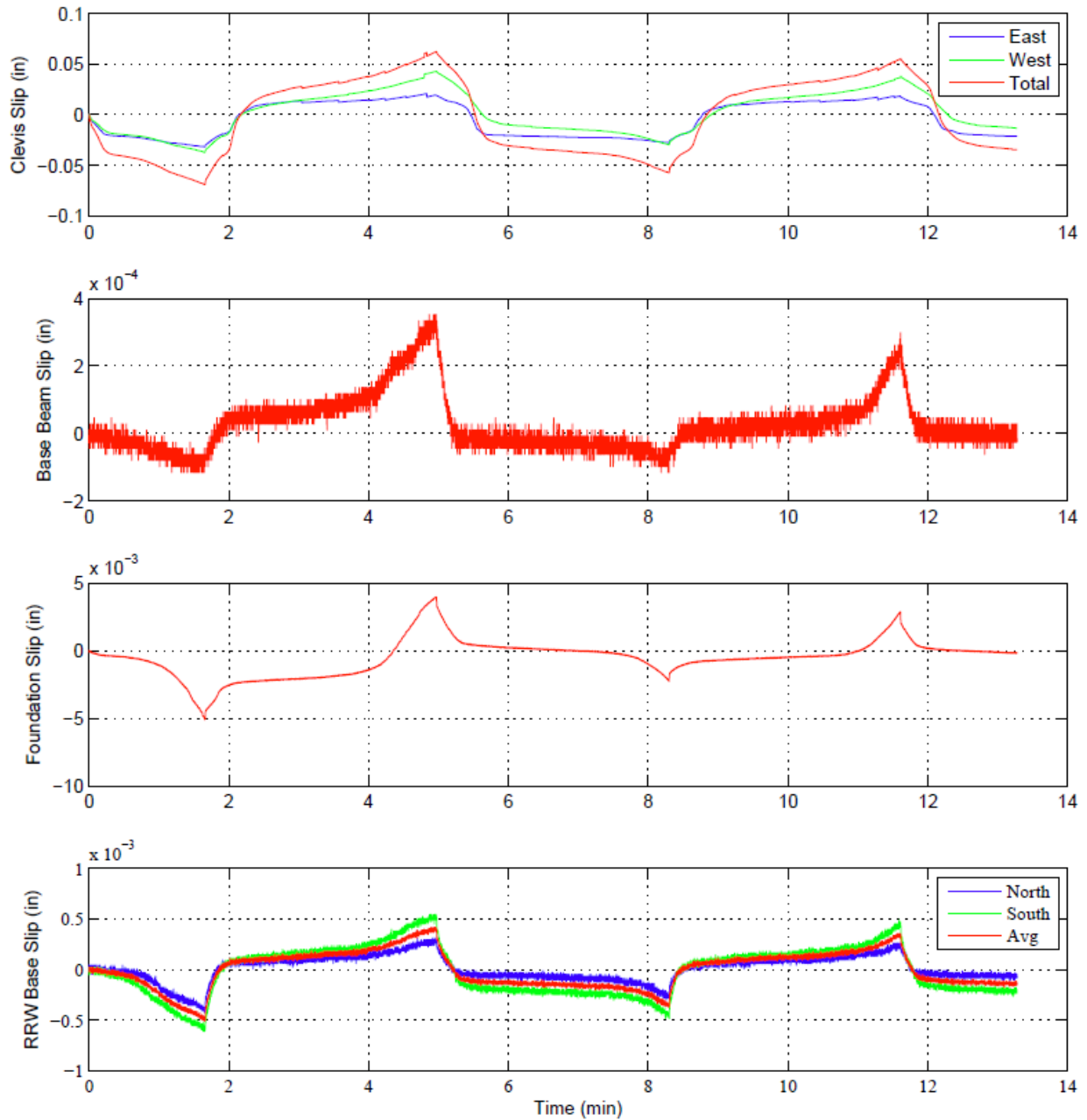
Figure B.5: Wall 1 +/-1 in Triangle Test Setup Slips

Figure B.6 shows the slips for the Wall 1 +/-1.5 in Triangle motion.
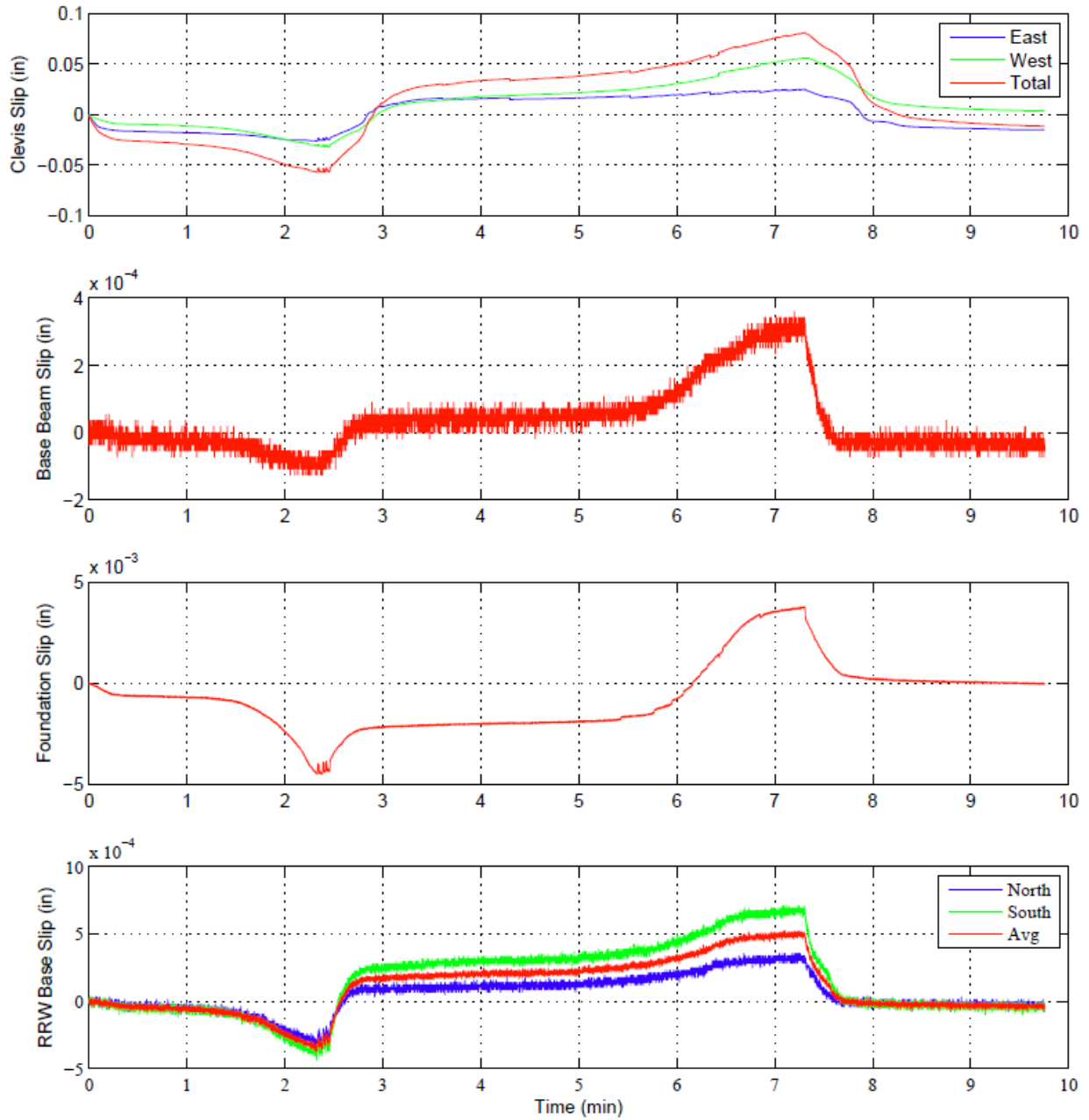
Figure B.6: Wall 1 +/-1.5 in Triangle Test Setup Slips

B.2 WALL 2 SLIPS

Figure B.7 shows the slips in the clevises for the Wall 2 OBE motion, and Figure B.8 shows the slips in the rest of the test setup for the Wall 2 OBE motion.

179
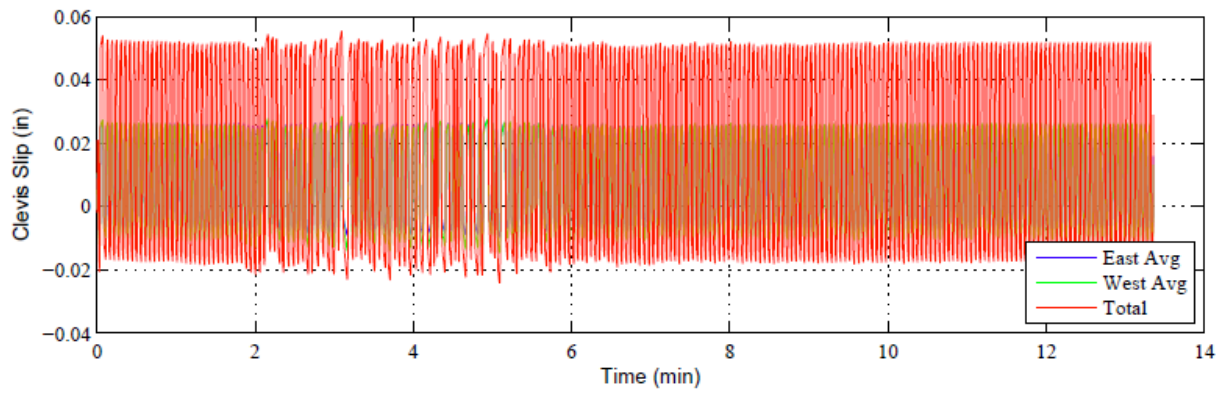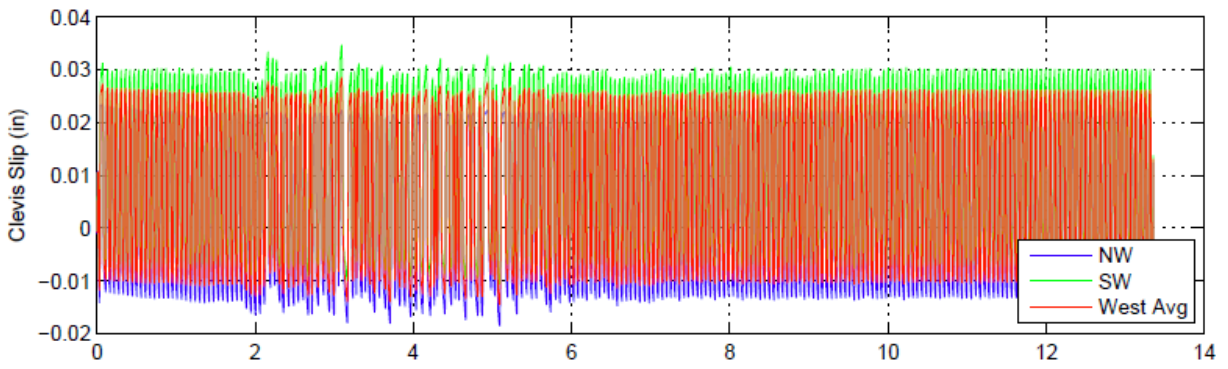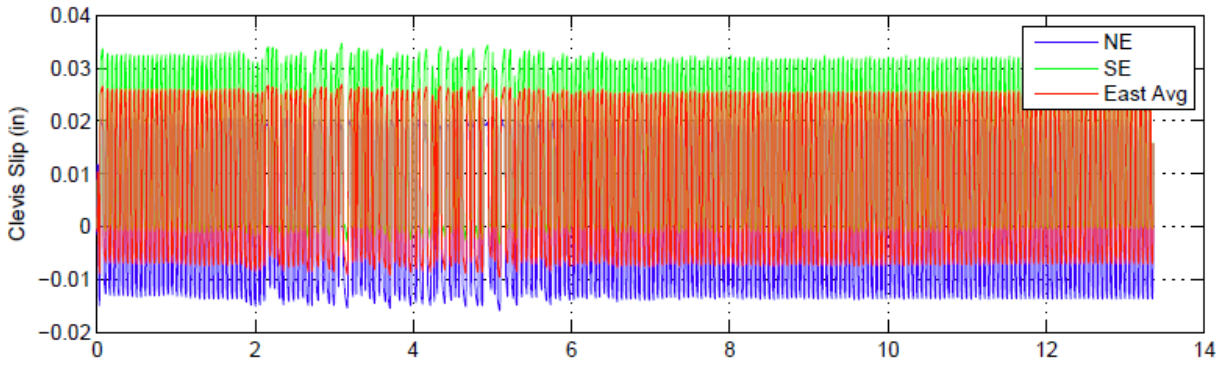
Figure B.7: Wall 2 OBE Clevis Slips

180
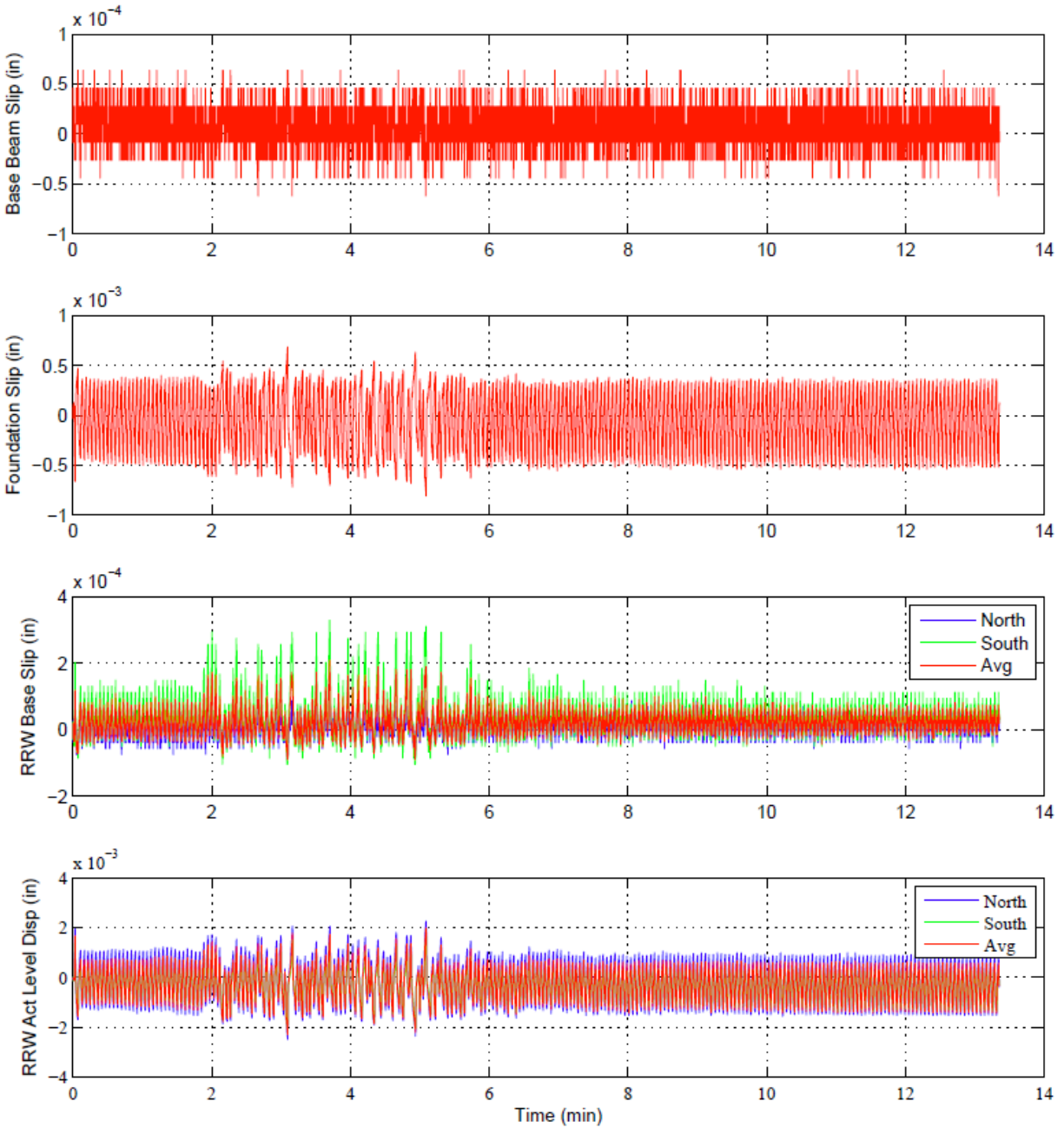
Figure B.8: Wall 2 OBE Test Setup Slips

Figure B.9 shows the slips in the clevises for the Wall 2 DBE Aftershock 1 motion, and Figure B.10 shows the slips in the rest of the test setup for the Wall 2 DBE Aftershock 1 motion.
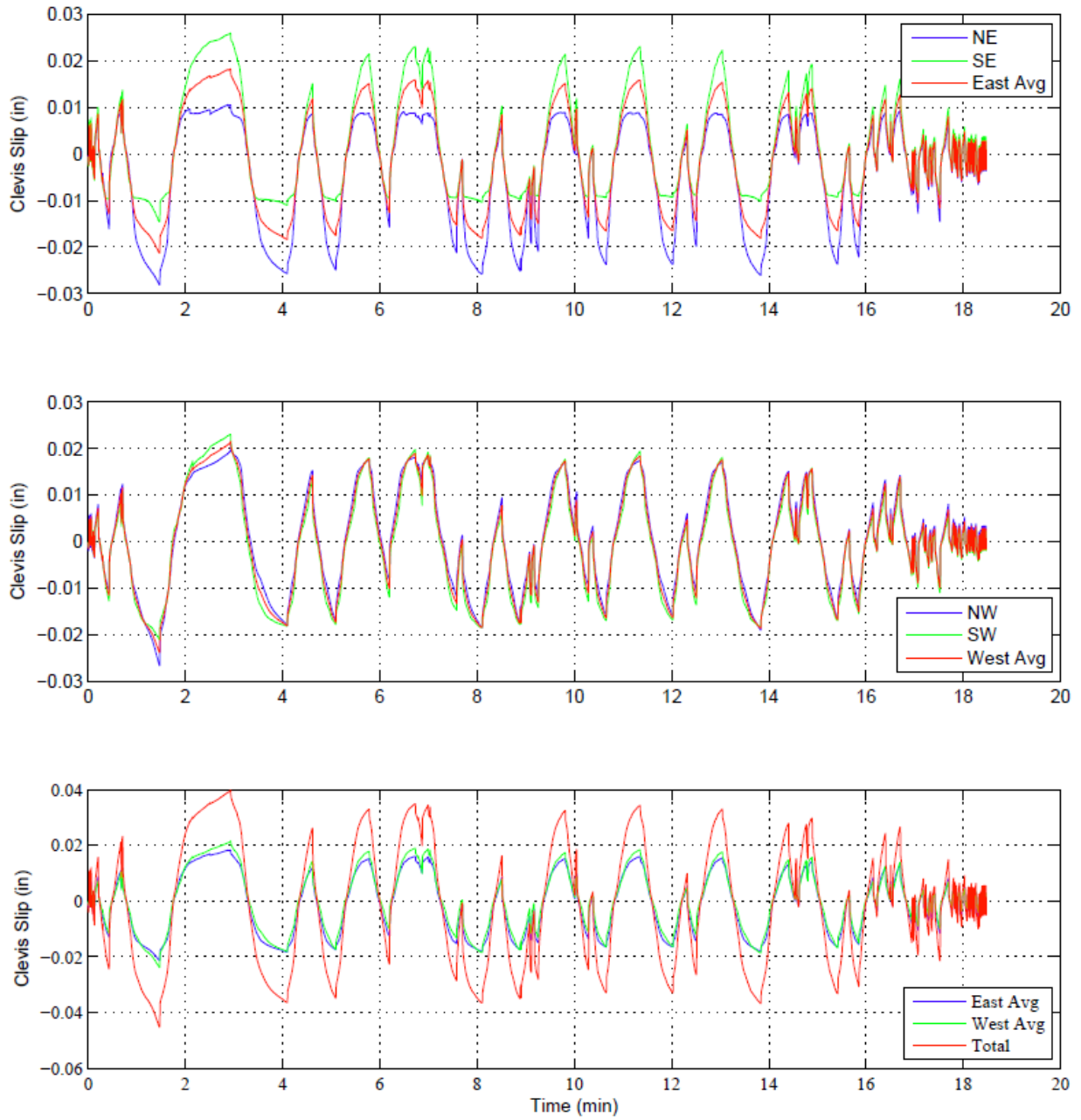
Figure B.9: Wall 2 DBE Aftershock 1 Clevis Slips
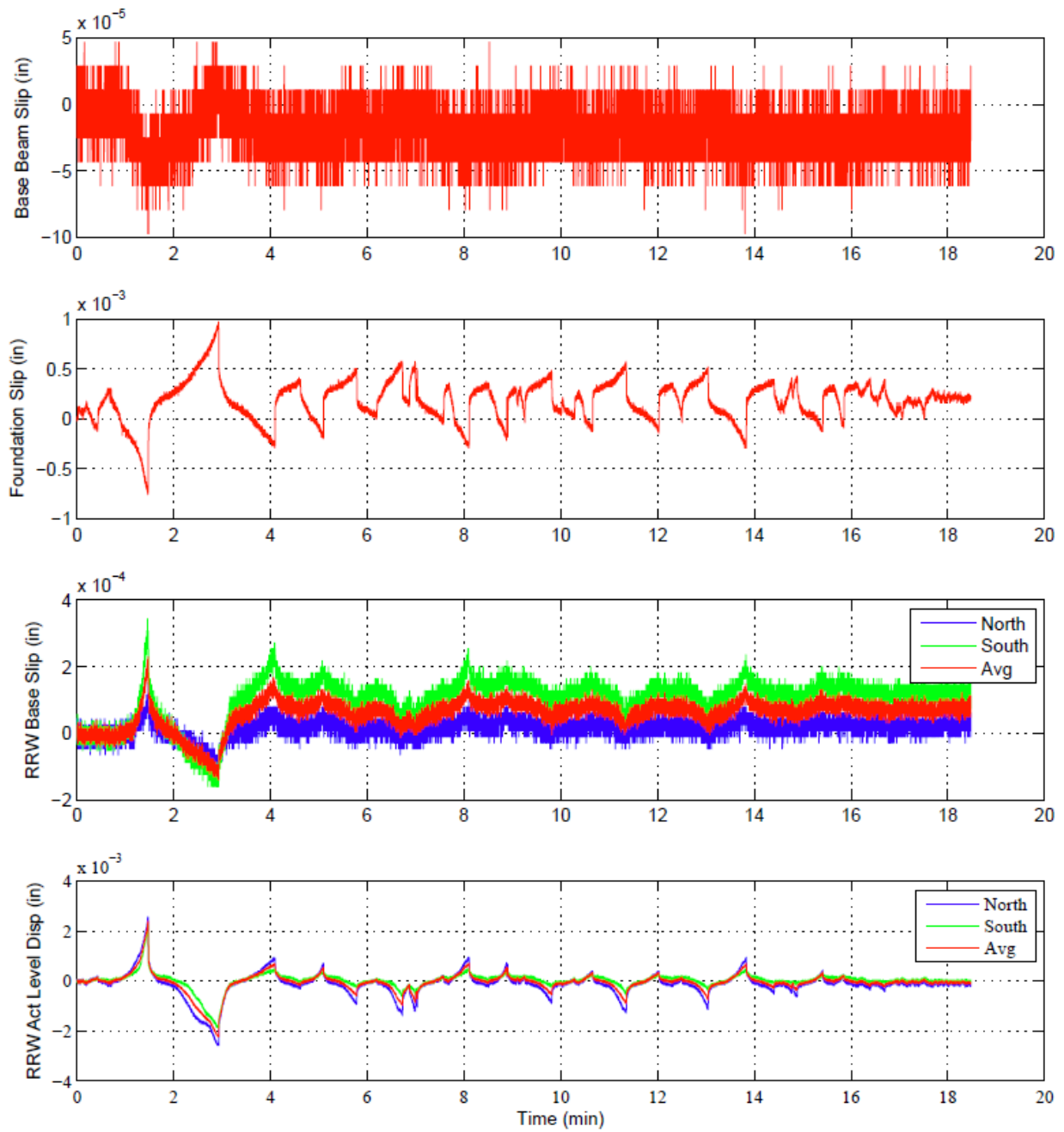
Figure B.10: Wall 2 DBE Aftershock 1 Test Setup Slips

Figure B.11 shows the slips in the clevises for the Wall 2 DBE Aftershock 2 motion, and Figure B.12 shows the slips in the rest of the test setup for the Wall 2 DBE Aftershock 2 motion.
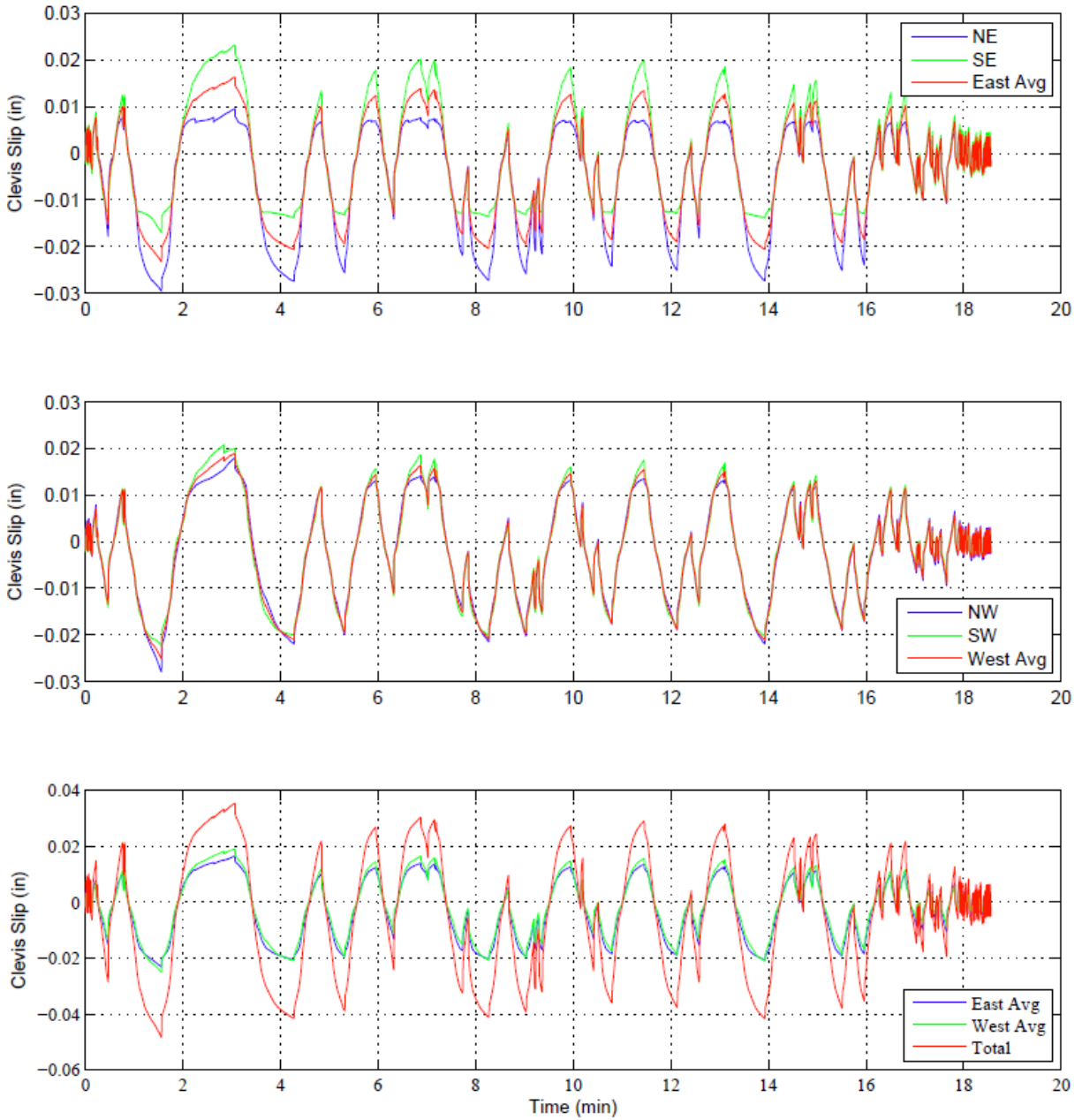
Figure B.11: Wall 2 DBE Aftershock 2 Clevis Slips
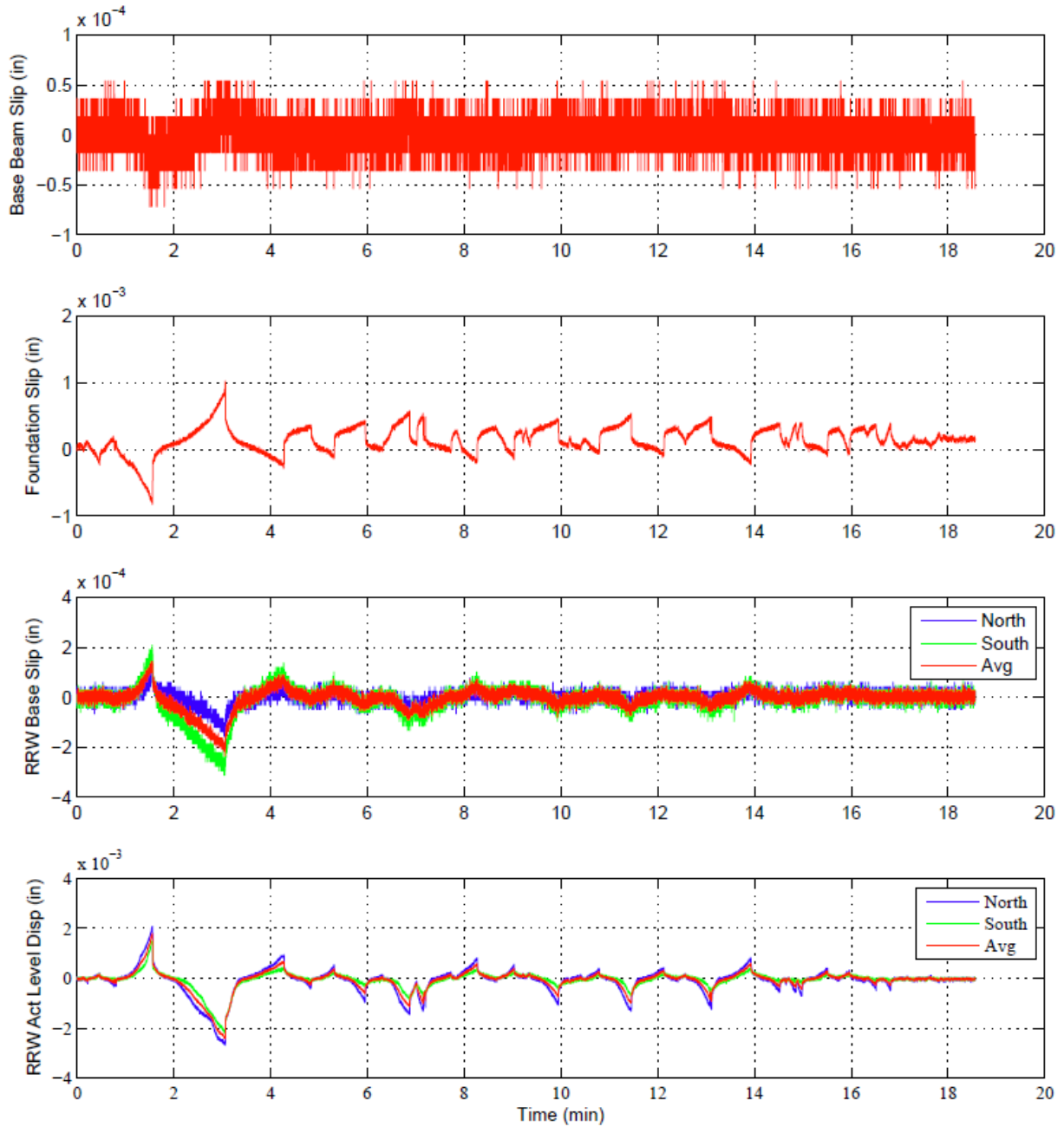
Figure B.12: Wall 2 DBE Aftershock 2 Test Setup Slips

Figure B.13 shows the slips in the clevises for the Wall 2 +/-1 in triangle motion, and Figure B.14 shows the slips in the rest of the test setup for the Wall 2 +/-1 in triangle motion.
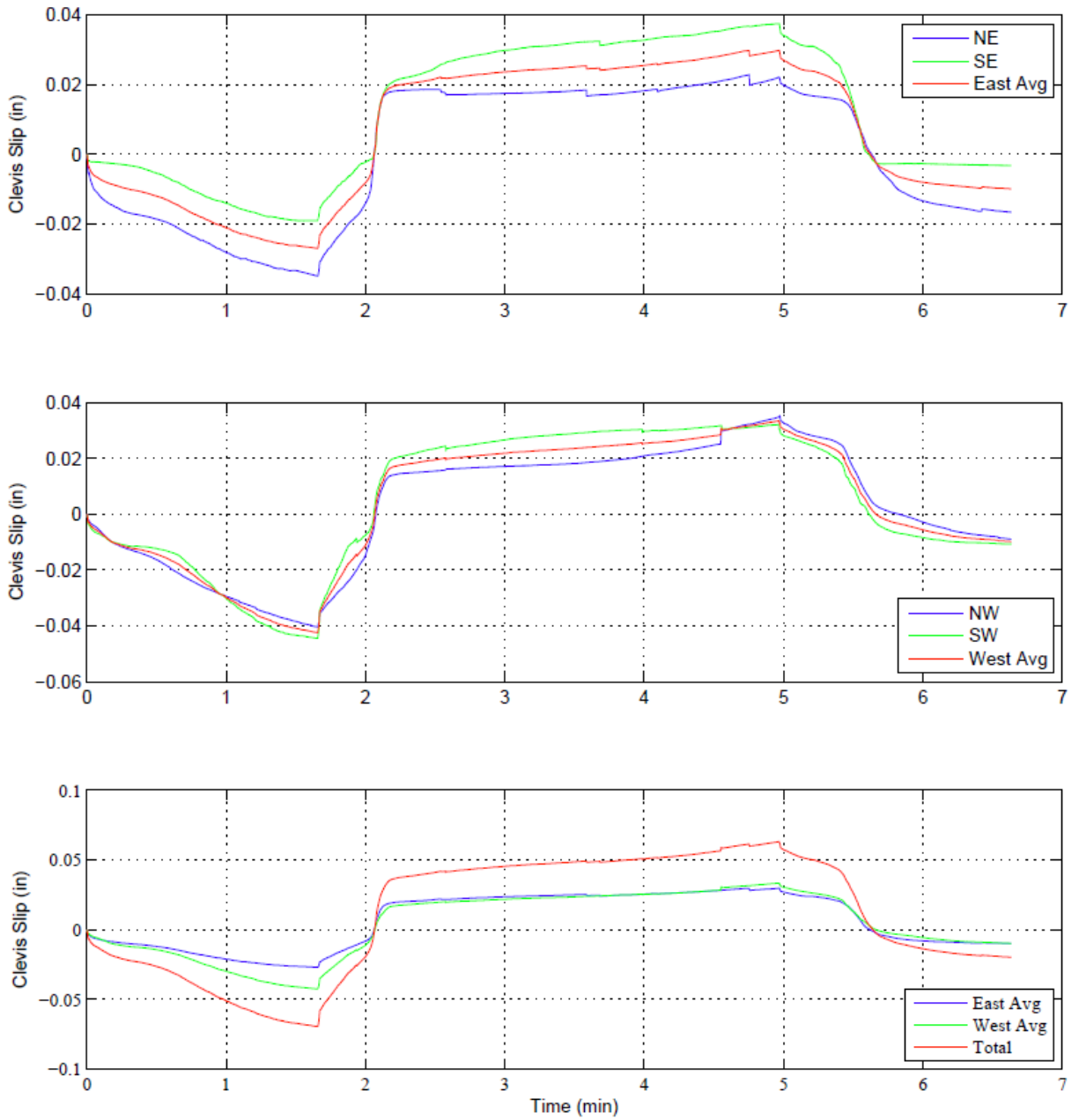
Figure B.13: Wall 2 +/-1 in Triangle Clevis Slips
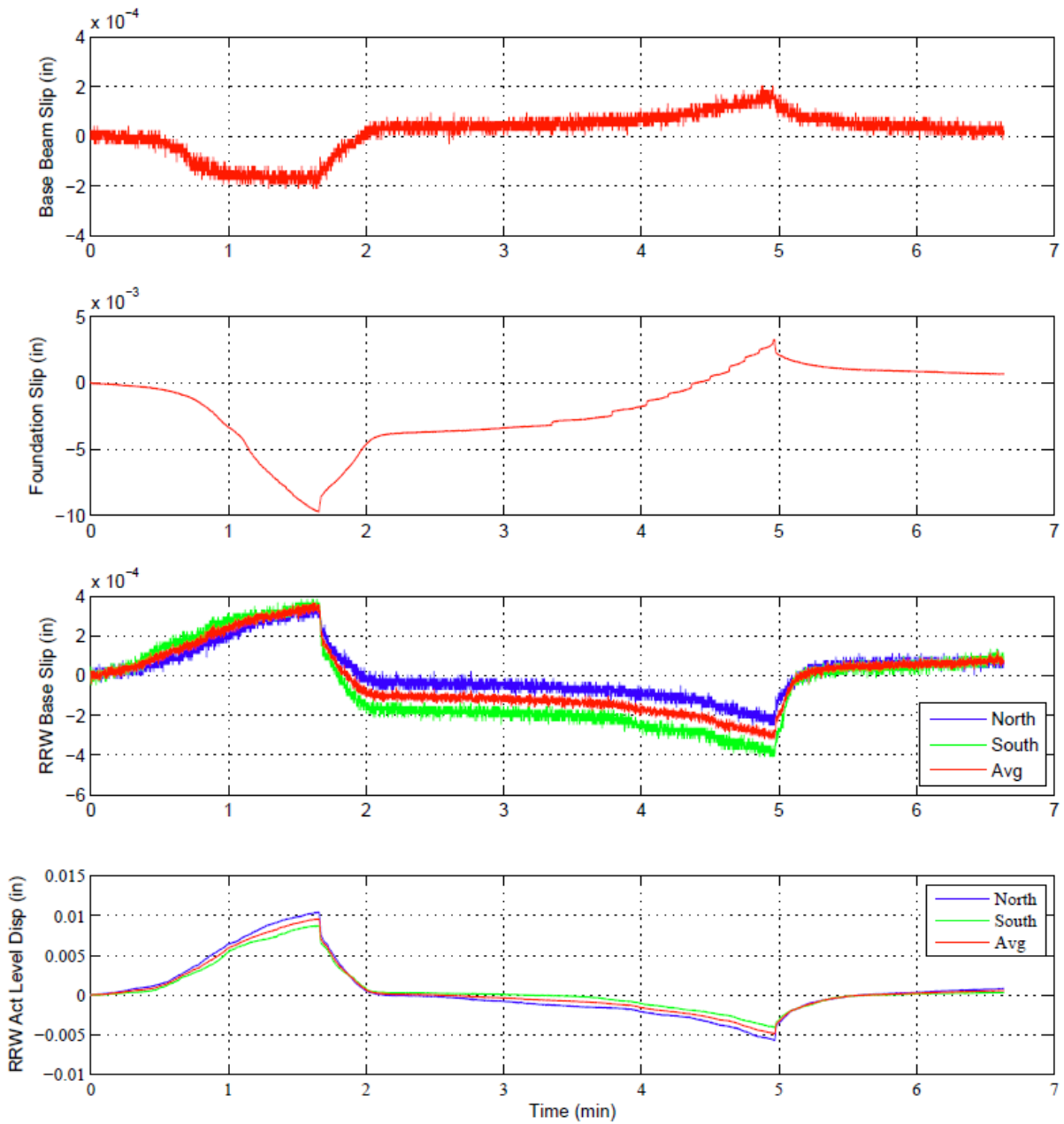
Figure B.14: Wall 2 +/-1 in Triangle Test Setup Slips

Figure B.15 shows the slips in the clevises for the Wall 2 +/-1.5 in triangle motion, and Figure B.16 shows the slips in the rest of the test setup for the Wall 2 +/-1.5 in triangle motion.
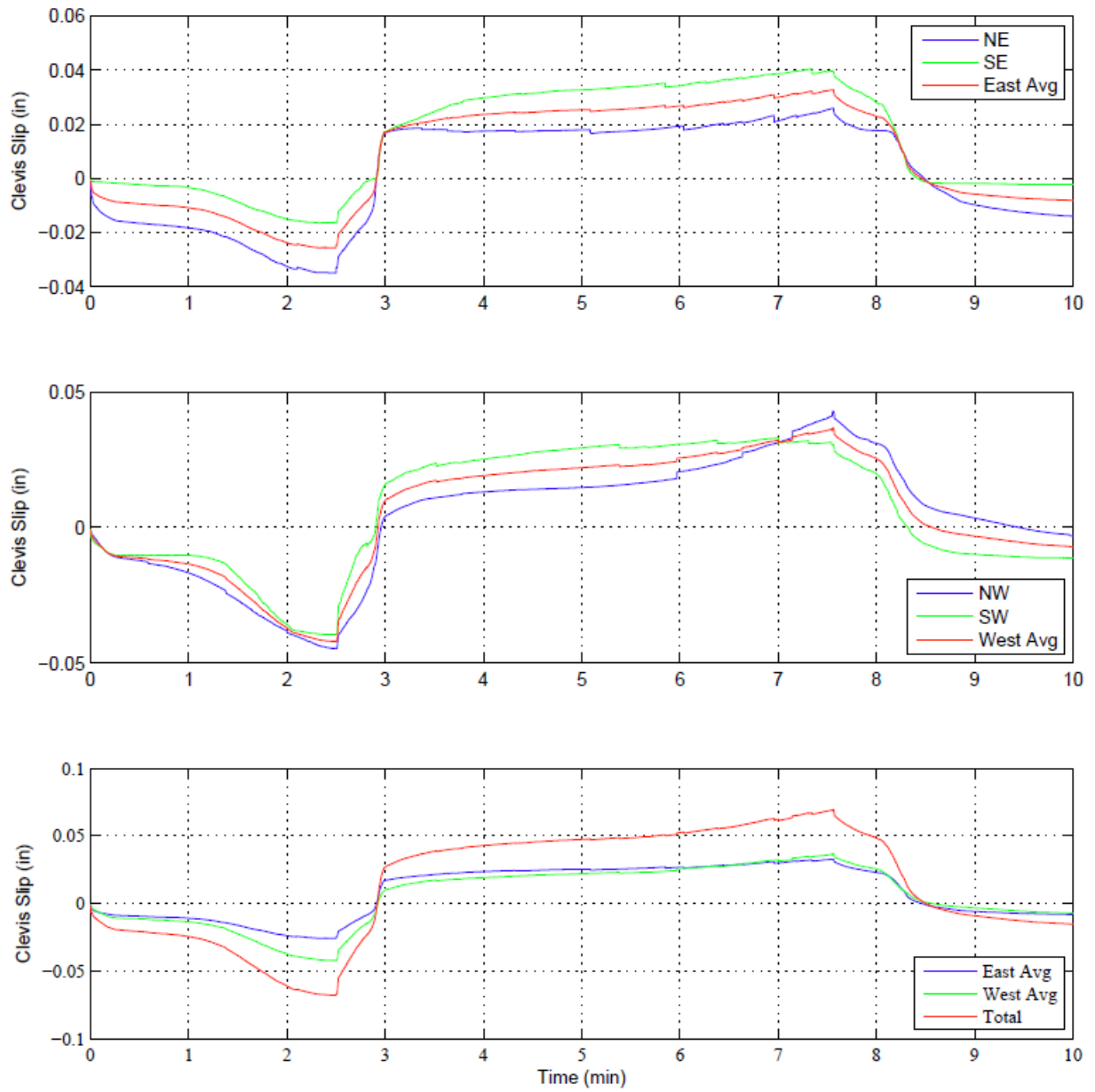
Figure B.15: Wall 2 +/-1.5 in Triangle Clevis Slips
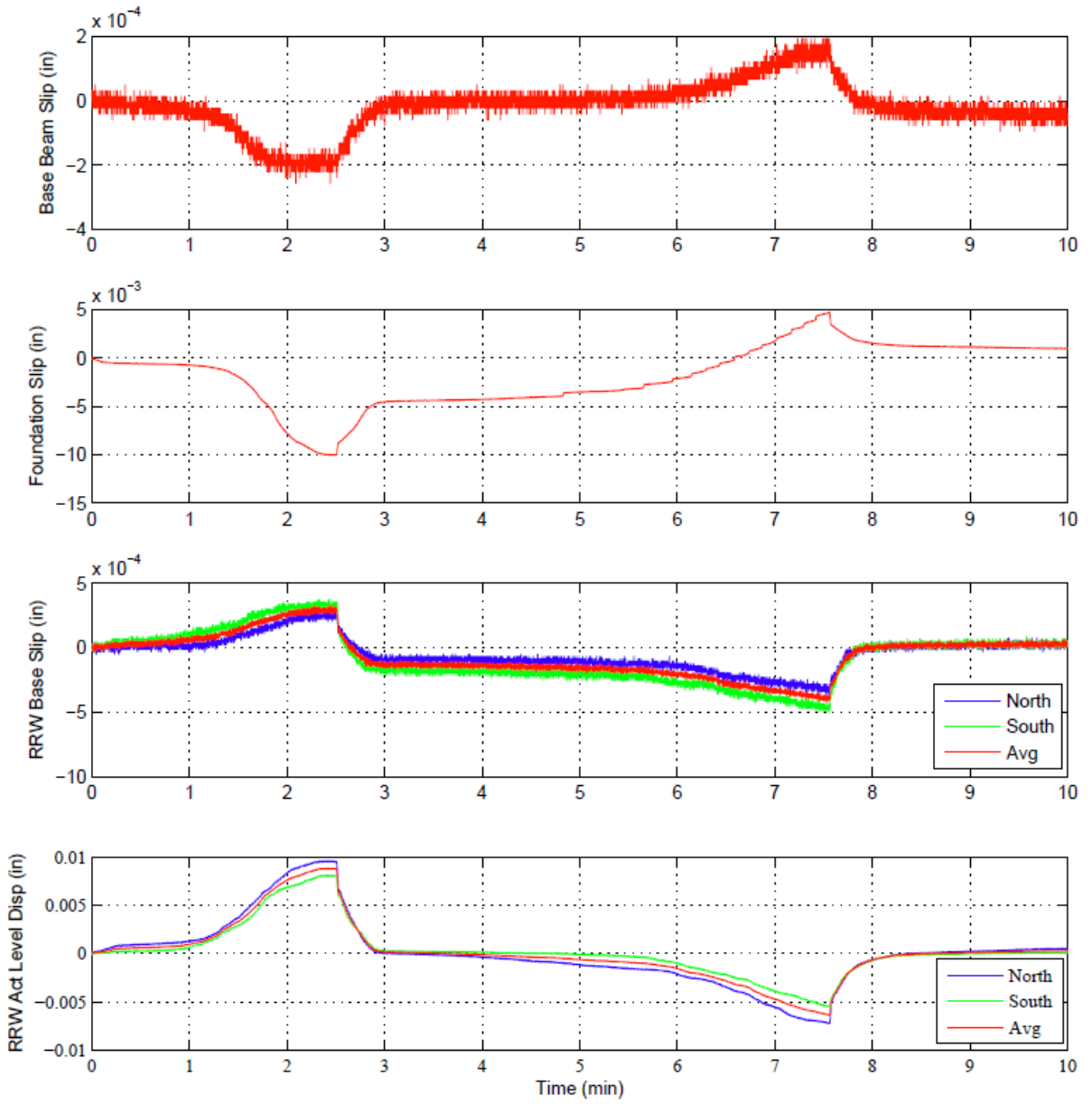
Figure B.16: Wall 2 +/-1.5 in Triangle Test Setup Slips

Appendix C: Displacement Response

C.1   WALL 1 IN-PLANE/OUT-OF-PLANE RESPONSE

The Wall 1 OBE Motion in-plane and out-of-plane displacements measured using triangulation at points along the height of the east side of the wall are shown in Figure C.1 and in Figure C.2 for points along the west side of the wall.
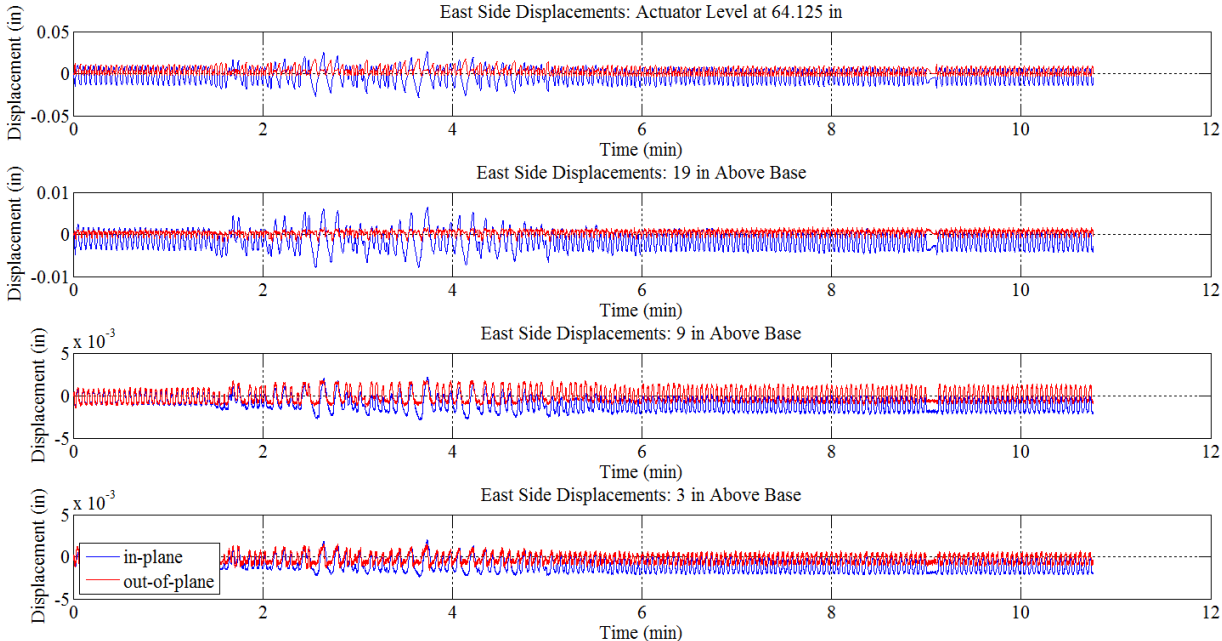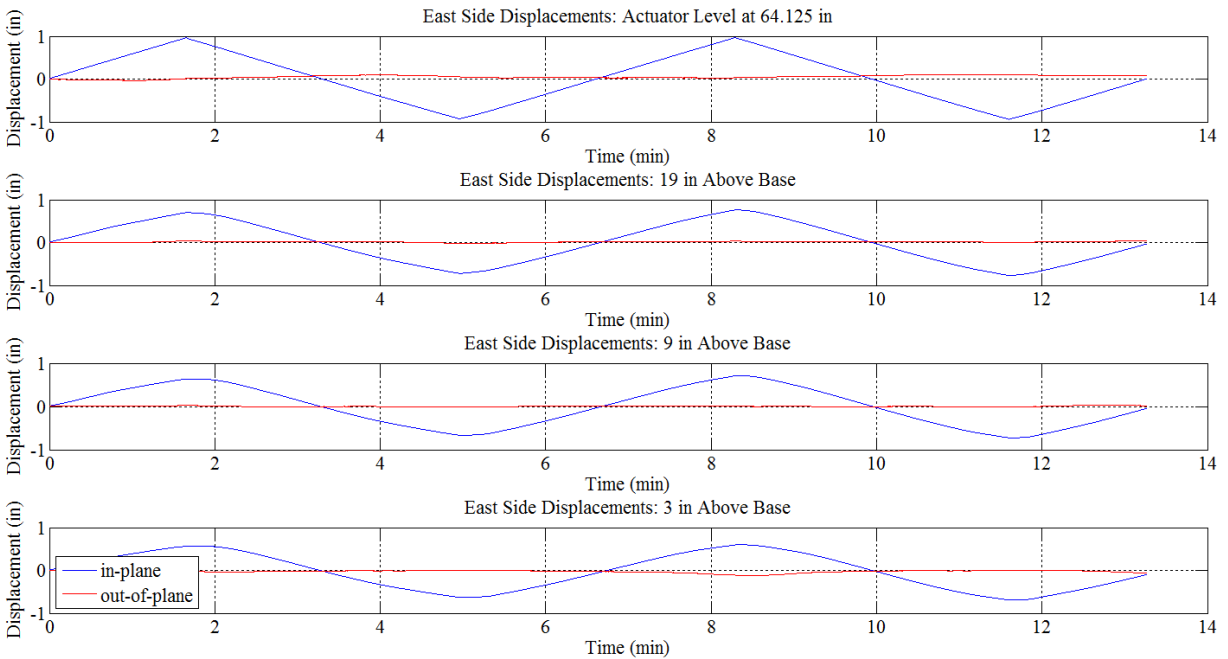

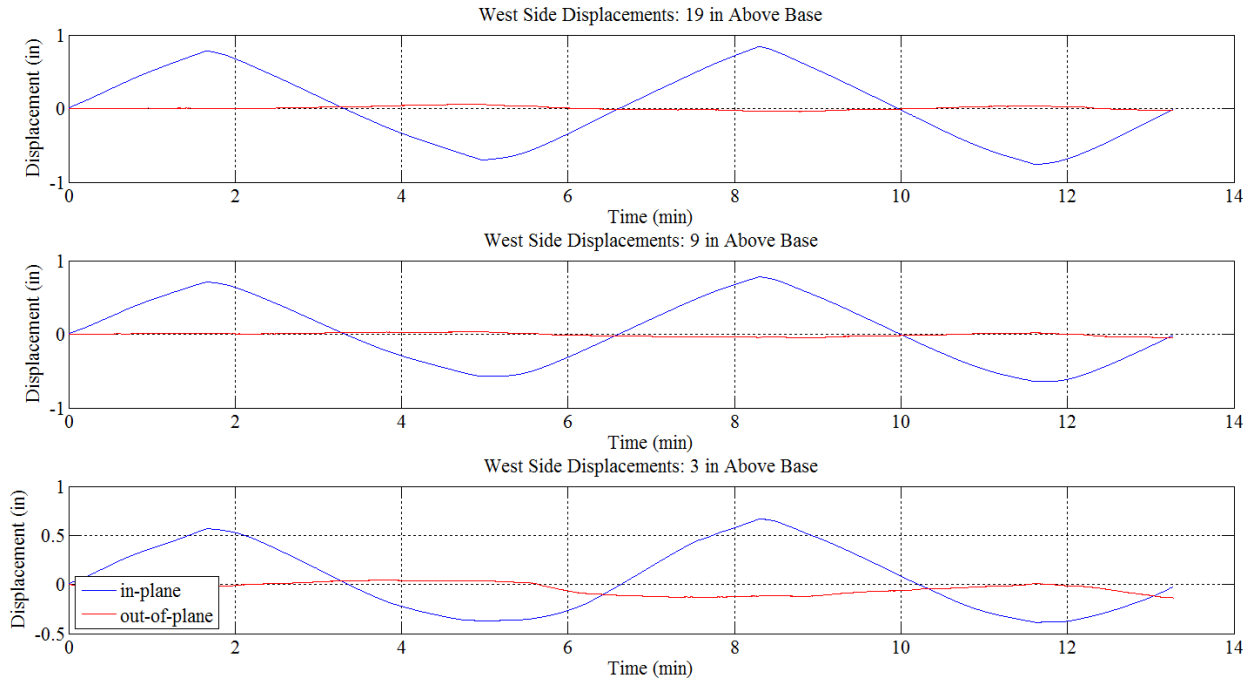**Figure C.1: Wall 1 East Side Displacements for OBE Motion**
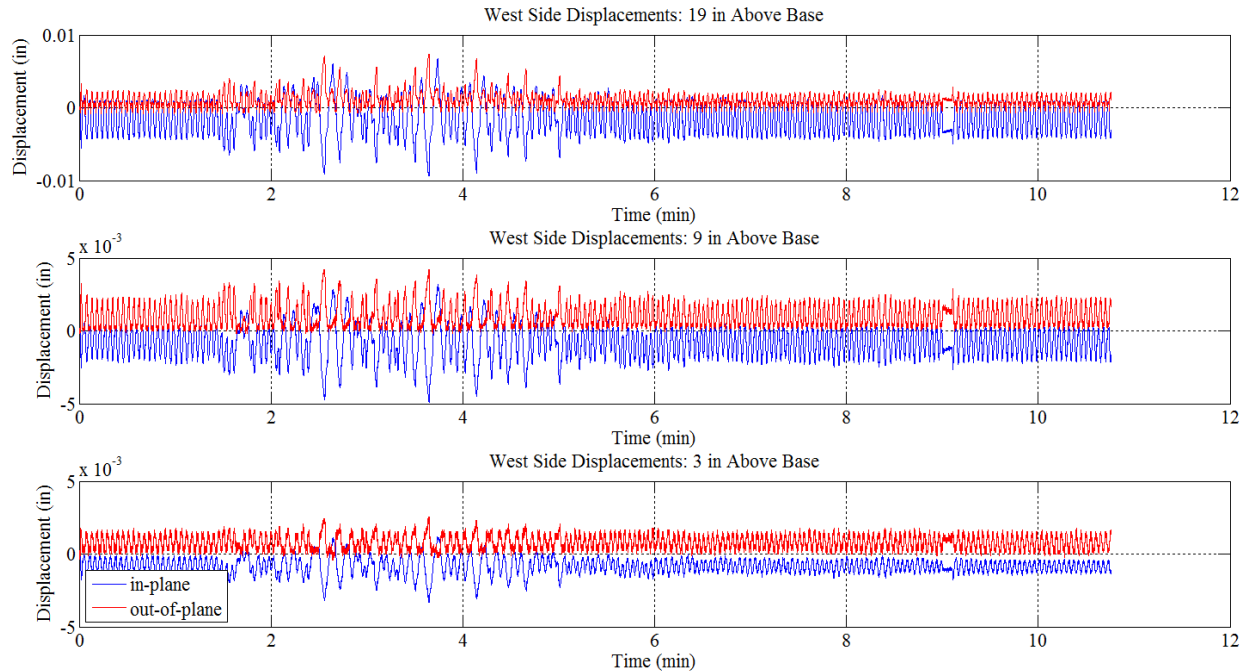
Figure C.2: Wall 1 West Side Displacements for OBE Motion

The Wall 1 DBE 0.11 Motion in-plane and out-of-plane displacements measured using triangulation at points along the height of the east side of the wall are shown in Figure C.3 and in Figure C.4 for points along the west side of the wall.
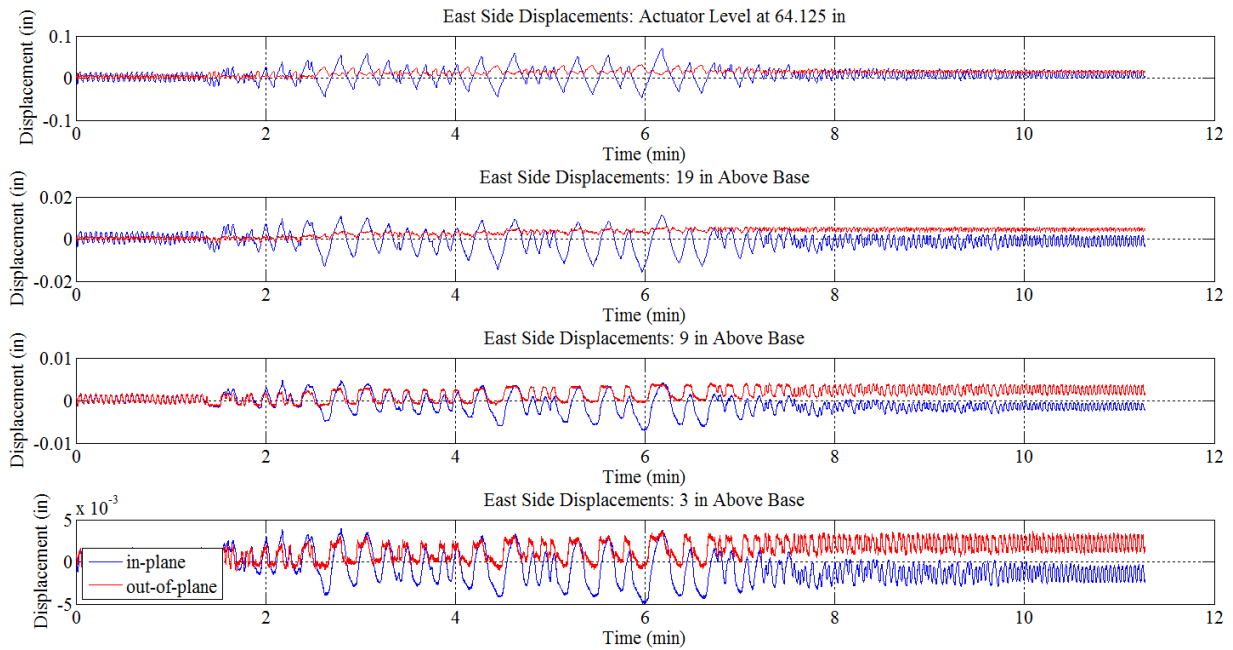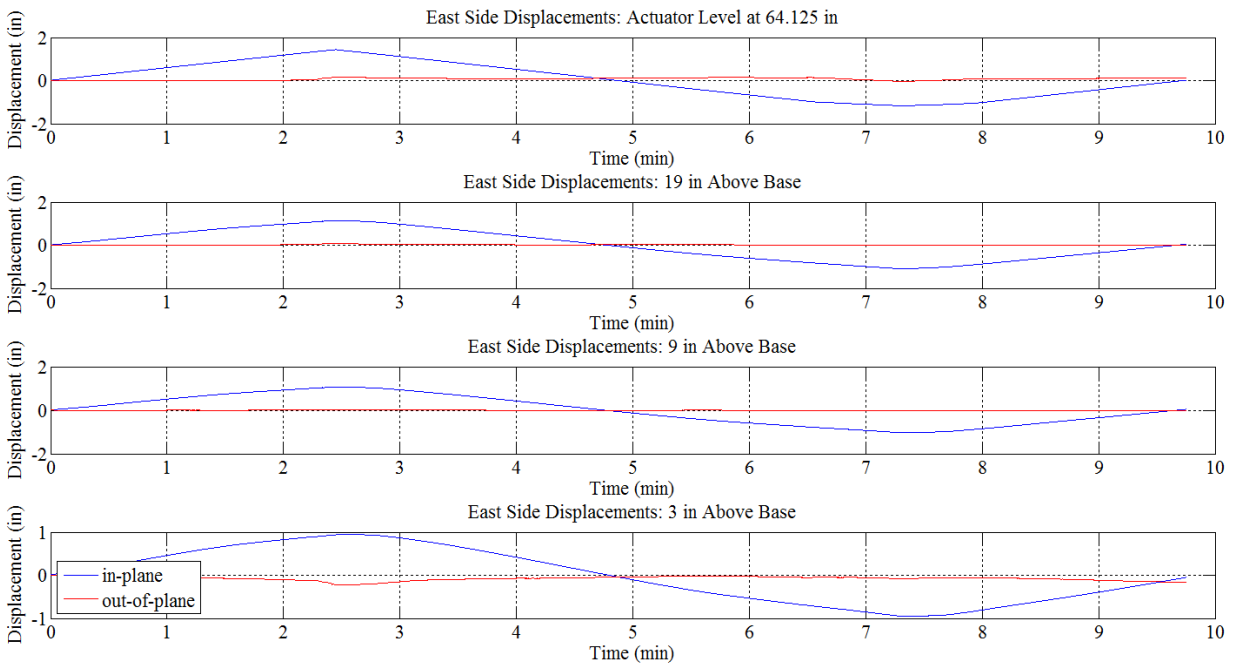

Figure C.3: Wall 1 East Side Displacements for DBE 0.11 Motion
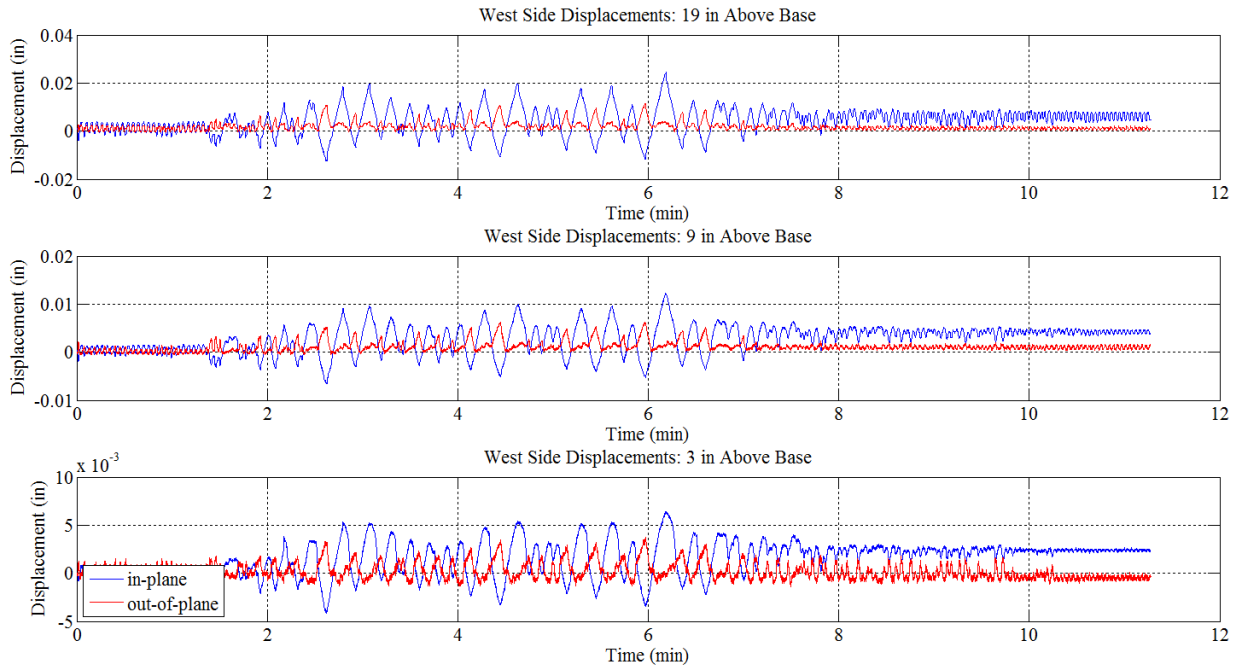
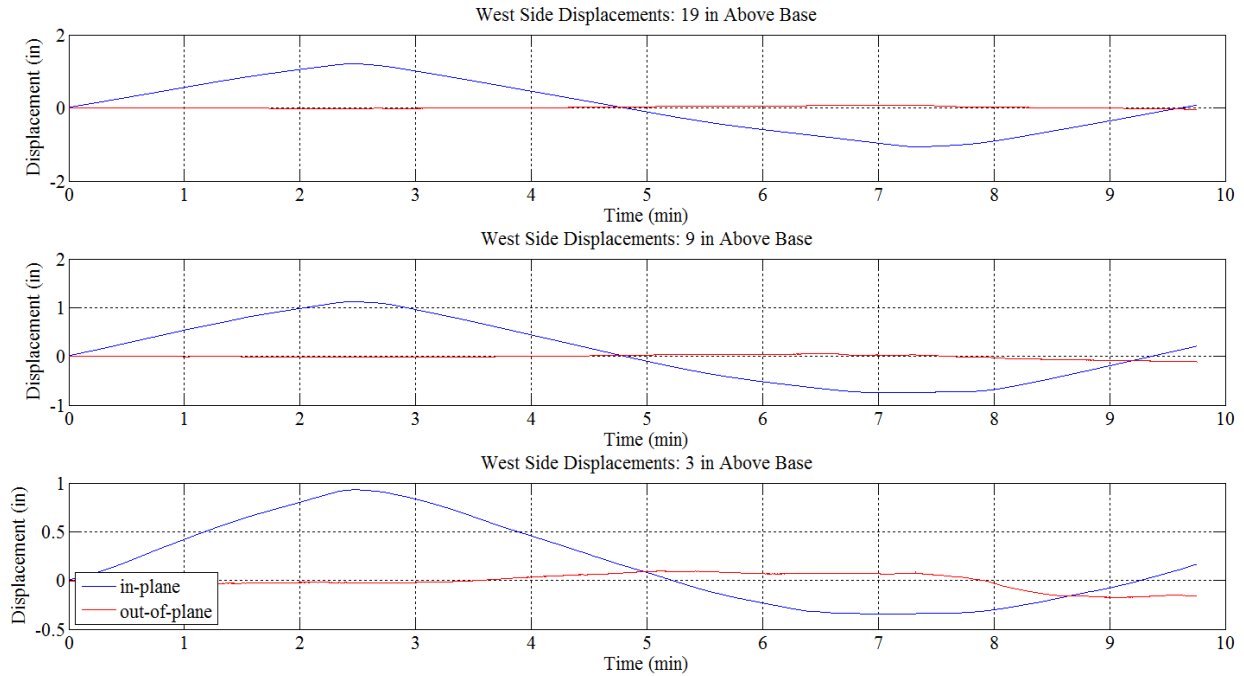**Figure C.4: Wall 1 West Side Displacements for DBE 0.11 Motion**

The Wall 1 DBE Motion in-plane and out-of-plane displacements measured using triangulation at points along the height of the east side of the wall are shown in Figure C.5 and in Figure C.6 for points along the west side of the wall.
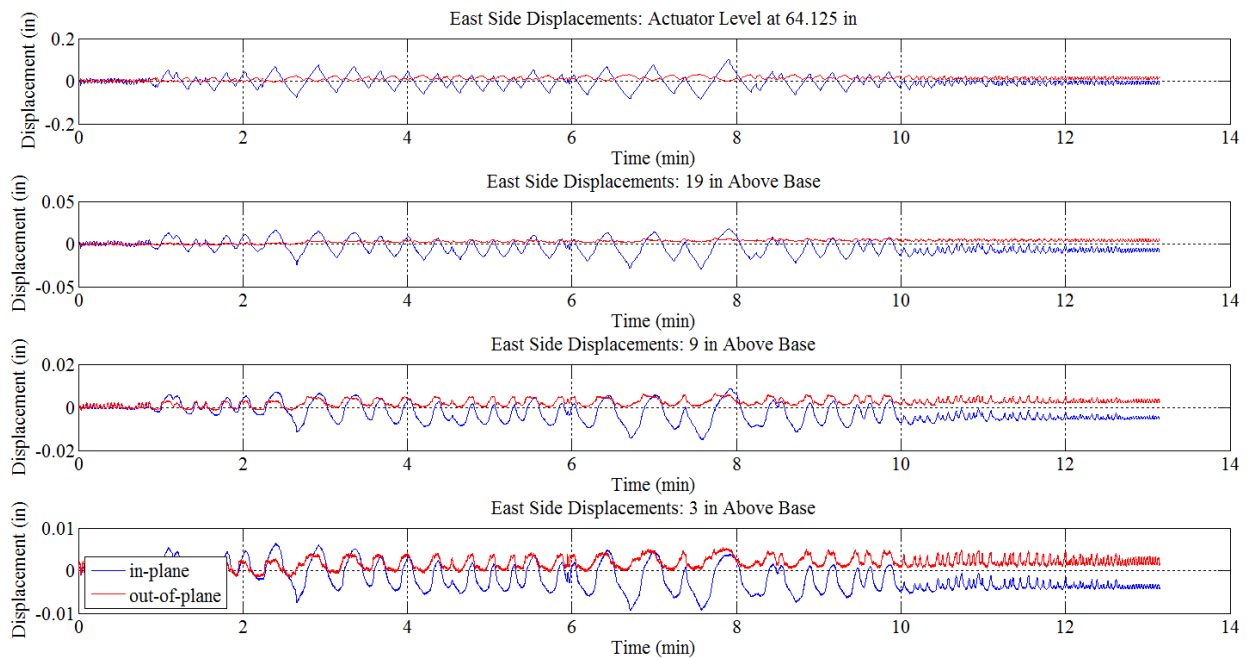
Figure C.5: Wall 1 East Side Displacements for DBE Motion
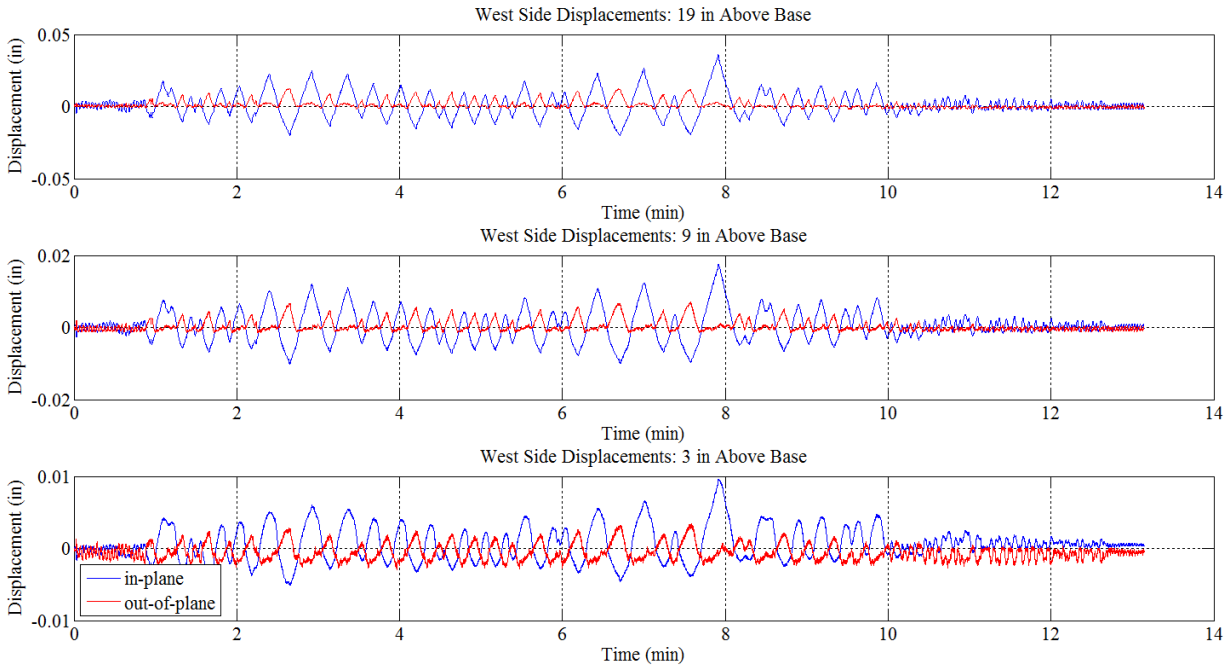
Figure C.6: Wall 1 West Side Displacements for DBE Motion

The Wall 1 DBE Aftershock Motion in-plane and out-of-plane displacements measured using triangulation at points along the height of the east side of the wall are shown in Figure C.7 and in Figure C.8 for points along the west side of the wall.
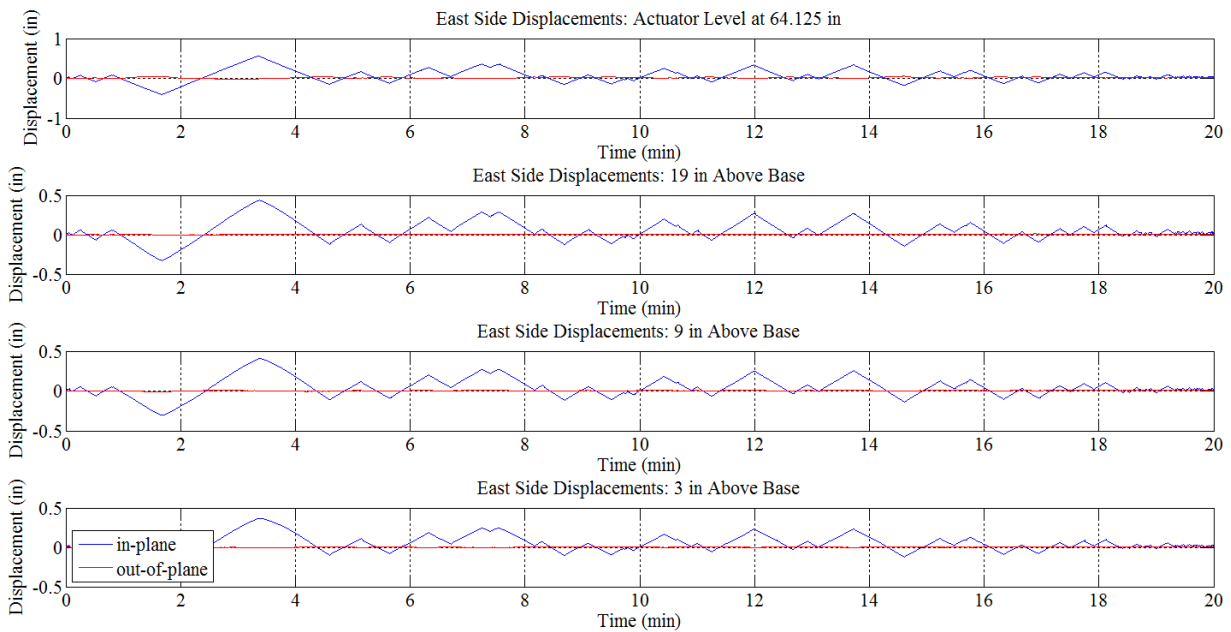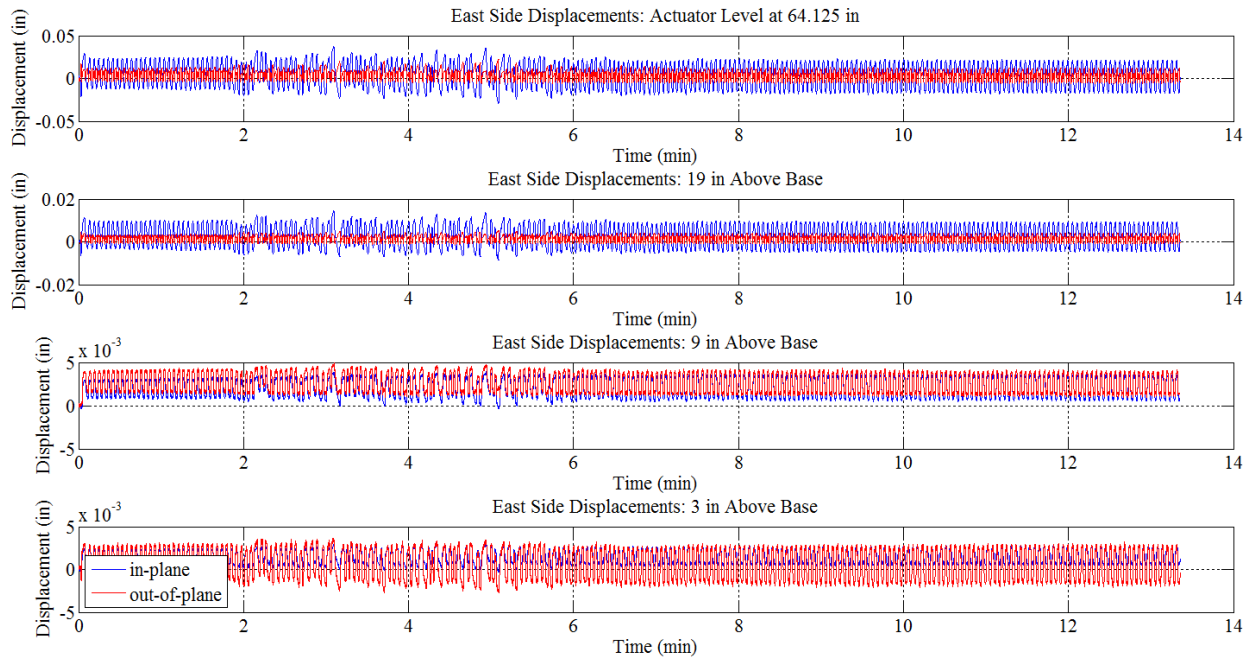

Figure C.7: Wall 1 East Side Displacements for DBE Aftershock Motion

193
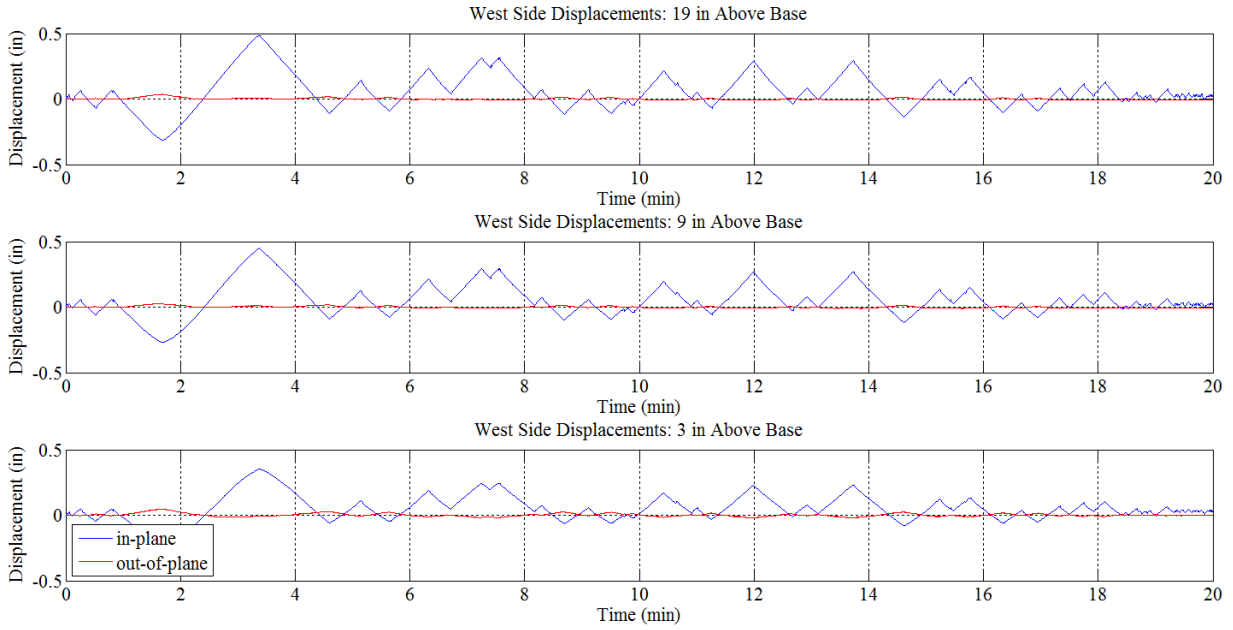
Figure C.8: Wall 1 West Side Displacements for DBE Aftershock Motion

The Wall 1 +\-1 in Triangle Motion in-plane and out-of-plane displacements measured using triangulation at points along the height of the east side of the wall are shown in Figure C.9 and in Figure C.10 for points along the west side of the wall.

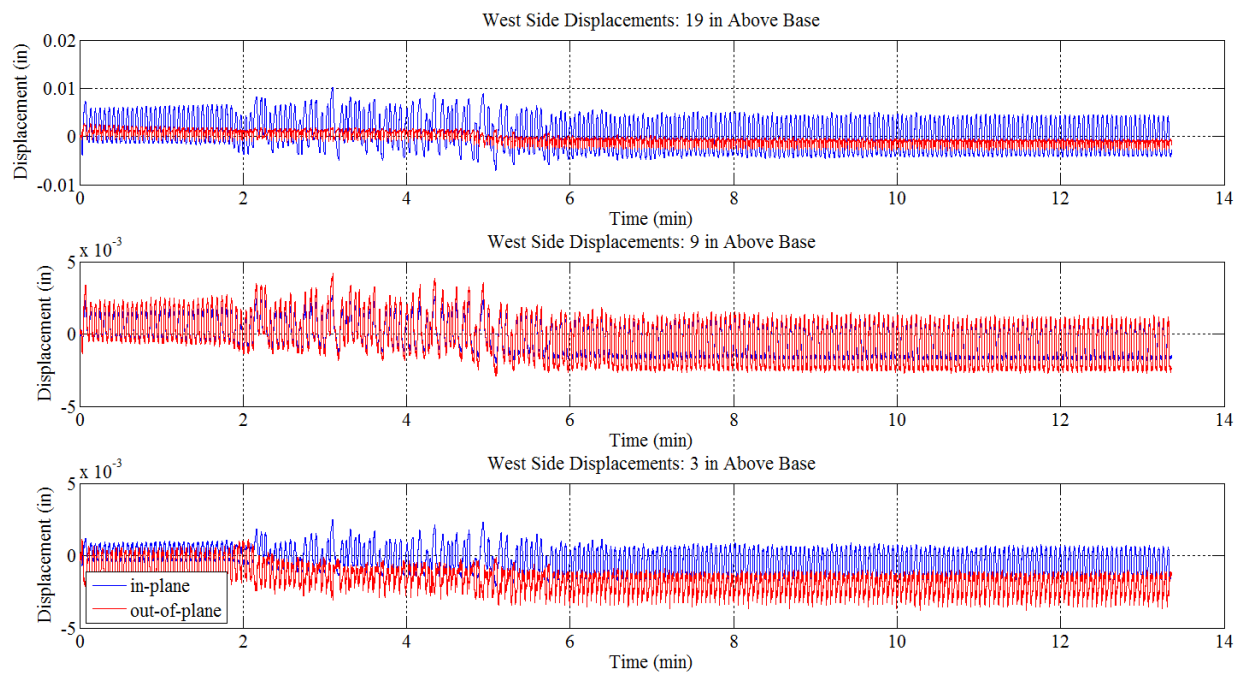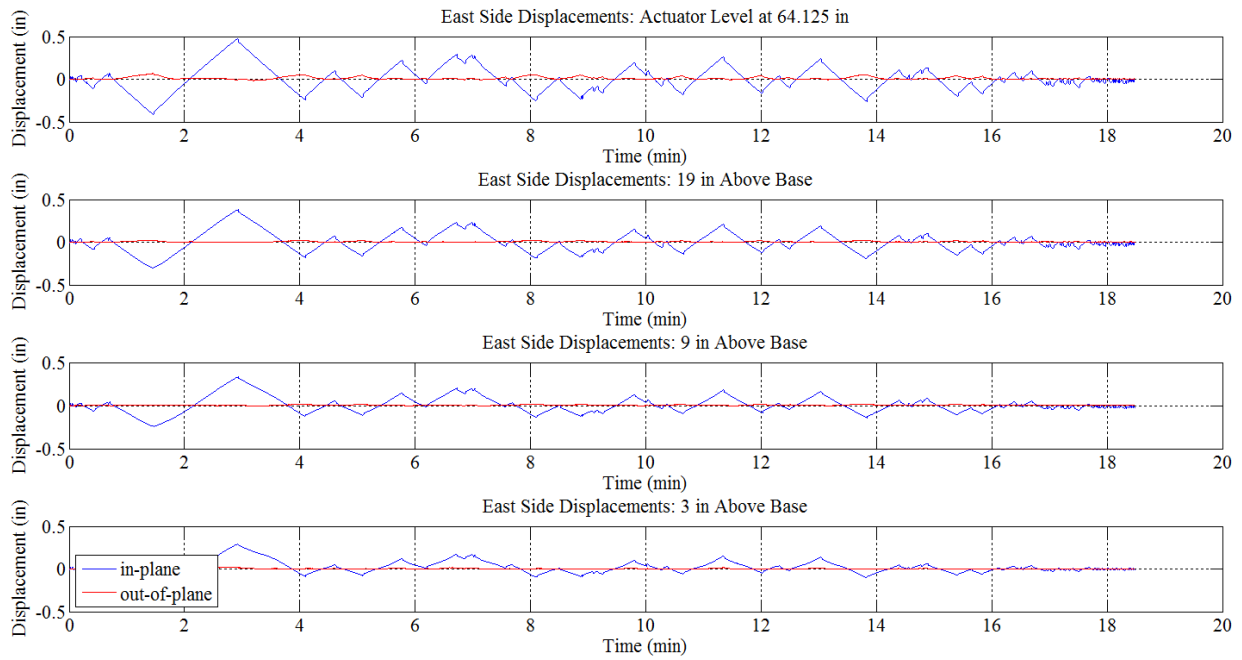**Figure C.9: Wall 1 East Side Displacements for +\-1 in Triangle Motion**

Figure C.10: Wall 1 West Side Displacements for +\-1 in Triangle Motion

The Wall 1 +\-1.5 in Triangle Motion in-plane and out-of-plane displacements measured using triangulation at points along the height of the east side of the wall are shown in Figure C.11 and in Figure C.12 for points along the west side of the wall.

Figure C.11: Wall 1 East Side Displacements for +\-1.5 in Triangle Motion

Figure C.12: Wall 1 West Side Displacements for +\-1.5 in Triangle Motion

C.2   WALL 2 IN-PLANE/OUT-OF-PLANE RESPONSE

The Wall 2 OBE Motion in-plane and out-of-plane displacements measured using triangulation at points along the height of the east side of the wall are shown in Figure C.13 and in Figure C.14 for points along the west side of the wall.

196

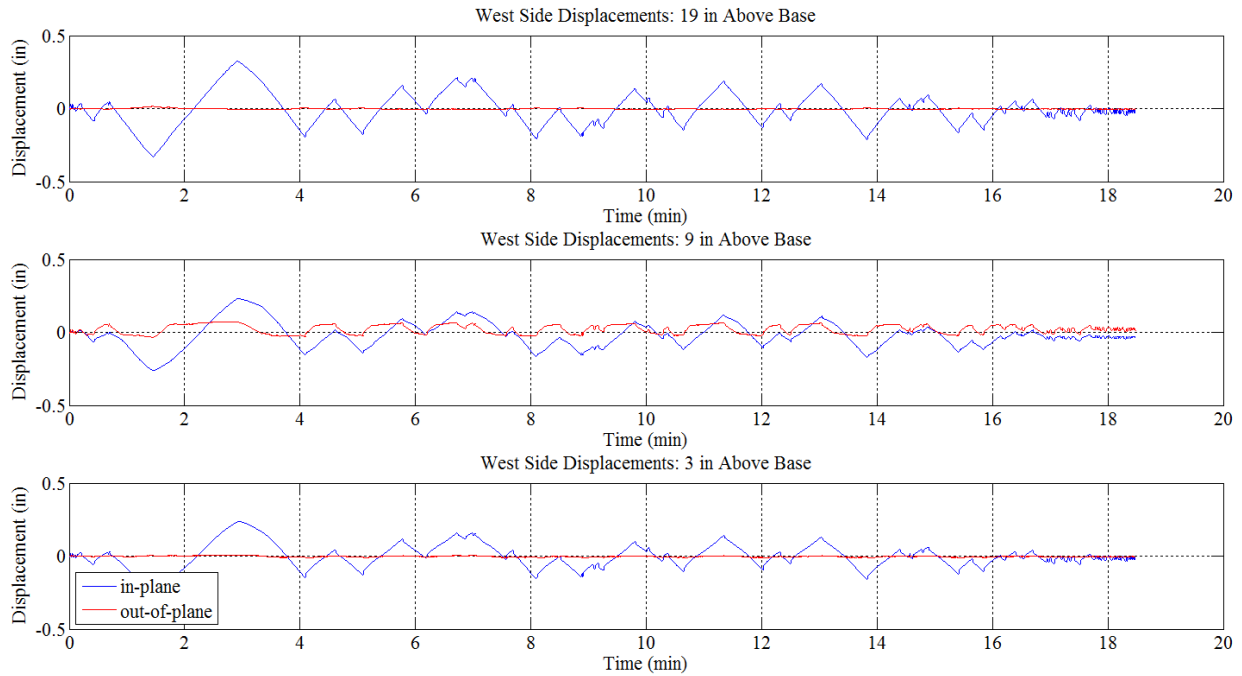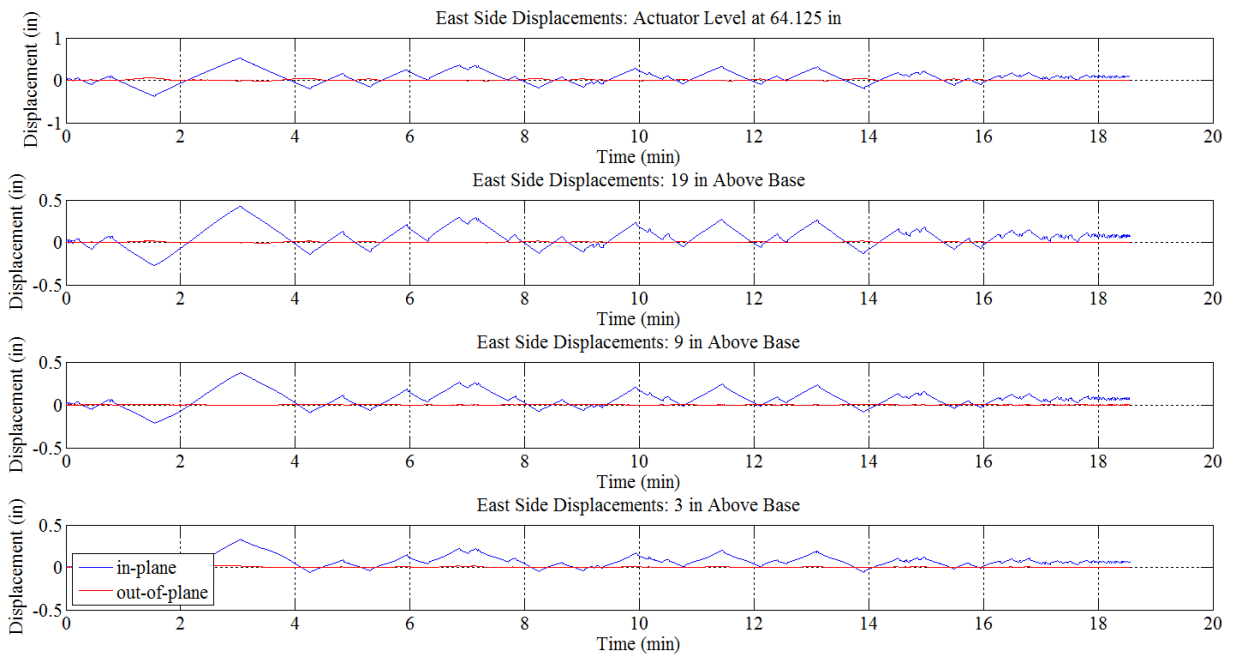**Figure C.13: Wall 2 East Side Displacements for OBE Motion**

Figure C.14: Wall 2 West Side Displacements for OBE Motion

The Wall 2 DBE Aftershock 1 Motion in-plane and out-of-plane displacements measured using triangulation at points along the height of the east side of the wall are shown in Figure C.15 and in Figure C.16 for points along the west side of the wall.

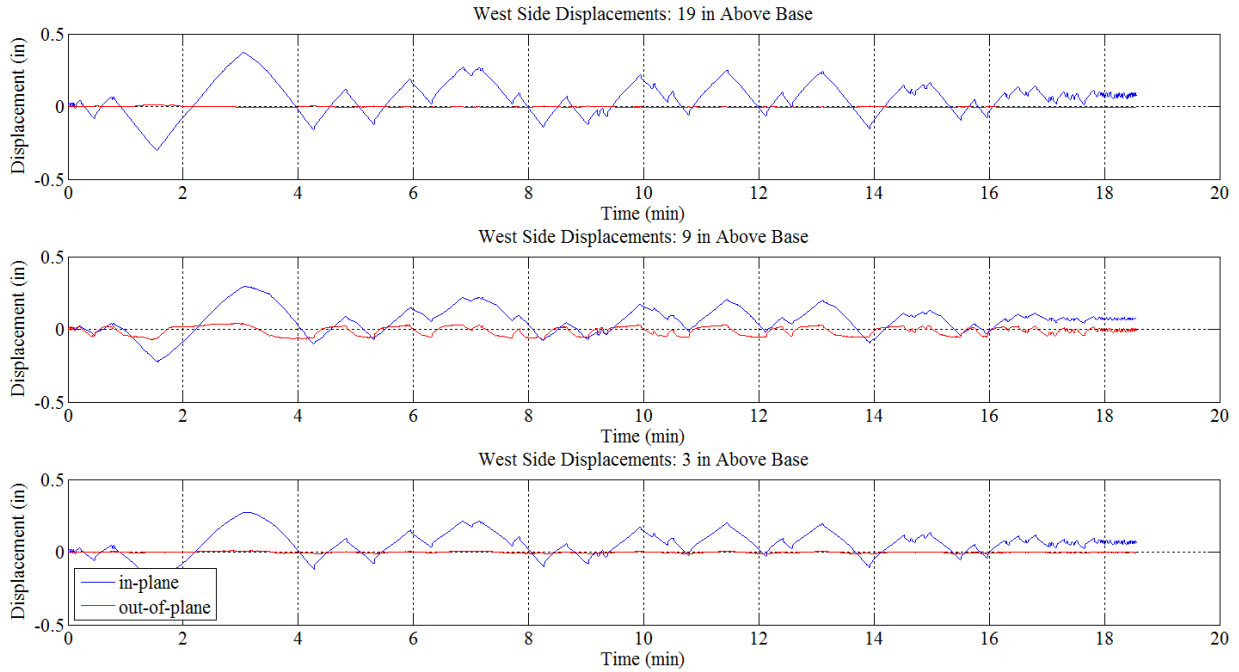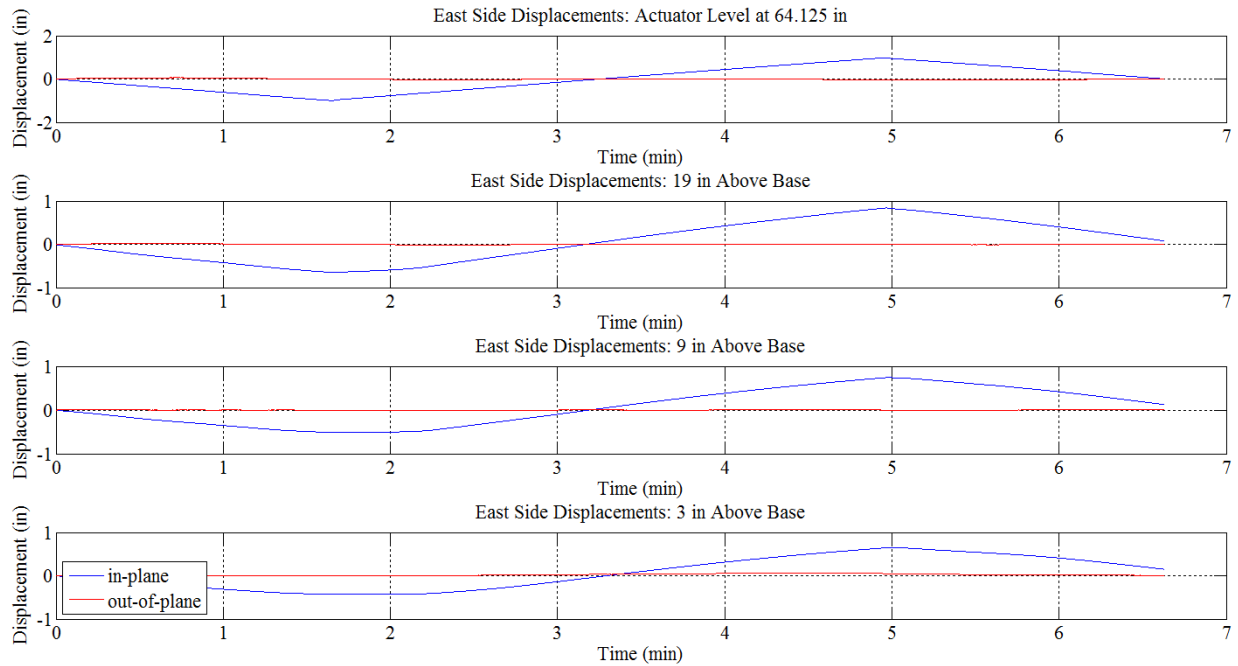**Figure C.15: Wall 2 East Side Displacements for DBE Aftershock 1 Motion**

Figure C.16: Wall 2 West Side Displacements for DBE Aftershock 1 Motion

The Wall 2 DBE Aftershock 2 Motion in-plane and out-of-plane displacements measured using triangulation at points along the height of the east side of the wall are shown in Figure C.17 and in Figure C.18 for points along the west side of the wall.

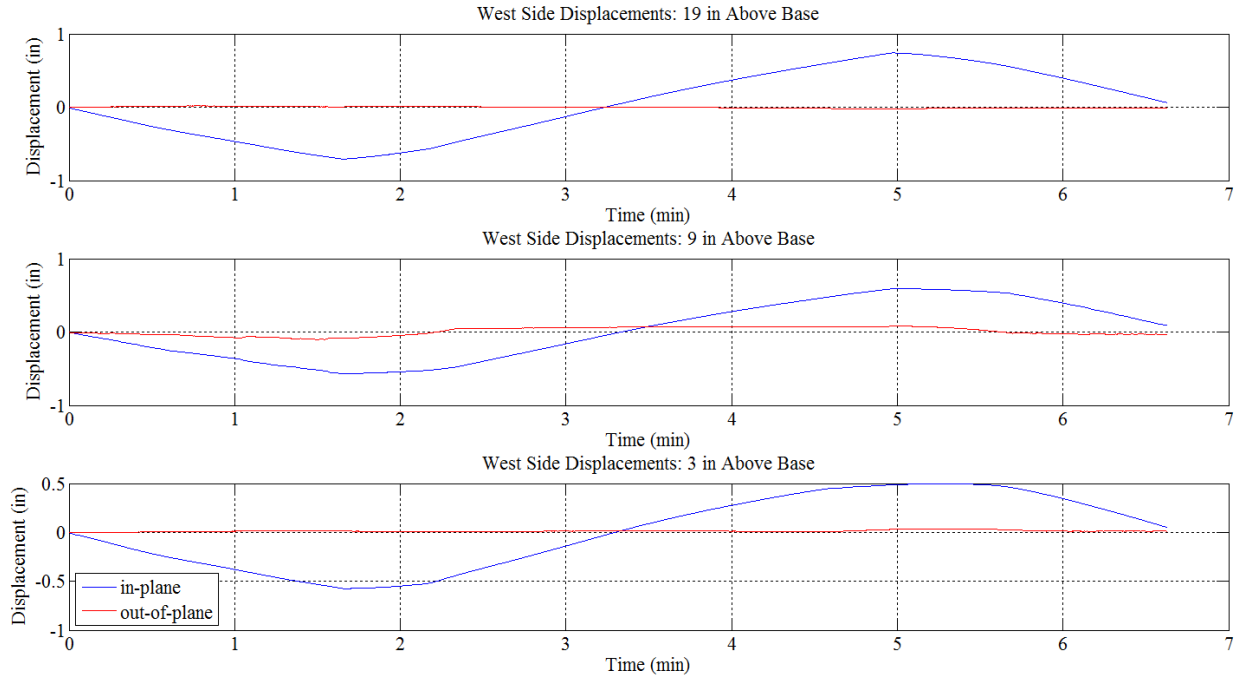**Figure C.17: Wall 2 East Side Displacements for DBE Aftershock 2 Motion**

Figure C.18: Wall 2 West Side Displacements for DBE Aftershock 2 Motion

The Wall 2 +\-1 in Triangle Motion in-plane and out-of-plane displacements measured using triangulation at points along the height of the east side of the wall are shown in Figure C.19 and in Figure C.20 for points along the west side of the wall.
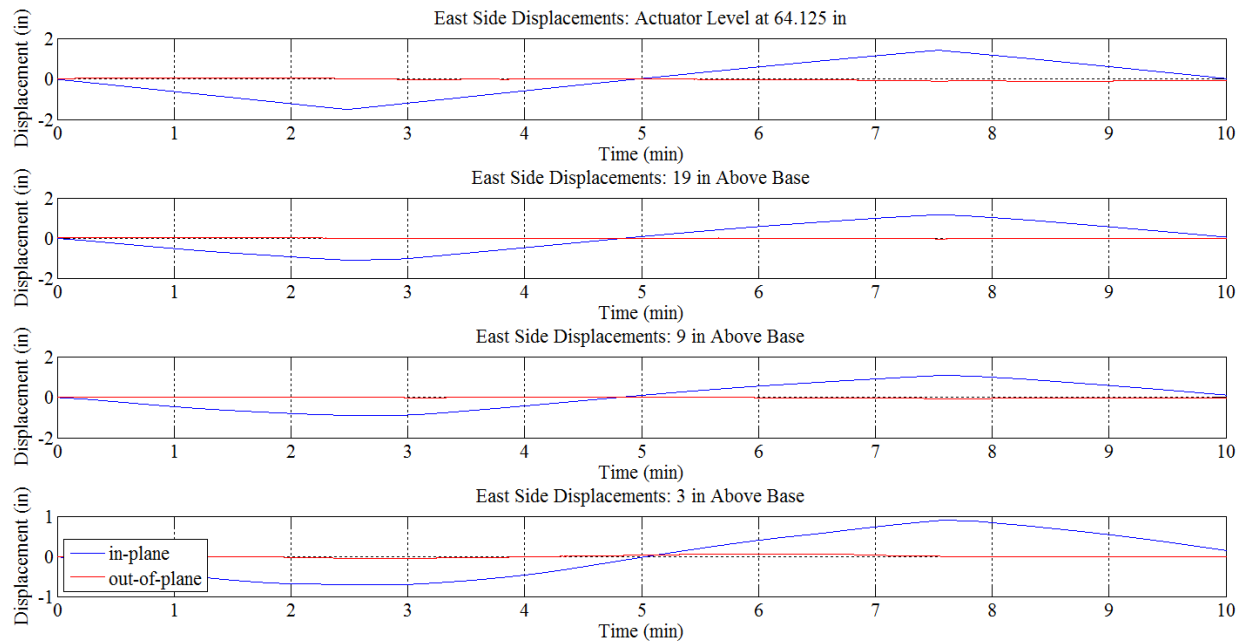

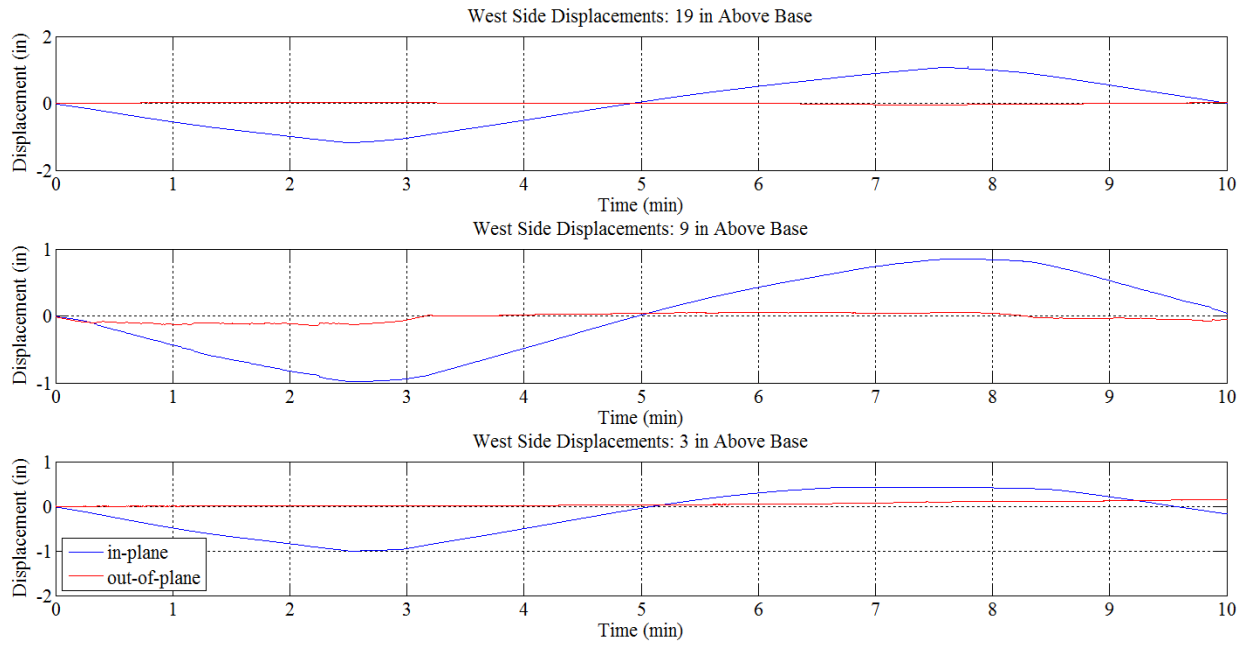**Figure C.19: Wall 2 East Side Displacements for +\-1 in Triangle Motion**

Figure C.20: Wall 2 West Side Displacements for +\-1 in Triangle Motion

The Wall 2 +\-1.5 in Triangle Motion in-plane and out-of-plane displacements measured using triangulation at points along the height of the east side of the wall are shown in Figure C.21 and in Figure C.22 for points along the west side of the wall.

Figure C.21: Wall 2 East Side Displacements for +\-1.5 in Triangle Motion

Figure C.22: Wall 2 West Side Displacements for +\-1.5 in Triangle Motion